Final Report

to

Dr. Gerald Witt
Air Force Office of Scientific Research

Low Noise Amplifiers Based on Lattice Engineered Substrates

AFOSR Program #F49620-00-1-0286

James S. Speck
Materials Department

Umesh K. Mishra
Electrical and Computer Engineering Department

University of California
Santa Barbara, CA 93106

BEST AVAILABLE COPY

20041119 019

REPORT DOCUMENTATION PAGE

AFRL-SR-AR-TR-04-

0577

data needed, and completing and reviewing this collection of information. Send comments regarding this burden estimate or any othe
this burden to Department of Defense, Washington Headquarters Services, Directorate for Information Operations and Reports (0704-
4302. Respondents should be aware that notwithstanding any other provision of law, no person shall be subject to any penalty for faili
valid OMB control number. **PLEASE DO NOT RETURN YOUR FORM TO THE ABOVE ADDRESS.**

the
ing
2-
ently

1. REPORT DATE *(DD-MM-YYYY)*
November 1, 2004

2. REPORT TYPE
Annual

3. DATES COVERED *(From - To)*
09/01/2002 - 08/31/2003

4. TITLE AND SUBTITLE
Low Noise Amplifiers Based on Lattice Engineered Substrates

5a. CONTRACT NUMBER
F49620-00-1-0286

5b. GRANT NUMBER

5c. PROGRAM ELEMENT NUMBER
61102F

6. AUTHOR(S)
James S. Speck
Umesh K. Mishra

5d. PROJECT NUMBER
2305B

5e. TASK NUMBER

5f. WORK UNIT NUMBER

7. PERFORMING ORGANIZATION NAME(S) AND ADDRESS(ES)

The Regents of the Univ. of
California
Univ. of California
Santa Barbara, Cheadle Hall
Santa Barbara, CA 93106-2050

8. PERFORMING ORGANIZATION REPORT NUMBER

9. SPONSORING / MONITORING AGENCY NAME(S) AND ADDRESS(ES)
USAF,AFRL
AFOSR
4015 Wilson Blvd, Room 713
Arlington, VA 22203-1954

NV

10. SPONSOR/MONITOR'S ACRONYM(S)

11. SPONSOR/MONITOR'S REPORT NUMBER(S)

12. DISTRIBUTION / AVAILABILITY STATEMENT

13. SUPPLEMENTARY NOTES

14. ABSTRACT

In this program we are developing novel strain relaxed templates for device applications including low noise amplifiers. The approach we are investigating utilizes the process of relaxation of a coherent hypercritical thickness ($h>h_{critical}$) strained semiconductor overlayer (*e.g.*, InGaAs). In the first two years of this program, we had focused on the relaxation of a strained layer in direct contact with an oxidizing Al containing semiconductor (AlAs or AlGaAs). In the third year of this program, most of our efforts were focused on determining the origin of the commonly observed cross-hatch morphology in strain-relaxed misfitting layers. We have also discovered new dislocation-related relaxation mechanisms in the group III nitrides. Finally, we have also provided new insight and modeling of threading dislocation reduction in lateral epitaxial overgrowth.

15. SUBJECT TERMS

16. SECURITY CLASSIFICATION OF:

a. REPORT

b. ABSTRACT

c. THIS PAGE

17. LIMITATION OF ABSTRACT

18. NUMBER OF PAGES

19a. NAME OF RESPONSIBLE PERSON

19b. TELEPHONE NUMBER *(include area code)*

In this program we developed novel strain relaxed templates for device applications including low noise amplifiers. The approach we investigated utilized the process of relaxation of a coherent hypercritical thickness ($h>h_{critical}$} strained semiconductor overlayer (*e.g.*, InGaAs) in direct contact with an oxidizing Al containing semiconductor (AlAs or AlGaAs). Wet oxidation of the Al-containing layer results in enhanced strain relaxation without generation of high densities of threading dislocations. These relaxed templates have been referred to as *Lattice Engineered Substrates* (*LES*). The LES templates are then used for the growth of low defect density strained layers. In addition to developing LES for large lattice constant materials, we have explored lateral oxidation as a new tool for charge control in both HEMTs and HBTs. We developed new analytical models for the commonly observed cross-hatch morphology in strain relaxed semiconductors. We developed new models for a recently observed strain relaxation phenomena in nitride semiconductors.

Summary of Key Findings

We provide a brief summary of the main results of our work and where possible, include the resulting publication from the work as an Appendix.

Basic Studies of Surface Morphology in Strain Relaxation.

In this program we developed a fundamental understanding of the commonly observed cross-hatch surface morphology in strain-relaxed heteroepitaxial films. We initially proposed that the cross-hatch morphology is directly related with strain relaxation via threading dislocation glide which results in both surface step and misfit dislocation formation [see Andrews *et al.*, *Appl. Phys. Lett.* **77**, 3740 (2000) and Andrews *et al. J. Appl. Phys.* **91**, 1933 (2002)]. We used solutions for the stress fields and displacement fields for periodic misfit dislocation arrays which include the effects of the free surface. These solutions avoid truncation errors associated with finite dislocation arrays that were used in our initial work. We calculated the surface height profile for relaxed films where the misfit dislocations were introduced randomly or the misfit dislocations were placed in groups with alternating sign of the normal component of their Burgers vector. We have calculated the surface height profiles where the slip step remains at the surface ('slip step only' or SSO) and where the slip step is eliminated ('slip step eliminated' or SSE) due to annihilation of opposite sense steps, such as could happen during growth or lateral mass transport. For relaxed films, we find that the surface height undulations, characteristic of cross-hatch, increase with increasing film thickness for the SSO case, whereas the surface becomes flatter for the SSE case. Experiments on relaxed $In_{0.25}Ga_{0.75}As$ films on (001) GaAs show that the surface height undulations in the [110] direction increase with increasing film thickness. Thus, we conclude that with increasing film thickness the cross-hatch in the slow diffusion [110] direction is best described by the SSO case. This body of work, supported under this program, is the first analytic treatment of cross-hatch – the most commonly observed morphology in strain relaxed films.

Full details of this work are given in the publications (provided as Appendices I, II, and III):

"Development of cross-hatch morphology during growth of lattice mismatched layers," A.M. Andrews, A.E. Romanov, J.S. Speck, M. Bobeth, W. Pompe, *Appl. Phys. Lett.* **77**, 3740 (2000).

"Modeling crosshatch surface morphology in growing mismatched layers,"
A.M. Andrews, J.S. Speck, A.E. Romanov, M. Bobeth, W. Pompe, *J. Appl. Phys.* **91**, 1933 (2002).

"Modeling crosshatch surface morphology in growing mismatched layers. Part II: Periodic boundary conditions and dislocation groups,"
A.M. Andrews, R. LeSar, M.A. Kerner, J.S. Speck, A.E. Romanov, A.L. Kolesnikova, M. Bobeth, W. Pompe, *J.Appl. Phys.* **95**, 6032 (2004).

Oxidation Control of GaAs pHEMTs for High Efficiency Applications

Substantial results were realized in the oxide-based electronics in this program. In the area of pHEMTs, we completed a comparative study of partially oxidized, unoxidized, and fully oxidized devices. Fully oxidized pHEMTs showed minimized substrate leakage, but suffered a large channel charge loss in comparison with unoxidized structures. Fully oxidized devices also showed transconductance peaking that could be removed by controlled partial oxidation. Partially oxidized pHEMTs showed improved power added efficiencies (PAEs) in comparison to fully oxidized or unoxidized devices and negligible charge loss.

Full details of this work were recently published and are given in Appendix IV:

"Oxidation Control of GaAs pHEMTs for High Efficiency Applications,"
Can Zheng, R. Coffie, D. Buttari, J. Champlain, and U. K. Mishra, *Electron Dev. Lett.* **23**, 380 (2002)).

Design and Fabrication of Collector-up Heterojunction BipolarTransistors with Oxide Confined Current Apertures

In the area of minority carrier devices, we worked on .collector-up heterojunction bipolar transistors (HBTs) with oxide confined current apertures. These devices offer a possible high-frequency, high-gain option for HBT design. Collector-up HBTs offer reduced base-collector capacitances, as compared to their emitter-up counterparts, that leads to an increase in their maximum frequency of oscillation (f_{max}). Standard collector-up HBTs suffer from reduced current gains due to the direct injection of carriers from the emitter into the base contacts. To overcome this deficiency, a current aperture must be adopted in the emitter to properly channel the carriers.

Appendix V is a manuscript that details our work on oxide aperture HBTs. This work examines the application of the collector-up HBT with a current aperture in the InP lattice-matched material system. The current aperture in the devices presented in this paper were produced by the partial oxidation of a high aluminum content emitter to form an oxide confinement layer around the aperture. Various aspects of the device's DC and RF performance were examined. A parasitic base-emitter (BE) capacitance resulting from the collector-up design, outside of the active portion of the transistor, in association with a relatively large emitter resistance was found to limit the transistor's current-gain cutoff frequency (f_T). Though limiting f_T, this parasitic BE capacitance was found to have little effect on f_{max}. A model of the device was developed and simulated to confirm these statements

Lateral oxidation of AlAsSb interlayers

In an effort to develop lattice engineered substrates for 6.1 Å applications, we studied lateral wet-oxidation of strained AlAsSb was studied. $AlAs_{0.80}Sb_{0.20}$ interlayers were grown on a GaAs substrate and capped with a lattice-matched $In_{0.25}Ga_{0.75}As$ layer. The AlAsSb was oxidized between 350–450 °C. Oxidation temperatures > 400 °C resulted in poor surface morphology and delamination. Oxidation of thicker AlAsSb interlayers ($h \approx 2000$ Å) resulted in metallic Sb layers forming between the AlO_x and the semiconductor interfaces. The remaining Sb metal at the oxide-semiconductor interface was ~15% oxidized. Lateral wet-oxidation of thinner AlAsSb interlayers ($h \leq 500$ Å) resulted in Sb inclusions at the oxide-semiconductor interface. The Sb inclusions were 1.5–2.0 μm in diameter and the inclusion thickness was approximately equal to the AlAsSb layer thickness. Methanol (CH_3OH) was added to the water mixture with the intent to stabilize the otherwise unstable stibine (SbH_3) such that Sb could be removed from the oxidizing structure.. However, methanol addition resulted in a decreased oxidation rate and a change in the Sb precipitate morphology. The Sb inclusions observed in pure water oxidation changed to a Sb finger-like morphology with increasing methanol concentration. The Sb fingers were 1.0–2.0 μm wide and as long as the oxidation depth. Oxidation of AlAsSb interlayers $h \leq 200$ Å were limited by the incorporation of Ga from the substrate and capping layer into the oxidation layer. Doping the oxidation AlAsSb interlayer $1\times10^{18}\ cm^{-3}$ n-type (Si or Te) did not result in any improvement in Sb segregation.

Full details of this work were recently published and are given in Appendix VI:

"Antimony segregation in the oxidation of AlAsSb interlayers,"
A.M. Andrews, K.L. van Horn, T. Mates, J.S. Speck, *J. Vac. Sci. Technol. A* **21**, 1883 (2003).

Stress Relaxation in Mismatched Layers due to Threading Dislocation Inclination

In this work, we developed a new model to explain recently observed mechanism of elastic stress relaxation in mismatched nitride layers. The relaxation is achieved by the inclination of pure edge threading dislocation lines with respect to the layer surface normal. The relaxation is not assisted by dislocation glide but rather is caused by the "effective climb" of edge dislocations. The effective dislocation climb may result from the film growth and it is not necessarily related to bulk diffusion processes. The contribution of the dislocation inclination to strain relaxation has been formulated and the energy release due to the dislocation inclination in mismatched stressed layers has been determined. This mechanism explains recently observed relaxation of compressive stresses in the (0001) growth of $Al_xGa_{1-x}N$ layers. This model explains the hitherto mystery of change of the sign of stress from compression to tension in III-nitride layers during growth and also provides the most likely explanation of cracking of nominally compressive III-nitride layers.

Full details of this work are given in the publication (provided as Appendix VII):

"Stress relaxation in mismatched layers due to threading dislocation inclination,"
A.E. Romanov, J.S. Speck, *Appl. Phys. Lett.* **83**, 2569 (2003).

Modeling the Extended Defect Evolution in Lateral Epitaxial Overgrowth of GaN: Subgrain Stability

This work is a natural extension of the collaborative work Dr. Alexei Romanov. The topic of extended defect structure stability in lateral epitaxial overgrowth (LEO) of GaN was addressed. We considered the experimental results of growth morphology and dislocation structure in LEO GaN on sapphire substrates in the context of to the crystallographic orientation of the stripe window openings. For $\langle 11\bar{2}0\rangle$-oriented stripes, the LEO material often exhibits a triangular cross-section morphology with inclined $\{10\bar{1}1\}$ facets. The threading dislocations (TDs) propagate vertically in the window region and then become unstable and bend toward the inclined sidewalls, to eventually lie in the basal plane. In the case of $\langle 1\bar{1}00\rangle$-oriented stripes, vertical $\{11\bar{2}0\}$ sidewalls may develop and, when realized, yield the lowest density of extended defects in the wing (overgrown) regions. Most of the TDs propagate vertically in the window regions and remain in loosely organized cell walls (subgrain boundaries). For this stripe orientation, a discernable crystallographic tilt of the LEO wing regions relative to the window region is also observed. This tilt is related to the appearance of edge dislocation arrays in the transition region between windows and wings. To understand the growth of dislocation-free wing regions, we developed a new model for dislocation subboundary cell structure stability during lateral overgrowth. The model provides a relation between structural parameters (such as cell size and misorientation) under which lateral defect-free growth is energetically favorable.

Full details of this work are given in the publication (provided as Appendix VIII):

"Modeling the extended defect evolution in lateral epitaxial overgrowth of GaN: Subgrain stability,"
A.E. Romanov, P. Fini, J.S. Speck, *J. Appl. Phys.* **93**, 106 (2003).

Personnel Supported:

Faculty:
James S. Speck – Materials Dept.
Umesh K. Mishra – ECE Dept.

Visiting Faculty:
Alexei Romanov – Materials Dept. (from Ioffe Institute, St. Petersburg, Russia)

Post-Doctoral Reseracher
S.H. Lim – Materials Dept.

Graduate Students
A. Maxwell Andrews – Materials Department (Ph.D. 2003)
Meghan Kerner – Materials Department (M.S., 2004)
James Champlain – ECE Department (Ph.D., 2003)
Yingda Dong – ECE Department (Ph.D. 2003)
Can Zheng – ECE Department (Ph.D., 2003)

Publications

"Development of cross-hatch morphology during growth of lattice mismatched layers,"
A.M. Andrews, A.E. Romanov, J.S. Speck, M. Bobeth, W. Pompe, *Appl. Phys. Lett.* **77**, 3740 (2000).

"Modeling crosshatch surface morphology in growing mismatched layers,"
A.M. Andrews, J.S. Speck, A.E. Romanov, M. Bobeth, W. Pompe, *J. Appl. Phys.* **91**, 1933 (2002).

"Modeling crosshatch surface morphology in growing mismatched layers. Part II: Periodic boundary conditions and dislocation groups,"
A.M. Andrews, R. LeSar, M.A. Kerner, J.S. Speck, A.E. Romanov, A.L. Kolesnikova, M. Bobeth, W. Pompe, *J.Appl. Phys.* **95**, 6032 (2004).

"Oxidation Control of GaAs pHEMTs for High Efficiency Applications,"
Can Zheng, R. Coffie, D. Buttari, J. Champlain, and U. K. Mishra, *Electron Dev. Lett.* **23**, 380 (2002)).

"Antimony segregation in the oxidation of AlAsSb interlayers,"
A.M. Andrews, K.L. van Horn, T. Mates, J.S. Speck, *J. Vac. Sci. Technol. A* **21**, 1883 (2003).

"Stress relaxation in mismatched layers due to threading dislocation inclination,"
A.E. Romanov, J.S. Speck, *Appl. Phys. Lett.* **83**, 2569 (2003).

"Modeling the extended defect evolution in lateral epitaxial overgrowth of GaN: Subgrain stability,"
A.E. Romanov, P. Fini, J.S. Speck, *J. Appl. Phys.* **93**, 106 (2003).

Appendices

Appendix I

"Development of cross-hatch morphology during growth of lattice mismatched layers,"
A.M. Andrews, A.E. Romanov, J.S. Speck, M. Bobeth, W. Pompe, *Appl. Phys. Lett.* **77**, 3740 (2000).

Appendix II

"Modeling crosshatch surface morphology in growing mismatched layers,"
A.M. Andrews, J.S. Speck, A.E. Romanov, M. Bobeth, W. Pompe, *J. Appl. Phys.* **91**, 1933 (2002).

Appendix III

"Modeling crosshatch surface morphology in growing mismatched layers. Part II: Periodic boundary conditions and dislocation groups,"
A.M. Andrews, R. LeSar, M.A. Kerner, J.S. Speck, A.E. Romanov, A.L. Kolesnikova, M. Bobeth, W. Pompe, *J.Appl. Phys.* **95**, 6032 (2004).

Appendix IV

"Oxidation Control of GaAs pHEMTs for High Efficiency Applications,"
Can Zheng, R. Coffie, D. Buttari, J. Champlain, and U. K. Mishra, *Electron Dev. Lett.* **23**, 380 (2002)).

Appendix V

"Design and Fabrication of Collector-up Heterojunction BipolarTransistors with Oxide Confined Current Apertures,"
James G. Champlain and Umesh K. Mishra

Appendix VI

"Antimony segregation in the oxidation of AlAsSb interlayers,"
A.M. Andrews, K.L. van Horn, T. Mates, J.S. Speck, *J. Vac. Sci. Technol. A* **21**, 1883 (2003).

Appendix VII

"Stress relaxation in mismatched layers due to threading dislocation inclination,"
A.E. Romanov, J.S. Speck, *Appl. Phys. Lett.* **83**, 2569 (2003).

Appendix VIII

"Modeling the extended defect evolution in lateral epitaxial overgrowth of GaN: Subgrain stability,"
A.E. Romanov, P. Fini, J.S. Speck, *J. Appl. Phys.* **93**, 106 (2003).

Appendix I

APPLIED PHYSICS LETTERS VOLUME 77, NUMBER 23 4 DECEMBER 2000

Development of cross-hatch morphology during growth of lattice mismatched layers

A. M. Andrews, A. E. Romanov,[a] and J. S. Speck[b]
Materials Department, University of California, Santa Barbara, California 93106

M. Bobeth and W. Pompe
Technical University of Dresden, Dresden, Germany 01609

(Received 25 August 2000; accepted for publication 13 October 2000)

An approach for understanding the cross-hatch morphology in lattice mismatched heteroepitaxial film growth is developed. It is argued that both strain relaxation associated with misfit dislocation formation and lateral surface step flow are required for the appearance of mesoscopic scale surface undulations during layer growth. The results of Monte Carlo simulations for dislocation assisted strain relaxation and consequent film growth predict the development of cross-hatch patterns with a characteristic surface undulation magnitude ~50 Å in an approximately 70% relaxed $\mathrm{In_{0.25}Ga_{0.75}As}$ layers. This is supported by atomic force microscopy observations of cross-hatch morphology in the same composition samples grown well beyond the critical thickness for misfit dislocation formation.
© *2000 American Institute of Physics.* [S0003-6951(00)05049-X]

The common undulating surface morphology, known as cross hatch, is often observed after strain relaxation of (001) oriented strained cubic semiconductor systems, e.g., InGaAs/GaAs, SiGe/Si, GaAsP/GaAs, and other cubic semiconductor systems.[1–3] The surface height undulations are elongated parallel to intersection of the slip planes with the free surface of the film, e.g., in the ⟨110⟩ directions for a (001) semiconductor film with {111} slip planes, and form a rectangular grid. These features can be readily observed by Nomarski optical microscopy or atomic force microscopy (AFM). This surface morphology is clearly related to plastic strain relaxation in the film and is only seen after its onset.[3–5] Despite the commonality of cross-hatch morphology, its origin remains controversial and unresolved. One proposed mechanism for cross-hatch development is enhanced growth over strain relaxed regions due to lateral mass transport via surface diffusion.[6–8] Alternative models have been proposed in which the undulations result primarily from misfit dislocation (MD) generation and glide processes.[3,5,9,10] An important observation was made by Springholz who found that there was no preferential growth due to the strain fields of underlying MDs for (111) oriented highly relaxed IV–VI layers.[2]

The aim of the present letter is to introduce a model for the cross-hatch surface height evolution that incorporates film relaxation and subsequent lateral mass transport. Here we will demonstrate that cross hatch is a consequence of the elimination of steps which were produced during plastic relaxation of the misfit strain.

To support the developed model, $\mathrm{In}_x\mathrm{Ga}_{1-x}\mathrm{As}$ samples that displayed cross-hatch morphologies were grown by molecular beam epitaxy. A 2000 Å GaAs buffer layer was grown at 580 °C on a vertical gradient freeze GaAs (001) substrate and all subsequent $\mathrm{In}_x\mathrm{Ga}_{1-x}\mathrm{As}$ layers were grown at 520 °C. Figure 1 shows a representative AFM image of an $\mathrm{In_{0.25}Ga_{0.75}As}$(1000Å)/GaAs, corresponding to a nominal misfit strain of ~2%. The thickness of this sample is ~$20h_c$, where h_c is the equilibrium Matthews–Blakeslee critical thickness for introduction of MDs. The extent of strain relaxation was determined by the separation of the film and substrate (115) and ($\bar{1}\bar{1}5$) x-ray diffraction peaks (following the method described in Ref. 11), corresponding to relaxation in the [110] direction, and by the separation of the

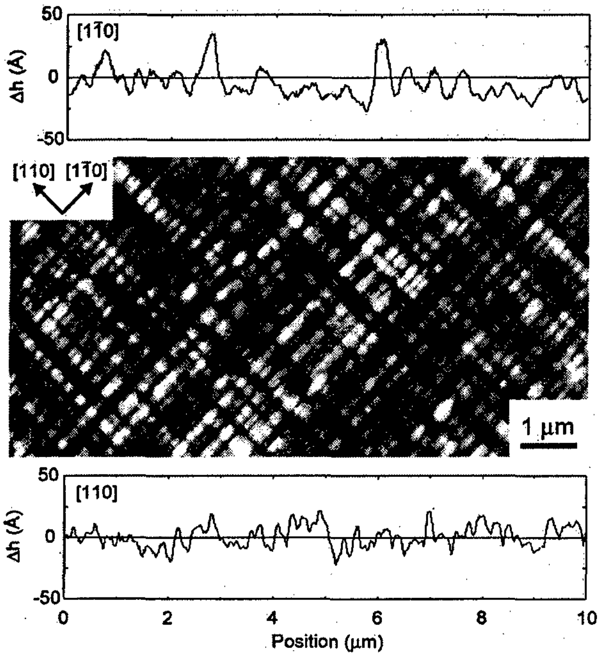

FIG. 1. 10×5 μmAFM image of the surface of an $\mathrm{In_{0.25}Ga_{0.75}As/GaAs(001)}$ sample grown to approximately $20h_c$. The anisotropy in strain relaxation and surface diffusion between the [110] and [1$\bar{1}$0] directions and their corresponding slip planes results in a greater amplitude and wavelength surface undulations in the [1$\bar{1}$0] direction (shown above the AFM image) than the [110] direction (shown below the AFM image).

---

[a] Present address: A. F. Ioffe Physico-Technical Institute, Russian Academy of Sciences, 194021 St. Petersburg, Russia.

[b] Electronic mail: speck@mrl.ucsb.edu

© 2000 American Institute of Physics

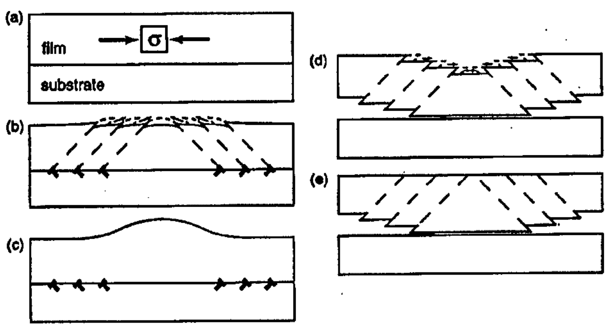

FIG. 2. Schematic representation of the film surface displacement due to the formation of MDs at the film/substrate interface and subsequent growth: (a) coherent, compressively strained layer; (b) plastic relaxation by dislocation formation and subsequent annihilation of opposite sense surface steps; (c) final film state with larger scale surface undulations. The transition from (a) to (c) can be viewed as an Eshelby-like process where the detached film (d) plastically relaxes and then (e) the steps are annihilated during overgrowth.

($\bar{1}15$) and ($1\bar{1}5$) x-ray peaks, corresponding to strain relaxation in the [$1\bar{1}0$] direction. For the film shown in Fig. 1, the strain relaxation in the [$1\bar{1}0$] direction is 67%. In the initial stages of growth, strain relaxation is almost solely confined to the planes perpendicular to the [110] direction, up to an observed 20% in the $10h_c$ samples, and as a result the formation of cross hatch begins in this direction first. As the film grows thicker, the amplitude and wavelength of the undulations increases.

We now present our basic description of cross-hatch formation and evolution, as displayed in the sequential schematic in Fig. 2. (a) We begin with an initially strained coherent film with a planar surface; (b) for films with thickness larger than h_c, plastic relaxation processes may take place. These processes may include initial dislocation motion and nucleation, MD formation by threading dislocation motion, and dislocation multiplication. MD formation is associated with dislocation glide and results in step formation at the film surface. In the absence of lateral mass transport, the steps remain frozen and the film thickness is uniform with relatively small local height undulations due to the steps and elastic strain fields from the MDs. (c) Large scale height undulations develop due to lateral mass transport which is driven by the tendency for the surface to eliminate steps, for example, in normal step flow growth. The locally smooth, mesoscopically rough, surface shown in (c) is due to true lateral thickness variations in the film. This may be better understood if we consider an Eshelby-like process in which (d) we detach the relaxed film with frozen-in step structure from the substrate and then (e) allow the steps on the top surface to flow—this ultimately leads to a step-free surface and a film with thickness variation. The hypothetical process of reattaching the film to the substrate [step (e)–(c) in Fig. 2] leads to a film with thickness variations and MDs at the film/substrate interface.

We have developed a one-dimensional Monte Carlo model to simulate the surface height evolution during and after strain relaxation. To initiate the Monte-Carlo simulation, we first select a dislocation source at the surface. The sources can have any prescribed distribution, strength, and stress dependence. The source distribution may be chosen between two extreme cases: random sources, resulting in random dislocation positions, and stress-determined sources, corresponding to dislocation nucleation at the location of the highest stress. To model the surface height evolution, we have used known analytical solutions for the stress and surface displacement for edge dislocations whose line direction are parallel to the free surface.[12,13] The location of the surface step is related to the operating source and the height of the step is given by the normal component of the Burgers vector for the MD. Both steps and elastic displacement contribute to the surface height profile. Far from the dislocation, this results in zero total surface displacement. The surface displacement for groups of dislocations can be obtained by linear superposition. The simplest way to model the lateral flow of steps (i.e., "step-flow growth") is to allow the steps to grow to the edge of the modeling domain. To accomplish this we merely do not introduce the step, which would be related to the dislocation. Instead we use the unmodified displacement formulas, which approximate the moving surface steps.

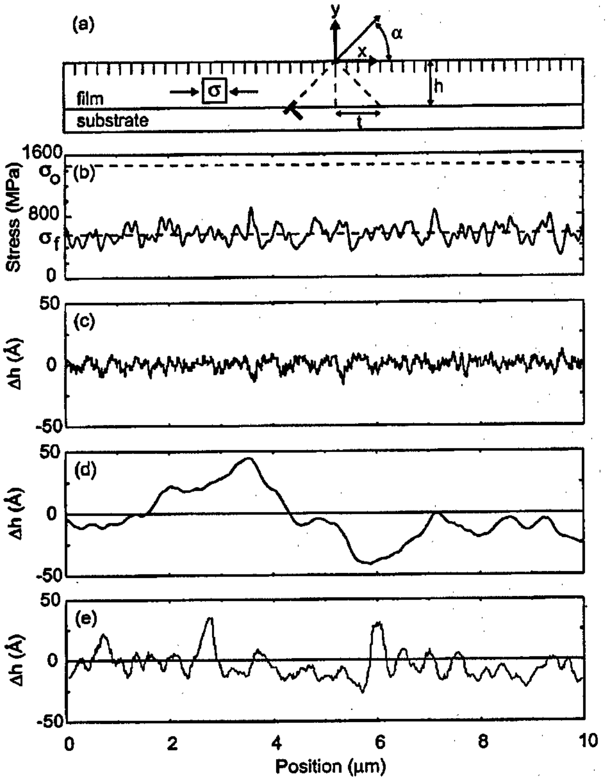

FIG. 3. Modeling of cross-hatch evolution and comparison with experimental surface profiles. The example here corresponds to a 2% mismatch film, e.g., $In_{0.25}Ga_{0.75}As$ on GaAs (001), grown to $20\times h_c$. (a) Schematic showing the geometry for the one-dimensional Monte-Carlo simulation of strain relaxation by dislocation nucleation at randomly distributed surface sources. Possible sites for dislocation sources are shown as ticks at the surface. Misfit dislocations have their slip planes oriented at angle α with respect to the surface. (b) Simulated stress distribution after 70% relaxation. σ_0 corresponds to the initial misfit stress and σ_f is the average stress after partial relaxation. (c) Simulated surface profile after partial relaxation due surface steps and the elastic displacements associated with MDs. Surface steps form during plastic relaxation via dislocation nucleation and motion. (d) Simulated surface profile after elimination of surface steps by lateral mass transport. (e) Experimental surface profile.

To predict the surface profile of the $In_{0.25}Ga_{0.75}As$ sample grown to $20h_c$ we chose to use random dislocation sources. The model, in Fig. 3, is a simple one-dimensional representation of a cross-sectional slice through the material.

For the model range of 10 μm, a total of 25 000 possible nucleation sites for dislocations at the film surface are considered with a spacing of $b=4$ Å(GaAs). A total of 500 MDs were introduced into the 10 μm wide epilayer to approximate a partially relaxed film that was originally 2% strained (700 MDs are required for full relaxation). The plot in Fig. 3(b) shows the magnitude of the modeled stress at the surface with respect to the stress of the coherent film σ_0. The surface profile, shown Fig. 3(c), results from only elastic displacement from the underlying MDs and surface steps. After complete step elimination, Fig. 3(d), the amplitude and wavelength of the surface displacement increases significantly. It is evident that the $[1\bar{1}0]$ surface cross section from Fig. 1, shown as Fig. 3(e) for comparison, actually corresponds to an intermediate stage between the two possible extremes: frozen steps and a step-free surface. We note that the peak surface height amplitude for the frozen step surface [Fig. 3(c)] is less than 10 Å, whereas the peak amplitude for the measured profile is ~30 Å and is closer to simulated case for a step-free surface [Fig. 3(d)].

With the understanding of cross-hatch formation and its relation to relaxation, stress and growth, the future goal of our work is to apply the model in reverse and develop insight into the distribution of dislocation sources, MD clustering, patterning, and dislocation blocking via AFM data. The simplicity and scale of AFM scans makes the technique ideal for understanding larger scale dislocation reactions: sources, multiplication, and grouping.

We conclude that surface step flow is required for the development of the mesoscale cross-hatch morphology in strained epitaxial layers. In case the step flow is inhibited, plastic relaxation itself can provide only microscopic undulations in the film surface.

This work was supported by DAPRA (W. Coblenz, program manager) and managed through AFOSR (D. Johnston and G. Witt, program managers).

[1] R. A. Burmeister, G. P. Pighini, and P. E. Greene, Trans. Metall. Soc. AIME **245**, 587 (1969).
[2] G. Springholz, Appl. Phys. Lett. **75**, 3099 (1999).
[3] K. H. Chang, R. Gibala, D. J. Srolovitz, P. K. Bhattacharya, and J. F. Mansfield, J. Appl. Phys. **67**, 4093 (1990).
[4] G. H. Olsen, J. Cryst. Growth **31**, 223 (1975).
[5] S. Kishino, M. Ogirima, and K. Kurata, J. Electrochem. Soc. **119**, 617 (1972).
[6] J. W. P. Hsu, E. A. Fitzgerald, Y. H. Xie, P. J. Silverman, and M. J. Cardillo, Appl. Phys. Lett. **61**, 1293 (1992).
[7] F. Jonsdottir and L. B. Freund, Mech. Mater. **20**, 337 (1995).
[8] H. Gao, J. Mech. Phys. Solids **42**, 741 (1994).
[9] S. Y. Shiryaev, F. Jensen, and J. W. Petersen, Appl. Phys. Lett. **64**, 3305 (1994).
[10] M. A. Lutz, R. M. Feenstra, F. K. LeGoues, P. M. Mooney, and J. O. Chu, Appl. Phys. Lett. **66**, 724 (1995).
[11] A. Krost, G. Bauer, and J. Woitok, in *Optical Characterization of Epitaxial Semiconductor Layers*, edited by G. Bauer and W. Richter (Springer, New York, 1996), p. 287.
[12] J. Lothe, in *Elastic Strain Fields and Dislocation Mobility*, edited by V. L. Indenbom and J. Lothe (North-Holland, New York, 1992), p. 361.
[13] A. E. Romanov and V. I. Vladimirov, in *Dislocations in Solids*, edited by F. R. N. Nabarro (Elsevier, New York, 1992), Vol. 9, p. 191.

Appendix II

JOURNAL OF APPLIED PHYSICS VOLUME 91, NUMBER 4 15 FEBRUARY 2002

Modeling cross-hatch surface morphology in growing mismatched layers

A. M. Andrews and J. S. Speck[a]
Department of Materials, University of California, Santa Barbara, California 93106

A. E. Romanov
A. F. Ioffe Physico-Technical Institute, 194021 St. Petersburg, Russia

M. Bobeth and W. Pompe
Technical University Dresden, Hallwachsstrasse 3, 01062 Dresden, Germany

(Received 16 August 2001; accepted for publication 24 October 2001)

We propose and investigate a model for the development of cross-hatch surface morphology in growing mismatched layers. The model incorporates two important elements: (i) strain relaxation due to dislocation glide in the layer (film) interior that is also associated with misfit dislocation formation at the film/substrate interface and (ii) lateral surface transport that eliminates surface steps that originated from dislocation glide. A combination of dislocation-assisted strain relaxation and surface step flow leads to the appearance of surface height undulations during layer growth. A Monte Carlo simulation technique was applied to model dislocation nucleation events in the course of strain relaxation. The simulation was used to model the influence of dislocations on film surface height profiles. The surface height displacement was calculated from the analytic elasticity solutions for edge dislocations near a free surface. The results of the modeling predict that the average amplitude of the surface undulations and their apparent wavelength both increase with increasing film relaxation and film thickness. The developed cross-hatch pattern is characterized by an atomically smooth but mesoscopically (lateral dimensions ~0.1–10 μm) rough surface morphology. The conclusions of the model are in agreement with atomic force microscopy observations of cross-hatch surface relief in $In_{0.25}Ga_{0.75}As/GaAs$ samples grown well beyond the critical thickness for misfit dislocation formation. *© 2002 American Institute of Physics.* [DOI: 10.1063/1.1428091]

I. INTRODUCTION

The control of the surface morphology of growing hetero-epitaxial mismatched films is an important issue in modern semiconductor science and technology.[1,2] The surface roughness that develops during hetero-epitaxial film growth may prevent the easy engineering of multilayer structures;[3] the height undulations lead to direct optical losses in optoelectronic devices;[4] even crack nucleation in semiconductor films can be initiated by nonuniformities in the film surface profile.[5]

The characteristic undulating surface morphology, known as cross hatch, is often observed after strain relaxation of (001) oriented strained cubic semiconductor systems, e.g., InGaAs/GaAs, SiGe/Si, GaAsP/GaAs, and other cubic semiconductor systems.[6–10] For this growth geometry, the surface height undulations are elongated parallel to the intersection of the slip planes with the free surface of the film, e.g., in the ⟨110⟩ directions for a (001) semiconductor film with {111} slip planes, and form an orthogonal grid. Different cross-hatch patterns may appear for other growth plane orientations.[11] For example, only one-directional surface undulations were observed for (110) growth of ZnSe on GaAs.[12] This is because only two {111} slip planes, with parallel surface trace, have a resolved shear stress for (110) oriented films. The cross-hatch morphology features can be readily observed by Nomarski interference optical microscopy or atomic force microscopy (AFM).

The development of surface undulations in cross-hatch patterns is clearly related to plastic strain relaxation in the film and is only seen after its onset.[7,13,14] It has also been demonstrated that the typical cross-hatch morphology with elongated hills and valleys is only observed for the film/substrate systems with moderate crystal lattice mismatch $\epsilon_m \leq 2\%$. In such systems the growth occurs by layer-by-layer or step flow mechanism. For systems with larger mismatch, growth proceeds by initial wetting followed by coherent islanding (Stranski–Krastanov) mechanism or by direct incoherent island formation (Volmer–Weber) mechanism.[1,7] Typically, in Volmer–Weber growth, the islands are relaxed as they grow (thus the term "incoherent" islanding)—that is, the misfit dislocations (MDs) form concurrently with the growing island. We do not treat the morphology development for such cases.

Despite the frequent observation of the cross-hatch morphology, its origin remains controversial and unresolved. One proposed mechanism for cross-hatch development is enhanced growth over strain relaxed regions due to lateral mass transport by surface diffusion.[15–17] Alternative models have been proposed in which the undulations result primarily from MD generation and glide processes.[7,14,18,19] An important ob-

---

[a]Electronic mail: speck@mrl.ucsb.edu

0021-8979/2002/91(4)/1933/11/$19.00 © 2002 American Institute of Physics

Downloaded 09 Mar 2002 to 128.111.74.212. Redistribution subject to AIP license or copyright, see http://ojps.aip.org/japo/japcr.jsp

servation was made by Springholz who found that there was no preferential growth due to the strain fields of underlying MDs for (111) oriented highly relaxed IV–VI layers.[11]

The aim of the present article is to develop a detailed model (originally proposed in Ref. 20) for the cross-hatch surface height evolution that incorporates both stress relaxation and subsequent lateral mass transport. The model will give a quantitative explanation for the change of cross-hatch morphology with the thickness of the growing layer and extent of strain relaxation. Here we demonstrate that cross hatch is mainly a consequence of the elimination of surface steps that were produced during plastic relaxation of the misfit strain.

II. BACKGROUND

In lattice mismatched heteroepitaxy, the film is uniformly stressed when it grows coherently on a thick substrate. In the case of a one-dimensional (1D) lattice mismatch, the nonzero component of stresses in the film are given as[17]

$$\sigma_{xx}^{1D}=\frac{2G}{1-\nu}\epsilon_m; \tag{1a}$$

$$\sigma_{zz}^{1D}=\frac{2\nu G}{1-\nu}\epsilon_m, \tag{1b}$$

where the x axis is chosen along the direction of lattice mismatch, which is characterized by the misfit parameter (misfit strain) ϵ_m, and the y axis is perpendicular to the film/substrate interface. The film material is assumed to be elastically isotropic with shear modulus G and Poisson ratio ν. In the case of equi-biaxial mismatch, the stress state in the film is given as

$$\sigma_{xx}^{2D}=\sigma_{zz}^{2D}=2G\frac{1+\nu}{1-\nu}\epsilon_m, \tag{2}$$

where the misfit strain ϵ_m is defined by the crystal lattice parameters of the film a_f and substrate a_s materials

$$\epsilon_m=\frac{a_s-a_f}{a_f}. \tag{3}$$

The stored elastic energy w per unit area of the film/substrate interface associated with the stresses given by Eqs. (1) or (2) is proportional to the film thickness h

$$w^{2D}=2(1+\nu)w^{1D}=2G\frac{1+\nu}{1-\nu}\epsilon_m^2 h. \tag{4}$$

Increasing the stored energy with increasing film thickness h will eventually lead to the onset for the manifestation of a variety of relaxation processes in the elastically stressed film. One may expect that there exists a critical value of the film thickness for relaxation to start.

Misfit dislocation generation at the interface between the film and substrate has been shown to be the most common mechanism for the relaxation of elastic stress.[21–24] In the majority of cases the MDs are associated with threading dislocations (TDs), which are concomitant to MDs but have their lines going through the film to the free surface.[24,25] The Matthews–Blakeslee[26] critical thickness h_c for MD generation may be derived[23] by considering the energetics of a combined MD-TD configuration in a stressed film

$$h_c=\frac{b}{\epsilon_m(1+\nu)8\pi\cos\lambda}(1-\cos^2\beta)\ln\left(\frac{\alpha_o h_c}{b}\right)\approx\frac{b}{\epsilon_m}, \tag{5}$$

where $b=|\mathbf{b}|$ is the magnitude of the dislocation Burgers vector $\mathbf{b}$, λ is the angle between the Burgers vector and a line that lies in the film/substrate interface normal to the MD line, β is the angle between the MD line and $\mathbf{b}$, and α_o is the dislocation core cutoff parameter.

For a completely relaxed film (when the film thickness $h \gg h_c$), the linear density of MDs $\rho_{\mathrm{MD,relaxed}}$ multiplied by the edge component of the MD Burgers vector parallel to the interface $b_\parallel = b\cos\lambda$, is equal to the misfit strain ϵ_m, i.e.

$$\rho_{\mathrm{MD,relaxed}}b_\parallel=\epsilon_m. \tag{6}$$

For films of finite thickness that are grown on semi-infinite substrates, the equilibrium linear MD density $\rho_{\mathrm{MD,equil}}$ may be shown to depend on the film thickness as follows:[27]

$$\rho_{\mathrm{MD,equil}}=\rho_{\mathrm{MD,relaxed}}\left(1-\frac{h_c}{h}\right). \tag{7}$$

The actual dislocation density realized at a particular stage of the film relaxation is almost always less than those given by Eqs. (6) and (7) $\rho_{\mathrm{MD,actual}}\leqslant\rho_{\mathrm{MD,equil}}<\rho_{\mathrm{MD,relaxed}}$. The extent of strain relaxation R can be therefore defined with the help of $\rho_{\mathrm{MD,actual}}$

$$R=\frac{\rho_{\mathrm{MD,actual}}}{\rho_{\mathrm{MD,relaxed}}}. \tag{8}$$

By taking into account that the residual elastic strain ϵ^* in the film during relaxation is $\epsilon^*=\epsilon_m-\rho_{\mathrm{MD,actual}}b_\parallel$, the expression for the extent of relaxation can be written in the equivalent form

$$R=\frac{\epsilon_m-\epsilon^*}{\epsilon_m}=\frac{a_s-a_f^*}{a_s-a_f}, \tag{9}$$

where a_f^* is the measured in-plane lattice spacing of the film. (The in-plane lattice spacing may be determined by measuring the film and substrate peak separation for paired reflections in off-axis x-ray diffraction.[28])

The most common wafer orientation for semiconductor heteroepitaxy is (001) and thus it is the orientation where cross hatch is commonly observed. In this article, we restrict our considerations to cube-on-cube epitaxy of fcc materials. Figure 1 illustrates the crystallography for dislocation-assisted strain relaxation in the film for this growth orientation. We treat relaxation that occurs via threading dislocation motion and MD formation on the inclined glide planes.[23] For semiconductor materials, such as $\mathrm{Si}_{1-x}\mathrm{Ge}_x$ and $\mathrm{In}_x\mathrm{Ga}_{1-x}\mathrm{As}$, the most common slip system is $a/2\langle 110\rangle\{111\}$. The Burgers vectors for this system are along the face diagonals of the

Downloaded 09 Mar 2002 to 128.111.74.212. Redistribution subject to AIP license or copyright, see http://ojps.aip.org/japo/japcr.jsp

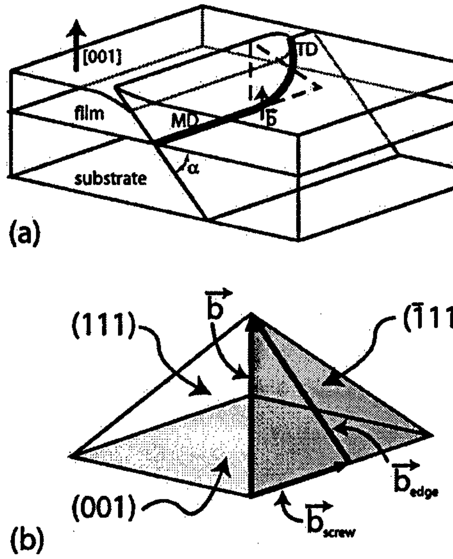

FIG. 1. Dislocation geometry in heteroepitaxial mismatched thin films. (a) One of the inclined {111} slip planes for a (001) oriented fcc film/substrate system with a gliding TD segment and a trailing MD. (b) Dislocation Burgers vector **b** for the shown inclined slip plane decomposed into edge $\mathbf{b}_{edge}$ and screw $\mathbf{b}_{screw}$ components.

cubic cell and are the shortest possible primitive lattice translation vectors. The set of possible Burgers vectors can be constructed by considering the edges of a half octahedron, as shown in Fig. 1(b). The half octahedron is oriented such that its square base is parallel to the (001) plane. The dislocation glide plane is for instance, $(\bar{1}11)$, which is inclined with respect to the film/substrate interface by the angle $\alpha=\cos^{-1}(1/\sqrt{3})\approx 54.7°$. In this example the MD is a mixed 60° dislocation with line direction along [110] and Burgers vector **b** parallel to $[0\bar{1}1]$ with $b=|\mathbf{b}|=a/\sqrt{2}$. Such an orientation of the dislocation line and Burgers vector leads to $\lambda=\beta=60°$ in Eq. (5). The dislocation Burgers vector can be decomposed into edge $\mathbf{b}_{edge}$ and screw $\mathbf{b}_{screw}$ components as shown in Fig. 1(b). Consequently, the edge component can be decomposed into parts parallel $\mathbf{b}_\parallel$ and perpendicular $\mathbf{b}_\perp$ to the film/substrate interface: $\mathbf{b}_{edge}=\mathbf{b}_\parallel+\mathbf{b}_\perp$. The absolute values of these subcomponents are

$$b_{edge}=b\frac{\sqrt{3}}{2};\quad b_\parallel=\frac{b}{2};\quad b_\perp=\frac{b}{\sqrt{2}}. \tag{10}$$

We note again that only edge dislocations with Burgers vector parallel to the film/substrate interface can contribute to strain relaxation in mismatched layers (assuming equibiaxial stress). The elastic properties of MDs can be derived from the solutions obtained for straight edge dislocations placed at some distance from a free surface of a semi-infinite body (see the Appendix).

III. EXPERIMENT

Epitaxial films of $In_xGa_{1-x}As$ were grown on GaAs (001) semi-insulating substrates by molecular beam epitaxy. For this study, $In_{0.25}Ga_{0.75}As$ layers, which correspond to 1.8% lattice mismatch, were deposited at 520 °C. The film

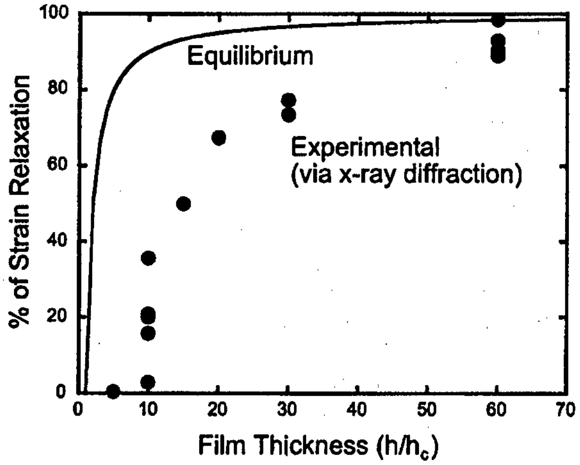

FIG. 2. Experimentally determined strain relaxation (points) as a function of film thickness h/h_c for $In_xGa_{1-x}As$/GaAs films ($x=0.25$). The solid curve represents the equilibrium strain relaxation given by Eq. (9).

thicknesses h were 250, 500, 1000, 1500, and 10 000 Å. Since $h_c\approx 50$ Å for this composition, where h_c is the equilibrium critical thickness for MD nucleation at the film/substrate interface,[23] the thicknesses were also approx. 5, 10, 15, 20, and 200 h_c. The extent of strain relaxation and the film composition were determined by measuring the separation of the film and substrate peak for {115} and $\{\bar{1}\bar{1}5\}$ reflections in double crystal high-resolution x-ray measurements (for full details of this technique, please see Ref. 28). As shown in Fig. 2, the strain relaxation starts at ~10 h_c and the magnitude of the relaxation is always smaller than the equilibrium value. AFM was used to determine the surface height profile.

Figure 3 illustrates some experimental observations of the surface cross-hatch patterns. In this case, AFM images [e.g., Fig. 3(a)] of a 70% strain relaxed 1000-Å-thick $In_{0.25}Ga_{0.75}As$ film on GaAs show a definite cross-hatch pattern in the orthogonal ⟨110⟩ directions. There is an anisotropy between the extent of strain relaxation in the orthogonal ⟨110⟩ directions. During the early stages of relaxation, the difference in relaxation in the ⟨110⟩ directions may be as large as ~20%. However, this difference decreases with increasing relaxation. The cross-hatch pattern first forms perpendicular to the $[0\bar{1}1]$ direction. As the film thickness increases [Fig. 3(b)], the variation in the surface height profile also increases. For the 1.8% mismatch strain in these samples the growth mode should be step flow or layer by layer.[7] The growth rate of less than 1 ML/s provides a significant amount of time for surface atom migration [we note that under similar molecular beam epitaxy (MBE) growth conditions, In can have diffusion as large as 15 μm[29]]. The peak-to-valley amplitude in the observed films increases with relaxation of the initial film strain. The relaxation of approximately $R=5\%$, 20%, 50%, 70%, and 100% resulted in maximum cross-hatch amplitudes of approximately 15, 25, 45, 60, and 100 Å, respectively. As the peak-to-valley amplitude increases so does the spacing between oscillations until

Downloaded 09 Mar 2002 to 128.111.74.212. Redistribution subject to AIP license or copyright, see http://ojps.aip.org/japo/japcr.jsp

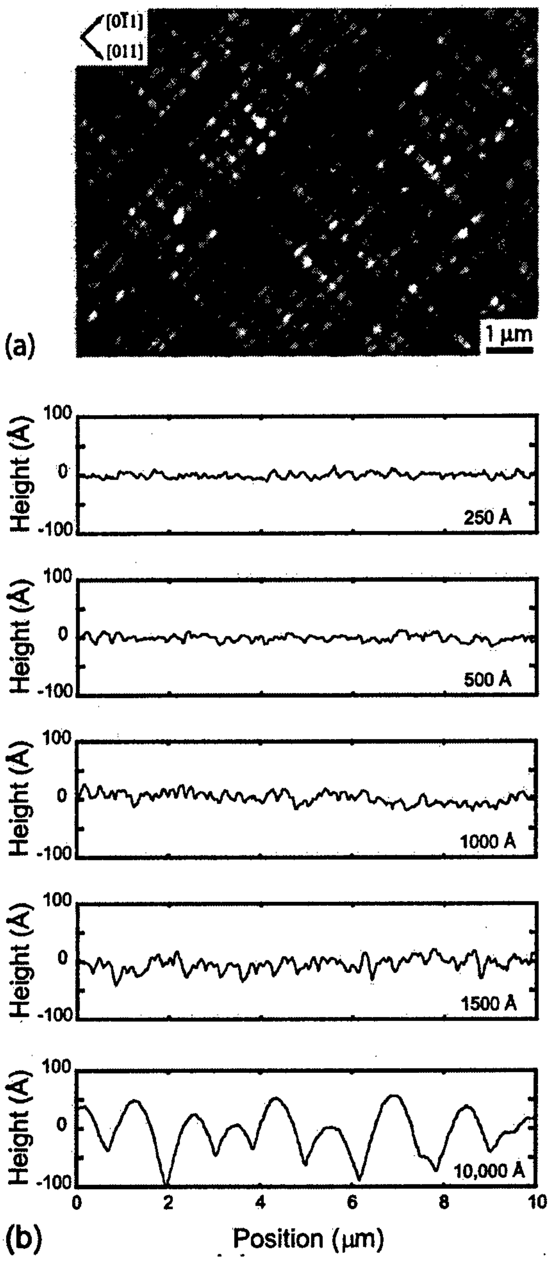

FIG. 3. AFM results of cross-hatch surface morphology in $In_{0.25}Ga_{0.75}As/GaAs$ ($\epsilon_m=1.8\%$) films. (a) Plan view surface cross-hatch topography for a typical 70% relaxed $h=1000$ Å thick film. (b) Surface height profile along the [011] line direction of $h=250$, 500, 1000, 1500, and 10 000 Å films. Note the increasing height variation and the formation of hillocks and valleys with increasing thickness.

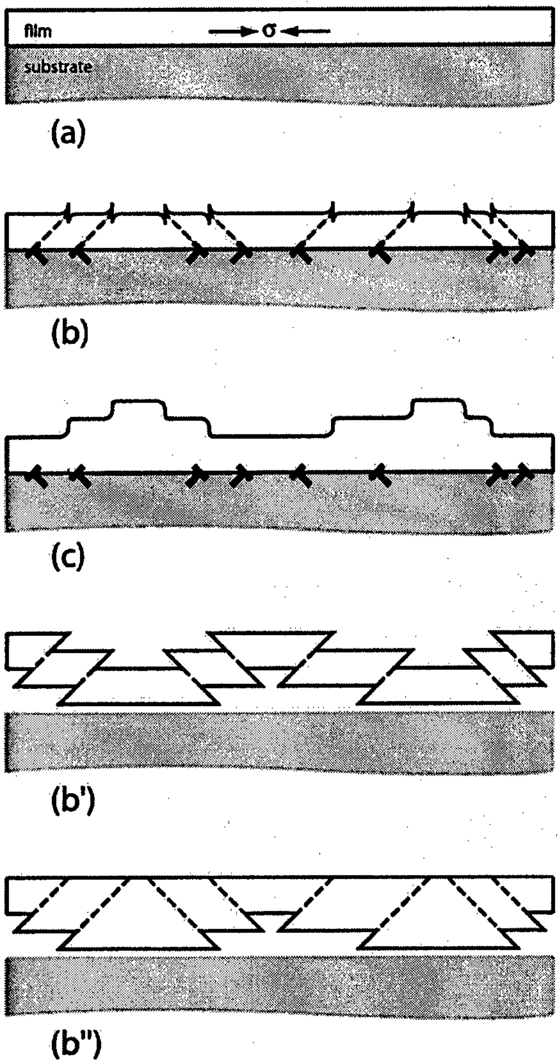

FIG. 4. Schematic depiction of the proposed mechanism for the formation of the cross-hatch surface morphology. (a) An unrelaxed compressively strained heteroepitaxial film coherently attached to substrate. (b) A partially strain-relaxed film with surface steps resulting from dislocation nucleation at the film surface; these dislocations glide towards the film/substrate interface to form a MD array. (c) Final film state resulting from subsequent film growth via surface step elimination. The evolution from (a) to (c) can be considered in an Eshelby-like process where the compressively strained film is removed from the substrate surface and plastically relaxed (b′). The upper surface steps created during relaxation are eliminated by lateral growth (b″) and the relaxed film is then reattached to the substrate (c), where the lower slip steps become the interface MDs.

they appear almost periodic (with wavelengths on the order of 0.15–0.3 μm depending on the crystallographic direction) and uniform at large thicknesses. For the 1 μm sample the total amplitude is ~100 Å with an apparent period greater than 1 μm. The root mean squared (rms) surface roughness of these samples increased from 4 to 35 Å in this film thickness range.

IV. MODELING

A. Qualitative description of cross hatch

The physical basis of the proposed model for the evolution of the surface of a strained heteroepitaxial film is presented in Fig. 4. In the initial state, a coherent compressively strained film [Fig. 4(a)] is deposited on a semi-infinite substrate. We use a compressive misfit strain for the sake of definiteness and to maintain correspondence with the experimental results presented in the previous section. The relaxation of the initial misfit stress by TD motion creates slip steps at the surface [Fig. 4(b)] and trailing MD segments at the film/substrate interface. Strain relaxation alone creates a locally rough (atomic scale), but mesoscopically (~0.1–10 μm) smooth surface. The local roughness is due to steps and is in the direction perpendicular to the steps. Lateral mass transport eliminates the steps produced during strain relaxation [Fig. 4(c)]. The subsurface MDs remain at the inter-

Downloaded 09 Mar 2002 to 128.111.74.212. Redistribution subject to AIP license or copyright, see http://ojps.aip.org/japo/japcr.jsp

face. The MDs contribute to the overall reduction of the stresses in the film but simultaneously produce local stresses near their core regions. The surface height profile develops hillocks where the film growth has eliminated surface slip steps. The plastic relaxation in the film interior, followed by surface step flow, can be treated as a hypothetical "Eshelby-like" process as shown in Figs. 4(b′) and 4(b″). In the hypothetical process, the strained film is removed from the substrate [Fig. 4(b′)]; and plastically deformed along slip planes, thus creating surface steps. The top surface steps are then eliminated by preferential growth at the step edge [Fig. 4(b″)], aided by lateral mass transport and step-flow growth. Subsequently, the film is reattached to the substrate. The bottom surface steps become the film/substrate MDs and the smoothed regions of the top surface become the hillocks [Fig. 4(c)].

In the model developed here, we do not treat details of the film growth, but rather treat the limiting cases where there is no lateral mass transport during film growth and thus no step elimination or where all steps are eliminated via lateral mass transport. The lateral mass transport can either take place during either growth or annealing. In the case in which the film is growing in a layer-by-layer mode, we anticipate that, over time, there will still be elimination of steps created during strain relaxation. In future articles, we will treat the evolution of the excess step density (i.e., by "excess step density" we refer to the density of steps that are geometrically unnecessary for misoriented substrates or epitaxial films) for different growth conditions.

Below we analyze the 1D model. We assume weak interactions between undulations that form in orthogonal directions on the film surface. This assumption is supported by cross-hatch anisotropy observations which show 1D character at the early stages of its evolution. That is, for (001) growth of III–V semiconductors, the cross hatch is often first observed in one of the two ⟨110⟩ directions.[30] With subsequent relaxation, the surface morphology shows different characteristics in the orthogonal ⟨110⟩ directions on the surface.[20,31] For the 1D case, the initial stress state in the film is given by Eqs. (1) (with the designation $\sigma_0=\sigma_{xx}^{1D}$) in the coordinate system xyz (with corresponding unit vectors **i**, **j**, **k**) chosen in accordance with the 1D lattice mismatch and expected cross-hatch orientation.

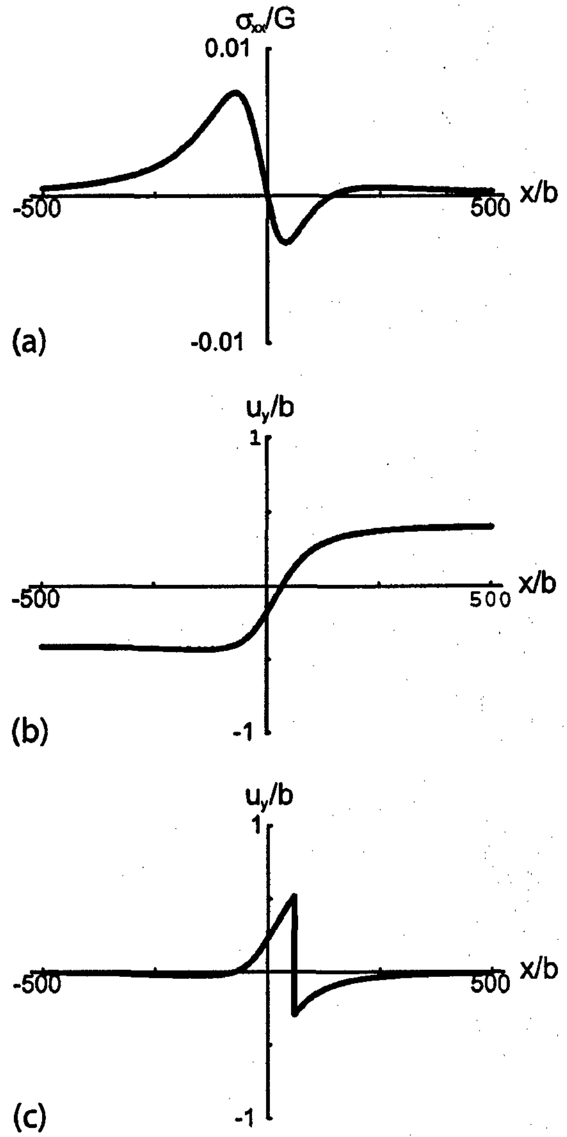

FIG. 5. Surface stress and displacement from a MD placed at the film/substrate interface. (a) The stress σ_{xx} at the film surface; G is shear modulus. (b) Elastic displacement u_y at the surface; no-step or slip step elimination (SSE) case. (c) Displacement u_y at the surface; step or slip step only (SSO) case. For these plots the MD glided left with respect to the surface nucleation site and was placed at the film/substrate interface, i.e., at $(0,-h)$. The film thickness $h=100b$ and Poisson's ratio $\nu=0.3$ were used.

B. Stresses and surface undulation due to a single misfit dislocation

To accurately model the surface profile resulting from strain relaxation and step elimination, the solutions for stress, strain, and displacement for subsurface MDs have to be used. The 60° dislocations under consideration have both edge and screw character. However, screw dislocations oriented parallel to the free surface do not result in surface height displacement and therefore are not considered in the model. As mentioned in Sec. II, the edge component of the Burgers vector can be decomposed into subcomponents parallel $\mathbf{b}_{\parallel}$ and perpendicular $\mathbf{b}_{\perp}$ to the film surface. Below we will distinguish between "left-generated" and "right-generated" dislocations. In this designation, the left-generated dislocations move to the left with respect to the surface source and have Burgers vector components $\mathbf{b}_{\parallel}=-(b/2)\mathbf{i}$ and $\mathbf{b}_{\perp}=-(b/\sqrt{2})\mathbf{j}$. Correspondingly, right-generated dislocations move to the right and have Burgers vector components $\mathbf{b}_{\parallel}=-(b/2)\mathbf{i}$ and $\mathbf{b}_{\perp}=+(b/\sqrt{2})\mathbf{j}$. The equations for the stress fields for edge subsurface dislocations with both perpendicular and parallel orientation of their Burgers vector are given in the Appendix. By applying these equations we find, for example, the tangential stress component $\sigma_{xx}^{\mathrm{MD}}$ at the surface for an individual MD

$$\sigma_{xx}^{\mathrm{MD}}=\frac{4G}{\pi(1-\nu)}\,\frac{xh(b_{\perp}h-b_{\parallel}x)}{(h^2+x^2)^2}. \tag{11}$$

Downloaded 09 Mar 2002 to 128.111.74.212. Redistribution subject to AIP license or copyright, see http://ojps.aip.org/japo/japcr.jsp

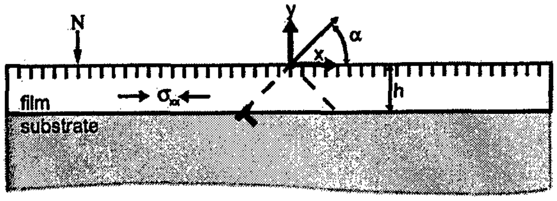

FIG. 6. Schematic of 1D Monte Carlo model for dislocation nucleation at the film surface. The possible dislocation nucleation sites are indicated by small vertical ticks. The film has an initial thickness h, the dislocation slip planes are at an angle α to the surface; at each randomly selected nucleation site N, dislocations can randomly choose "left" or "right" glide planes and corresponding Burgers vector.

Figure 5(a) shows the stress distributions along the surface plotted with the help of Eq. (11) for a dislocation placed at depth $h=100b$ on an inclined (111) slip plane.

There are two limiting cases for the surface displacement u_y we considered for the model: slip step only (SSO), where strain relaxation is by TD motion only, and slip step elimination (SSE), where there is complete elimination of the surface step by lateral mass transport (i.e., surface step annihilation). To model these two cases we use the results presented in the Appendix (also see Fig. 12), where we treat the surface profile for edge dislocations introduced into subsurface layers by different deformation paths. The dislocation displacement field u_y at the surface in the SSE case corresponds to the dislocation path from the material interior towards the surface (as shown in Fig. 12(a)). The displacement field for the left-generated MD can be derived from Eqs. (A4) and (A5)

$$u_y|_{y=0}=\frac{b_\parallel}{\pi}\frac{h^2}{x^2+h^2}+\frac{b_\perp}{\pi}\left(-\frac{xh}{x^2+h^2}-\tan^{-1}\frac{x}{h}\right); \tag{12}$$

This result is plotted in Fig. 5(b), where the displacement u_y from the inclined MD is the combination of the symmetric displacement from $\mathbf{b}_\parallel$ and the asymmetric displacement from $\mathbf{b}_\perp$. The addition of a plastic surface step at the position of the intersection of the dislocation's slip plane with the free surface, via a Heaviside step function, to the displacement u_y [Fig. 5(c)] corresponds to the SSO case (deformation path from the surface to material interior) with negligible displacement at large distances from the dislocation and the surface step. This step is located at the nucleation point of the MD.

C. Simulation of misfit dislocation nucleation

A Monte Carlo algorithm was used for randomly selecting a position for dislocation nucleation at the film surface and for choosing the left or right glide plane orientation to generate the corresponding MD at the film/substrate interface. Figure 6 shows the geometry for the 1D simulation. The possible dislocation nucleation sites are shown as vertical ticks. The orientation of the slip plane is given by the angle α. All possible intersections of the {111} planes with the (001) film surface were allowed as dislocation nucleation sites. Each generation of a MD increases the strain relaxation in the film interior and reduces the initial level of the film stresses σ_0 but is also accompanied by the formation of a slip step at the intersection of the dislocation glide plane with the film surface. The modeling of the evolution of film stress and surface morphology was achieved by superimposing the stress and surface height profiles for each newly introduced dislocation. The simulation continued until a final level of the stress σ_f or a prescribed number of dislocations was reached. For the simulations reported here, we used a pseudo-random number generator described in Ref. 32. To include the effect of neighboring film regions, four additional identical dislocations were simultaneously added during each nucleation event to both sides of the model domain at periods equal to the model domain length. Since the details of the dislocation nucleation processes are unknown, we described the nucleation events as being completely independent. A more accurate analysis should include the dependence of the dislocation nucleation probability on the value of the local internal stresses. Only a single dislocation was introduced into the film during each simulation cycle. It is likely, however, that many MDs and TDs are generated from a single surface source in real systems. This is also the subject for future work.

D. Simulation results

In the present study the film and substrate material properties were taken as those for an $\mathrm{In_{0.25}Ga_{0.75}As}$ film grown on a (001) oriented GaAs substrate. Then, the following model parameters result: elastic moduli $G=2.90$ GPa; $\nu=0.32$; lattice mismatch strain $\epsilon_m=1.8\%$ with corresponding initial stress level $\sigma_0=-1502$ MPa. The modeled domain size was $25\,000b$, which corresponds to ~ 10.1 μm. The equilibrium number of dislocations necessary for 100% relaxation was 880 for this domain size. As it was done for a single subsurface dislocation, two types of surface height profiles were generated in the course of modeling. The SSO profile was the superposition of the plastic and elastic displacements [Fig. 5(c)] and the SSE profile was the superposition of only the elastic displacements [Fig. 5(b)].

The results for the stress evolution in the film are presented in Fig. 7. Within our model, the SSE and SSO give rise to the same stress evolution as we do not treat the effects of local strain relaxation due to surface roughness. The set of coordinates in the plots in Fig. 7 includes: (i) the total number of MDs in the model domain (strain relaxation is directly proportional to this number) or the film thickness; (ii) the position across the surface undulations (~ 10 μm length); and (iii) the stress magnitude at the film surface. With increasing strain relaxation (i.e., with the introduction of MDs), the magnitude of the initial misfit stress at the surface σ_0 reduces to a final average stress $\sigma_f=0$. Due to the random character of both the dislocation nucleation positions and the choice of the glide plane, the modeled stress profile, σ_{xx}, oscillates considerably along the surface in the direction orthogonal to the 1D cross-hatch morphology. This effect becomes more prevalent with increasing strain relaxation, as is shown in Fig. 7(a). For a completely strain-

Downloaded 09 Mar 2002 to 128.111.74.212. Redistribution subject to AIP license or copyright, see http://ojps.aip.org/japo/japcr.jsp

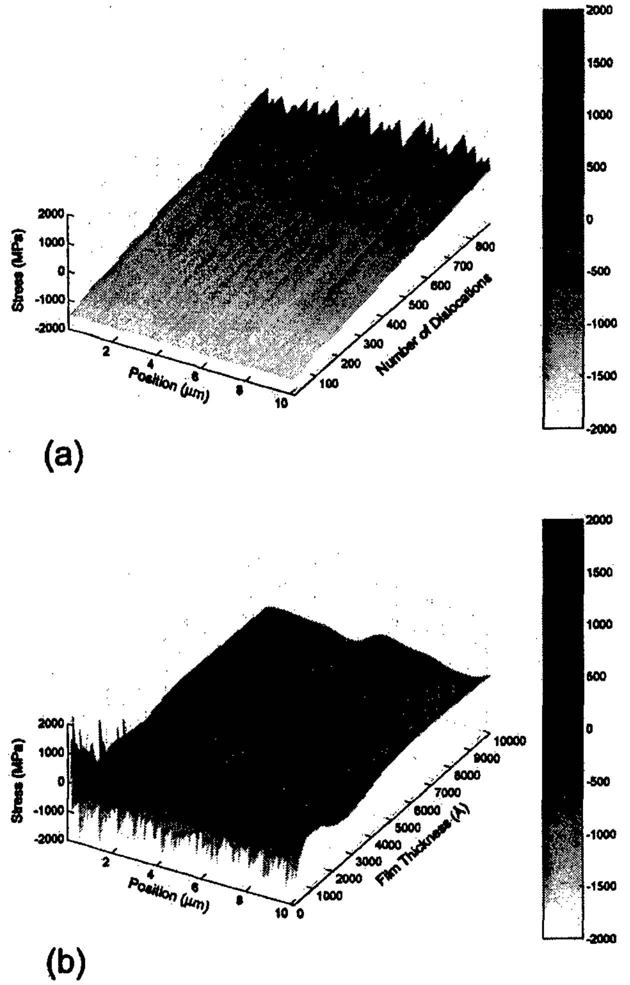

FIG. 7. Value of the stress component σ_{xx} at the film surface during development of cross-hatch morphology. (a) Dependence of σ_{xx} on the extent of relaxation for a 1000-Å-thick film. (b) Dependence of σ_{xx} on film thickness for 100% relaxed films. The modeled film composition $In_{0.25}Ga_{0.75}As$ corresponds to $G=2.90$ GPa, $\nu=0.32$, and $\epsilon_m=1.8\%$.

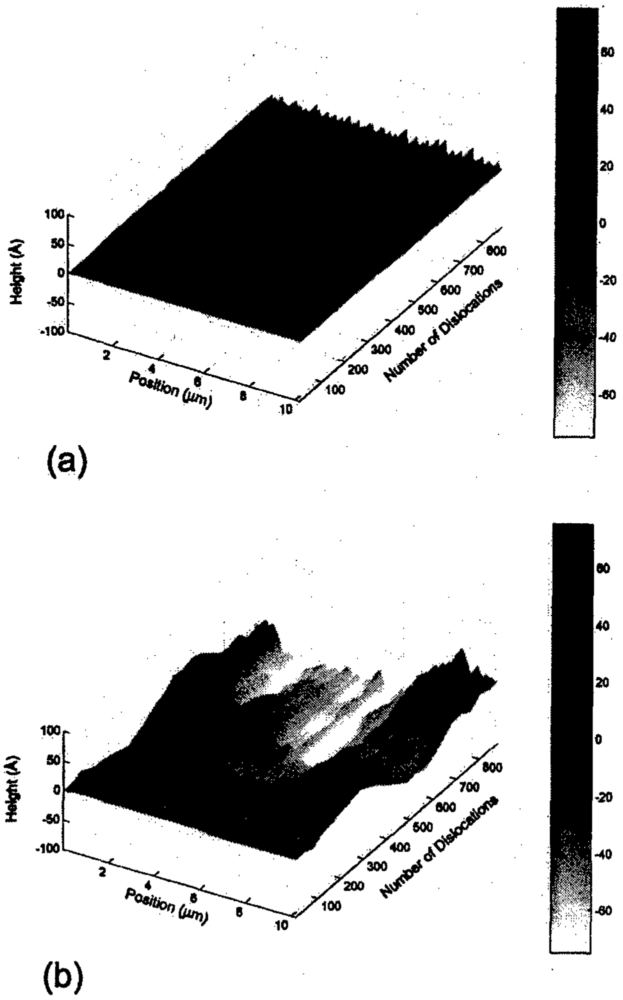

FIG. 8. Surface height profile evolution with increasing strain relaxation. (a) SSO case where there is little variation in the surface height profile. (b) SSE case where there are large variations in surface height profile. The modeled film composition $In_{0.25}Ga_{0.75}As$ corresponds to $G=2.90$ GPa, $\nu=0.32$, and $\epsilon_m=1.8\%$; film thickness $h=1000$ Å.

relaxed film [Fig. 7(b)] there is a rapid decay in the stress magnitude σ_{xx} at the surface as the film thickness increases. This results in a smoother σ_{xx} profile and reduction in the nonuniformity of the stress on the surface in thicker films.

The evolution of surface undulations with increasing strain relaxation and increasing film thickness is shown in Figs. 8 and 9, respectively. The SSO case results in mesoscopically (0.1–10 μm) smooth film surfaces that are atomically rough. As the number of dislocations (strain relaxation) increases, the surface roughens on the atomic scale. The cross-hatch surface undulations in $h=1000$ Å-thick film [SSO, Fig. 8(a)] is characterized by a root mean square (rms) roughness $r=4.9$ Å. The SSE case, shown in Fig. 8(b), results in an atomically smooth film surface with a larger roughness (rms $r=32.1$ Å) on the mesoscale (0.1–10 μm). There are significant changes in the surface height profile as more dislocations are added. The surface profile develops both large-scale features with smooth transitions and large wavelengths combined with smaller superimposed undulating features with much shorter wavelengths. As the film thickness increases the difference between the SSO and SSE plots [Figs. 9(a) and 9(b)] becomes less apparent. For large film thickness, nanoscale (10–1000 Å) fluctuations emerge in the SSO surface profile. The fluctuations are due to the diminished screening of the dislocation elastic fields by the film free surface. The surface displacement profiles [shown in Figs. 5(b) and 5(c)] broaden when the dislocation moves further onto the material interior. The SSE profile becomes smoother with increasing film thickness resulting in larger amplitude and longer wavelength surface height undulation. In our future work, we will pursue Fourier analysis and correlation analysis of the surface height profiles to further quantify the surface height profile.

V. DISCUSSION

The proposed model for cross-hatch formation demonstrates significant similarities with the experimentally observed surface profiles in heteroepitaxial films. Below we

Downloaded 09 Mar 2002 to 128.111.74.212. Redistribution subject to AIP license or copyright, see http://ojps.aip.org/japo/japcr.jsp

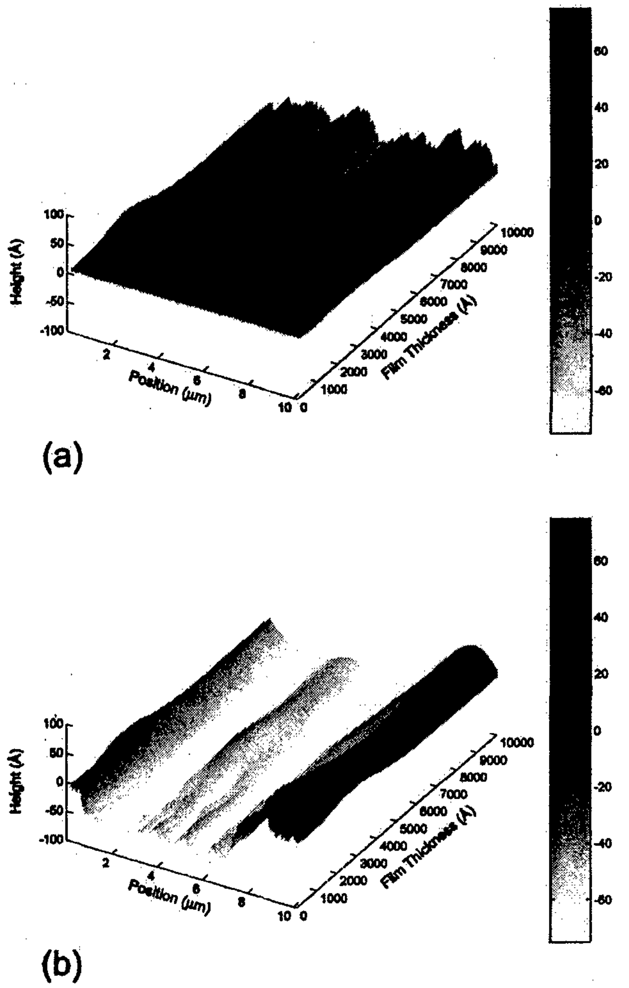

FIG. 9. Evolution of the surface profile with increasing film thickness in 100% relaxed films. (a) *SSO case* where the atomic scale height profile begins to show an increasing amplitude as the film thickness increases. (b) *SSE case* where the mesoscale height profile smoothes with increasing film thickness. The modeled film composition $In_{0.25}Ga_{0.75}As$ corresponds to $G = 2.90$ GPa, $\nu = 0.32$, and $\epsilon_m = 1.8\%$; 100% relaxation corresponds to 880 dislocations per ~10 μm of film length.

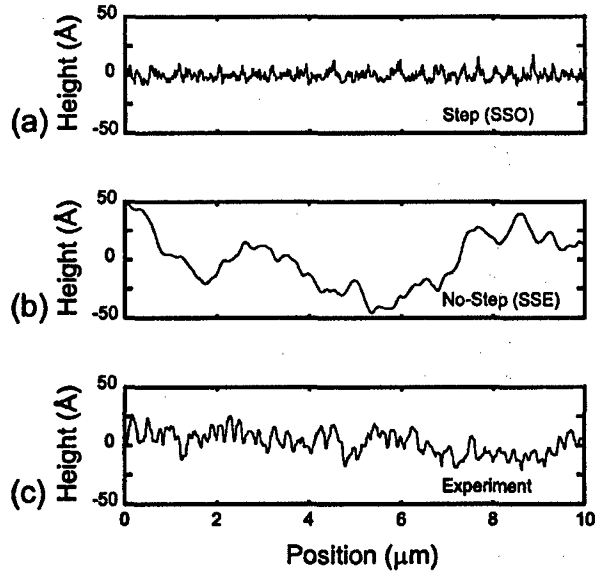

FIG. 10. Comparison with experimental data for approx. 70% strain relaxed $In_{0.25}Ga_{0.75}As$ 1000-Å-thick films. (a) Modeled surface height profile with no step elimination (SSO case), rms roughness $r = 3.8$ Å. (b) Modeled surface height profile with complete step elimination (SSE case), rms roughness $r = 23.1$ Å. (c) Experimental surface height profile, rms roughness $r = 10.4$ Å.

discuss some observations concerning the film stress and surface morphology resulting from Monte Carlo modeling of dislocation-assisted relaxation processes in the film/substrate system.

The model predicts the existence of nonuniform elastic stresses, which are particular to the originally mismatched, but finally relaxed, layers with cross-hatch morphology. Random introduction of MDs creates an oscillatory stress profile with average spacing on the order of the film thickness. The magnitude of the peak amplitude of the stress at the film surface is extremely large when the growing film is thin and dislocations are close to its surface. The stresses at the surface, however, fall off quickly with increasing film thickness.

The qualitative agreement of the experimentally observed surface cross hatch with the model is good. The first limiting case, slip step only (SSO), produces surface profiles with little to no height undulation. The surface slip steps created during relaxation are the only major source of roughness in the thin films. As the films become thicker, the SSO surface begins to roughen at the mesoscale due to the diminishment of the elastic field of the MDs. In the "unscreening" effect, dislocations contribute to surface profile at larger distances from their lines. For the dislocation placed at some distance h from the stress-free surface, the dislocation elastic fields are screened and localized in the region with lateral size $2h$ above the dislocation core. Beyond this region, the stresses diminish inversely proportional with the square distance from the dislocation. When the dislocation is placed at larger distance from the surface (as in the case of thicker films) the absolute value of the screening distance increases and we observe the effect of unscreening of the dislocation elastic fields. For the second limiting case, slip step elimination (SSE), the surface displacement resulting from strain relaxation and subsequent surface step flow is large. Thin films (e.g., $h < 200$ Å) show both large scale surface undulations and small scale more frequent undulations in the surface height profile. As the SSE films become thicker, their surface locally smoothes reducing the smaller undulations and creating only the large amplitude long wavelength undulations.

The quantitative agreement between experimentally observed, ~70% strain relaxed, 1000-Å-thick $In_{0.25}Ga_{0.75}As$ surface profile and the modeled profiles are shown in Fig. 10. The SSO case [Fig. 10(a)] predicts a rms roughness of $r = 3.8$ Å and the SSE case [Fig. 10(b)] predicts a rms roughness of $r = 23.1$ Å while the experimental (AFM measured) surface profile [Fig. 10(c)] possesses a rms roughness of only $r = 10.4$ Å. The experimentally determined surface features appear to be intermediate ones between those for SSO and SSE cases. The model results for a 10 000-Å-thick film are compared to a ~100% strain relaxed $In_{0.25}Ga_{0.75}As$ surface

Downloaded 09 Mar 2002 to 128.111.74.212. Redistribution subject to AIP license or copyright, see http://ojps.aip.org/japo/japcr.jsp

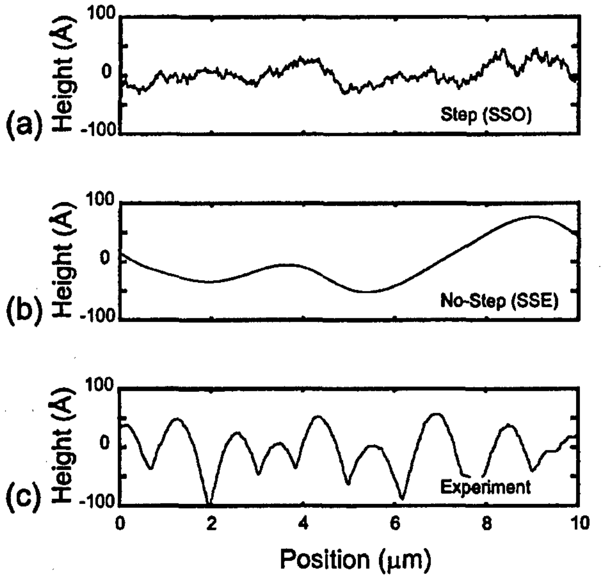

FIG. 11. Comparison with experimental data for ~100% strain relaxed $In_{0.25}Ga_{0.75}As$ 10000 Å thick films. (a) Modeled surface height profile with no film growth (SSO case), rms roughness $r=16.3$ Å. (b) Modeled surface height profile with complete step elimination (SSE case), rms roughness $r=38.9$ Å. (c) Experimental surface height profile with a cross-sectional scan, rms roughness $r=33.8$ Å.

in Fig. 11. At this film thickness, the SSO case [Fig. 11(a)] provides a rms roughness of $r=16.3$ Å, the SSE case [Fig. 11(b)] shows a rms roughness of $r=38.9$ Å, and the experimentally observed surface [Fig. 11(c)] has a rms roughness of $r=33.8$ Å. As seen in Fig. 11, the experimental cross-hatch pattern has ~1 μm wavelength undulations in comparison with ~3 μm wavelength undulations for the SSE case. The discrepancy in wavelength may be due to many factors presently not included in the model. For the 1D model there is no dislocation blocking from perpendicular dislocation pileups. More importantly, the model does not allow for any dislocation nucleation or multiplication sources in the film interior.

As we have shown, the limiting cases for cross-hatch evolution (i.e., SSO and SSE) can be readily modeled. The partial elimination of steps is a complex problem that requires knowledge of the relevant surface diffusion lengths, growth temperature, growth rate, substrate miscut, and other factors. Our ultimate goal is therefore to learn more about these dislocation and growth processes and their influence on the strained film surface profile. From the experimental data we would like to use cross hatch to learn about relaxation pathways, particularly sources of dislocations, blocking, multiplication and possible routes to more efficient relaxation.

VI. SUMMARY AND CONCLUSIONS

We have presented a model to explain cross-hatch surface morphology in partially or fully relaxed epitaxial films that have grown in a layer-by-layer or step-flow mode. The model accounts for both the plastic and elastic surface height displacement resulting from subsurface misfit dislocations which result from nucleation events at the film surface. Using random dislocation nucleation, the model cross-hatch patterns exhibit surface height profiles similar to the experimentally observed height profiles. We have demonstrated that elimination of the plastic slip steps leads to large scale surface height undulations. Thus, we attribute fully developed cross-hatch patterns to a process in which all surface steps produced by plastic relaxation are eliminated (via lateral mass transport). The fully developed cross-hatch patterns are thus locally smooth but mesoscopically rough.

ACKNOWLEDGMENTS

This work was supported in part by DARPA (through programs sponsored by W. Coblenz), AFOSR (D. Johnstone and G. Witt program managers), and through a subcontract from NCA&T.

APPENDIX: ELASTIC FIELDS OF EDGE DISLOCATIONS IN SUBSURFACE LAYERS

The derivation of the elastic fields for dislocations placed in the vicinity of a traction-free surface is one of the classical problems in dislocation theory.[33–35] Head gave the first solution for an edge dislocation parallel to the interface between two semi-infinite isotropic media with different elastic properties; the solution included the free surface as a limiting case.[36] Below we provide expressions for dislocation stresses by applying the technique originally developed by Eshelby for finding the Airy stress function of an edge dislocation in an infinite elastic medium.[37] In this technique the elastic characteristics for straight edge dislocations are obtained by substituting the dislocation with a wedge disclination dipole having an infinitesimally small arm. Then dislocation elastic fields can be easily calculated by taking the appropriate partial derivatives of the disclination solutions.[37,38] The other, even simpler, method to obtain solutions for edge dislocations utilizes the formulas for straight twist disclination dipoles.[38] In the case of isotropic semi-infinite media, the analytical expressions for elastic stresses of straight twist disclinations were obtained by Romanov and Vladimirov.[39]

Consider an elastic isotropic half space, which occupies the region $y \leqslant 0$. The line of an edge dislocation is parallel to the free surface. The coordinate system x, y, z (with $\mathbf{i}$, $\mathbf{j}$, $\mathbf{k}$ being the unit vectors along the corresponding axes) is chosen in such manner that the z axis is parallel to the dislocation line direction $\mathbf{l}=+\mathbf{k}$. The dislocation position is $(0, -h)$, i.e., the dislocation is placed at a distance h from the surface. There exist two possible orientations for an edge dislocation Burgers vector: parallel $\mathbf{b}_{\parallel}=b_{\parallel}\mathbf{i}$ and perpendicular $\mathbf{b}_{\perp}=b_{\perp}\mathbf{j}$ to the free surface. The components of the dislocation stress tensors $\sigma_{ij}^{b_{\parallel}}$ and $\sigma_{ij}^{b_{\perp}}$ for these two orientations of the Burgers vector are

Downloaded 09 Mar 2002 to 128.111.74.212. Redistribution subject to AIP license or copyright, see http://ojps.aip.org/japo/japcr.jsp

$$\sigma_{xx}^{b_\parallel}=\frac{Gb_\parallel}{2\pi(1-\nu)}\left[-\frac{(y+h)(3x^2+(y+h)^2)}{(x^2+(y+h)^2)^2}+\frac{(y-h)(3x^2+(y-h)^2)}{(x^2+(y-h)^2)^2}\right.$$
$$\left.+\frac{2h(-x^4+6x^2y(y+h)-y^4-2y^3h+2yh^3+h^4)}{(x^2+(y+h)^2)^3}\right], \tag{A1a}$$

$$\sigma_{yy}^{b_\parallel}=\frac{Gb_\parallel}{2\pi(1-\nu)}\left[\frac{(y+h)(x^2-(y+h)^2)}{(x^2+(y+h)^2)^2}-\frac{(y-h)(x^2-(y-h)^2)}{(x^2+(y-h)^2)^2}\right.$$
$$\left.+\frac{2h(-x^4-6x^2y(y+h)+3y^4+10y^3h+12y^2h^2+6yh^3+h^4)}{(x^2+(y+h)^2)^3}\right], \tag{A1b}$$

$$\sigma_{xy}^{b_\parallel}=\frac{Gb_\parallel}{2\pi(1-\nu)}\left[-\frac{x(x^2-(y+h)^2)}{(x^2+(y+h)^2)^2}+\frac{x(x^2-(y-h)^2)}{(x^2+(y-h)^2)^2}+\frac{4xyh(x^2-3(y+h)^2)}{(x^2+(y+h)^2)^3}\right], \tag{A1c}$$

$$\sigma_{zz}^{b_\parallel}=\nu(\sigma_{xx}^{b_\parallel}+\sigma_{yy}^{b_\parallel}), \tag{A1d}$$

$$\sigma_{xx}^{b_\perp}=\frac{Gb_\perp}{2\pi(1-\nu)}\left[-\frac{x(x^2-(y+h)^2)}{(x^2+(y+h)^2)^2}-\frac{x(x^2-(y-h)^2)}{(x^2+(y-h)^2)^2}\right.$$
$$\left.+\frac{2x(x^4+6x^2yh+4x^2h^2-(y+h)^4+4h(y+h)^3-6yh(y+h)^2)}{(x^2+(y+h)^2)^3}\right], \tag{A2a}$$

$$\sigma_{yy}^{b_\perp}=\frac{Gb_\perp}{2\pi(1-\nu)}\left[-\frac{x(x^2+3(y+h)^2)}{(x^2+(y+h)^2)^2}-\frac{x(x^2+3(y-h)^2)}{(x^2+(y-h)^2)^2}+\frac{2x(x^4+4x^2(y+h)^2-2x^2yh+3(y+h)^4+6yh(y+h)^2)}{(x^2+(y+h)^2)^3}\right], \tag{A2b}$$

$$\sigma_{xy}^{b_\perp}=\frac{Gb_\perp}{2\pi(1-\nu)}\left[\frac{(y+h)(x^2-(y+h)^2)}{(x^2+(y+h)^2)^2}+\frac{(y-h)(x^2-(y-h)^2)}{(x^2+(y-h)^2)^2}+\frac{2y(-x^4-6x^2h(y+h)+(y+h)^4+2h(y+h)^3)}{(x^2+(y+h)^2)^3}\right], \tag{A2c}$$

$$\sigma_{zz}^{b_\perp}=\nu(\sigma_{xx}^{b_\perp}+\sigma_{yy}^{b_\perp}), \tag{A2d}$$

where G and ν are the shear modulus and Poisson ratio of an isotropic elastic material, respectively.

In the formulas for stresses, the first terms in the large brackets correspond to the dislocation stresses in infinite media. The second terms correspond to stresses of an "image" dislocation placed at the position $(0,+h)$. With the aid of the image terms, the part of the boundary conditions at the free surface is satisfied. To fulfill all the boundary conditions at the traction free surface, additional stresses must be superimposed and they are given by the third terms. The dislocation stresses given in Eqs. (A1) and (A2) satisfy both the boundary conditions at $y=0$ and the differential equilibrium equations $\sigma_{ij,j}=0$ in the material interior. The stresses (A1) and (A2) written in different notations can be also found in Refs. 34 and 35.

The displacement field associated with the dislocation can be determined by the integration of the corresponding components of the elastic strain tensor. For the purpose of the present study we are interested in the component of the displacement u_y in the direction of the y axis measured directly at the surface

$$u_y(x)|_{y=0}=\int_{-\infty}^{0}\epsilon_{yy}(x,y)dy, \tag{A3}$$

where ϵ_{yy} is the component of the dislocation strain tensor, which can be found by applying Hooke's law to the stresses (A1) or (A2). Direct integration leads to the following result:

$$u_y^{b_\parallel}|_{y=0}=\frac{b_\parallel}{\pi}\frac{h^2}{x^2+h^2}, \tag{A4}$$

$$u_y^{b_\perp}|_{y=0}=\frac{b_\perp}{\pi}\left(-\frac{xh}{x^2+h^2}-\tan^{-1}\frac{x}{h}\right) \tag{A5}$$

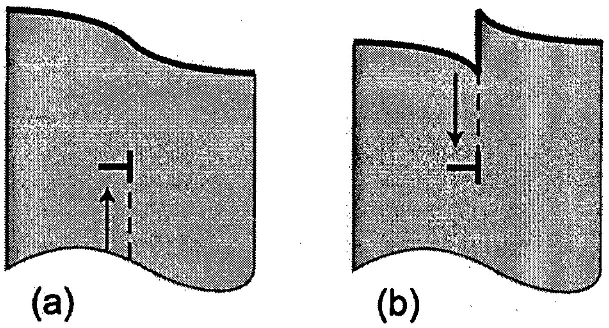

FIG. 12. No-step (SSE) vs step (SSO) surface profile associated with an edge dislocation. (a) The edge dislocation arrived in the subsurface region from the material interior. (b) The edge dislocation glided to the subsurface region after nucleation at the surface (the surface dislocation nucleation involves the formation of a surface step).

Downloaded 09 Mar 2002 to 128.111.74.212. Redistribution subject to AIP license or copyright, see http://ojps.aip.org/japo/japcr.jsp

for edge dislocations with Burgers vector parallel or perpendicular to the free surface, respectively.

Analysis shows that the surface profiles given by Eqs. (A4) and (A5) correspond only to the elastic part of the total displacement field associated with the subsurface dislocations. The solution (A5) can therefore be prescribed to the dislocation arriving in the subsurface layer from the material interior, as is shown in Fig. 12(a). To include the plastic displacement related to the glide of the dislocation resulting from the surface nucleation (Fig. 12b), the step-like function $b_\perp[H(x)-1/2]$ [where $H(x)$ is the Heaviside function] must be added to the formula (A5) for displacement $u_y^{b_\perp}$. This leads to the relation, which accounts for the surface step

$$u_y^{b_\perp}|_{y=0}=\frac{b_\perp}{\pi}\left(-\frac{xh}{x^2+h^2}+\tan^{-1}\frac{h}{x}\right). \qquad \text{(A6)}$$

Sometimes in the literature[35] the dislocation displacement near the free surface are given in the form (A6).

In our modeling we refer to the surface profile associated with an edge dislocation having the component of the Burgers vector perpendicular to the surface as *no-step* or *slip step elimination (SSE) case* when it corresponds to the scheme shown in Fig. 12(a) and is described by the Eq. (A5) and as *step* or *slip step only (SSO) case* when it corresponds to the scheme shown in Fig. 12(b) and is described by the Eq. (A6).

[1] John A. Venables, *Introduction to Surface and Thin Film Processes* (Cambridge University Press, Cambridge, 2000).

[2] A. Pimpinelli and J. Villain, *Physics of Crystal Growth* (Cambridge University Press, Cambridge, 1998).

[3] K. Samonji, H. Yonezu, T. Takagi, and N. Ohshima, J. Appl. Phys. **86**, 1331 (1999).

[4] D. K. Fork, F. Armani-Leplingard, and J. J. Kingston, MRS Bull. **21** , 53 (1996).

[5] M. Yoon, B. Lee, J.-H. Baek, H.-H. Park, E.-H. Lee, and J. Y. Lee, Appl. Phys. Lett. **68**, 16 (1996).

[6] R. A. Burmeister, G. P. Pighini, and P. E. Greene, Trans. Metall. Soc.-AIME **245**, 587 (1969).

[7] K. H. Chang, R. Gibala, D. J. Srolovitz, P. K. Bhattacharya, and J. F. Mansfield, J. Appl. Phys. **67**, 4093 (1990).

[8] G. P. Watson, E. A. Fitzgerald, Y.-H. Xie, and D. Monroe, J. Appl. Phys. **75**, 263 (1994).

[9] C. Tatsuyama, T. Asano, T. Nakao, H. Matada, T. Tambo, and H. Ueba, Thin Solid Films **369**, 161 (2000).

[10] E. A. Fitzgerald, Y. H. Xie, D. Monroe, P. J. Silverman, J. M. Kuo, A. R. Kortan, F. A. Thiei, and B. E. Weir, J. Vac. Sci. Technol. B **10**, 1807 (1992).

[11] G. Springholz, Appl. Phys. Lett. **75**, 3099 (1999).

[12] N. Samarth (private communication).

[13] G. H. Olsen, J. Cryst. Growth **31**, 223 (1975).

[14] S. Kishino, M. Ogirima, and K. Kurata, J. Electrochem. Soc. **119**, 618 (1972).

[15] J. W. P. Hsu, E. A. Fitzgerald, Y. H. Xie, P. J. Silverman, and M. J. Cardillo, Appl. Phys. Lett. **61**, 1293 (1992).

[16] F. Jonsdottir and L. B. Freund, Mech. Mater. **20**, 337 (1995).

[17] H. Gao, J. Mech. Phys. Solids **42**, 741 (1994).

[18] S. Y. Shiryaev, F. Jensen, and J. W. Petersen, Appl. Phys. Lett. **64**, 3305 (1994).

[19] M. A. Lutz, R. M. Feenstra, F. K. LeGoues, P. M. Mooney, and J. O. Chu, Appl. Phys. Lett. **66**, 724 (1995).

[20] A. M. Andrews, A. E. Romanov, J. S. Speck, M. Bobeth, and W. Pompe, Appl. Phys. Lett. **77**, 3740 (2000).

[21] J. W. Matthews, in *Dislocations in Solids*, edited by F. R. N. Nabarro (North-Holland, Amsterdam, 1979), Vol. 2, p. 461.

[22] E. A. Fitzerald, Mater. Sci. Rep. **7**, 87 (1991).

[23] L. B. Freund, MRS Bull. **17**, 52 (1992).

[24] R. Beanland, D. J. Dunstan, and P. J. Goodhew, Adv. Phys. **45**, 87 (1996).

[25] J. S. Speck, M. A. Brewer, G. E. Beltz, A. E. Romanov, and W. Pompe, J. Appl. Phys. **80**, 3808 (1996).

[26] J. W. Matthews and A. E. Blakeslee, J. Cryst. Growth **27**, 118 (1974).

[27] J. Y. Tsao, *Materials Fundamentals of Molecular Beam Epitaxy* (Academic, New York, 1993).

[28] A. Krost, G. Bauer, and J. Woitok, in *Optical Characterization of Epitaxial Semiconductor Layers*, edited by G. Bauer and W. Richter (Springer, New York, 1996), p. 287.

[29] B. D. Gerardot, G. Subramanian, S. Minvielle, H. Lee, J. A. Johnson, W. V. Schoenfeld, D. Pine, J. S. Speck, and P. M. Petroff (unpublished).

[30] K. Samonji, H. Yonezu, Y. Takagi, and N. Ohshima, J. Appl. Phys. **86**, 1331 (1999).

[31] M. T. Bulsara, V. Yang, A. Thilderkvist, E. A. Fitzgerald, K. Hausler, and K. Eberl, J. Appl. Phys. **83**, 592 (1998).

[32] D. Stauffer, *Random Number Generation, in Computational Physics*, edited by K. H. Hoffmann and M. Schreiber (Springer, Berlin, 1996), p. 1.

[33] J. D. Eshelby, in *Dislocations in Solids*, edited by F. R. N. Nabarro (North-Holland, Amsterdam, 1979), Vol. 1, p. 167.

[34] J. P. Hirth and J. Lothe, *Theory of Dislocations* (Wiley, New York, 1982).

[35] J. Lothe, in *Elastic Strain Fields and Dislocation Mobility*, edited by V. L. Indenbom and J. Lothe (North-Holland, New York, 1992), p. 361.

[36] A. K. Head, Proc. Phys. Soc. London, Sect. B **66**, 793 (1953).

[37] J. D. Eshelby, Br. J. Appl. Phys. **17**, 1131 (1966).

[38] A. E. Romanov and V. I. Vladimirov, in *Dislocations in Solids*, edited by F. R. N. Nabarro (Elsevier, New York, 1992), Vol. 9, p. 191.

[39] A. E. Romanov and V. I. Vladimirov, Phys. Status Solidi A **63**, 109 (1981).

Downloaded 09 Mar 2002 to 128.111.74.212. Redistribution subject to AIP license or copyright, see http://ojps.aip.org/japo/japcr.jsp

Appendix III

TML ABSTRACT + LINKS

JOURNAL OF APPLIED PHYSICS VOLUME 95, NUMBER 11 1 JUNE 2004

Modeling crosshatch surface morphology in growing mismatched layers. Part II: Periodic boundary conditions and dislocation groups

A. M. Andrews, R. LeSar, M. A. Kerner, and J. S. Speck[a]
Materials Department, University of California, Santa Barbara, California 93106

A. E. Romanov
Ioffe Physico-Technical Institute, Russian Academy of Sciences, Polytechnicheskaya 26, RU-194021, St. Petersburg, Russia

A. L. Kolesnikova
Institute for Problems of Mechanical Engineering, Russian Academy of Sciences, Bolshoj 61, Vas. Ostrov, RU-199178, St. Petersburg, Russia

M. Bobeth and W. Pompe
Technical University Dresden, Hallwachsstrasse 3, 01062, Dresden, Germany

(Received 10 December 2003; accepted 25 February 2004)

We present further developments and understanding of the commonly observed crosshatch surface morphology in strain-relaxed heteroepitaxial films. We have previously proposed that the crosshatch morphology is directly related with strain relaxation via threading dislocation glide which results in both surface step and misfit dislocation (MD) formation [see Andrews *et al.*, J. Appl. Phys. **91**, 1933 (2002)—now referred to as Part I]. In this article, we have used solutions for the stress fields and displacement fields for periodic MD arrays which include the effects of the free surface. These solutions avoid truncation errors associated with finite dislocation arrays that were used in Part I. We have calculated the surface height profile for relaxed films where the misfit dislocations were introduced randomly or the misfit dislocations were placed in groups with alternating sign of the normal component of their Burgers vector. We have calculated the surface height profiles where the slip step remains at the surface ["slip step only" (SSO)] and where the slip step is eliminated ["slip step eliminated" (SSE)] due to annihilation of opposite sense steps, such as could happen during growth or lateral mass transport. For relaxed films, we find that the surface height undulations, characteristic of crosshatch, increase with increasing film thickness for the SSO case, whereas the surface becomes flatter for the SSE case. Experiments on relaxed $In_{0.25}Ga_{0.75}As$ films on (001) GaAs show that the surface height undulations in the [110] direction increase with increasing film thickness. Thus, we conclude that with increasing film thickness the crosshatch in the slow diffusion [110] direction is best described by the SSO case. © *2004 American Institute of Physics.*

[DOI: 10.1063/1.1707208]

I. INTRODUCTION

Crosshatch is a common surface morphology that is observed after plastic strain relaxation in the heteroepitaxy of mismatched layers which grow in a two-dimensional mode (either layer-by-layer or step-flow growth). Crosshatch surfaces show a characteristic undulating morphology with hills and valleys parallel to the intersection of slip planes with the crystal surface. For the common case of the (001) growth of semiconductors with fcc lattices (e.g., $Si_{1-x}Ge_x$ on Si or $In_xGa_{1-x}As$ on GaAs), the undulating surface morphology exhibits ridges and grooves parallel to the [110] and $[\bar{1}10]$ directions on the surface. A representative crosshatch morphology is shown in Fig. 1 for a partially strain-relaxed 0.25-μm-thick $In_{0.25}Ga_{0.75}As$ layer on (001) GaAs. The crosshatch typically has peak-to-valley heights of 10–100 Å and peak-to-peak spacings of 0.1 μm to several microns depending on the mismatch, film thickness, and growth conditions.

Recently, we have proposed that crosshatch is related to the formation of misfit dislocations (MDs) and surface steps via glide of threading dislocation (TD), which is accompanied by the appearance of surface steps (also called slip steps).[1] Full details of this work were presented previously and we refer to that paper now as Part I.[2] It is expected that these surface steps may be eliminated to a certain degree by step motion due to mass transport on the surface during film growth or annealing. Two equal slip steps moving in the opposite direction will annihilate when they meet. (001) surfaces of zincblende semiconductors have twofold symmetry. For (001) GaAs, molecular beam epitaxy growth typically takes place on surfaces with (2×4) reconstructions. This reconstruction consists of missing As dimer rows in the $[\bar{1}10]$ direction. Experimentally, it has been established that $[\bar{1}10]$ is the fast ad-species diffusion direction and [110] is the slow diffusion direction.[3,4] Kley *et al.* calculated a diffusional barrier of 1.2 eV in the $[\bar{1}10]$ direction and 1.5 eV in the [110] direction.[5] Because of the difference in the diffu-

---

[a]Electronic mail: speck@mrl.ucsb.edu

Downloaded 29 May 2004 to 128.111.74.212. Redistribution subject to AIP license or copyright, see http://jap.aip.org/jap/copyright.jsp

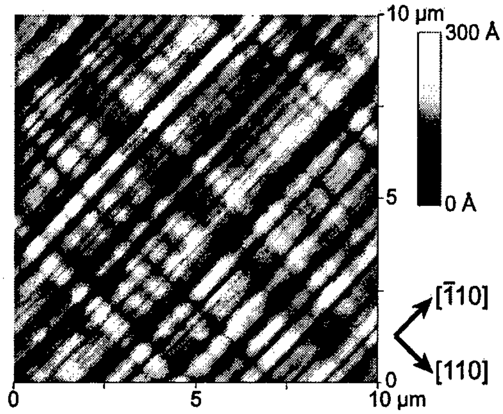

FIG. 1. Characteristic AFM image of a crosshatch pattern for a 0.25-μm-thick $In_{0.25}Ga_{0.75}As$ layer on a (001) oriented GaAs substrate.

sion coefficient in the [110] and [$\bar{1}$10] directions on the $In_{0.25}Ga_{0.75}As$ surface, the degree of step elimination should differ in the two directions.

For a quantitative understanding of crosshatch patterns, the surface morphology development was studied by means of Monte Carlo simulations in Part I. The simulation procedure was based on analytic solutions for the stress field and displacement field which appear at the film surface due to the introduction of a MD at the film/substrate interface. In the simulation, the surface profile changes due to the superposition of the normal component of the displacement from many MDs which were introduced at the film/substrate interface. Since diffusion and growth processes were not included in the model, two limiting cases of the behavior of slip steps were considered: (i) the complete absence of step motion; and (ii) the complete elimination of slip steps by step motion and annihilation. These two cases have been called "slip step only" (SSO) and "slip step eliminated" (SSE), respectively. The simulations in Part I were performed within a finite cell using analytic solutions for a laterally infinite film/substrate system. To reduce finite size effects, the stress and displacement fields of four further cells on each side of the simulation cell were superposed.

Comparison of the simulation results with experimental data showed that the proposed mechanisms can in principal explain the crosshatch pattern observed by atomic force microscopy (AFM). It was found that slip step elimination was necessary to achieve surface height profiles comparable with the experimental values for partially relaxed ~0.1-μm-thick $In_{0.25}Ga_{0.75}As$ films. However, for thicker films (e.g., 1 μm), the simulated height profiles showed large height undulations for the SSE case, where we expected progressive smoothing for the SSE case for large thickness. We now believe that the results for large film thickness were impacted by the finite number of repeat cells used in adjacency to our simulation cell.

In the present article, a more accurate analysis of crosshatch formation is given, with the eventual aim of the determination of MD nucleation mechanisms in stressed semiconductor layers. The Monte Carlo simulations were improved by using rigorous periodic boundary conditions in order to avoid artifacts by truncation errors. To this end, exact analytic solutions for the stress and displacement fields of an infinite periodic array of MDs have been derived. On the basis of these solutions, it is possible to simulate the development of physically relevant crosshatch surface morphology. A main result of the simulations is that the measured surface height profile is best described by an arrangement of groups of MDs with the same normal component of their Burgers vector.

II. BACKGROUND

In this article, we consider cube-on-cube epitaxy of materials with fcc lattices. We use the same formalism as developed in Part I. Within the body of the text we take the x and z axes are parallel to the film/substrate interface and the y axis is perpendicular to the film/substrate interface. The x and z axes coincide with the orthogonal MD line directions. For (001) oriented semiconductors with face-centered-cubic lattices (e.g., zinc blende or diamond cubic structures), the x and z directions are parallel to $\langle 110\rangle$ directions. The lattice mismatch is given as ε_m:

$$\varepsilon_m=\frac{a_s-a}{a}, \tag{1}$$

where a_s and a are the substrate and relaxed film cubic lattice constants. For the case of equibiaxial mismatch, the stress state in the film is given as

$$\sigma_{xx}=\sigma_{zz}=2G\frac{1+\nu}{1-\nu}\varepsilon_m, \tag{2}$$

where G and ν are the shear modulus and Poisson's ratio, respectively. For simplicity, the elastic properties of the film and substrate are assumed to be isotropic and we use the same elastic constants for the film and substrate.

The stored elastic energy w per unit area of the film/substrate interface associated with the misfit stresses is proportional to the film thickness h. Increasing the stored energy with increasing film thickness h will eventually lead to the onset of strain relaxation. MD generation at the interface between the film and substrate has been shown to be the most common mechanism for the relaxation of elastic stress.[6–9] In the majority of cases the MDs are associated with TDs, which are concomitant to MDs but have their lines going through the film to the free surface.[8,10] The Matthews–Blakeslee[11] critical thickness h_c for MD generation may be derived[8] by considering the energetics of a combined MD–TD configuration in a stressed film

$$h_c=\frac{b}{\varepsilon_m(1+\nu)8\pi\cos\lambda}(1-\cos^2\beta)\ln\left(\frac{\alpha_0 h_c}{b}\right)\approx\frac{b}{\varepsilon_m}, \tag{3}$$

where $b=|\mathbf{b}|$ is the magnitude of the dislocation Burgers vector $\mathbf{b}$, λ is the angle between the Burgers vector and a line that lies in the film/substrate interface normal to the MD line, β is the angle between the MD line and $\mathbf{b}$, and α_0 is the dislocation core cutoff parameter.

Downloaded 29 May 2004 to 128.111.74.212. Redistribution subject to AIP license or copyright, see http://jap.aip.org/jap/copyright.jsp

For a completely relaxed film, the linear density of MDs $\rho_{\mathrm{MD,relaxed}}$ multiplied by the edge component of the MD Burgers vector parallel to the interface $b_{\|}=b\cos\lambda$, is equal to the misfit strain ε_m, i.e.:

$$\rho_{\mathrm{MD,relaxed}} b_{\|}=\varepsilon_m. \tag{4}$$

For films of finite thickness that are grown on semi-infinite substrates, the equilibrium linear MD density $\rho_{\mathrm{MD,equil}}$ depends on the film thickness as follows:[12]

$$\rho_{\mathrm{MD,equil}}=\rho_{\mathrm{MD,relaxed}}\left(1-\frac{h_c}{h}\right),\quad h>h_c. \tag{5}$$

The actual MD density realized at a particular stage of the film relaxation is almost always less than those given by Eqs. (4) and (5) $\rho_{\mathrm{MD,actual}}\leq\rho_{\mathrm{MD,equil}}<\rho_{\mathrm{MD,relaxed}}$. The extent of strain relaxation R can be therefore defined as

$$R=\frac{\rho_{\mathrm{MD,actual}}}{\rho_{\mathrm{MD,relaxed}}} \tag{6}$$

Figure 2 illustrates the crystallography for dislocation-assisted strain relaxation in the film growth on (001) oriented substrates. The relaxation occurs by TD motion and MD formation on the inclined glide planes.[8] For semiconductor materials, such as $\mathrm{Si}_{1-x}\mathrm{Ge}_x$ and $\mathrm{In}_x\mathrm{Ga}_{1-x}\mathrm{As}$, the most common slip system is $\frac{1}{2}\langle 110\rangle\{111\}$, where a is the film lattice parameter. The Burgers vectors for this system are of the type $\frac{1}{2}\langle 110\rangle$. They are directed along the face diagonals of the cubic cell and are the shortest possible primitive translation vectors. The set of possible Burgers vectors can be constructed by considering the edges of a half-octahedron, as shown in Fig. 2(b). The half-octahedron is oriented such that its square base is parallel to the (001) plane. For instance, if the dislocation glide plane is $(\bar{1}11)$, which is inclined with respect to the film/substrate interface by the angle $\alpha=\cos^{-1}(1/\sqrt{3})\approx 54.7°$, then the MD will have a [110] line direction. For this example, if the Burgers vector $\mathbf{b}=\frac{1}{2}[0\bar{1}1]$ with $b=|\mathbf{b}|=a/\sqrt{2}$, where a is the lattice parameter of the unit cell, the MD is a mixed 60° dislocation. Such mixed misfit dislocations with their lines laying at (001) film/substrate interface are typical for heteroepitaxy of semiconductors with fcc crystal lattice.[7,9] The orientation of the dislocation line and Burgers vector leads to $\lambda=\beta=60°$ in Eq. (3). The dislocation Burgers vector can be decomposed into edge $\mathbf{b}_{\mathrm{edge}}$ and screw $\mathbf{b}_{\mathrm{screw}}$ components as shown in Fig. 2(b). Consequently, the edge component can be decomposed into parts parallel $\mathbf{b}_{\|}$ and perpendicular $\mathbf{b}_{\perp}$ to the film/substrate interface: $\mathbf{b}_{\mathrm{edge}}=\mathbf{b}_{\|}+\mathbf{b}_{\perp}$. The absolute values of the above components and subcomponents are

$$|\mathbf{b}_{\mathrm{screw}}|=b_{\mathrm{screw}}=\frac{b}{2}=a\frac{\sqrt{2}}{4}, \tag{7a}$$

$$|\mathbf{b}_{\mathrm{edge}}|=b_{\mathrm{edge}}=b\frac{\sqrt{3}}{2}=\frac{a}{2}\sqrt{\frac{3}{2}}, \tag{7b}$$

$$|\mathbf{b}_{\|}|=b_{\|}=\frac{b}{2}=a\frac{\sqrt{2}}{4}, \tag{7c}$$

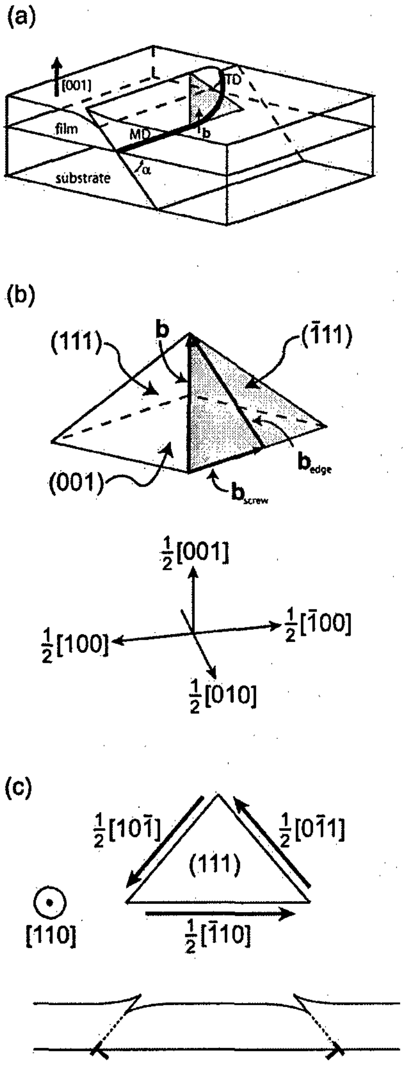

FIG. 2. The geometry for TD motion in a strained film with fcc crystal structure. (a) TD gliding on a {111} slip plane with trailing MD, which appears at film/substrate interface as a result of TD motion. (b) Dislocation Burgers vector decomposition into the edge and screw components. (c) Projection down the [110] direction, showing both the $(\bar{1}11)$ and $(1\bar{1}1)$ slip planes in projection. Glide on $(1\bar{1}1)$ with $\mathbf{b}=\frac{1}{2}[10\bar{1}]$ results in a down-step (see the slip step on the left side of the schematic). Glide on $(\bar{1}11)$ with $\mathbf{b}=\frac{1}{2}[0\bar{1}1]$ results in an up-step (see the slip step on the right side of the schematic).

$$|\mathbf{b}_{\perp}|=b_{\perp}=\frac{b}{\sqrt{2}}=\frac{a}{2}. \tag{7d}$$

For this example $\mathbf{b}_{\mathrm{screw}}=\frac{1}{4}[\bar{1}\bar{1}0]$, $\mathbf{b}_{\mathrm{edge}}=\frac{1}{4}[1\bar{1}2]$, $\mathbf{b}_{\|}=\frac{1}{4}[1\bar{1}0]$, and $\mathbf{b}_{\perp}=\frac{1}{2}[001]$. The decomposition of the MD Burgers vector, as described here, will be used in Sec. IV for the modeling of crosshatch formation.

III. EXPERIMENT PROCEDURE AND OBSERVATIONS

In the present work, epitaxial films of $\mathrm{In}_{0.25}\mathrm{Ga}_{0.75}\mathrm{As}$ on GaAs (001) semi-insulating substrates were investigated. The InGaAs layers were grown by molecular beam epitaxy at 500–520 °C and were produced by concurrent Ga and In

Downloaded 29 May 2004 to 128.111.74.212. Redistribution subject to AIP license or copyright, see http://jap.aip.org/jap/copyright.jsp

fluxes. The film thickness of the three samples shown in this report were $h=0.1$, 0.25, and 1.0 μm. The lattice mismatch for $In_{0.25}Ga_{0.75}As$ on GaAs is 1.8% and the critical thickness h_c for this mismatch is ~50 Å [see Eq. (3)] for this composition. Consequently, the film thicknesses were also approximately 20, 50, and 200 h_c. The surface height profiles of the InGaAs films were determined by AFM in tapping mode (Digital Instruments Dimension or Nanoscope).

The extent of strain relaxation and the film composition were determined by measuring the separation of the film and substrate peak for (115) and $(\bar{1}\bar{1}5)$ reflections in double crystal high-resolution x-ray measurements (for details of this technique see Ref. 13). Significant strain relaxation ($R > \sim 0.05$) was observed for $h \sim 10h_c = 500$ Å. The magnitude of the relaxation was always smaller than the equilibrium value (see Part I for further details). For instance, 1000-Å-thick films ($\sim 20h_c$) were ~70% strain relaxed whereas the equilibrium relaxation at this thickness is ~95%.

The crosshatch morphology typically shows a strong anisotropy in III–V semiconductors, as shown in Fig. 1. Generally, the crosshatch shows larger height undulations in the [110] direction than in the $[\bar{1}10]$ direction. As discuss earlier, $[\bar{1}10]$ is the fast diffusion direction on (001) GaAs surfaces and [110] is the slow diffusion direction. Figures 3 and 4 show measured surface height profiles in the [110] and $[\bar{1}10]$ directions, respectively, for 0.1- and 0.25-μm-thick films. In both the [110] and $[\bar{1}10]$ directions, the crosshatch amplitude increases with increasing film thickness.

For a better characterization of the surface height profile, the one-dimensional height–height correlation function of a surface cross section was calculated. It is defined as

$$C(r)=\langle[h(x)-\bar{h}][h(x+r)-\bar{h}]\rangle_x, \qquad (8)$$

where $h(x)$ is the surface height at a point x, $\bar{h}=\langle h(x)\rangle_x$ is the average height, and $\langle....\rangle_x=(1/L)\int_0^L....dx$ is an average over the lateral sample length L. The height profile is actually given only at discrete points x_i both in the measurement and in the simulations. Thus, the correlation function was calculated as

$$C(r)=\frac{1}{N}\sum_{i=1}^{N}[h(x_i)-\bar{h}][h(x_i+r)-\bar{h}], \qquad (9)$$

where N is the number of data points and r is the distance between two points x_i and x_j. The correlation function $C(r)$ reflects the overall patterning of the hills and valleys in the considered direction on the surface. $C(r=0)$ is just the variance of the surface height, i.e., the square of the rms roughness of the analyzed length interval.

The height–height correlation function resulting from the experimental profiles reveals characteristic correlation lengths. The height–height correlation function for the experimental profiles shows clear correlations in the hill and valley structure. In the [110] direction [Fig. 3(c)], the first peak-to-peak spacing of $C(r)$ increases from ~0.5 to ~0.7 μm and the amplitude of $C(r)$ also increases with increasing film thickness. In the $[\bar{1}10]$ direction [Fig. 4(c)], the 0.1-μm-thick sample shows small height variation whereas the 0.25-μm-thick sample shows more characteristic crosshatch [see the line scan in Fig. 4(b)].

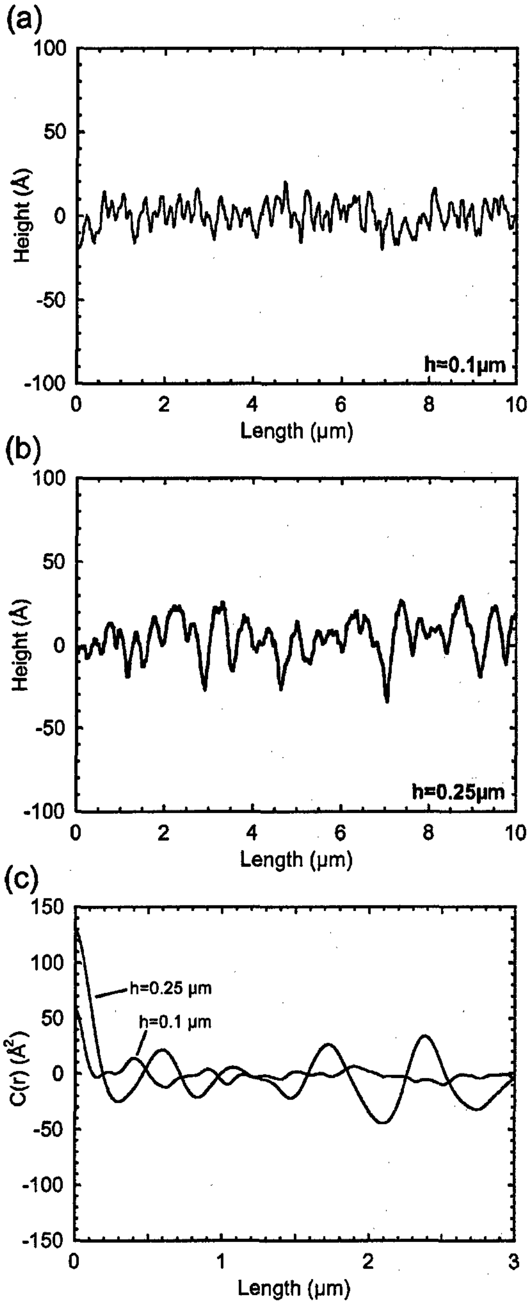

FIG. 3. Height profiles, from AFM images of $In_{0.25}Ga_{0.75}As$/GaAs films, along the [110] direction. (a), (b) Sample surface profiles for 0.1- and 0.25-μm-thick films, respectively. (c) Height–height correlation functions for profiles shown in parts (a) and (b).

IV. THEORETICAL MODEL AND SIMULATION RESULTS

A. Misfit dislocation formation at the film/substrate interface

As a first step, we briefly describe the basis of our model for crosshatch development proposed in Part I. The model examines the creation of surface steps arising from the glide

Downloaded 29 May 2004 to 128.111.74.212. Redistribution subject to AIP license or copyright, see http://jap.aip.org/jap/copyright.jsp

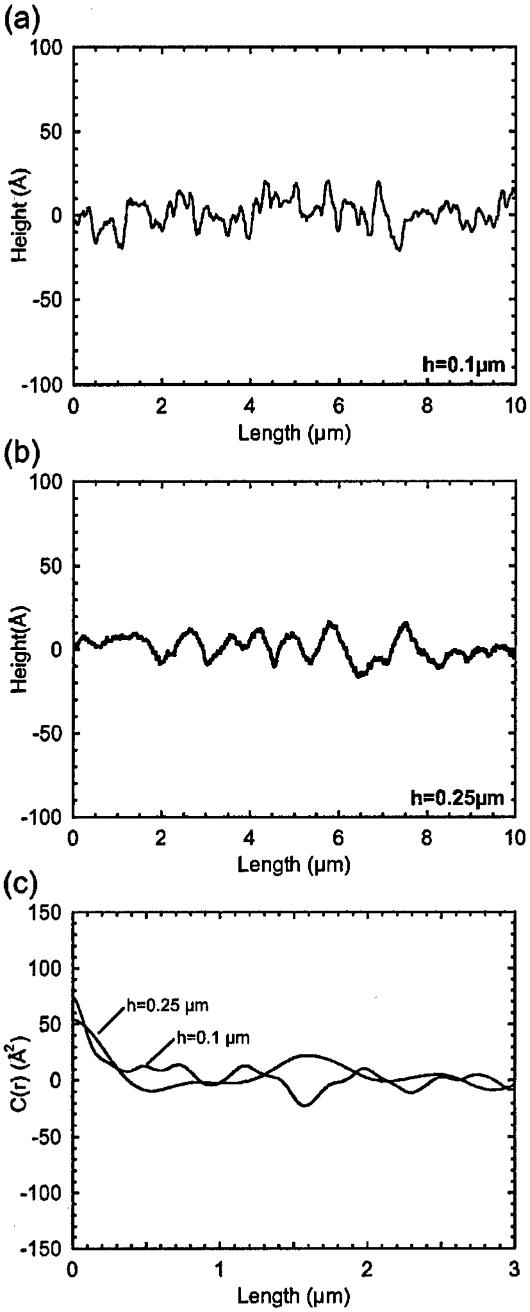

FIG. 4. Height profiles, from AFM images of $In_{0.25}Ga_{0.75}As/GaAs$ films, along the $[\bar{1}10]$ direction. (a), (b) Sample surface profiles for $h=0.1$ and 0.25 μm, respectively. (c) Height–height correlation functions for profiles shown in parts (a) and (b).

of TDs along opposing {111} slip planes, as shown schematically in Fig. 2(c), and the consequent development of MDs at the film/substrate interface. We note that only the MDs Burgers vector edge component parallel to the film/substrate interface $\mathbf{b}_{\parallel}$ can contribute to strain relaxation in mismatched layers (assuming equibiaxial stress). The same component of $\mathbf{b}_{\parallel}$ can be realized with different orientation Burgers vectors. For instance, MDs with [110] line direction can be generated either via glide of TDs with $\mathbf{b}=\frac{1}{2}[0\bar{1}1]$ on $(\bar{1}11)$ or glide of TDs with $\mathbf{b}=\frac{1}{2}[10\bar{1}]$ on $(1\bar{1}1)$, as shown in Fig. 2(c). In both cases, $\mathbf{b}_{\parallel}=\frac{1}{4}[1\bar{1}0]$. However, for this example, glide on $(\bar{1}11)$ corresponds to $\mathbf{b}_{\perp}=\frac{1}{2}[001]$ and glide on $(1\bar{1}1)$ corresponds to $\mathbf{b}_{\perp}=\frac{1}{2}[00\bar{1}]$. When viewed along the [110] direction and taking the positive x-direction parallel to $[\bar{1}10]$, then the slip step associated with glide on $(\bar{1}11)$ corresponds to an "up-step" and glide on $(1\bar{1}1)$ corresponds to a "down-step," as shown in Fig. 2(c). In the context of Fig. 2(c), we designate dislocations gliding on $(1\bar{1}1)$ as "left" dislocations and those gliding on $(\bar{1}11)$ as "right" dislocations.

Figure 5(a) shows the geometry used for the one-dimensional Monte Carlo simulations in Part I. Dislocations were randomly introduced at the possible nucleation sites at the surface [shown as ticks in Fig. 5(a)] and were then assumed to glide until they reached the film/substrate interface. While the nucleation sites could be located at every lattice site (~4 Å apart), we used a larger spacing of 20 Å. The angle of the glide direction $[\alpha=\pm\cos^{-1}(\sqrt{1/3})=\pm 54.74°]$ was also randomly selected for each dislocation, with some dislocations gliding left and some right, with equal numbers of the two types to keep a net Burgers vector of zero. More than one dislocation was allowed at each site. Dislocations were added until either the average stress reached a prescribed value or until a set number of dislocations was reached to achieve a relaxed film. The misfit strain ($\varepsilon_m = 1.8\%$) was taken to match that of $In_{0.25}Ga_{0.75}As$, leading to a relaxed film with 866 MDs per 10 μm length with a mean dislocation spacing of about 115 Å. The surface height was calculated from the displacement fields of the dislocations. In Part I, linear elasticity was used to calculate the surface profile associated with a single MD placed at film/substrate interface, such that the net surface displacement was a superposition of the displacements from individual dislocations. We introduced and explored two limiting cases for the formation of cross-hatch: SSO case and SSE case. For the SSO case the surface profile was assumed to be related entirely with steps formed by dislocation glide from the film surface modulated by MD elastic field. The SSE case corresponds to complete elimination of the surface steps in the considered computational cell, as would be realized by step annihilation during growth. Mathematically the SSE case was realized by adding the step-like heaviside function to the displacement determined for SSO case (for detail please refer to Part I). Periodic boundary conditions were approximated by considering the fields from the simulation cell and four replica cells on each side of the central cell. Surface heights were calculated for the SSE and SSO cases for a range of film thicknesses h and were compared with experiment.

There was a serious limitation to the earlier model owing to the truncation of the displacement fields of MDs at a finite number of periods. Elastic fields from dislocation fields are long range and thus the use of truncated solutions can be problematic for large film thicknesses compared with the period of the computational cell. In the present article, we have solutions (see the Appendix) for infinitely periodic arrays of dislocations and thus can eliminate truncation errors.

The compressive stress σ_{xx} at the film surface, arising from an infinite periodic array of MDs at the film/substrate interface, was derived from Eqs. (A15b) and (A16b) with properly transformed coordinates

Downloaded 29 May 2004 to 128.111.74.212. Redistribution subject to AIP license or copyright, see http://jap.aip.org/jap/copyright.jsp

$$\sigma_{xx}=\frac{Gb_{\parallel}}{(1-\nu)}\frac{4\pi\frac{h}{l}\left[1-\cos\left(2\pi\frac{x}{l}\right)\cosh\left(2\pi\frac{h}{l}\right)\right]-2\sinh\left(2\pi\frac{h}{l}\right)\left[\cos\left(2\pi\frac{x}{l}\right)-\cosh\left(2\pi\frac{h}{l}\right)\right]}{l\left[\cos\left(2\pi\frac{x}{l}\right)-\cosh\left(2\pi\frac{h}{l}\right)\right]^2}$$

$$\pm\frac{Gb_{\perp}}{(1-\nu)}\frac{4\pi h\sin\left(2/\pi\frac{x}{l}\right)\sinh\left(2\pi\frac{h}{l}\right)}{l^2\left[\cos\left(2\pi\frac{x}{l}\right)-\cosh\left(2\pi\frac{h}{l}\right)\right]^2}, \tag{10}$$

where we assume that one MD from the array is placed at the position $(0,-h)$, the array period is l, $b_{\perp}=b/\sqrt{2}=a/2$ and $b_{\parallel}=b/2=a\sqrt{2}/4$ with the sign "+" or "−" corresponding to the left or right MD, respectively. In Fig. 5(b) we show σ_{xx} for a periodic array of MDs in a film with thickness $h=100b$ and repeat period $l=2500b$. The total stress in the film after introducing the fixed number of MDs is given by the summation of the individual contributions given by Eq. (10).

The displacement component u_y (i.e., normal component of the displacement) at the surface (for the SSO case) of the periodic MD array was derived from Eqs. (A10a) and (A11a):

$$u_y=b_{\parallel}\frac{h}{l}\frac{\sinh\left(2\pi\frac{h}{l}\right)}{\left[\cos\left(2\pi\frac{x}{l}\right)-\cosh\left(2\pi\frac{h}{l}\right)\right]}$$

$$\mp b_{\perp}\left\{\frac{1}{\pi}\tan^{-1}\left[\cot\left(\pi\frac{x}{l}\right)\tanh\left(\pi\frac{h}{l}\right)\right]\right.$$

$$\left.+\frac{h}{l}\frac{\sin\left(2\pi\frac{x}{l}\right)}{\left[\cos\left(2\pi\frac{x}{l}\right)-\cosh\left(2\pi\frac{h}{l}\right)\right]}\right\}. \tag{11}$$

The displacement for the case with step elimination can be found by adding a step-like function to the solution given by Eq. (11). The step of the height $b_{\perp}$ is added to left boundary of the computational cell for the right nucleated MD and to the right boundary for the left nucleated MD. In Fig. 5(c), there is a sharp spike in the displacement profile associated with a surface step (the SSO case), while in Fig. 5(d) we see the more uniform displacement found when either growth or diffusive transport have eliminated the step (SSE). In Figs. 11 and 12 in the Appendix, we compare displacements and stresses, respectively, for the infinitely periodic system and those from a single, nonperiodic, MD.

B. Simulated surface profiles

Figure 6 presents calculated surface profiles for three film thicknesses ($h=0.1$, 1.0, and 10 μm) based on a random placement of dislocations at the nucleation sites of Fig. 5(a) and with a net Burgers vector of zero. Results are shown for both the SSO and SSE limits. The distribution of dislocations was the same in all plots. The corresponding height-height correlation functions $C(r)$ are shown in Fig. 7. In Fig. 6(a), we see that the surface profile in the SSO case for a thickness of $h=0.1$ μm produces a film that is microscopically rough, but mesoscopically smooth, which is verified by the flat height–height correlation function $C(r)$ in Fig. 7(a). As the thickness is increased, the SSO surface becomes increasingly rough [Figs. 6(b) and 6(c)] owing to the broadening of the stress and displacement fields at increasing thickness. By $h=10$ μm, the SSO surface is extremely rough, with complete surface steps that resemble stacked monolayers. In Fig. 7(a), we see that there is a broadening of the height–height correlation with thickness, but with no real structure, as expected from random surfaces. The long wavelength undulation in the height–height correlation function $C(r)$ for the $h=10$ μm case is the result of presenting a single realization of the system—if averages over many runs were shown, the $C(r)$ would be flat for all thickness, as expected for random surfaces.

When the slip steps are eliminated by diffusive transport or growth (SSE case), the local morphology is smooth for thin films with a long mesoscale undulation [Figs. 6(a) and 7(b)]. As the film thickness increases, the SSE film becomes mesocopically smoother until it is perfectly flat at $h=10$ μm [Figs. 6(c) and 7(b)]. Once again, this behavior is expected for a random distribution of dislocations.

The surface height profiles were also calculated for groups of MDs, as shown in Fig. 8. Repeated patterns of n left dislocations and n right dislocations were placed in the one-dimensional simulation cell, with n varying from 12 to 48 such that the MD–MD spacing corresponds to a fully relaxed $In_{0.25}Ga_{0.75}As$ film. Thus, the repeat periods $2n=24$, 48, and 96 correspond to lateral dimensions of ~0.28, 0.56, and 1.12 μm, respectively. The surface height was calculated in each case for both the SSO and SSE limits as a function of film thickness. In the hypothetical case in which the MDs group size is larger then the film thickness, as illustrated in Fig. 8(a) ($n=12$ case for a 0.01-μm-thick film), we see that the SSE case gives rise to large hills and valleys whereas the SSO surface shows slight undulations and atomic-scale roughness. This result is consistent with our earlier interpretation of crosshatch.[1,2] When the film thickness is comparable or much larger than the group [see Figs.

Downloaded 29 May 2004 to 128.111.74.212. Redistribution subject to AIP license or copyright, see http://jap.aip.org/jap/copyright.jsp

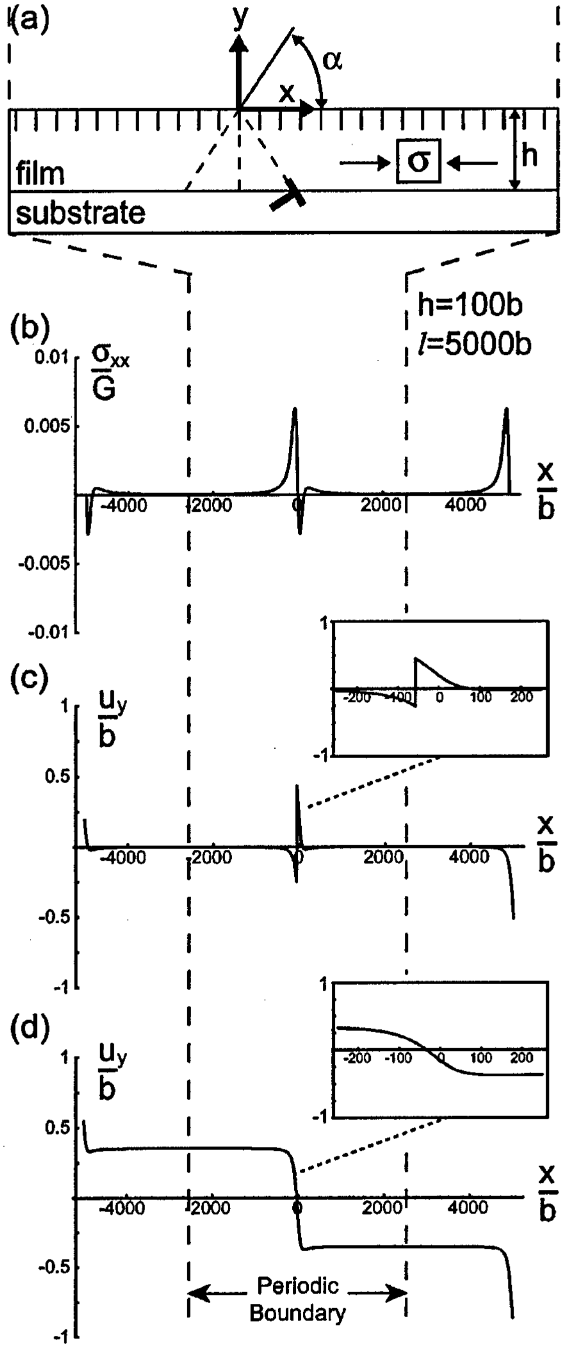

FIG. 5. One-dimensional model for dislocation assisted strain relaxation in mismatched films. (a) Schematic for showing the geometry used for introducing dislocations into the strained film. (b) Example of analytical solution for stress σ_{xx} at the film surface due to the periodic array of MDs. (c) Example of analytical solution for displacement u_y at the film surface. The displacement profile includes the surface step created as a result MD introduction via TD motion; referred to as SSO case. (d) Example of analytical solution for displacement u_y at the film surface with the surface step removed. The displacement profile resembles the effect of surface step elimination from lateral mass transport; referred to as SSE case. For the plots in parts (b)–(d) b is the magnitude of the full dislocation Burgers vector; the film thickness was taken as $h=100b$; the periodic spacing between dislocations was $l=2500b$; Poisson's ratio $\nu=0.32$.

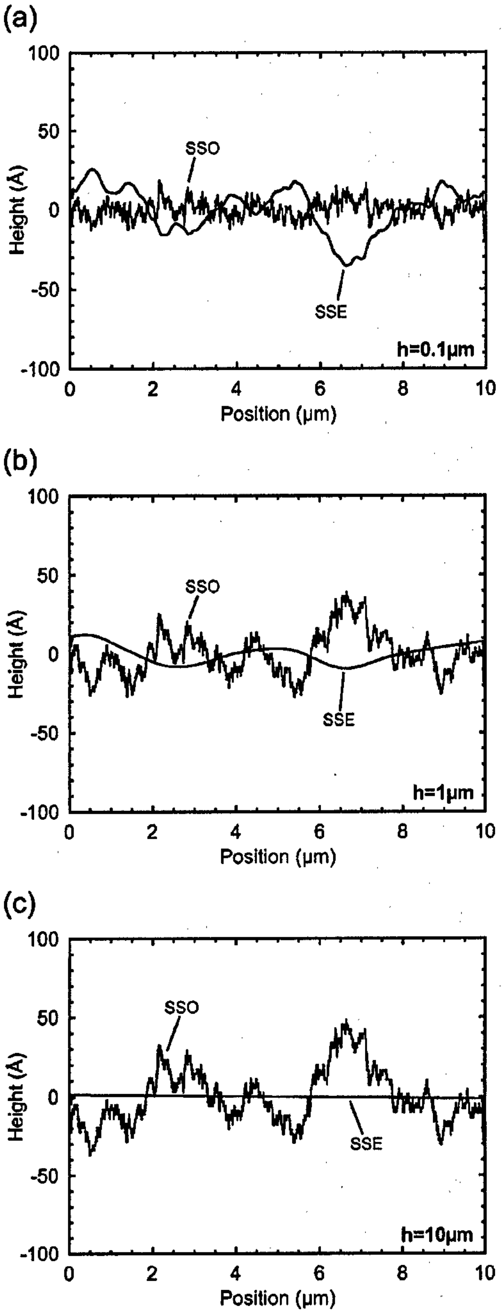

FIG. 6. Surface profiles for the model with randomly nucleated dislocations. (a), (b), and (c) Surface height profiles for $h=0.1$, 1.0, and 10 μm, respectively. The modeled film composition $\mathrm{In}_{0.25}\mathrm{Ga}_{0.75}\mathrm{As}$ corresponds to $\nu=0.32$, and $\varepsilon_m=1.8\%$; 100% strain relaxation corresponds to 866 dislocations for 10 μm of film length.

8(b) and 8(c) for $n=12$ and $h=0.1$ and 1.0 μm, respectively] we find that the behavior reverses and the SSE cases show smaller height undulations than the SSO cases. This is expected, as with increasing film thickness the SSE cases correspond to "filling" of the valleys with material from the peaks. Figure 8(d) shows the amplitude of the peak oscillations (peak-to-valley height) for a film thickness from 0.01 to 1.0 μm for both the SSO and SSE cases for $n=12$, 24, and 48. Note that the SSE surface is essentially flat when the film thickness is comparable to the repeat period of the MD

Downloaded 29 May 2004 to 128.111.74.212. Redistribution subject to AIP license or copyright, see http://jap.aip.org/jap/copyright.jsp

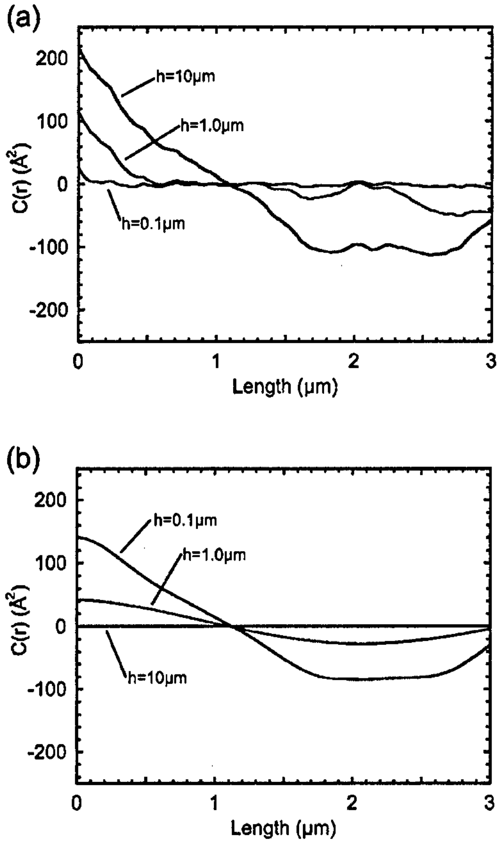

FIG. 7. Height–height correlation functions $C(r)$ for surface profiles in the model with randomly nucleated dislocation for SSO (a) and SSE (b) cases for different film thicknesses. The data correspond to a fully relaxed $In_{0.25}Ga_{0.75}As$ layer with $\nu = 0.32$, and $\varepsilon_m = 1.8\%$.

groups. In contrast, for the system with no diffusion (SSO), the amplitude increases both with increasing film thickness and with the increasing repeat period of the MDs. There is an approximately linear correlation between period and surface amplitude for the 1-μm-thick films.

In Fig. 9(a) we show an AFM image for a 1 μm film of $In_{0.25}Ga_{0.75}As$ grown at 520 °C. This film showed the characteristic undulating crosshatch pattern in the [110] direction and weak patterns in the orthogonal $[\bar{1}10]$ direction, as shown in the line scans in Fig. 9(b). From the height–height correlation function [Fig. 9(c)], the peak-to-peak spacing is at a distance of ~1.25 μm along the [110] direction with a peak-to-valley height of ~100 Å [the measured averaged peak-to-valley height was 103.5 Å for the line scan shown in Fig. 9(b)]. In contrast, the peak-to-peak height is at a distance of ~2.5 μm along the $[\bar{1}10]$ direction with a peak-to-valley height of ~20 Å. Based on Fig. 8, the experimental result can be interpreted as showing that the undulating surface height profile in the [110] direction is due to groups of MDs with little or no step elimination (SSO case). In contrast, the surface profile in the $[\bar{1}10]$ direction is smooth and suggests that the surface steps have been eliminated via lateral transport during growth. We note that the results for the SSE case in Fig. 8 demonstrate that the film thickness must be comparable to the wavelength of the group period to re-

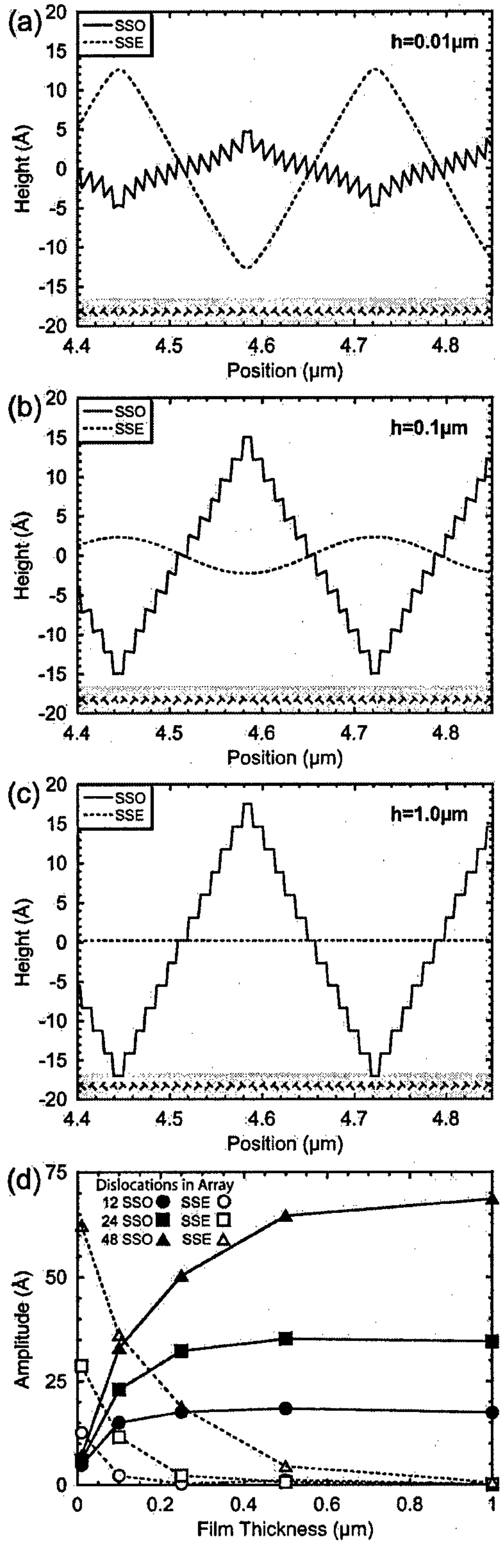

FIG. 8. Surface displacement from dislocation group arrays. (a), (b), and (c) Surface profile for a periodic array of 12 similar dislocation in the period for $h = 0.01$, 0.1, and 1.0 μm, respectively film. The schematic for dislocation groups is also shown in the bottom of each part. (d) Surface profile amplitude vs film thickness for dislocation arrays of 12, 24, and 48 dislocations. The SSO case is shown with solid markers and the SSE case with open markers.

Downloaded 29 May 2004 to 128.111.74.212. Redistribution subject to AIP license or copyright, see http://jap.aip.org/jap/copyright.jsp

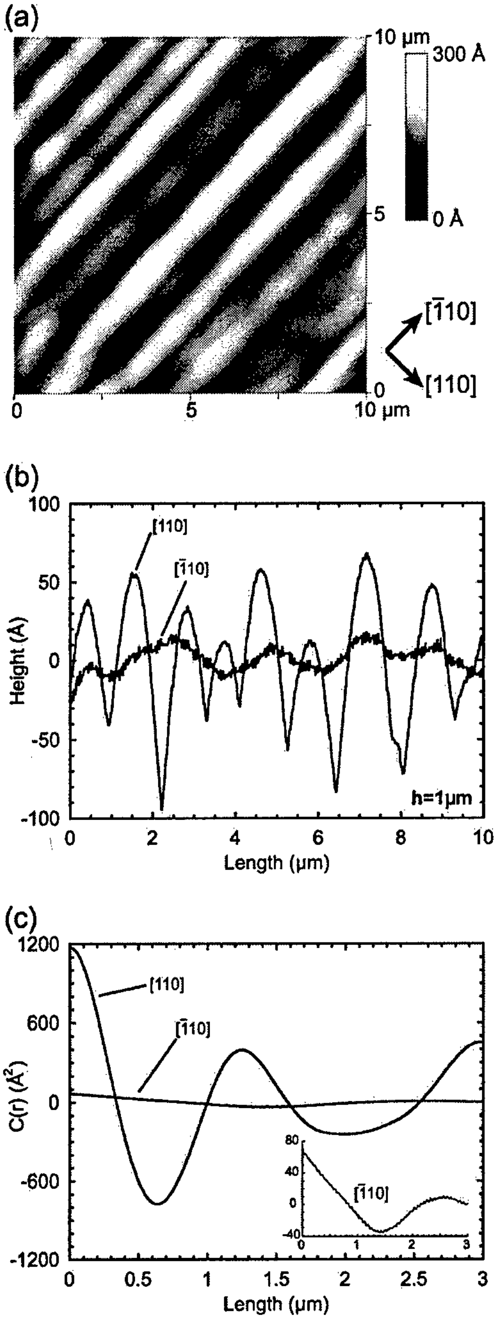

FIG. 9. Example of strongly anisotropic crosshatch pattern in $h=1$ μm $In_{0.25}Ga_{0.75}As$ layer on a (001) oriented GaAs substrate. (a) AFM image showing the crosshatch pattern. (b) Line scans of the AFM image in the [110] and [$\bar{1}$10] direction. (c) Height–height correlation functions in the [110] and [$\bar{1}$10] direction.

alize a flat surface. Thus, the slight undulations in the [$\bar{1}$10] direction may be possibly due to the relatively large wavelength of the undulation (~2.5 μm) in comparison with the film thickness (1 μm). We should make clear, however, that this is only a speculative conclusion as the MDs orthogonal to the [$\bar{1}$10] direction may have a more random distribution in their normal component.

V. DISCUSSION

In this article, we have implemented solutions for the stress fields and displacements for infinite arrays of MDs for the calculation of crosshatch morphologies. These solutions now provide the expected behavior for the surface profiles for all film thicknesses. As shown in Part I (see Fig. 5 of Part I), the film thickness is the characteristic lateral "decay" length for either the stress field or displacement field for a single MD; i.e., the far-field elastic fields or displacement fields for a MD are only asymptotically realized at lateral dimensions many times the film thickness. Thus, the solutions for truncated MD arrays used in Part I were excellent approximations for thin films (e.g., 1000 Å), however, the solutions did not present the expected behavior for thicker films (e.g., 1 μm). Using the fully periodic solutions, the surfaces become smoother with increasing film thickness for the SSE case, as shown in Fig. 6 for the case of randomly introduced MDs and Fig. 8 for MD groups. In contrast, the roughness for the SSO case increases with film thickness, either due to random groups (Fig. 6) or periodic groups (Fig. 8) and then remains essentially constant at film thicknesses comparable or larger than the lateral MD group size.

MD groups provide an easy way to understand the surface profile at large film thicknesses. Consider groups of n left MDs and n right MDs, as shown in Fig. 8, in the SSO case the n left MDs correspond to n down-steps (considering the height profile from left to right in all figures in this article) and the n right MDs correspond to n up-steps. In the SSO case, these n up-steps and n down-steps persist at all film thicknesses. When the film thickness is large in comparison with the period of the MDs ($2n$ MDs), the displacement field from an individual MD spreads, as shown in Fig. 11, however, there is still a discrete step in the SSO case. Thus, the surface height profile at large film thicknesses is essentially given by the addition of n negative heaviside step functions (down-steps) and n positive heaviside step functions (up steps)—each positioned at intersection of the slip plane of the MD with the free surface. In contrast, the surface height profile from an individual MD in the SSE case broadens with increasing film thickness. When the film thickness becomes large in comparison to the MD group size ($2n$ MDs), then the displacements cancel and the surface is flat. Figure 8(d) shows that the peak-to-valley height will increase with increasing film thickness in the SSO case (in contrast, the peak-to-valley height follows the opposite trend in the SSE case). Thus, for relaxed films, the change in the surface profile with increasing film thickness should be a strong indicator of whether the crosshatch morphology is more appropriately described by the SSO or SSE cases. In the [110] direction [see Figs. 3(c) and 9(c) of this article and Fig. 3(b) of Part I], the surface height undulations increase with increasing film thickness. Thus, we conclude that the morphology in the [110] direction is associated with groups of MDs with period at least as large as the film thickness. In the [$\bar{1}$10] direction, the trend in the height profile with increasing film thickness evolution is less clear [see Figs. 4(c) and 9(c)], but we speculate that the crosshatch is reduced in this direction due to surface diffusion.

In the simulations in this article, we randomly introduced the MD location and whether the MD corresponded to an up-step or down-step (i.e., glide to the right or left, respectively). Since the MDs were randomly introduced, the

Downloaded 29 May 2004 to 128.111.74.212. Redistribution subject to AIP license or copyright, see http://jap.aip.org/jap/copyright.jsp

height–height correlation function $C(r)$ showed a monotonic decay with increasing distance r and no subsidiary maxima. In contrast, the experimental height–height correlation functions showed strong secondary maxima which we attribute to groups of MDs with the same normal component. We believe that these MD groups themselves are the result of either heterogeneous sources for dislocations, or multiplication processes, which result in parallel arrays of MDs with the same Burgers vector. We are currently studying the freshly desorbed surfaces of arsenic-capped $In_{0.25}Ga_{0.75}As$ layers with AFM and scanning tunneling microscopy to observe the surface structure (with a particular focus on the step structure). Our preliminary results show that the surfaces have a high step density in both the [110] and $[\bar{1}10]$ directions and thus lends support that the crosshatch is largely related to the SSO case.

In general, a pronounced crosshatch can be also related to MD patterning, i.e., formation of local regions at the film/substrate interface with a high density of MDs separated by regions with a low density of MDs. Such patterning phenomena have been observed experimentally and studied in the framework of dislocation reaction-kinetic model (see Ref. 14, and references therein). However, it is clear that the energy of a nonuniform MD distribution is higher than the energy of a periodic array of MDs.[15] In the analysis of MD patterning it was always assumed a pure edge character of dislocations with their Burgers vector parallel to the interface. On the other hand, consideration of left and right generated MD with opposite component of Burgers vector allows the formation of dislocation patterns with lower energy than simple nonuniform distribution of MDs. Therefore, our current efforts are also directed to the theoretical study of the energetics of such MD groups with alternating normal component of their Burgers vector.

VI. SUMMARY AND CONCLUSIONS

In this article, we have presented solutions for the stress and displacement fields for periodic MD arrays which include the effects of the free surface. These solutions were used in simulations of crosshatch formation. The surface height profiles have been simulated for periodic MD arrays of randomly introduced dislocations as well as for regular dislocation arrangements, i.e., groups of dislocations having the same component of their Burgers vector normal to the film/substrate interface. The surface height profile evolves due to the appearance of slip steps at the film surface and subsequent step motion. Two limiting cases of step motion have been modeled: extremely slow step motion (SSO case) and extremely fast step motion leading to complete step elimination (SSE case). For random MD arrangement, the rms surface roughness increases with increasing film thickness in the SSO case, whereas in the SSE case it decreases at higher film thickness. Experimentally observed surface height profiles showed a certain degree of periodicity. Therefore, they can be better described by the solutions for groups of MDs with alternating sign of the normal component of the dislocation Burgers vector. However, also for this case, the SSE limit leads to a decrease of the rms surface roughness with increasing film thickness. Experimentally we have found that the rms roughness of relaxed $In_{0.25}Ga_{0.75}As$ films on GaAs (001) increase with increasing film thickness in the [110] direction. Thus, we conclude that the crosshatch morphology is predominantly described by the SSO case.

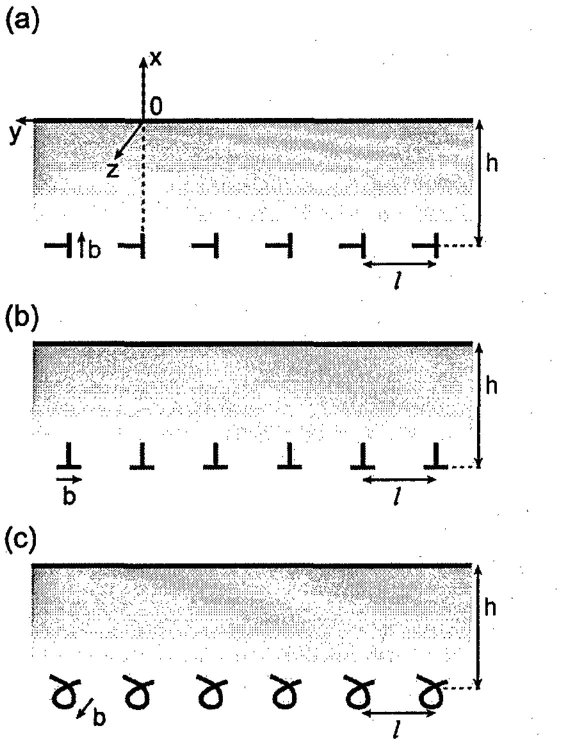

FIG. 10. Schematic for periodic dislocation arrays. (a) Edge dislocation array with Burgers vector perpendicular to the surface. (b) Edge dislocation array with Burgers vector parallel to the free surface. (c) Screw dislocation array.

ACKNOWLEDGMENTS

This work was supported by DARPA (W. Coblenz program manager) and monitored by AFOSR (G. Witt).

APPENDIX: DISPLACEMENTS AND ELASTIC STRESSES OF PERIODIC DISLOCATION ARRAYS IN SUBSURFACE LAYERS

Here we present analytical expressions for displacements and elastic stresses for periodic dislocation arrays placed near a free surface of an elastically isotropic material. The geometry of the arrays is given in Fig. 10, together with the chosen right-handed coordinate system. We note that this coordinate system corresponds to that conventionally used in dislocation mechanics. However, this coordinate system differs from commonly used coordinate systems for thin films, such as we use in the body of this article. The following considers three fundamental orientations of the dislocation Burgers vector with respect to the free surface: (i) edge dislocations with Burgers vector normal to the free surface $\mathbf{b}=b_x\mathbf{e}_x$ [Fig. 10(a)]; (ii) edge dislocations with Burgers vector parallel to the free surface $\mathbf{b}=-b_y\mathbf{e}_y$ [Fig. 10(b)]; and (iii) screw dislocations with Burgers vector parallel to the free surface $\mathbf{b}=b_z\mathbf{e}_z$ [Fig. 10(c)]. b_i are the magnitudes of

Downloaded 29 May 2004 to 128.111.74.212. Redistribution subject to AIP license or copyright, see http://jap.aip.org/jap/copyright.jsp

the Burgers vectors and $\mathbf{e}_i$ are the unit vectors along the corresponding coordinate axes. The dislocation line direction is $\mathbf{e}_z$, the arrays are at the distance h from the surface, and the dislocation spacing is l. Note that the solutions for a screw dislocation given later are not used in this article.

We start the derivation of the displacement and stresses for infinite dislocation arrays with the corresponding fields for individual dislocations calculated in a semi-infinite elastic body. The solution for stresses σ_{ij} can be found for example in references[16–18] and satisfy the boundary condition at the free surface and also differential equilibrium conditions in the bulk

$$\sigma_{xj}(x=0,y,z)=0, \tag{A1a}$$

$$\frac{\partial\sigma_{ij}}{\partial x_j}=0. \tag{A1b}$$

In our earlier article (Part I),[2] the expressions for the dislocation stresses were not transformed to the appropriate coordinate system.

The solutions for displacements are not so well-known in the literature. Their derivation assumes the additional integration of strains, as it was done for an isolated edge dislocation in Refs. 2 and 19. The displacements can also be determined as a result of direct solution of the elasticity problem. We will use a different method which mimics the structure of the solutions for stresses for a dislocation near a free surface.

The stresses due to a subsurface dislocation σ_{ij} can be written as the superposition of three terms

$$\sigma_{ij}=\sigma_{ij}^{\infty}+\sigma_{ij}^{i}+\sigma_{ij}^{a}, \tag{A2}$$

where σ_{ij}^{∞} is the stress of a dislocation in an infinite medium; σ_{ij}^{i} is the stress of an image dislocation, which is a mirror reflection of the real dislocation (introduction of the image dislocation fulfills part of the boundary conditions at the free surface); and an additional stress σ_{ij}^{a} that assures that all free-surface boundary conditions are satisfied.[17] For a screw dislocation, no additional terms are needed and the complete solution is found with the inclusion of a single image dislocation.

The term σ_{ij}^{a} can be determined by a variety of techniques. Here we employ the method of virtual surface dislocations.[20] In this approach σ_{ij}^{a} is generated by a continuous distribution of surface dislocations

$$\sigma_{ij}^{a}(x,y)=\int_{-\infty}^{+\infty}f(y',h)\sigma_{ij}^{\infty}(x,y-y')dy', \tag{A3}$$

where the dislocation distribution function $f(y,h)$ is chosen such that the boundary conditions (A1) are satisfied. Once the distribution function is found, the dislocation displacement fields are given by equations similar in form to those for stress in Eqs. (A2) and (A3):

$$u_i=u_i^{\infty}+u_i^{i}+u_i^{a} \tag{A4}$$

with

$$\text{with } u_i^{a}(x,y)=\int_{-\infty}^{+\infty}f(y',h)u_i^{\infty}(x,y-y')dy'. \tag{A5}$$

In Eqs. (A4) and (A5), all terms on the right-hand side are displacements arising from dislocations in an infinite media, the forms of which can be easily derived or found in the literature. Employing the distribution functions for surface dislocations found in Ref. 20, we obtain the following displacement fields for a single dislocation placed at the position $(-h,0)$ near a free surface.

(i) For an edge dislocation with $\mathbf{b}=b_x\mathbf{e}_x$:

$$\begin{aligned}u_x^{b_x}=&\frac{b_x}{2\pi}\left(\tan^{-1}\frac{x-h}{y}-\tan^{-1}\frac{x+h}{y}\right)\\&+\frac{b_x}{4\pi(1-\nu)}\left\{\frac{(x+h)y}{(x+h)^2+y^2}\right.\\&+(3-4\nu)\frac{yh}{(x-h)^2+y^2}-\frac{xy}{(x-h)^2+y^2}\\&\left.+4xyh\frac{(x-h)}{\{(x-h)^2+y^2\}^2}\right\},\end{aligned} \tag{A6a}$$

$$\begin{aligned}u_y^{b_x}=&\frac{b_x}{4\pi(1-\nu)}\left\{\frac{1-2\nu}{2}\ln\frac{(x-h)^2+y^2}{(x+h)^2+y^2}-\frac{(x+h)^2}{(x+h)^2+y^2}\right.\\&+(3-4\nu)\frac{(x-h)h}{(x-h)^2+y^2}+\frac{x(x+h)}{(x-h)^2+y^2}\\&\left.-4xh\frac{(x-h)^2}{[(x-h)^2+y^2]^2}\right\},\end{aligned} \tag{A6b}$$

$$u_z^{b_x}=0, \tag{A6c}$$

where ν is the Poisson's ratio of elastically isotropic material.

(ii) For an edge dislocation with $\mathbf{b}=-b_y\mathbf{e}_y$:

$$\begin{aligned}u_x^{b_y}=&-\frac{b_y}{4\pi(1-\nu)}\left\{\frac{1-2\nu}{2}\ln\frac{(x+h)^2+y^2}{(x-h)^2+y^2}\right.\\&-\frac{(x+h)^2}{(x+h)^2+y^2}+2(1-2\nu)\frac{(x-h)h}{(x-h)^2+y^2}\\&\left.+\frac{x^2-2xh-h^2}{(x-h)^2+y^2}+4xh\frac{(x-h)^2}{[(x-h)^2+y^2]^2}\right\},\end{aligned} \tag{A7a}$$

$$\begin{aligned}u_y^{b_y}=&-\frac{b_y}{2\pi}\left(\tan^{-1}\frac{x-h}{y}-\tan^{-1}\frac{x+h}{y}\right)\\&+\frac{b_y}{4\pi(1-\nu)}\left\{\frac{(x+h)y}{(x+h)^2+y^2}\right.\\&+(3-4\nu)\frac{yh}{(x-h)^2+y^2}-\frac{xy}{(x-h)^2+y^2}\\&\left.-4xhy\frac{(x-h)}{[(x-h)^2+y^2]^2}\right\},\end{aligned} \tag{A7b}$$

$$u_z^{b_y}=0. \tag{A7c}$$

(iii) For a screw dislocation with $\mathbf{b}=b_z\mathbf{e}_z$:

$$u_x^{b_z}=0, \tag{A8a}$$

$$u_y^{b_z}=0, \tag{A8b}$$

Downloaded 29 May 2004 to 128.111.74.212. Redistribution subject to AIP license or copyright, see http://jap.aip.org/jap/copyright.jsp

$$u_z^{b_z}=\frac{b_z}{2\pi}\left(\tan^{-1}\frac{x-h}{y}-\tan^{-1}\frac{x+h}{y}\right). \tag{A8c}$$

The displacement fields all include a characteristic dislocation term proportional to $\tan^{-1}$, which provides the multivalue character of dislocation displacements and accounts for the generation of plastic jumps as dislocations pass through the body of a material or of an atomic step as dislocations arrive at the material surface (for a discussion of this problem see the Appendix in Part I).

The displacement field of a periodic dislocation array is given by the sum of contributions from the individual dislocations

$$u_i^{\text{array}}=\sum_{n=-\infty}^{n=+\infty}u_i^{\text{individual}}(x,h,y-nl). \tag{A9}$$

The summation of $u_i^{\text{individual}}$ [Eqs. (6)–(7)] in Eq. (9) can be performed analytically and yields the following results for the displacement fields of an infinite dislocation array.

(i) For an array of edge dislocations with $\mathbf{b}=b_x\mathbf{e}_x$:

$$\begin{aligned}u_x^{\Sigma b_x}={}&\frac{b_x}{2\pi}\{\tan^{-1}[\tanh\pi(\tilde{x}-\tilde{h})\cot\pi\tilde{y}]-\tan^{-1}[\tanh\pi(\tilde{x}+\tilde{h})\cot\pi\tilde{y}]\}+\frac{b_x}{4\pi(1-\nu)}\\&\times\left\{\pi(\tilde{x}+\tilde{h})\frac{\sin 2\pi\tilde{y}}{\cosh 2\pi(\tilde{x}+\tilde{h})-\cos 2\pi\tilde{y}}+(3-4\nu)\pi\tilde{h}\frac{\sin 2\pi\tilde{y}}{\cosh 2\pi(\tilde{x}-\tilde{h})-\cos 2\pi\tilde{y}}\right.\\&\left.-\pi\tilde{x}\frac{\sin 2\pi\tilde{y}}{\cosh 2\pi(\tilde{x}-\tilde{h})-\cos 2\pi\tilde{y}}+4\pi^2\tilde{x}\tilde{h}\frac{\sinh 2\pi(\tilde{x}-\tilde{h})\sin 2\pi\tilde{y}}{[\cosh 2\pi(\tilde{x}-\tilde{h})-\cos 2\pi\tilde{y}]^2}\right\},\end{aligned} \tag{A10a}$$

$$\begin{aligned}u_y^{\Sigma b_x}={}&\frac{b_x}{4\pi(1-\nu)}\left\{\frac{1-2\nu}{2}\ln\frac{\cosh 2\pi(\tilde{x}-\tilde{h})-\cos 2\pi\tilde{y}}{\cosh 2\pi(\tilde{x}+\tilde{h})-\cos 2\pi\tilde{y}}-\pi(\tilde{x}+\tilde{h})\frac{\sinh 2\pi(\tilde{x}+\tilde{h})}{\cosh 2\pi(\tilde{x}+\tilde{h})-\cos 2\pi\tilde{y}}+(3-4\nu)\pi\tilde{h}\right.\\&\left.\times\frac{\sinh 2\pi(\tilde{x}-\tilde{h})}{\cosh 2\pi(\tilde{x}-\tilde{h})-\cos 2\pi\tilde{y}}+\pi\tilde{x}\frac{\sinh 2\pi(\tilde{x}-\tilde{h})}{\cosh 2\pi(\tilde{x}-\tilde{h})-\cos 2\pi\tilde{y}}+4\pi^2\tilde{x}\tilde{h}\frac{1-\cosh 2\pi(\tilde{x}-\tilde{h})\cos 2\pi\tilde{y}}{[\cosh 2\pi(\tilde{x}-\tilde{h})-\cos 2\pi\tilde{y}]^2}\right\},\end{aligned} \tag{A10b}$$

$$u_z^{\Sigma b_x}=0. \tag{A10c}$$

(ii) For an array of edge dislocations with $\mathbf{b}=-b_y\mathbf{e}_y$:

$$\begin{aligned}u_x^{\Sigma b_y}={}&-\frac{b_y}{4\pi(1-\nu)}\left\{\frac{1-2\nu}{2}\ln\frac{\cosh 2\pi(\tilde{x}+\tilde{h})-\cos 2\pi\tilde{y}}{\cosh 2\pi(\tilde{x}-\tilde{h})-\cos 2\pi\tilde{y}}-\pi(\tilde{x}+\tilde{h})\frac{\sinh 2\pi(\tilde{x}+\tilde{h})}{\cosh 2\pi(\tilde{x}+\tilde{h})-\cos 2\pi\tilde{y}}+2(1-2\nu)\pi\tilde{h}\right.\\&\left.\times\frac{\sinh 2\pi(\tilde{x}-\tilde{h})}{\cosh 2\pi(\tilde{x}-\tilde{h})-\cos 2\pi\tilde{y}}+\pi(\tilde{x}+\tilde{h})\frac{\sinh 2\pi(\tilde{x}-\tilde{h})}{\cosh 2\pi(\tilde{x}-\tilde{h})-\cos 2\pi\tilde{y}}-4\pi^2\tilde{x}\tilde{h}\frac{1-\cosh 2\pi(\tilde{x}-\tilde{h})\cos 2\pi\tilde{y}}{[\cosh 2\pi(\tilde{x}-\tilde{h})-\cos 2\pi\tilde{y}]^2}\right\},\end{aligned} \tag{A11a}$$

$$\begin{aligned}u_y^{\Sigma b_y}={}&-\frac{b_y}{2\pi}\{\tan^{-1}[\tanh\pi(\tilde{x}-\tilde{h})\cot\pi\tilde{y}]-\tan^{-1}[\tanh\pi(\tilde{x}+\tilde{h})\cot\pi\tilde{y}]\}+\frac{b_y}{4\pi(1-\nu)}\\&\times\left\{\pi(\tilde{x}+\tilde{h})\frac{\sin 2\pi\tilde{y}}{\cosh 2\pi(\tilde{x}+\tilde{h})-\cos 2\pi\tilde{y}}+(3-4\nu)\pi\tilde{h}\frac{\sin 2\pi\tilde{y}}{\cosh 2\pi(\tilde{x}-\tilde{h})-\cos 2\pi\tilde{y}}\right.\\&\left.-\pi\tilde{x}\frac{\sin 2\pi\tilde{y}}{\cosh 2\pi(\tilde{x}-\tilde{h})-\cos 2\pi\tilde{y}}-4\pi^2\tilde{x}\tilde{h}\frac{\sinh 2\pi(\tilde{x}-\tilde{h})\sin 2\pi\tilde{y}}{[\cosh 2\pi(\tilde{x}-\tilde{h})-\cos 2\pi\tilde{y}]^2}\right\},\end{aligned} \tag{A11b}$$

Downloaded 29 May 2004 to 128.111.74.212. Redistribution subject to AIP license or copyright, see http://jap.aip.org/jap/copyright.jsp

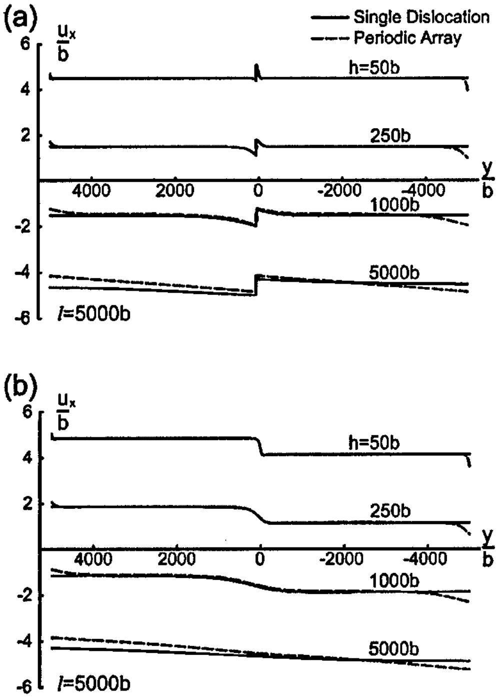

FIG. 11. Comparison of surface profiles for a single MD and for periodic array of MDs for SSO (a) and SSE (b) cases. MDs (single or in array) with the Burgers vector $\mathbf{b}=[(\sqrt{2}/\sqrt{3})\mathbf{e}_x+(1/\sqrt{3})\mathbf{e}_y]b$ are placed at distance h from the surface as indicated in the figure. For these plots Poisson's ratio $\nu=0.32$. The Cartesian coordinates correspond to those used in Fig. 10.

$$u_z^{\Sigma b_y}=0. \tag{A11c}$$

(iii) For an array of screw dislocations with $\mathbf{b}=b_z\mathbf{e}_z$:

$$u_x^{\Sigma b_z}=0, \tag{A12a}$$

$$u_y^{\Sigma b_z}=0, \tag{A12b}$$

$$u_z^{\Sigma b_z}=\frac{b_z}{2\pi}[\tan^{-1}[\tanh \pi(\tilde{x}-\tilde{h})\cot \pi\tilde{y}] - \tan^{-1}[\tanh \pi(\tilde{x}+\tilde{h})\cot \pi\tilde{y}]]. \tag{A12c}$$

In Eqs. (A10)–(A12) we employed the normalized coordinates and film thickness: $\tilde{x}=x/l$, $\tilde{y}=y/l$, and $\tilde{h}=h/l$.

In Fig. 11 we compare the displacements of a single edge dislocation and a (infinite) periodic array of edge dislocations. The two sets of plots presented in Figs. 11(a) and 11(b) cover the two cases of the orientation of the slip step created when dislocations are introduced into the material, i.e., towards the free surface (SSO) and towards the bulk of the material (SSE), respectively.

The strains are defined by

$$\varepsilon_{ij}=\frac{1}{2}\left(\frac{\partial u_i}{\partial x_j}+\frac{\partial u_j}{\partial x_i}\right). \tag{A13}$$

When applying Eq. (A13) to dislocation displacement fields, we must separate elastic and plastic deformations, as proposed by DeWit.[21] The plastic contribution can be identified by characteristic discontinuous step-like terms and can be omitted in the expression for elastic strains. Finally, elastic stresses are derived from Hooke's law

$$\sigma_{ij}=2G\left(\varepsilon_{ij}+\frac{\nu}{1-2\nu}\varepsilon_{kk}\delta_{ij}\right), \tag{A14}$$

where the shear modulus G and Poisson's ratio ν are the elastic constants for isotropic solid. For convenience, we also define $D=G/2\pi(1-\nu)$.

The components of the stress tensor for individual dislocations are as following.

(i) For an edge dislocations with $\mathbf{b}=b_x\mathbf{e}_x$:

$$\sigma_{xx}^{b_x}=Db_x\left\{-\frac{y[3(x+h)^2+y^2]}{[(x+h)^2+y^2]^2}+\frac{y[3(x-h)^2+y^2]}{[(x-h)^2+y^2]^2} -4xyh\frac{3(x-h)^2-y^2}{[(x-h)^2+y^2]^3}\right\}, \tag{A15a}$$

$$\sigma_{yy}^{b_x}=Db_x\left\{\frac{y[(x+h)^2-y^2]}{[(x+h)^2+y^2]^2}+\frac{y(7h^2-6hx-x^2+y^2)}{[(x-h)^2+y^2]^2} +4xyh\frac{3(x-h)^2-y^2}{[(x-h)^2+y^2]^3}\right\}, \tag{A15b}$$

$$\sigma_{xy}^{b_x}=Db_x\left\{\frac{(x+h)[(x+h)^2-y^2]}{[(x+h)^2+y^2]^2} -\frac{(x+h)[(x-h)^2-y^2]}{[(x-h)^2+y^2]^2} +4xh(x-h)\frac{(x-h)^2-3y^2}{[(x-h)^2+y^2]^3}\right\}, \tag{A15c}$$

$$\sigma_{zz}^{b_x}=D\nu b_x\left\{-\frac{2y}{(x+h)^2+y^2} +\frac{2y(5h^2-6hx+x^2+y^2)}{[(x-h)^2+y^2]^2}\right\}, \tag{A15d}$$

$$\sigma_{xz}^{b_x}=\sigma_{yz}^{b_x}=0. \tag{A15e,f}$$

(ii) For an edge dislocation with $\mathbf{b}=-b_y\mathbf{e}_y$:

$$\sigma_{xx}^{b_y}=-Db_y\left\{\frac{(x+h)[(x+h)^2-y^2]}{[(x+h)^2+y^2]^2}+\frac{(x-h)[(x-h)^2-y^2]}{[(x-h)^2+y^2]^2} +2x\frac{h^4-2h^3x-x^4-6h^2y^2+y^4+2h(x^3+3xy^2)}{[(x-h)^2+y^2]^3}\right\}, \tag{A16a}$$

$$\sigma_{yy}^{b_y}=-Db_y\left\{\frac{(x+h)[(x+h)^2+3y^2]}{[(x+h)^2+y^2]^2} -\frac{h^3+h^2x-5h(x^2+y^2)+x(3x^2+y^2)}{[(x-h)^2+y^2]^2} -2x\frac{h^4-2h^3x-x^4-6h^2y^2+y^4+2h(x^3+3xy^2)}{[(x-h)^2+y^2]^3}\right\}, \tag{A16b}$$

Downloaded 29 May 2004 to 128.111.74.212. Redistribution subject to AIP license or copyright, see http://jap.aip.org/jap/copyright.jsp

$$\sigma_{xy}^{b_y}=-Db_y\left\{\frac{y[(x+h)^2-y^2]}{[(x+h)^2+y^2]^2}+\frac{y(-h^2-2hx+3x^2+y^2)}{[(x-h)^2+y^2]^2}-4xy\frac{2h^3-3h^2x+x^3-2hy^2+xy^2}{[(x-h)^2+y^2]^3}\right\}, \tag{A16c}$$

$$\sigma_{zz}^{b_y}=-D\nu b_y\left\{\frac{2(x+h)}{(x+h)^2+y^2}-\frac{2[h^3-h^2x+x(x^2+y^2)-h(x^2+3y^2)]}{[(x-h)^2+y^2]^2}\right\}; \tag{A16d}$$

$$\sigma_{xz}^{b_y}=\sigma_{yz}^{b_y}=0. \tag{A16e,f}$$

(iii) For a screw dislocation with $\mathbf{b}=b_z\mathbf{e}_z$:

$$\sigma_{xx}^{b_z}=\sigma_{yy}^{b_z}=\sigma_{zz}^{b_z}=\sigma_{xy}^{b_z}=0; \tag{A17a,b,c,d}$$

$$\sigma_{xz}^{b_z}=-\frac{Gb_z}{2\pi}\left\{\frac{y}{(x+h)^2+y^2}-\frac{y}{(x-h)^2+y^2}\right\}; \tag{A17e}$$

$$\sigma_{yz}^{b_z}=\frac{Gb_z}{2\pi}\left\{\frac{x+h}{(x+h)^2+y^2}-\frac{x-h}{(x-h)^2+y^2}\right\}. \tag{A17f}$$

The components of the stress tensor for an array of subsurface dislocations array stresses are as follows.

(i) For an array of edge dislocations with $\mathbf{b}=b_x\mathbf{e}_x$:

$$\sigma_{xx}^{\Sigma b_x}=D\frac{b_x}{l}\pi\left\{\sin 2\pi\tilde{y}\frac{\cos 2\pi\tilde{y}-\cosh 2\pi(\tilde{x}+\tilde{h})-2\pi(\tilde{x}+\tilde{h})\sinh 2\pi(\tilde{x}+\tilde{h})}{[\cosh 2\pi(\tilde{x}+\tilde{h})-\cos 2\pi\tilde{y}]^2}-\sin 2\pi\tilde{y}\frac{\cos 2\pi\tilde{y}-\cosh 2\pi(\tilde{x}-\tilde{h})-2\pi(\tilde{x}-\tilde{h})\sinh 2\pi(\tilde{x}-\tilde{h})}{[\cosh 2\pi(\tilde{x}-\tilde{h})-\cos 2\pi\tilde{y}]^2}-4\pi^2\tilde{x}\tilde{h}\sin 2\pi\tilde{y}\frac{-3+\cosh 4\pi(\tilde{x}-\tilde{h})+2\cosh 2\pi(\tilde{x}-\tilde{h})\cos 2\pi\tilde{y}}{[\cosh 2\pi(\tilde{x}-\tilde{h})-\cos 2\pi\tilde{y}]^3}\right\}, \tag{A18a}$$

$$\sigma_{yy}^{\Sigma b_x}=D\frac{b_x}{l}\pi\left\{\sin 2\pi\tilde{y}\frac{\cos 2\pi\tilde{y}-\cosh 2\pi(\tilde{x}+\tilde{h})+2\pi(\tilde{x}+\tilde{h})\sinh 2\pi(\tilde{x}+\tilde{h})}{[\cosh 2\pi(\tilde{x}+\tilde{h})-\cos 2\pi\tilde{y}]^2}-\sin 2\pi\tilde{y}\frac{\cos 2\pi\tilde{y}-\cosh 2\pi(\tilde{x}-\tilde{h})+2\pi(\tilde{x}+3\tilde{h})\sinh 2\pi(\tilde{x}-\tilde{h})}{[\cosh 2\pi(\tilde{x}-\tilde{h})-\cos 2\pi\tilde{y}]^2}+4\pi^2\tilde{x}\tilde{h}\sin 2\pi\tilde{y}\frac{-3+\cosh 4\pi(\tilde{x}-\tilde{h})+2\cosh 2\pi(\tilde{x}-\tilde{h})\cos 2\pi\tilde{y}}{[\cosh 2\pi(\tilde{x}-\tilde{h})-\cos 2\pi\tilde{y}]^3}\right\}, \tag{A18b}$$

$$\sigma_{xy}^{\Sigma b_x}=D\frac{b_x}{l}\pi\left\{2\pi(\tilde{x}+\tilde{h})\frac{\cos 2\pi\tilde{y}\cosh 2\pi(\tilde{x}+\tilde{h})-1}{[\cosh 2\pi(\tilde{x}+\tilde{h})-\cos 2\pi\tilde{y}]^2}-2\pi(\tilde{x}+\tilde{h})\frac{\cos 2\pi\tilde{y}\cosh 2\pi(\tilde{x}-\tilde{h})-1}{[\cosh 2\pi(\tilde{x}-\tilde{h})-\cos 2\pi\tilde{y}]^2}+4\pi^2\tilde{x}\tilde{h}\frac{[-3+\cos 4\pi\tilde{y}+2\cos 2\pi\tilde{y}\cosh 2\pi(\tilde{x}-\tilde{h})]\sinh 2\pi(\tilde{x}-\tilde{h})}{[\cosh 2\pi(\tilde{x}-\tilde{h})-\cos 2\pi\tilde{y}]^3}\right\}, \tag{A18c}$$

$$\sigma_{zz}^{\Sigma b_x}=-D\nu\frac{b_x}{l}\pi\left\{\frac{2\sin 2\pi\tilde{y}}{\cosh 2\pi(\tilde{x}+\tilde{h})-\cos 2\pi\tilde{y}}+2\sin 2\pi\tilde{y}\frac{\cos 2\pi\tilde{y}-\cosh 2\pi(\tilde{x}-\tilde{h})+4\pi\tilde{h}\sinh 2\pi(\tilde{x}-\tilde{h})}{[\cosh 2\pi(\tilde{x}-\tilde{h})-\cos 2\pi\tilde{y}]^2}\right\}; \tag{A18d}$$

$$\sigma_{xz}^{\Sigma b_x}=\sigma_{yz}^{\Sigma b_x}=0. \tag{A18e,f}$$

(ii) For an array of edge dislocations with $\mathbf{b}=-b_y\mathbf{e}_y$:

Downloaded 29 May 2004 to 128.111.74.212. Redistribution subject to AIP license or copyright, see http://jap.aip.org/jap/copyright.jsp

$$\sigma_{xx}^{\Sigma b_y}=D\frac{b_y}{l}\pi\left\{-2\pi(\tilde{x}+\tilde{h})\frac{\cosh 2\pi(\tilde{x}+\tilde{h})\cos 2\pi\tilde{y}-1}{[\cosh 2\pi(\tilde{x}+\tilde{h})-\cos 2\pi\tilde{y}]^2}-2\pi(\tilde{x}-\tilde{h})\frac{\cosh 2\pi(\tilde{x}-\tilde{h})\cos 2\pi\tilde{y}-1}{[\cosh 2\pi(\tilde{x}-\tilde{h})-\cos 2\pi\tilde{y}]^2}\right.$$
$$+2\pi\tilde{x}\frac{3\cos 2\pi\tilde{y}-\cosh 2\pi(\tilde{x}-\tilde{h})(3+\cos 4\pi\tilde{y})}{[\cosh 2\pi(\tilde{x}-\tilde{h})-\cos 2\pi\tilde{y}]^3}$$
$$\left.+2\pi\tilde{x}\frac{[\cosh 4\pi(\tilde{x}-\tilde{h})+2\pi\tilde{h}\sinh 4\pi(\tilde{x}-\tilde{h})]\cos 2\pi\tilde{y}-2\pi\tilde{h}\sinh 2\pi(\tilde{x}-\tilde{h})(3-\cos 4\pi\tilde{y})}{[\cosh 2\pi(\tilde{x}-\tilde{h})-\cos 2\pi\tilde{y}]^3}\right\}, \tag{A19a}$$

$$\sigma_{yy}^{\Sigma b_y}=D\frac{b_y}{l}\pi\left\{\frac{2\pi(\tilde{x}+\tilde{h})[\cosh 2\pi(\tilde{x}+\tilde{h})\cos 2\pi\tilde{y}-1]+2\sinh 2\pi(\tilde{x}+\tilde{h})\cos 2\pi\tilde{y}-\sinh 4\pi(\tilde{x}+\tilde{h})}{[\cosh 2\pi(\tilde{x}+\tilde{h})-\cos 2\pi\tilde{y}]^2}\right.$$
$$+\frac{2\pi(\tilde{x}+3\tilde{h})[\cosh 2\pi(\tilde{x}-\tilde{h})\cos 2\pi\tilde{y}-1]-2\sinh 2\pi(\tilde{x}-\tilde{h})\cos 2\pi\tilde{y}+\sinh 4\pi(\tilde{x}-\tilde{h})}{[\cosh 2\pi(\tilde{x}-\tilde{h})-\cos 2\pi\tilde{y}]^2}$$
$$-2\pi\tilde{x}\frac{3\cos 2\pi\tilde{y}-\cosh 2\pi(\tilde{x}-\tilde{h})(3+\cos 4\pi\tilde{y})}{[\cosh 2\pi(\tilde{x}-\tilde{h})-\cos 2\pi\tilde{y}]^3}$$
$$\left.-2\pi\tilde{x}\frac{[\cosh 4\pi(\tilde{x}-\tilde{h})+2\pi\tilde{h}\sinh 4\pi(\tilde{x}-\tilde{h})]\cos 2\pi\tilde{y}-2\pi\tilde{h}\sinh 2\pi(\tilde{x}-\tilde{h})(3-\cos 4\pi\tilde{y})}{[\cosh 2\pi(\tilde{x}-\tilde{h})-\cos 2\pi\tilde{y}]^3}\right\}, \tag{A19b}$$

$$\sigma_{xy}^{\Sigma b_y}=D\frac{b_y}{l}\pi\left\{-\sin 2\pi\tilde{y}\frac{2\pi(\tilde{x}+\tilde{h})\sinh 2\pi(\tilde{x}+\tilde{h})+\cos 2\pi\tilde{y}-\cosh 2\pi(\tilde{x}+\tilde{h})}{[\cosh 2\pi(\tilde{x}+\tilde{h})-\cos 2\pi\tilde{y}]^2}\right.$$
$$+\sin 2\pi\tilde{y}\frac{-2\pi(\tilde{x}+\tilde{h})\sinh 2\pi(\tilde{x}-\tilde{h})+\cos 2\pi\tilde{y}-\cosh 2\pi(\tilde{x}-\tilde{h})}{[\cosh 2\pi(\tilde{x}-\tilde{h})-\cos 2\pi\tilde{y}]^2}+4\pi\tilde{x}\sin 2\pi\tilde{y}$$
$$\left.\times\frac{2\pi\tilde{h}\cosh 2\pi(\tilde{x}-\tilde{h})\cos 2\pi\tilde{y}-3\pi\tilde{h}+\pi\tilde{h}\cosh 4\pi(\tilde{x}-\tilde{h})+\sinh 2\pi(\tilde{x}-\tilde{h})[\cosh 2\pi(\tilde{x}-\tilde{h})-\cos 2\pi\tilde{y}]}{[\cosh 2\pi(\tilde{x}-\tilde{h})-\cos 2\pi\tilde{y}]^3}\right\}, \tag{A19c}$$

$$\sigma_{zz}^{\Sigma b_y}=D\nu\frac{b_y}{l}\pi\left\{\frac{-2\sinh 2\pi(\tilde{x}+\tilde{h})}{[\cosh 2\pi(\tilde{x}+\tilde{h})-\cos 2\pi\tilde{y}]}\right.$$
$$\left.+\frac{-8\pi\tilde{h}+8\pi\tilde{h}\cosh 2\pi(\tilde{x}-\tilde{h})\cos 2\pi\tilde{y}-2\sinh 2\pi(\tilde{x}-\tilde{h})\cos 2\pi\tilde{y}+\sinh 4\pi(\tilde{x}-\tilde{h})}{[\cosh 2\pi(\tilde{x}-\tilde{h})-\cos 2\pi\tilde{y}]^2}\right\}, \tag{A19d}$$

$$\sigma_{xz}^{\Sigma b_y}=\sigma_{yz}^{\Sigma b_y}=0. \tag{A19e,f}$$

(iii) For an array of screw dislocations with $\mathbf{b}=b_z\mathbf{e}_z$:

$$\sigma_{xx}^{\Sigma b_z}=\sigma_{yy}^{\Sigma b_z}=\sigma_{zz}^{\Sigma b_z}=\sigma_{xy}^{\Sigma b_z}=0, \tag{A20a,b,c,d}$$

$$\sigma_{xz}^{\Sigma b_z}=G\frac{b_z}{2l}\left[-\frac{\sin 2\pi\tilde{y}}{\cosh 2\pi(\tilde{x}+\tilde{h})-\cos 2\pi\tilde{y}}+\frac{\sin 2\pi\tilde{y}}{\cosh 2\pi(\tilde{x}-\tilde{h})-\cos 2\pi\tilde{y}}\right], \tag{A20e}$$

$$\sigma_{yz}^{\Sigma b_z}=G\frac{b_z}{2l}\left[\frac{\sinh 2\pi(\tilde{x}+\tilde{h})}{\cosh 2\pi(\tilde{x}+\tilde{h})-\cos 2\pi\tilde{y}}-\frac{\sinh 2\pi(\tilde{x}-\tilde{h})}{\cosh 2\pi(\tilde{x}-\tilde{h})-\cos 2\pi\tilde{y}}\right]. \tag{A20f}$$

Downloaded 29 May 2004 to 128.111.74.212. Redistribution subject to AIP license or copyright, see http://jap.aip.org/jap/copyright.jsp

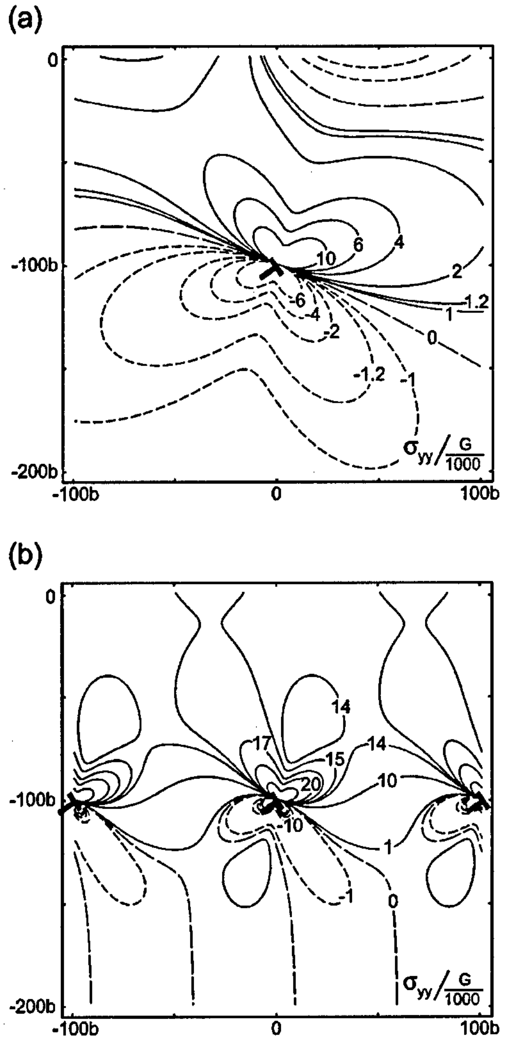

FIG. 12. Examples of stress distribution due to MDs. Contour plots of MD stresses σ_{yy} for an individual dislocation (a) and periodic dislocation array (b). For these plots dislocations with Burgers vector $\mathbf{b}=[(\sqrt{2}/\sqrt{3})\mathbf{e}_x+(1/\sqrt{3})\mathbf{e}_y]b$ were at the distance $h=100\,b$ from the free surface, periodicity in the array was $l=100\,b$, Poisson's ratio $\nu=0.32$. Stresses are in the units of 10^{-3} G. The Cartesian coordinates correspond to those used in Fig. 10.

The stresses in Eqs. (A15)–(A20), satisfy the boundary and equilibrium conditions given by Eqs. (A1).

The stresses for the periodic dislocation array [Eqs. (A18)–(A20)] can be transformed back to the solution for a single dislocation placed at the distance h from the free surface [Eqs. (A15)–(A17)] by solving for the limit as $l\rightarrow\infty$. The agreement with known results for a single dislocation provides a good check on the Eqs. (A16)–(A20). Figure 12 shows the comparison between the tangential component of the stress σ_{yy} arising from a dislocation array with those from a single edge dislocation.

We note here that the derived displacements and stress fields for periodic subsurface dislocations could be obtained in a different way from summation of Fourier series expressions given in Ref. 22 for dislocation arrays in two dissimilar elastic phase material. Using this technique, the formulas for the stresses of periodic subsurface edge dislocation arrays [which are equivalent to Eqs. (A18) and (A19)] were obtained in Ref. 23. The stresses for screw dislocation arrays were already used in Ref. 24. Finally, the normal component of the displacement field originating from subsurface edge dislocation arrays was utilized in Ref. 25 when studying the surface profile of InAs/GaAs (110) films.

In our modeling of crosshatch surface morphology, we use the displacements and stresses at the film surface, which can be easily extracted from the general solutions by putting $x=0$. In addition, to make the presentation of the modeling results more convenient, the stress and displacements equations are transformed so that sample surface is along the x axis, the sample surface normal is along the y axis, and the dislocation is at $(0,-h)$. This orientation is used for all the figures in the main text.

[1] A. M. Andrews, A. E. Romanov, J. S. Speck, M. Bobeth, and W. Pompe, Appl. Phys. Lett. **77**, 3740 (2000).
[2] A. M. Andrews, J. S. Speck, A. E. Romanov, M. Bobeth, and W. Pompe, J. Appl. Phys. **91**, 1933 (2002).
[3] H. Norenberg, L. Daweritz, P. Schutzendube, and K. Ploog, J. Appl. Phys. **81**, 2611 (1997).
[4] T. Ogura, D. Kishimoto, and T. Nishinaga, J. Cryst. Growth **226**, 179 (2001).
[5] A. Kley, P. Ruggerone, and M. Scheffler, Phys. Rev. Lett. **79**, 5278 (1997).
[6] J. W. Matthews, in *Dislocations in Solids*, edited by F. R. N. Nabarro (North-Holland, Amsterdam, 1979), Vol. 2, p. 461.
[7] E. A. Fitzgerald, Mater. Sci. Rep. **7**, 87 (1991).
[8] L. B. Freund, MRS Bull. **17**, 52 (1992).
[9] R. Beanland, D. J. Dunstan, and P. J. Goodhew, Adv. Phys. **45**, 87 (1996).
[10] J. S. Speck, M. A. Brewer, G. E. Beltz, A. E. Romanov, and W. Pompe, J. Appl. Phys. **80**, 3808 (1996).
[11] J. W. Matthews and A. E. Blakeslee, J. Cryst. Growth **27**, 118 (1974).
[12] J. Y. Tsao, *Materials Fundamentals of Molecular Beam Epitaxy* (Academic, New York, 1993).
[13] A. Krost, G. Bauer, J. Woitok, in *Optical Characterization of Epitaxial Semiconductor Layers* edited by G. Bauer and W. Richter (Springer, New York, 1996), Chap. 6.
[14] K. Cholevas, N. Liosatos, A. E. Romanov, M. Zaiser, and E. C. Aifantis, Phys. Status Solidi B **209**, 295 (1998).
[15] U. Jain, S. C. Jain, A. Atkinson, J. Nijs, R. P. Mertens, and R. Van Overstraeten, J. Appl. Phys. **73**, 1773 (1993).
[16] A. K. Head, Proc. Phys. Soc. London, Sect. B **66**, 793 (1953).
[17] J. D. Eshelby, in *Dislocations in Solids*, edited by F. R. N. Nabarro (North-Holland, Amsterdam, 1979), Vol. 1, p. 167.
[18] J. P. Hirth and J. Lothe, *Theory of Dislocations* (Wiley, New York, 1982).
[19] M. Dynna, J. L. Vassent, A. Marty, and B. Gilles, J. Appl. Phys. **80**, 2650 (1996).
[20] K. Jagannadham and M. J. Marcinkowski, J. Mater. Sci. **15**, 709 (1980).
[21] R. De Wit, J. Res. Natl. Bur. Stand. **77A**, 607 (1973).
[22] R. Bonnet and J. L. Verger-Gaugry, Philos. Mag. A **66**, 849 (1992).
[23] A. Bourret, Surf. Sci. **432**, 37 (1999).
[24] A. E. Romanov, P. M. Petroff, and J. S. Speck, Appl. Phys. Lett. **74**, 2280 (1999).
[25] J. G. Belk, D. W. Pashley, B. A. Joyce, and T. S. Jones, Phys. Rev. B **58**, 16194 (1998).

Downloaded 29 May 2004 to 128.111.74.212. Redistribution subject to AIP license or copyright, see http://jap.aip.org/jap/copyright.jsp

Appendix IV

Oxidation Control of GaAs pHEMTs for High Efficiency Applications

Can Zheng, R. Coffie, D. Buttari, J. Champlain, and U. K. Mishra, *Fellow, IEEE*

***Abstract*—In this letter, for the first time, an investigation of partially oxidized GaAs-on-insulator (GOI) AlGaAs/InGaAs/GaAs pseudomorphic HEMTs is reported. Fully oxidized pHEMTs demonstrated minimized substrate leakage current and high output impedance, but suffered from 30 ~ 40% charge loss. Fully oxidized devices also showed transonductance peaking that could be removed by controlled partial oxidation. Partially oxidized pHEMT devices showed improved power added efficiencies (PAEs) at a low supply voltage of 3.0 V compared to fully oxidized or unoxidized devices and negligible charge loss (< 10%).**

***Index Terms*—Heterojunctions, impact ionization, MODFETs, oxidation, semiconductor defects.**

I. Introduction

High efficiency components are key elements of solid state amplifiers for wireless application. Portable applications require reduced supply voltages to minimize weight and size and enhanced efficiency to ensure long battery lifetime. GOI MESFET technology has been shown to provide ultrahigh efficiencies [1]. This was due to the enhanced charge control provided by the GOI technology, which reduced the parasitic substrate leakage and increased transconductance near pinchoff as compared to a conventional MESFET. Extending the GOI technology to pHEMTs is of great interest since pHEMTs are widely used for low noise and high power applications in the microwave and millimeter wave frequency ranges due to their superior power, efficiency and linearity performance.

Charge loss in fully oxidized GOI MESFETs, which has detrimental effects on current and output power, has been a serious problem for the practical application of GOI technology [2]. The charge loss was believed to be due to the depletion of charge by the high defect density oxide–semiconductor interface. The stresses developed as a result of the volume shrinkage of the oxidized layer, as well as arsenic accumulation appear to contribute to the formation of defects close to the interface and in the layers adjacent to the oxide layer [3]. There are several ways to minimize the charge loss. It was observed that the presence of low-temperature (LT) GaAs layer in the vicinity of the oxidized layer enhances the oxidation rate and develops better oxide/GaAs interfaces compared to reference samples without an LT GaAs layer [4], [5]. A thin layer of AlAs can be used as a defect diffusion barrier above the oxidation layer to minimize the diffusion of point defects generated during the oxidation into the active channel region [6], [7]. Partial oxidation of the active channel was explored here to take advantage of the insulating oxide buffer, while minimizing the charge loss.

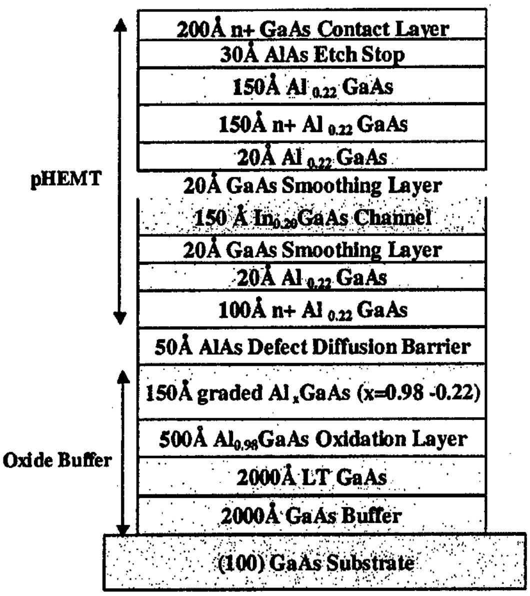

Fig. 1. Epitaxial structure of the double-side doped GaAs-on-insulator (GOI) AlGaAs/InGaAs/GaAs pHEMT.

II. Epitaxial Structure and Device Fabrication

The epitaxial structure of the double-side doped AlGaAs/InGaAs/GaAs GOI pHEMT is shown in Fig. 1. The pHEMT material was grown by MBE on a semi-insulating GaAs substrate with the following growth sequence: a 2000 Å GaAs buffer, a 2000 Å low temperature (LT) GaAs grown at 270°C, a 500 Å $Al_{0.98}Ga_{0.02}As$ oxidation layer, a 150 Å graded $Al_xGa_{1-x}As$ with Al composition (x) graded from 0.98 to 0.22, a 50 Å AlAs defect diffusion barrier, a 100 Å n^+ $Al_{0.22}Ga_{0.78}As$ bottom electron supply layer, a 20 Å $Al_{0.22}Ga_{0.78}As$/20 Å GaAs spacer, a 150 Å $In_{0.2}Ga_{0.8}As$ channel, a 20 Å GaAs/20 Å $Al_{0.22}Ga_{0.78}As$ spacer, a 150 Å n^+ $Al_{0.22}Ga_{0.78}As$ top electron supply layer, a 150 Å $Al_{0.22}Ga_{0.78}As$ barrier, a 30 Å AlAs etch stop layer, a 200 Å n^+ GaAs ohmic contact layer. The growth was finished with a 50 Å AlAs etch stop layer and a 200 Å GaAs layer to protect the sample surface during the oxidation process. Hall measurement showed an electron sheet charge density of $3.5 \times 10^{12}/\text{cm}^2$ and a mobility of 6470 $\text{cm}^2/\text{V} \cdot \text{s}$ at room temperature after the removal of the n^+ GaAs ohmic contact layer.

Manuscript received February 22, 2002; revised May 6, 2002. This work was supported by the U.S. Air Force Office of Scientific Research. The review of this letter was arranged by D. Ueda.

The authors are with the Department of Electrical and Computer Engineering, University of California, Santa Barbara, CA 93106 USA.

Publisher Item Identifier S 0741-3106(02)06243-2.

0741-3106/02$17.00 © 2002 IEEE

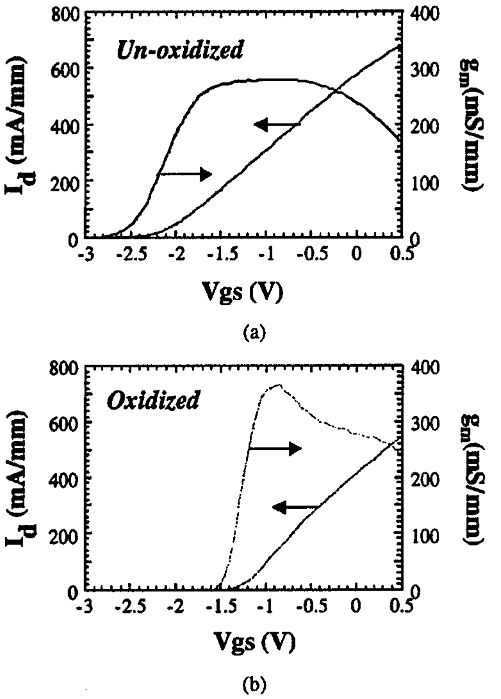

(a)

(b)

Fig. 2. Drain current and transconductance versus gate bias at 2.5 V V_{DS} of (a) an unoxidized sample with a maximum g_m of 280 mS/mm and (b) a fully oxidized sample with a peaked transconductance as high as 370 mS/mm near the pinch off voltage.

GOI pHEMT process flow is similar to the conventional FET process with an additional oxidation process. First, a 2000 Å Si_xN_y mask is deposited by PECVD, then patterned and selectively removed using a CF_4 based RIE etch. Next a Cl_2 based RIE etch is used to open the oxidation window in the exposed semiconductor surface to allow lateral oxidation of the $Al_{0.98}Ga_{0.02}As$ layer from the sidewall [8]. The oxidation was carried out at 400°C with N_2 bubbling through 80°C DI water. After oxidation, the sample was annealed at 600°C for 3 min with a GaAs proximity cap to annihilate point defects generated during the oxidation process. The Si_xN_y mask was then completely removed. Mesa isolation was obtained by a Cl_2 based RIE etch. Ni/AuGe/Ni/Au were deposited for the source/drain ohmic contacts and annealed at 430°C for 30 s. Finally, a 0.7 μm long and 150 μm wide gate was defined and a single recess to remove the n^+ GaAs was performed using a citric acid based selective wet etch. Ti/Pt/Au gate metals were deposited to complete the GOI pHEMT process.

III. RESULTS AND DISCUSSION

Fully oxidized pHEMTs and unoxidized control sample were fabricated at the same time. Low subthreshold leakage current, sharp transconductance turn on near pinchoff and high output impedance were observed for fully oxidized GOI pHEMTs due to the introduction of the insulating oxide buffer. Compared to unoxidized devices, fully oxidized pHEMTs showed transconductance peaking up to 50% near pinch-off voltage (see Fig. 2), as well as charge loss up to 30% due to back depletion from the oxide-semiconductor interface. Capacitance–voltage (C-V) measurements of the fully oxidized Schottky diodes indicated charge compensation of the channel and doped layers compared to unoxidized diodes. Gain peaking could be due to an increase in drain current induced by threshold voltage shift. The threshold voltage shift is attributed to impact ionization of the traps underneath the gate by hot electrons, which can take place at substantially lower drain bias compared to the electron-hole pair generation by band to band ionization [9]. Electrons removed from the deep levels shift the threshold voltage toward negative values, therefore causing the increase in current [10]. This is analogous to the phenomena responsible for the kink effect in SOI MOSFETs [11]. In this study, partial oxidation was investigated to minimize the charge loss and gain peaking associated with the fully oxidized pHEMTs.

A series of partially to fully oxidized pHEMTs were fabricated with the edge of oxidation front varying from below the source contact to beyond the drain contact. The unoxidized pHEMTs were also fabricated on the same wafer. The extent of the oxide formed by lateral wet oxidation of the AlGaAs underneath the device active region was controlled by varying the distance between the edge of the oxidation window and the source contact edge as shown in Fig. 3(a). It was found that the largest transconductance peaking and charge loss occurred for devices with an oxidation front extending beyond the gate region [Fig. 4(a)]. This is consistent with the threshold voltage shift due to impact ionization of traps underneath the gate as the cause for the transconductance peaking. Devices with the oxidation front stopped around the source edge showed flat transconductance curves and charge loss of less than 10%. An ATN load-pull system was used for the large signal continuous-wave (CW) measurements at 8 GHz. and devices were tuned for maximum efficiency. As shown in Fig. 4(b), improved power added efficiencies (PAEs) as high as 55% have been achieved with class AB bias condition. The associated power gains were around 15 to 17 dB at a low V_{DS} bias of 3.0 V. Repeated experiments of various pHEMT samples showed improved PAE by $5 \sim 10\%$ for partially oxidized samples with oxidation front stopped around the source edge compared to an unoxidized control samples. The improved PAE could be attributed to decreased substrate leakage current (see Fig. 3(b)) and improved g_m near pinchoff. It has been shown that with the oxide extending further into the channel, the substrate leakage current was blocked more effectively. Although fully oxidized devices showed low substrate leakage and larger dc g_m near pinchoff, pulsed current–voltage (I–V) measurements revealed a large amount of dispersion compared to unoxidized and partially oxidized devices with oxidation fronts that stop before the drain edge of the gate. Dispersion caused by traps induced by the oxidation process reduces the maximum RF current, RF gm, and increases the knee voltage, all of which reduce PAE. These preliminary results indicate that partially oxidized pHEMTs are promising for high efficiency and low voltage wireless applications.

IV. CONCLUSION

In conclusion, low subthreshold leakage current, sharp transconductance turn-on near pinchoff, and high output impedance were observed for fully oxidized GOI pHEMTs

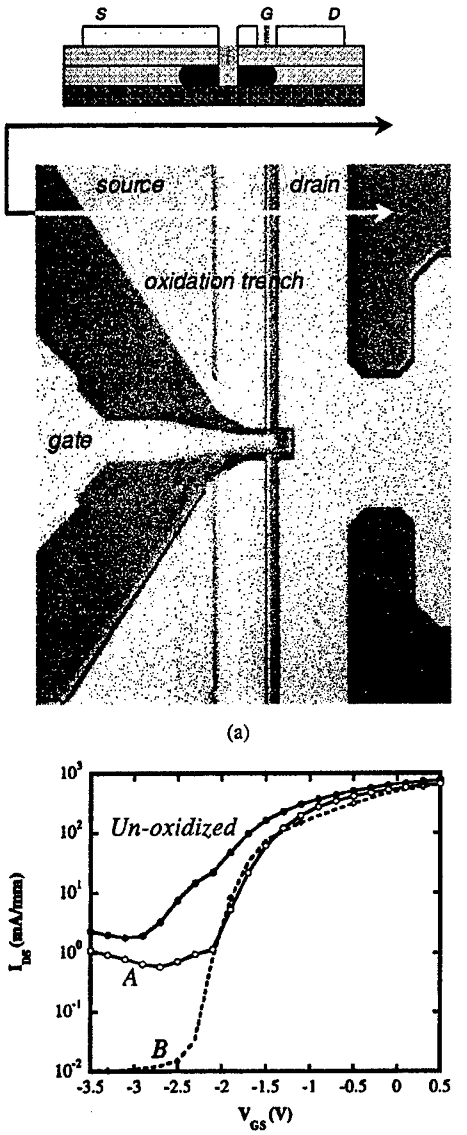

(b)

Fig. 3. (a) The pHEMT device layout and cross section. (b) The drain current I_{DS} versus V_{GS} at 2.5 V V_{DS} of an unoxidized pHEMT, (A) a pHEMT with the oxidation front stopped between source and gate and (B) a pHEMT with the oxidation front stopped between gate and drain.

due to the introduction of the insulating oxide buffer. Fully oxidized pHEMTs suffered from transconductance peaking and charge loss up to 30%. Partially oxidized pHEMT devices still benefited from an insulating oxide buffer and showed negligible change loss and improved PAE for oxidation fronts stopped before the drain edge of the gate.

REFERENCES

[1] T. Jenkins, L. Kehias, P. Parikh, J. Ibbetson, U. Mishra, D. Doctor, M. Le, J. Pusl, and D. Widman, "Ultrahigh efficiency obtained with GaAs-on-Insulator MESFET technology," *IEEE J. Solid-State Circuits*, vol. 34, pp. 1239–1245, Sept. 1999.

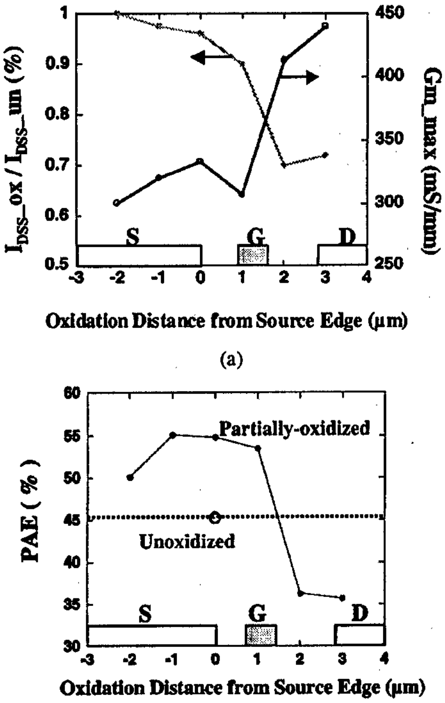

(b)

Fig. 4. (a) Normalized I_{DSS} and maximum transconductance at 2.5 V V_{DS} of partially oxidized pHEMTs. (b) Power added efficiency of pHEMTs at 8 GHz in class AB operation. The drain bias was 3.0 V.

[2] P. Parikh, P. Chavarka, and U. K. Mishra, "GaAs MESFETs on a truly insulating buffer layer: Demonstration of the GaAs on insulator technology," *IEEE Electron Device Lett.*, vol. 18, pp. 111–114, Mar. 1997.

[3] S. Guha, F. Agahi, B. Pezeshki, J. A. Kash, D. W. Kisker, and N. A. Bojarczuk, "Microstructure of AlGaAs-oxide heterolayers formed by wet oxidation," *Appl. Phys. Lett.*, vol. 68, no. 7, pp. 906–908, 1996.

[4] J. C. Ferrer, Z. Liliental-Weber, H. Reese, Y. J. Chiu, and E. Hu, "Improvement of the interface quality during thermal oxidation of Al/sub 0.98/Ga/sub 0.02/As layers due to the presence of low-temperature-grown GaAs," *Appl. Phys. Lett.*, vol. 77, no. 2, pp. 205–207, 2000.

[5] H. Reese, Y. J. Chiu, and E. Hu, "Low-temperature-grown GaAs enhanced wet thermal oxidation of Al/sub 0.98/Ga/sub 0.02/As," *Appl. Phys. Lett.*, vol. 73, no. 18, pp. 2624–2626, 1998.

[6] L.-W. Yin, Y. Hwang, J. H. Lee, R. M. Kolbas, R. J. Trew, and U. K. Mishra, "Improved breakdown voltage in GaAs MESFETs utilizing surface layers of GaAs grown at a low temperature by MBE," *IEEE Electron Device Lett.*, vol. 11, pp. 561–563, Dec. 1990.

[7] M. N. Chang, K. C. Hsieh, T.-E. Nee, and J.-I. Chyi, "Effects of point defect distribution on arsenic precipitation in low-temperature grown III-V arsenides," *J. Appl. Phys.*, vol. 86, no. 5, pp. 2442–2447, 1999.

[8] K. D. Choquette, K. M. Geib, C. I. H. Ashby, R. D. Twesten, O. Blum, H. Q. Hou, D. M. Follstaedt, B. E. Hammons, D. Mathes, and R. Hull, "Advances in selective wet oxidation of AlGaAs alloys," *IEEE J. Select. Topics Quant. Electron.*, vol. 3, pp. 916–926, June 1997.

[9] L. Partain, D. Day, and R. Powell, "Metastable impact ionization of traps model for lock-on in GaAs photoconductive switches," *J. Appl. Phys.*, vol. 74, no. 1, pp. 335–340, 1993.

[10] J. Haruyama, H. Negishi, Y. Nishimura, and Y. Nashimoto, "Substrate-related kink effects with a strong light-sensitivity in AlGaAs/InGaAs PHEMT," *IEEE Trans. Electron Devices*, vol. 44, pp. 25–33, Jan. 1997.

[11] T. Ushiki, K. Kotani, T. Funaki, K. Kawai, and T. Ohmi, "New aspects and mechanism of kink effect in static back-gate transconductance characteristics in fully-depleted SOI MOSFETs on high-dose SIMOX wafers," *IEEE Trans. Electron Devices*, vol. 47, pp. 360–366, Feb. 2000.

Appendix V

Design and Fabrication of Collector-up Heterojunction Bipolar Transistors with Oxide Confined Current Apertures

James G. Champlain and Umesh K. Mishra

Abstract – Collector-up heterojunction bipolar transistors (HBTs) with oxide confined current apertures offer a possible high-frequency, high-gain option for HBT design. Collector-up HBTs offer reduced base-collector capacitances, as compared to their emitter-up counterparts, that leads to an increase in their maximum frequency of oscillation (f_{max}). Standard collector-up HBTs suffer from reduced current gains due to the direct injection of carriers from the emitter into the base contacts. To overcome this deficiency, a current aperture must be adopted in the emitter to properly channel the carriers.

This paper examines the application of the collector-up HBT with a current aperture in the InP lattice-matched material system. The current aperture in the devices presented here was produced by the partial oxidation of a high aluminum content emitter to form an oxide confinement layer around the aperture. Various aspects of the device's DC and RF performance were examined. A parasitic base-emitter (BE) capacitance resulting from the collector-up design, outside of the active portion of the transistor, in association with a relatively large emitter resistance was found to limit the transistor's current-gain cutoff frequency (f_τ). Though limiting f_τ, this parasitic BE capacitance was found to have little effect on f_{max}. A model of the device was developed and simulated to confirm these statements.

I. INTRODUCTION

The ever-growing demand in communication and radar technology for increased bit-rates and frequency resolution requires systems capable of providing increased bandwidth and clock rates [1, 2]. This demand is eventually reflected in the requirement that the devices, which are the building blocks of these systems, must be capable of operating at higher frequencies [3-6].

For example, integrated circuits for optical fiber communications that are capable of providing transmissions at 40 Gb/s are currently in development. The eventual emergence of higher bit-rate systems (i.e., 160 Gb/s) will require amplifiers with larger bandwidths (i.e., ~100 GHz). High bandwidth military radar and communication systems require analog-digital converters (ADCs), digital-analog converters (DACs), and direct-digital frequency synthesizers (DDFSs) with very high frequency resolution. This demands devices that can operate well over 100 times the signal bandwidth of the system [2].

Two well-known measures or figures-of-merit useful in evaluating the high frequency performance of a transistor are the current-gain cutoff frequency, f_τ, and maximum frequency of oscillation, f_{max}. f_τ is defined as the frequency at which the short-circuit current gain (h_{21}) goes to unity; f_{max} is defined as the frequency at which the power gain goes to unity. Though finally dependent on the application, transistors with increased f_τ and f_{max} must be realized in order to meet the demand in bandwidth of the next generation of systems.

For a heterojunction bipolar transistor (HBT), f_τ is written as:

$$f_\tau = \frac{1}{2\pi}\left(\frac{\eta kT}{qI_C}\left(C_{BE}+C_{BC}\right)+\frac{W_B{}^2}{2D_{min}}\right.$$
$$\left.+\frac{W_C}{2v_{sat}}+\left(R_E+R_C\right)C_{BC}\right)^{-1} \tag{1}$$

where

η	ideality factor;
k	Boltzmann's constant (8.62×10^5 eV/K);
T	absolute temperature of the device;
q	electronic charge (1.602×10^{19} C);
I_C	collector current;
C_{BE}	base-emitter capacitance;
C_{BC}	base-collector capacitance;
W_B	neutral bases width;
D_{min}	minority carrier diffusion coefficient in the base;
W_C	base-collector depletion width;
v_{sat}	saturation velocity in the depleted collector;
R_E	emitter resistance;
R_C	collector resistance.

The first and last terms in (1) correspond to the time associated with charging the base-emitter capacitance (C_{BE}) through the junction's dynamic resistance ($\eta kT / qI_C$) and the base-collector capacitance (C_{BC}) through the emitter (R_E), collector (R_C), and base-emitter dynamic resistances. The second and third terms correspond to the transit time of carriers through the neutral base and depleted collector.

A somewhat straightforward understanding of f_τ may be achieved by examining the roles of the various terms in (1). The first and last terms are RC charging times associated with the base-emitter and base-collector junctions. These charging times represent the time that the junctions require to adjust the potential in the base, under given bias conditions (e.g., I_C, V_{CE}), in response to a variation in the input current. The second and third terms are carrier transit times through the neutral base and depleted collector, respectively. Together, they represent the time it takes for a charge carrier, once ejected from the emitter, to be imaged or "collected" at the collector contact. The summation of these time constants may be thought of corresponding to the *minimum* total time that the transistor requires to respond to a variation in its input and collect the resultant transited carrier, with f_τ as the corresponding *maximum* frequency.

The unilateral power gain is the maximum power gain achievable by the transistor. f_{max} may be defined as the frequency at which the transistor's unilateral power gain drops to unity:

$$f_{max} = \sqrt{\frac{f_\tau}{8\pi R_B C_{BC}}} \tag{2}$$

where R_B is the base resistance. f_{max} also marks the boundary in frequency between the transistor behaving as an active or passive network.

The intent of the HBT design presented here is to introduce a method to increase f_{max} that can be adopted into nearly any material system and existing transistor design. Though it is not of direct concern within the scope of this paper, it should be mentioned that there are various means to increase f_τ. Most of these approaches are dependent upon device layer design and material selection, such as bandgap grading in the base [7, 8], base doping profiles [9, 10], and Schottky collectors [11]; all of which may be adopted into the HBT design presented here.

In order to increase the f_{max} of the transistor, a collector-up design, as opposed to the conventional emitter-up design (Fig. 1a), was adopted. Using a collector-up design makes possible the reduction of the transistor's relatively large C_{BC}, thereby increasing the device's f_{max}, by physically reducing the active base-collector junction area. Simply adopting a "plain" collector-up design would result in a reduced current gain, or possibly no gain at all, due to an active emitter-base junction that is larger than the corresponding base-collector junction, giving rise to an increased recombination of carriers into the base contacts (Fig. 1b). Therefore, in order to maintain a high current gain, a current aperture must be introduced into the emitter to channel the carriers that are injected into the base/collector (Fig. 1c). An additional benefit of the collector-up design is that it easily allows the use of a Schottky collector, as opposed to a conventional ohmic collector/sub-collector commonly used in emitter-up designs. The benefit of using a Schottky contact for the collector contact is that it removes the collector resistance (R_C) from (1), reducing the collector-charging time associated with it, increasing both f_τ and f_{max} [11].

II. DEVICE GROWTH AND FABRICATION

The HBTs presented in this paper were grown by solid-source molecular beam epitaxy. The layer structure (from substrate to surface) consisted of: a semi-insulating InP (SI InP) substrate; a 6000 Å n$^+$ (Te: 1×10^{19} cm^{-3}) $GaAs_{0.49}Sb_{0.51}$ sub-emitter; a 500 Å n$^+$ (Te: 1×10^{19} cm^{-3}) linear step grade from $GaAs_{0.49}Sb_{0.51}$ to $AlAs_{0.56}Sb_{0.44}$ (emitter grade); a 200 Å n$^+$ (Te: 5×10^{18} cm^{-3}) $AlAs_{0.56}Sb_{0.44}$ emitter, which is the source material for the oxide current confinement layer; a 500 Å n (Te: 1×10^{18} cm^{-3}) linear step grade from $AlAs_{0.56}Sb_{0.44}$ to $GaAs_{0.49}Sb_{0.51}$ (base-emitter grade); a 500 Å p$^+$ (Be: 5×10^{19} cm^{-3}) $GaAs_{0.49}Sb_{0.51}$ base; and a 3000 Å n$^-$ (Te: 5×10^{16} cm^{-3}) $In_{0.53}Ga_{0.47}As$

collector (Fig. 2). The InP lattice-matched quarternary $Al_xGa_{1-x}As_ySb_{1-y}$ ($y \approx 0.50$), used in the linear step grades between $GaAs_{0.49}Sb_{0.51}$ and $AlAs_{0.44}Sb_{0.56}$, was grown as a digital alloy of $AlAs_{0.44}Sb_{0.56}$ and $GaAs_{0.49}Sb_{0.51}$. Tellurium (Te) was used as the n-type dopant because silicon, as a result of its amphoteric nature, incorporates as an acceptor in Sb-based semiconductors [12]. The thickness of the base-emitter grade, between the oxide current confinement layer and base-emitter *pn* junction, is critical with respect to the junction's current-voltage characteristics. The thickness chosen here is a result of previous experiments with standard *pn* junction diodes with oxide current confinement layers [13].

The fabrication of the HBT, with the exception of the oxidation of the $AlAs_{0.56}Sb_{0.44}$ emitter, is similar to most conventional three-tiered mesa RF HBTs. The fabrication process began with the deposition of a 1 μm tall SiO_2 dummy collector by standard photolithography, SiO_2 e-beam evaporation, and lift-off. A SiO_2 dummy collector was used at this stage to facilitate the later fabrication of a Schottky collector, as opposed to a metal collector that would undergo an anneal during the oxidation process, forming an ohmic collector. Following the deposition of the SiO_2 dummy collector, the base mesa was defined using standard photolithography and a phosphoric acid-based etch (H_3PO_4:H_2O_2:H_2O [3:1:50]). The mesa was etched down to the $GaAs_{0.49}Sb_{0.51}$ sub-emitter with the intention of exposing the $AlAs_{0.56}Sb_{0.44}$ emitter for oxidation (Fig. 3a). The $AlAs_{0.56}Sb_{0.44}$ emitter was partial oxidized using a wet, thermal oxidation process by bubbling nitrogen through deionized water at 90 °C into a three-zone furnace held at 350 °C (Fig. 3b), and was oxidized to a depth such that the active emitter area (A_E) was less than the active collector area (A_C). After the $AlAs_{0.56}Sb_{0.44}$ emitter was oxidized to form the oxide current confinement layer, the $In_{0.53}Ga_{0.47}As$ collector mesa was defined using standard photolithography and a selective citric acid-based etch (1 M citric acid:H_2O_2 [1:2]). Ti/Pt/Au (100/50/1000 Å) base and emitter contacts were deposited next by e-beam evaporation. An emitter mesa etch, using the phosphoric acid-based etchant, down to the SI InP electrically isolates the device (Fig. 3c).

A co-planar waveguide (CPW) transmission line structure and microwave probe pads are deposited on the SI InP to facilitate microwave measurements. The wafer is then planarized for subsequent interconnect processing. After gold interconnect posts are deposited by e-beam evaporation, the planarization resist is blanket etched to expose the SiO_2 dummy collector. Following the interconnect lithography, the SiO_2 dummy collector is removed in buffered hydrofluoric acid to expose the collector. Ti/Pt/Au (100/50/10k Å) interconnect metal is deposited by e-beam evaporation, forming a Schottky contact on the collector. The fabrication is completed by opening vias for contacting the CPW lines (Fig. 3d). Fig. 4 shows a photograph of a completed device.

One distinct difference in the design of these HBTs as compared to conventional HBTs is the layout of the base mesa to the uppermost mesa: the collector mesa in these HBTs, the emitter mesa in conventional emitter-up HBTs. In conventional RF HBTs, the overall dimensions of the base mesa are reduced as much as possible in order to reduce the associated base-collector junction area and capacitance. Towards one end of the base, the mesa is commonly extended to accommodate interconnect metallization for connecting to the transmission line (Fig. 5a). In the case of the HBT presented in this paper, the base mesa must be similar is shape and centered on the collector mesa (Fig. 5b). This is because at the time of this work, the only method for controlling the oxidation depth is oxidation time and temperature, which results in the oxidation depth being equidistant from the outer mesa edge. While a design like that used in a conventional HBT is desirable, the oxide confinement layer would not extend underneath the interconnect region, thereby not properly confining emitter current to only within the collector area, ruining the device's current gain characteristics (Fig. 5c). Future work will be oriented toward a self-limiting oxidation process that would allow for more aggressive scaling of the base mesa and overall device.

III. DC MEASUREMENTS

Gummel and common-emitter characteristics for three sizes of HBTs are shown in Fig. 6: a transistor with a 0.5 × 9.5 μm^2 emitter area (A_E) and 1 × 10 μm^2 collector area (A_C), referred to as a 1 × 10 transistor; a transistor with $A_E = 1.5 \times 9.5\ \mu m^2$ and $A_C = 2 \times 10\ \mu m^2$, 2 × 10 transistor; and a transistor with $A_E = 3.5 \times 9.5\ \mu m^2$ and $A_C = 4 \times 10\ \mu m^2$, 4 × 10 transistor. These devices show excellent ideality factors for the base and collector currents ($\eta_B \approx 1.18$, $\eta_C \approx 1$).

The fact that the emitter resistance (R_E), measured by floating-collector measurements, increases linearly with the inverse of A_E indicates that the internal (vertical) resistance ($R_{E,int}$) of the wide bandgap $AlAs_{0.56}Sb_{0.44}$ emitter, which scales with A_E, dominates over the access (lateral) resistance ($R_{E,acc}$) of the highly doped $GaAs_{0.49}Sb_{0.51}$ sub-emitter, which is essentially independent of A_E (Fig. 7). This is not surprising given the poor mobility of electrons in $AlAs_{0.56}Sb_{0.44}$ ($\mu_n \approx 40\ cm^2/Vsec$ at $n = 2 \times 10^{18}\ cm^{-3}$). The relatively high R_E also resulted in an increase in the knee voltage for these devices ($V_{knee} \approx 1$ V at ~80 kA/cm2).

The breakdown of these devices was lower than expected (Fig. 8). The lower breakdown and increase in output conductance, especially at higher current densities, is believed to be due to impact ionization in the depleted collector. Impact ionization in $In_{0.53}Ga_{0.47}As$ can occur at lower electric fields, as compared to other III-V semiconductors, due to a high ionization coefficient (α_n) [14, 15]. Additionally, the increased initial kinetic energy of electrons entering the collector as a result of the conduction band offset between the $GaAs_{0.49}Sb_{0.51}$ base and $In_{0.53}Ga_{0.47}As$ collector ($\Delta E_C \approx 0.31$ eV, Fig. 2), which acts like an electron launcher, reduces the required energy for ionization and, consequently, electric field for impact ionization to occur, leading to increased impact ionization at lower collector-base (and therefore collector-emitter) voltages [16].

Examination of the Gummel plots (Fig. 6) shows a reduction in the common-emitter current gain (β) as A_E decreases. The best device measured ($A_E = 2.5 \times 8.5\ \mu m^2$, $A_C = 4 \times 10\ \mu m^2$) showed a higher current gain of $\beta \approx 80$ (Fig. 9). The increased gain of this transistor and reduced gains of the 2 × 10 and 1 × 10 devices, relative to the 4 × 10 transistor, are attributed to the lateral diffusion of injected electrons directly into the base contacts.

In a device where A_C is on the order of A_E and the base contacts are located within the path of injected carriers, lateral diffusion of injected carriers outside of the collector area can lead to a reduction of gain. Using a simple model for current gain in which injected carriers are assumed to laterally diffuse once injected into the base (solely as a result of concentration gradients) and the collector current (I_C) is composed only of carriers remaining within A_C at the base-collector junction, it can be seen that as the areas of the emitter and collector are reduced, a greater portion of electrons diffuse outside of the collector area leading to a reduction in gain (Fig. 10).

The validity of this model requires that the emitter current density ($J_E = I_E / A_E = (I_B + I_C) / A_E$) be approximately constant with respect to A_E. Fig. 11 shows this to be true.

A. Misaligned HBTs

Unlike conventional HBTs in which A_C is larger than A_E, the HBTs presented in this paper have a collector and emitter areas that are approximately the same size. As a result, the alignment of the emitter and collector strongly affects the transistor's characteristics.

Simply stated, a misaligned emitter-collector results in carriers not being directly injected into the collector but into both the collector and the base contacts. The result is an increase in the base current and decrease in the collector current for the same emitter current, which translates into a decreased current gain. Fig. 12 shows examples of misaligned HBTs' Gummel and common-emitter characteristics compared to an aligned transistor.

IV. RF MEASUREMENTS

Scattering parameter (*S*-parameter) measurements were performed on the HBTs to evaluate the transistors' frequency performance. The maximum measured f_{max} for these devices was 17.76 GHz for a 2×10 HBT biased at $I_C \approx 9$ mA ($J_C \approx 45$ kA/cm^2) and $V_{CE} = 2$ V, the corresponding f_τ was 8.3 GHz (Fig. 13).

The measured values of f_τ and f_{max} (Fig. 14) were much lower than expected. Calculations, using the measured emitter resistance and base resistance and assuming a fully depleted collector, suggests these devices should have an f_τ on the order of 25 GHz and $f_{max} \approx 35$ GHz. These values were calculated using a classical hybrid-π model for a bipolar transistor.

Re-examination of the structure of the HBT suggests that an additional parasitic capacitance in the base-emitter junction exists as a result of the collector-up design (Fig. 15a). A parasitic capacitor/resistor network, similar to a lossy transmission line, would more accurately model the extrinsic portion of the base-emitter junction; but to make the problem of solving for f_τ under the influence of a parasitic capacitance tractable, a single capacitor is used and the resistances outside of the parasitic capacitor are assumed to be negligible due to the high conductivity of the base and sub-emitter.

The resultant hybrid-π model of the HBT, including the parasitic capacitance (C_x), is presented in Fig. 15b. The various elements of the model are defined as follows: R_B, R_E, and R_C are the total resistances (extrinsic and intrinsic) of the base, emitter, and collector, respectively; $g_m = g_{mo} \exp[-j\omega(\tau_B + \tau_C)]$ is the transconductance, where $g_{mo} = \eta kT / qI_C$ is the DC transconductance, ω is the measurement frequency, $\tau_B = W_B^2 / 2D_{min}$ is the base transit time, and $\tau_C = W_C / 2v_{sat}$ is the collector transit time; r_π is related to the dynamic resistance of the base-emitter junction and is equal to β_o / g_{mo}, where β_o is the DC common-emitter current gain; C_{BE} is the base-emitter junction/depletion capacitance and $C_D = g_{mo}(\tau_B + \tau_C)$ is a diffusion capacitance associated with charge transport through the base and collector; C_{BC} is the junction/depletion capacitance of the base-collector junction; and C_x is the parasitic capacitance in the extrinsic portion of the base-emitter junction.

f_τ of this modified model can be found using the Method of Time Constants. Taking only the first order terms, f_τ of the modified model (refered to as $f_{\tau,x}$) is:

$$f_{\tau,x} = \frac{1}{2\pi}\left[\frac{\eta kT}{qI_C}\left(C_{BE}+C_{BC}\right)+\frac{W_B{}^2}{2D_{\min}} + \frac{W_C}{2v_{sat}}+\left(R_E+R_C\right)C_{BC} + \left(\frac{\eta kT}{qI_C}+\frac{R_B}{\beta_o}+R_E\right)C_x\right]^{-1} \tag{3}$$

Recognizing the relative terms, (3) may be rewritten as:

$$f_{\tau,x} = \frac{1}{2\pi}\left[\tau_{std}+\left(\frac{\eta kT}{qI_C}+\frac{R_B}{\beta_o}+R_E\right)C_x\right]^{-1} \tag{4}$$

where:

$$\tau_{std} = \frac{1}{2\pi f_{\tau,std}} \tag{5}$$

and $f_{\tau,std}$ in (5) is as defined in (1).

Maximum available power is achieved when both the input and output of the device is matched to the network. In the case of the modified hybrid-π model (Fig. 15b), this effectively removes C_X from the device, resulting in the f_{max} of the modified model ($f_{max,x}$) being equivalent to f_{max} of the standard model ($f_{max,std}$):

$$f_{max,x} = f_{max,std} = \sqrt{\frac{f_{\tau,std}}{8\pi R_B C_{BC}}} \neq \sqrt{\frac{f_{\tau,x}}{8\pi R_B C_{BC}}} \tag{6}$$

The implications of (4) and (6) are profound. Equation (4) states that the parasitic input capacitor (C_X) enters into f_τ as an additional "charging" time constant, resulting in a reduced f_τ; but (6), which commonly relates f_τ to f_{max} of a transistor, asserts f_{max} is not proportional to the f_τ of the device as presented in (4) but to the f_τ of the device without the parasitic input capacitor as in (1). In other words, C_x has no effect on f_{max} in this model.

By applying (4) to the measured data (assuming C_x is simply the dielectric capacitance of the oxide/$Al_xGa_{1-x}As_ySb_{1-y}$ emitter and realizing that $f_{\tau,std}$ should be independent of device size, given that $A_E \approx A_C$) $f_{\tau,std}$ was determined to be ~26.3 GHz, approximately that calculated using the classical hybrid-π model. The measured f_τ decreases with decreasing A_E due to the influence of the RC_x term in (4), which increases due to an increase in R_E with decreasing A_E (Fig. 16).

Examination of f_τ as a function of collector-emitter voltage (V_{CE}) and collector current (I_C) shows that f_τ is essentially independent of bias at higher I_C, suggesting that f_τ is dominated by the RC_x term (Fig. 17). In contrast, f_{max} increases with increasing V_{CE} suggesting that the collector is not fully depleted, which resulted in an increased C_{BC} and therefore the lower than expected f_{max}.

V. HIGH-FREQUENCY DEVICE MODEL

Proper high-frequency model extraction requires:

1) a well-behaved, stable device from which the model parameters will be extracted;
2) Y-parameters that accurately represent the device.

The HBTs presented in this paper are very stable, showing reproducible results, which involved multiple measurements spanning many weeks. The difficulty in modeling the HBTs are in presenting an accurate representation of the device in terms of Y-parameters.

The DC Y-parameters for the model presented in Fig. 16:

$$\mathbf{Y}\Big|_{\omega\to 0} \approx \begin{bmatrix} \left(r_\pi + R_B + \beta_o R_E\right)^{-1} & 0 \\ \beta_o\left(r_\pi + R_B + \beta_o R_E\right)^{-1} & 0 \end{bmatrix} \tag{7}$$

were derived assuming that the base-collector resistance (r_{BC}) and output resistance (r_o) were infinite, and are therefore not a completely accurate representation of the HBT.

Assuming r_{BC} is not infinite, it can be shown that the DC parameters become:

$$\begin{aligned} Y_{11} &\approx \frac{r_\pi + r_{BC}}{R_B\left(r_\pi + \beta_o R_E\right) + r_{BC}\left(r_\pi + R_B + \beta_o R_E\right)} \\ Y_{12} &\approx \frac{-\left(r_\pi + \beta_o R_E\right)}{R_B\left(r_\pi + \beta_o R_E\right) + r_{BC}\left(r_\pi + R_B + \beta_o R_E\right)} \\ Y_{21} &\approx \frac{\beta_o\left(r_{BC} - R_E\right)}{R_B\left(r_\pi + \beta_o R_E\right) + r_{BC}\left(r_\pi + R_B + \beta_o R_E\right)} \\ Y_{22} &\approx \frac{\beta_o\left(R_B + R_E\right)}{R_B\left(r_\pi + \beta_o R_E\right) + r_{BC}\left(r_\pi + R_B + \beta_o R_E\right)} \end{aligned} \tag{8}$$

Setting $r_{BC} \to \infty$, (8) reduces to (7).

Equation (8), though still not completely correct, is a more accurate representation of the HBT and can be used for an initial estimate of the base-collector resistance, r_{BC}. Together with the measured emitter resistance ($R_E \approx 34\ \Omega$, Fig. 7), base resistance ($R_B \approx 117\ \Omega - R_E = 83\ \Omega$, Fig. 18), current gain ($\beta_o = h_{21}\big|_{\omega\to 0} \approx 12.7$, Fig. 13), transconductance ($g_{mo} = \eta kT / qI_C \approx 350$ mS), an initial estimate for r_{BC} between 4 and 7 kΩ from (8), and an initial estimate for C_{BC} of 40 fF (calculated from the results of (4) and Fig. 16); a model for the 2 × 10 HBT ($I_C \approx 9$ mA, $V_{CE} = 2$ V) was created (Fig. 19).

Comparison of the *S*-parameters, the short-circuit current gain (h_{21}), and the unilateral power gain (U) from an actual device with that from the model show fairly good agreement (Fig. 20 and Fig. 21). In the model presented in Fig. 19, r_{BC} is relatively low as a result of the impact ionization present in the collector. Conversely, r_o has been set equal to infinity to reflect the very low collector-emitter leakage present in the actual device ($r_o \approx 1.33$ MΩ for $I_B = 0$ mA); though $r_o \rightarrow \infty$ is not physically possible, it was found that reducing r_o to as low as 10 kΩ had essentially no effect on the model. Setting $r_o \rightarrow \infty$ merely simplifies the analysis.

Removal of the parasitic base-emitter capacitance, C_x, drastically affected the *S*-parameters of the model (Fig. 22), which translated into a marked increase in f_τ with only a small perturbation of f_{max}, as expected from (4) and (6) (Fig. 23).

VI. CONCLUSIONS

Collector-up HBTs with oxide confined current apertures were developed in the InP material system. Devices showed excellent DC performance with base and collector idealities of ~1.18 and ~1, respectively, and common-emitter current gains (β_o) up to ~50. As a result of the emitter and collector areas begin approximately the same size ($A_E \approx A_C$), alignment of the emitter and collector was shown to be critical, with misalignments of 1 μm resulting in β_o dropping over an order in magnitude.

The maximum measured f_{max} was 17.76 GHz, with an associated $f_\tau \approx 8.3$ GHz ($A_E = 1.5 \times 9.5$ μm^2, $A_C = 2 \times 10$ μm^2 HBT). Though the frequency performance of these devices was shown to be limited by a parasitic base-emitter capacitance inherent to the collector-up HBT design, the validity of the design for RF performance has been shown.

Future work will be oriented toward improving the device's frequency behavior with emphasis on oxidation control, which would allow for aggressive device scaling resulting in reduced parasitics, and improvement of the device/material structure for increased DC and RF performance (e.g., reduced doping in the collector, alternative emitter/collector materials, bandgap grading in the base).

VII. REFERENCES

[1] S. Mohammadi, J.-W. Park, D. Pavlidis, J.-L. Guyauz, and J. C. Garcia, "Design optimization and characterization of high-gain GaInP/GaAs HBT distributed amplifiers for high-bit-rate," *IEEE Transactions on Microwave Theory and Techniques*, vol. 48, pp. 1038-44, 2000.

[2] M. J. W. Rodwell, M. Urteaga, T. Mathew, D. Scott, D. Mensa, Q. Lee, J. Guthrie, Y. Bester, S. C. Martin, R. P. Smith, S. Jaganathan, S. Krishnan, S. I. Long, R. Pullela, B. Agarwal, U. Bhattacharya, L. Samoska, and M. Dahlstrom, "Submircon scaling of HBTs," *IEEE Transactions on Electron Devices*, vol. 48, pp. 2606-24, 2001.

[3] B. Agarwal, Q. Lee, R. Pullela, D. Mensa, J. Guthrie, and M. J. W. Rodwell, "A transferred-substrate HBT wide-band differential amplifier to 50 GHz," *IEEE Microwave and Guided Wave Letters*, vol. 8, pp. 263-5, 1998.

[4] M. Sokolich, A. R. Kramer, Y. K. Boegeman, and R. R. Martinez, "Demonstration of sub-5 ps CML ring oscillator gate delay with reduced parasitic AlInAs/InGaAs HBT," *IEEE Electron Device Letters*, vol. 22, pp. 309-11, 2001.

[5] T. Mathew, H.-J. Kim, D. Scott, S. Jaganathan, S. Krishnan, Y. Wei, M. Urteaga, S. Long, and M. J. W. Rodwell, "75 GHz ECL static frequency divider using InAlAs/InGaAs HBTs," *Electronics Letters*, vol. 37, pp. 667-8, 2001.

[6] T. Mathew, S. Jaganathan, D. Scott, S. Krishnan, Y. Wei, M. Urteaga, M. J. W. Rodwell, and S. Long, "2-bit adder: carry and sum logic circuits at 19 GHz clock frequency in InAlAs/InGaAs HBT technology," *Electronics Letters*, vol. 37, pp. 1156-7, 2001.

[7] K. Kurishima, H. Nakajima, S. Yamahata, T. Kobayashi, and Y. Matsuoka, "Effects of a compositionally-graded $In_xGa_{1-x}As$ base in abrupt-emitter InP/InGaAs heterojunction bipolar transistors," presented at 1994 International Conference on Solid State Devices and Materials, 1995.

[8] Q. M. Zhang, G. L. Tan, J. M. Xu, and D. J. Day, "Current gain and transit-time effects in HBTs with graded emitter and base regions," *IEEE Electron Device Letters*, vol. 11, pp. 508-10, 1990.

[9] Y. Zebda, A. Elnagar, and A. Hussein, "Minimisation of base transit time in AlGaAs/GaAs heterostructure bipolar transistor (HBT)," *IEE Proceedings-Circuits, Devices and Systems*, vol. 144, pp. 375-7, 1997.

[10] K. Dong Myong, "Electrical characteristics of Npn-AlGaAs/GaAs HBTs with modulated base doping structures," *Journal of the Korean Physical Society*, vol. 33, pp. 607-11, 1998.

[11] U. Bhattacharya, "Transferred Substrate Heterojunction Bipolar Transistors," in *Electrical and Computer Engineering*. Santa Barbara: University of California, 1996, pp. 135.

[12] B. R. Bennett, W. J. Moore, M. J. Yang, and B. V. Shanabrook, "Transport properties of Be- and Si-doped AlSb," *Journal of Applied Physics*, vol. 87, pp. 7876-9, 2000.

[13] J. G. Champlain, Y. K. Seck, and U. K. Mishra, "Base-emitter Junction Design for Collector-up

Heterojunction Bipolar Transistors with Oxide Current Apertures," *Journal of Applied Physics*, 2002.

[14] K. Yang, J. C. Cowles, J. R. East, and G. I. Haddad, "Theoretical and experimental DC characterization of InGaAs-based abrupt emitter HBTs," *IEEE Transactions on Electron Devices*, vol. 42, pp. 1047-58, 1995.

[15] C. Canali, C. Forzan, L. Neviani, L. Vendrame, E. Zanoni, R. A. Hamm, R. J. Malik, F. Capasso, and S. Chandrasekhar, "Measurement of the electron ionization coefficient at low electric fields in InGaAs-based heterojunction bipolar transistors," *Applied Physics Letters*, vol. 66, pp. 1095-7, 1995.

[16] B. Jalali, Y.-K. Chen, R. N. Nottenburg, D. Sivco, D. A. Humphrey, and A. Y. Cho, "Influence of base thickness on collector breakdown in abrupt AlInAs/InGaAs heterostructure bipolar transistors," *IEEE Electron Device Letters*, vol. 11, pp. 400-2, 1990.

CAPTIONS

Fig. 1. (a) Emitter-up design: high gain, high base-collector capacitance (C_{BC}). (b) Collector-up design: reduced gain, reduced C_{BC}. (c) Collector-up design with oxide current confinement layer: high gain, reduced C_{BC}. The arrows indicate the flow of injected carriers.

Fig. 2. Band diagram of the HBT presented in this paper. The shaded region indicates the location of the $AlAs_{0.56}Sb_{0.44}$ wide bandgap emitter and oxide current confinement layer.

Fig. 3. Process flow for the HBT presented in this paper. (a) Deposition of the SiO_2 dummy collector and etch of the base mesa; (b) oxidation of the $AlAs_{0.56}Sb_{0.44}$ emitter; (c) etch of the collector mesa, deposition of the base/emitter contacts, and etch of the emitter mesa; and (d) deposition of the Schottky collector transmission lines.

Fig. 4. Photo of a completed HBT. The device shown here has a $4 \times 10\ \mu m^2$ collector contact.

Fig. 5. Base mesa designs for (a) a conventional emitter-up RF HBT and (b) the HBT presented in this paper. (c) A collector-up HBT with a conventional HBT base mesa using an oxide current confinement layer, a direct leakage path between the emitter and base contact would exist underneath the base interconnect.

Fig. 6. Gummel and common-emitter characteristic plots of (a) a 1 × 10 HBT ($I_B = 0 \sim 1.5$ mA at 150 μA steps), (b) a 2 × 10 HBT ($I_B = 0 \sim 1.25$ mA at 125 μA steps), and (c) a 4 × 10 HBT ($I_B = 0 \sim 0.5$ mA at 50 μA steps).

Fig. 7. Emitter resistance (R_E), determined from floating-collector measurements, versus inverse emitter area ($1/A_E$). The linear dependence of R_E on $1/A_E$ indicates that the internal (vertical) resistance ($R_{E,int}$) of the $AlAs_{0.56}Sb_{0.44}$ emitter dominates over the access (lateral) resistance ($R_{E,acc}$) of the $GaAs_{0.49}Sb_{0.51}$ sub-emitter.

Fig. 8. Common-emitter characteristics of a 4 × 10 HBT ($I_B = 0 \sim 0.6$ mA at 100 μA steps) showing breakdown at low biases for the higher collector current densities (J_C).

Fig. 9. Gummel and common-emitter characteristic plots of a $A_E = 2.5 \times 8.5\ \mu m^2$, $A_C = 4 \times 10\ \mu m^2$ HBT ($I_B = 0 \sim 0.2$ mA at 20 μA steps).

Fig. 10. Measured (solid) and modeled (hollow) current gain (β) versus collector area (A_C).

Fig. 11. Emitter current density (J_E) for HBTs with different emitter areas (A_E). J_E is essentially independent of A_E as a function of base-emitter voltage (V_{BE}).

Fig. 12. Gummel and common-emitter characteristic plots for misaligned HBTs ($A_E = 3.5 \times 9.5\ \mu m^2$, $A_C = 4 \times 10\ \mu m^2$) with (a) 0 μm misalignment between emitter-base and base-collector junctions, (b) a 1 μm misalignment, and (c) a 2 μm misalignment. For all the characteristics $I_B = 0 \sim 0.5$ mA at 50 μA steps. The $I_B = 50$ μA curve from the 0 μm misalignment HBT common-emitter characteristic (dashed curve) is included for comparison.

Fig. 13. Short-circuit current gain (h_{21}) and unilateral power gain (U) from S-parameter measurements of a 2 × 10 HBT ($I_C = 9.015$ mA, $V_{CE} = 2.0$ V).

Fig. 14. f_τ and f_{max} as a function of emitter current density (J_E) for a 1 × 10 HBT (V_{CE} = 1.5V), a 2 × 10 HBT (V_{CE} = 1.3 V), and a 4 × 10 HBT (V_{CE} = 1.25 V).

Fig. 15. (a) Illustration of the HBT indicating the location of the parasitic base-emitter capacitance, C_x. (b) The modified hybrid-π model of the HBT that includes the parasitic base-emitter capacitance, C_x.

Fig. 16. f_τ versus emitter area (A_E). f_τ increases as A_E increases due to the reduced effect of the $R_E C_x$ time constant from (4). $f_{\tau,std}$, determined using (4), is approximately 26.3 GHz.

Fig. 17. f_τ and f_{max} versus collector current (I_C) at two collector-emitter biases (V_{CE}) for a 2 × 10 HBT. Note that f_τ saturates to approximately the same value (8.3 GHz) independent of V_{CE}.

Fig. 18. The dynamic resistance (r_d, heavy line) of the base-emitter diode from a 2 × 10 HBT. At higher currents, the r_d is equivalent to the sum of the base and emitter resistances ($R_B + R_E$).

Fig. 19. The hybrid-π model used for the simulation of the HBT presented in this paper.

Fig. 20. Measured S-parameters of a 2 × 10 HBT (dashed lines) and simulated S-parameters of the model presented in Fig. 19 (solid lines). I_C = 9.015 mA, V_{CE} = 2.0 V.

Fig. 21. Measured and simulated short-circuit current gain (h_{21}) and unilateral power gain (U) versus frequency for a 2 × 10 HBT (I_C = 9.015 mA, V_{CE} = 2.0 V).

Fig. 22. Measured S-parameters of a 2 × 10 HBT (dashed lines) and simulated S-parameters of the model presented in Fig. 19 with the parasitic base-emitter capacitance (C_x) removed (solid lines). $I_C = 9.015$ mA, $V_{CE} = 2.0$ V.

Fig. 23. Measured short-circuit current gain (h_{21}) and unilateral power gain (U) versus frequency for a 2 × 10 HBT and simulated h_{21} and U for the model presented in Fig. 19 with the parasitic base-emitter capacitance (C_x) removed ($I_C = 9.015$ mA, $V_{CE} = 2.0$ V).

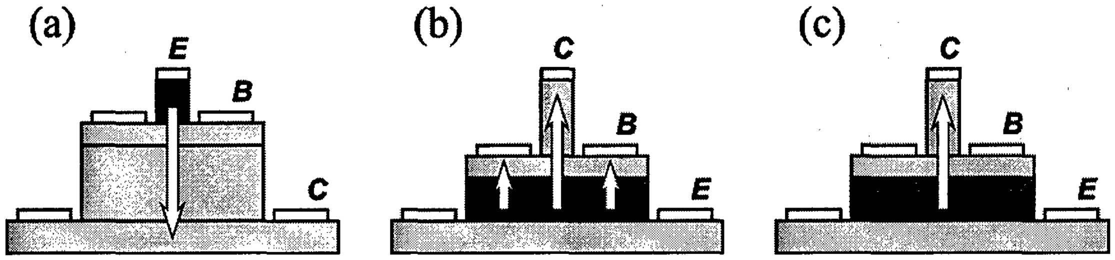
(a)
E
B
C
(b)
C
B
E
(c)
C
B
E

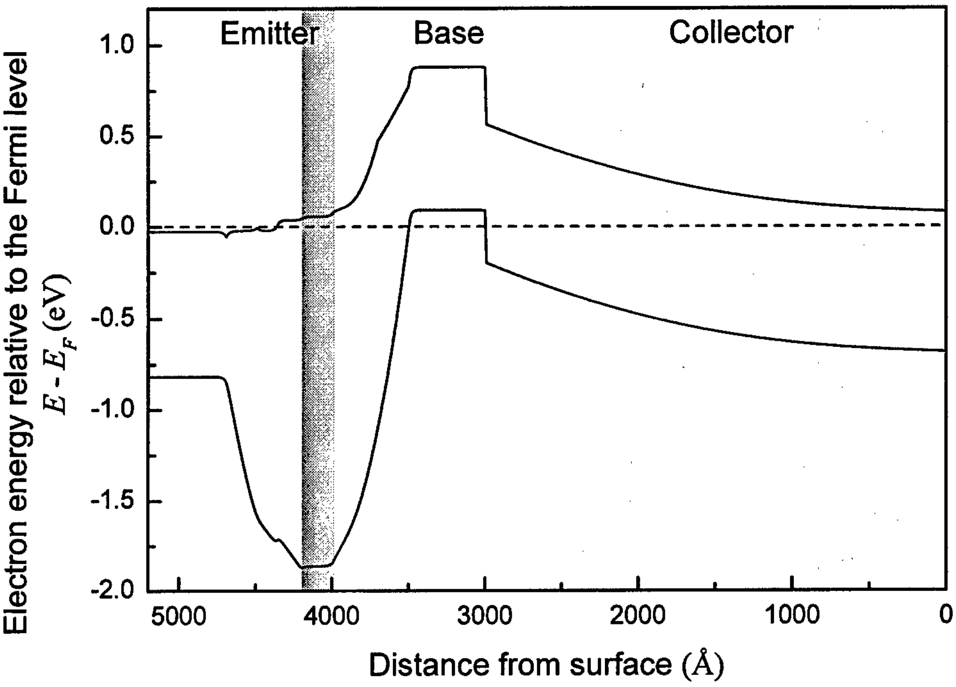
Emitter
Base
Collector
1.0
0.5
0.0
-0.5
-1.0
-1.5
-2.0
Electron energy relative to the Fermi level
$E - E_F$ (eV)
5000
4000
3000
2000
1000
0
Distance from surface (Å)

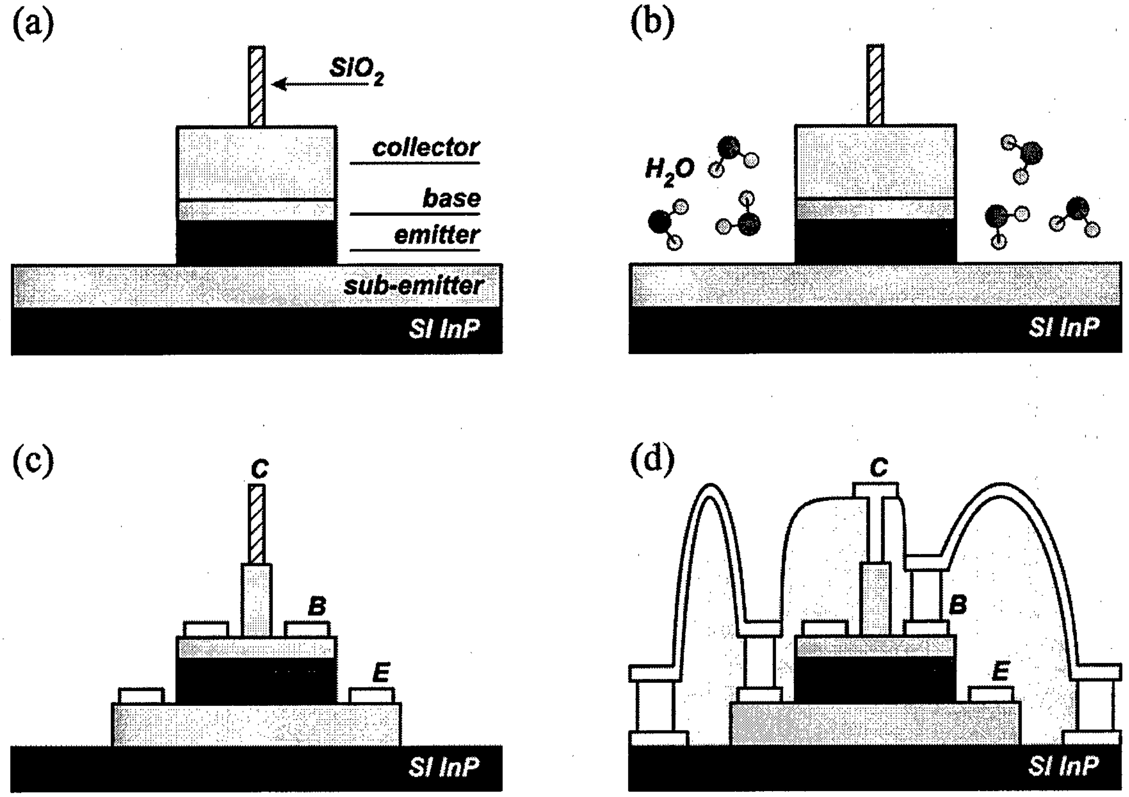
(a)
SiO2
collector
base
emitter
sub-emitter
SI InP
(b)
H2O
SI InP
(c)
C
B
E
SI InP
(d)
C
B
E
SI InP

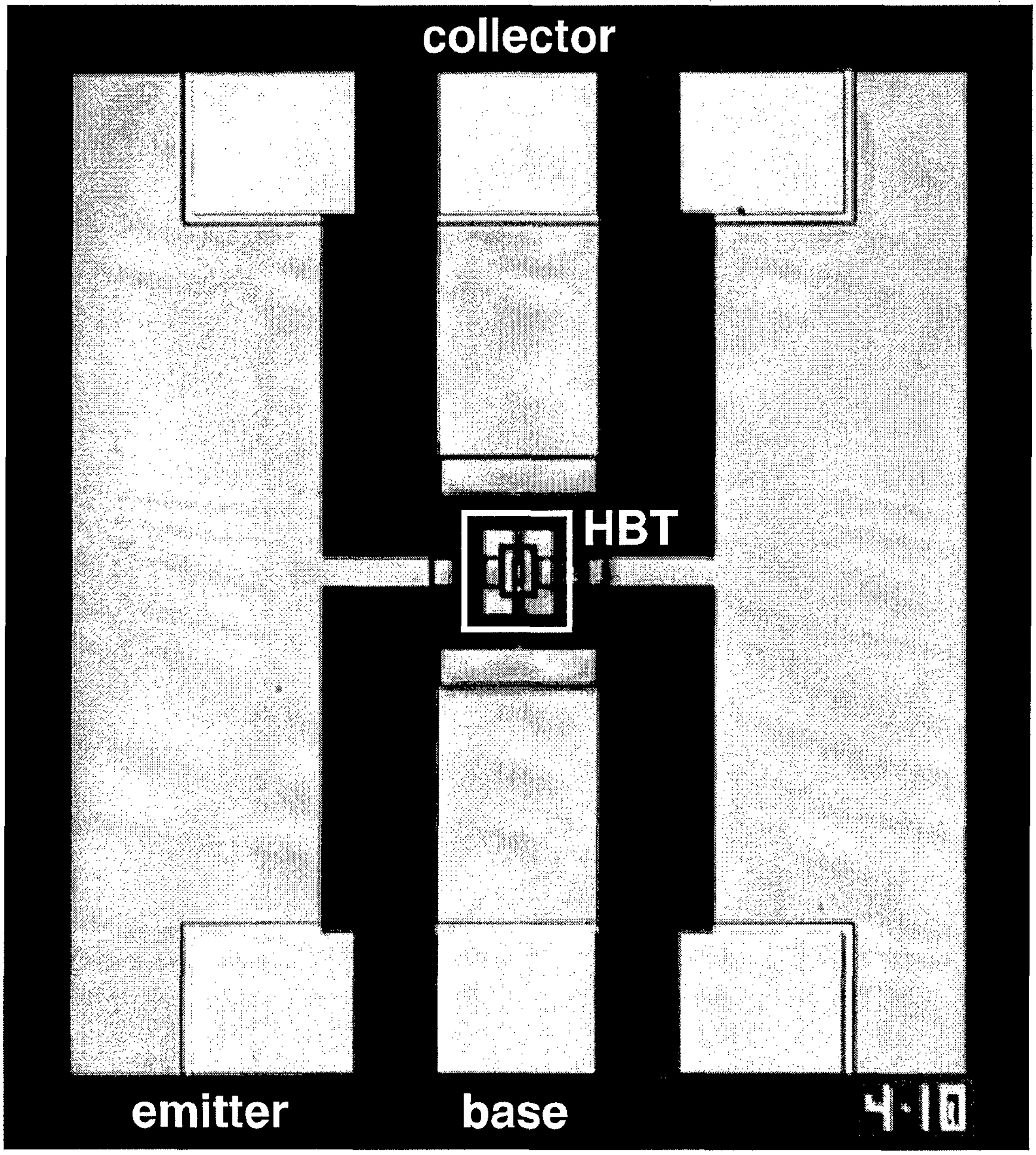
collector
HBT
emitter
base
4·10

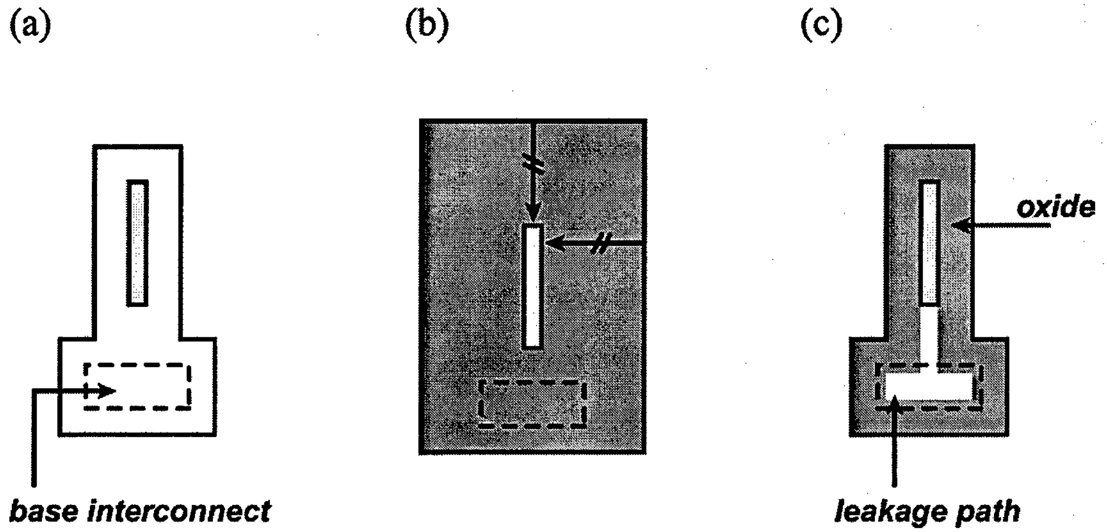
(a)
(b)
(c)
oxide
base interconnect
leakage path

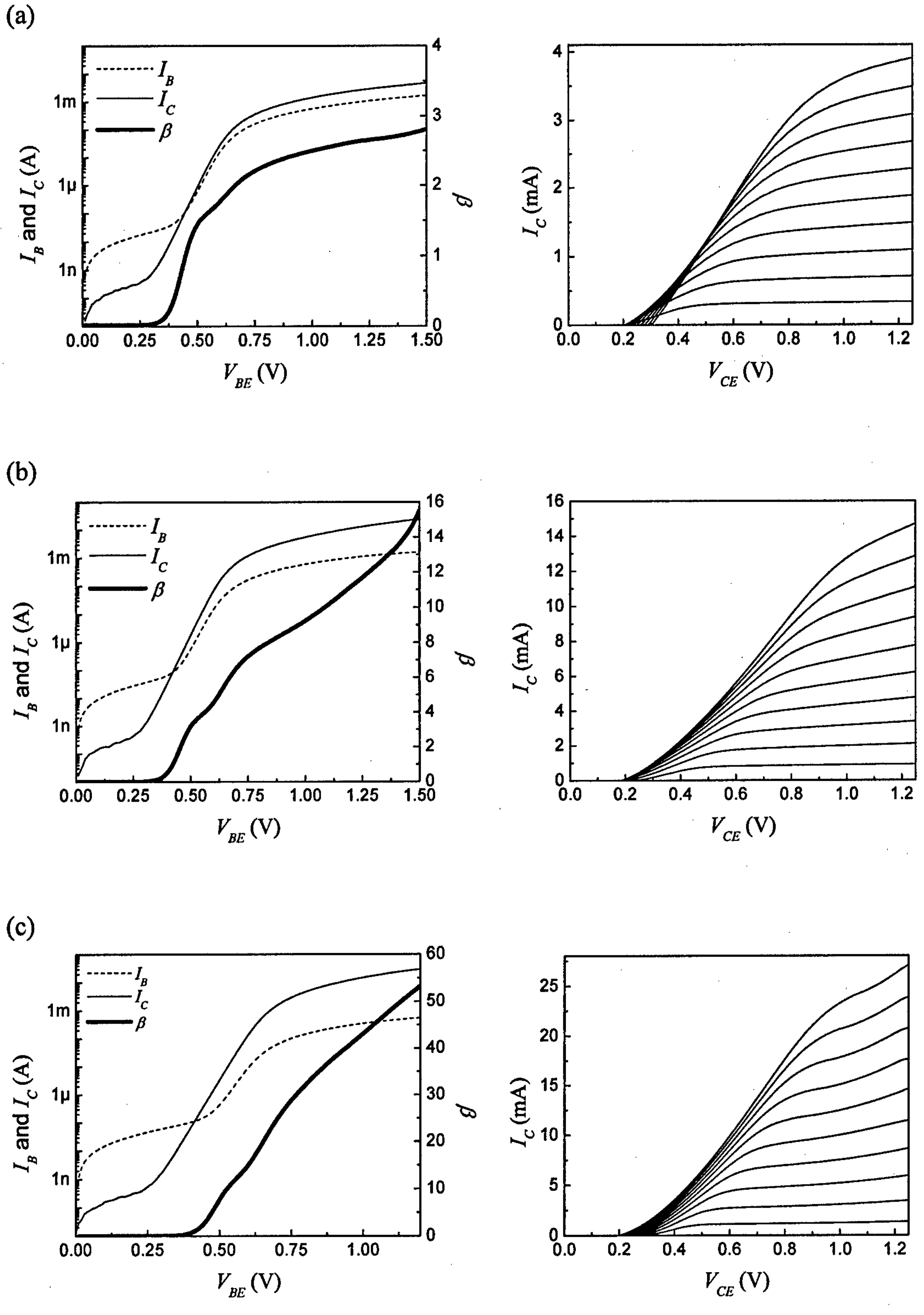
(a)
I_B
I_C
β
I_B and I_C (A)
1m
1μ
1n
β
0
1
2
3
4
0.00
0.25
0.50
0.75
1.00
1.25
1.50
V_{BE} (V)
I_C (mA)
0
1
2
3
4
0.0
0.2
0.4
0.6
0.8
1.0
1.2
V_{CE} (V)
(b)
I_B
I_C
β
I_B and I_C (A)
1m
1μ
1n
β
0
2
4
6
8
10
12
14
16
0.00
0.25
0.50
0.75
1.00
1.25
1.50
V_{BE} (V)
I_C (mA)
0
2
4
6
8
10
12
14
16
0.0
0.2
0.4
0.6
0.8
1.0
1.2
V_{CE} (V)
(c)
I_B
I_C
β
I_B and I_C (A)
1m
1μ
1n
β
0
10
20
30
40
50
60
0.00
0.25
0.50
0.75
1.00
V_{BE} (V)
I_C (mA)
0
5
10
15
20
25
0.0
0.2
0.4
0.6
0.8
1.0
1.2
V_{CE} (V)

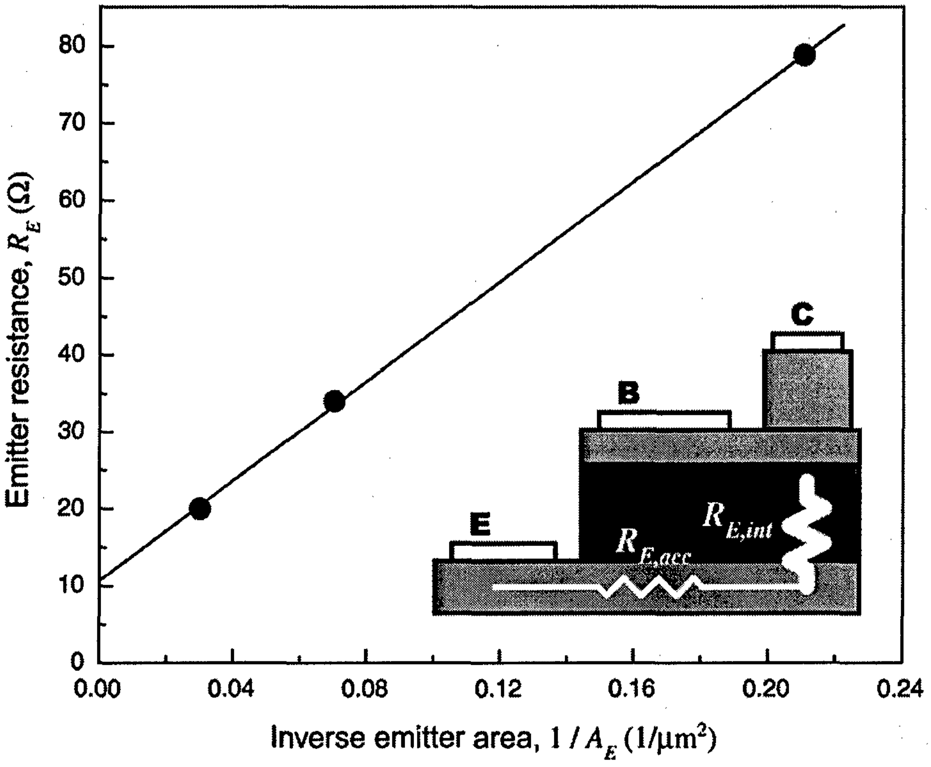
Emitter resistance, R_E (Ω)
0
10
20
30
40
50
60
70
80
0.00
0.04
0.08
0.12
0.16
0.20
0.24
Inverse emitter area, $1 / A_E$ ($1/\mu m^2$)
C
B
E
$R_{E,int}$
$R_{E,acc}$

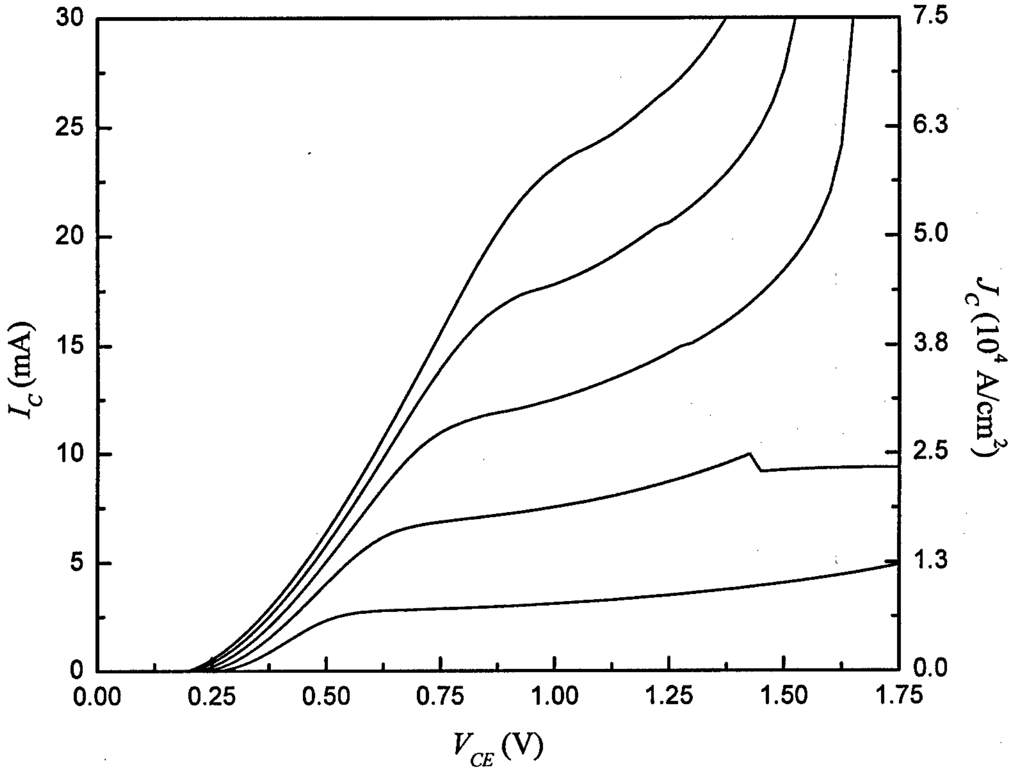
30
25
20
15
10
5
0
I_C (mA)
7.5
6.3
5.0
3.8
2.5
1.3
0.0
J_C (10^4 A/cm^2)
0.00
0.25
0.50
0.75
1.00
1.25
1.50
1.75
V_{CE} (V)

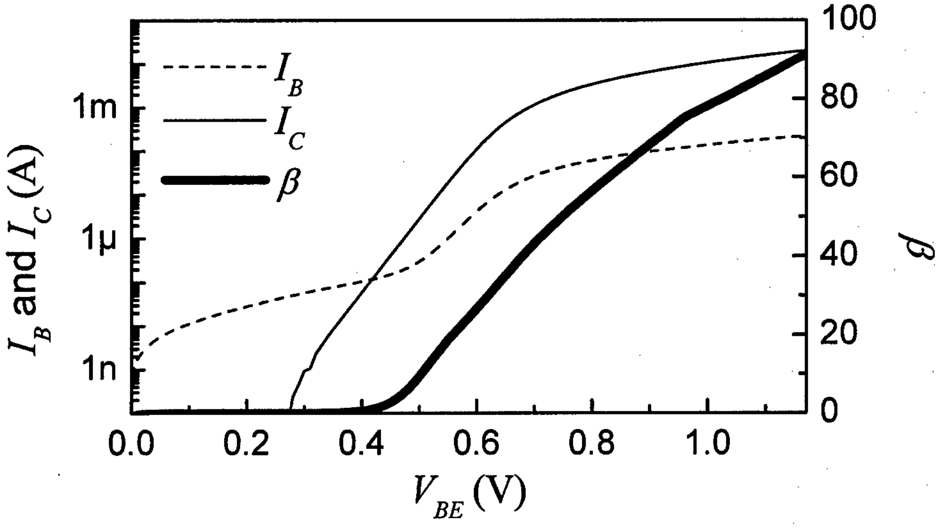

I_B
I_C
β
1m
1μ
1n
I_B and I_C (A)
100
80
60
40
20
0
β
0.0
0.2
0.4
0.6
0.8
1.0
V_{BE} (V)

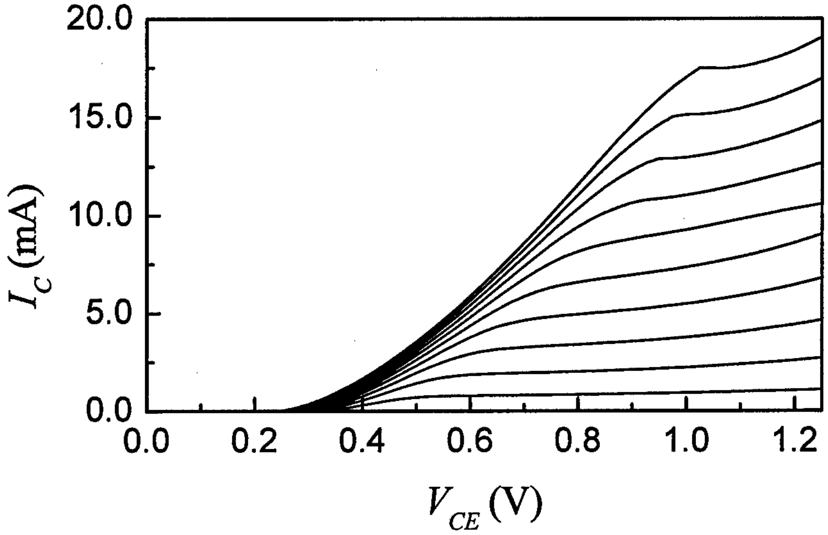

20.0
15.0
10.0
5.0
0.0
I_C (mA)
0.0
0.2
0.4
0.6
0.8
1.0
1.2
V_{CE} (V)

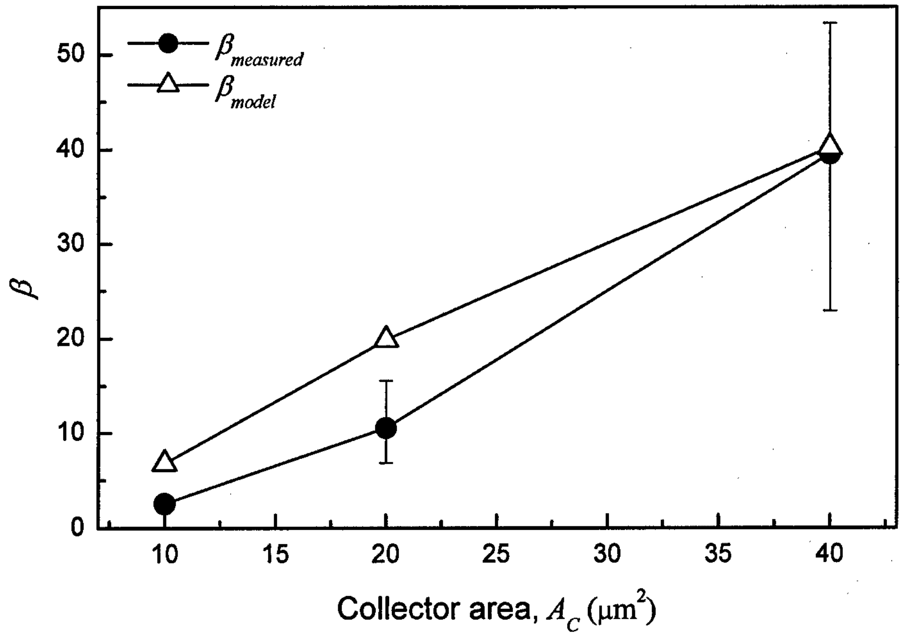
$\beta_{measured}$
β_{model}
0
10
20
30
40
50
β
10
15
20
25
30
35
40
Collector area, A_C (μm^2)

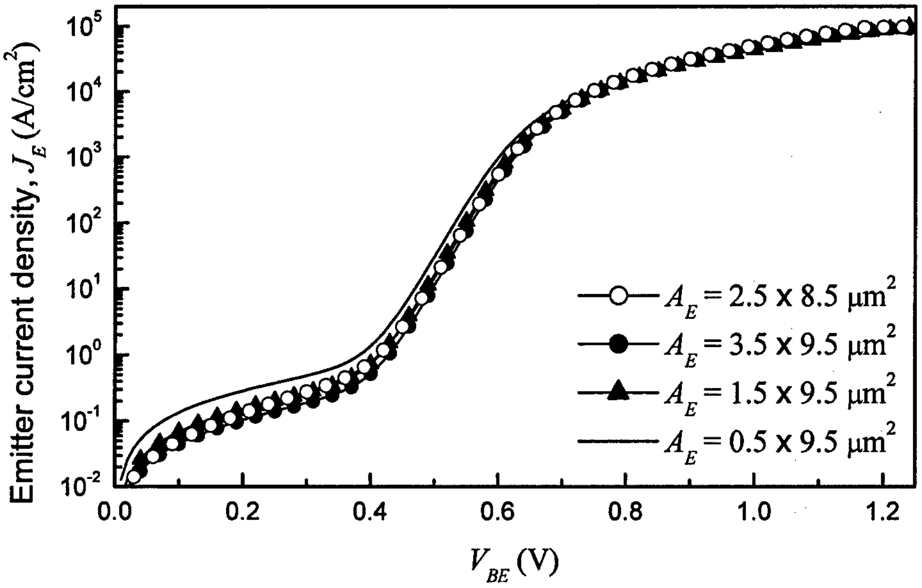
Emitter current density, J_E (A/cm^2)
10^5
10^4
10^3
10^2
10^1
10^0
10^{-1}
10^{-2}
0.0
0.2
0.4
0.6
0.8
1.0
1.2
V_{BE} (V)
$A_E = 2.5 \times 8.5\ \mu m^2$
$A_E = 3.5 \times 9.5\ \mu m^2$
$A_E = 1.5 \times 9.5\ \mu m^2$
$A_E = 0.5 \times 9.5\ \mu m^2$

(a)

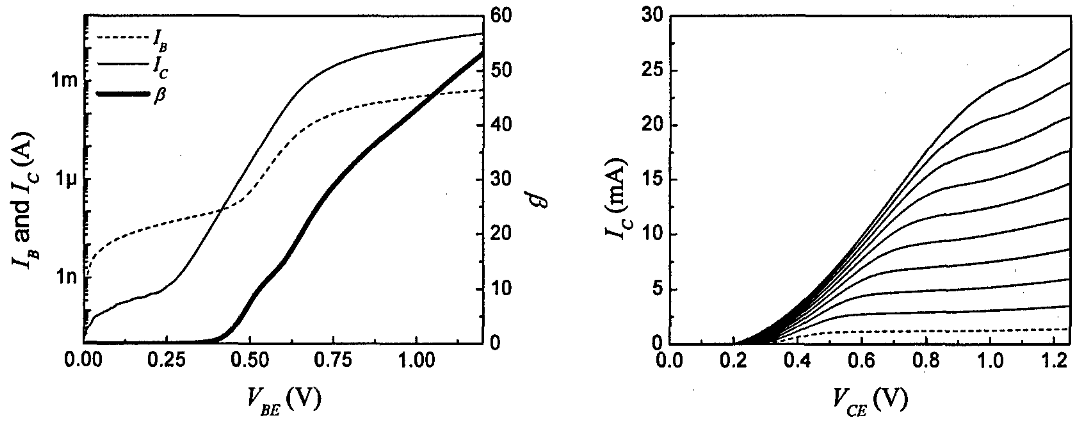
I_B
I_C
β
1m
1µ
1n
I_B and I_C (A)
0.00
0.25
0.50
0.75
1.00
V_{BE} (V)
60
50
40
30
20
10
0
β
30
25
20
15
10
5
0
I_C (mA)
0.0
0.2
0.4
0.6
0.8
1.0
1.2
V_{CE} (V)

(b)

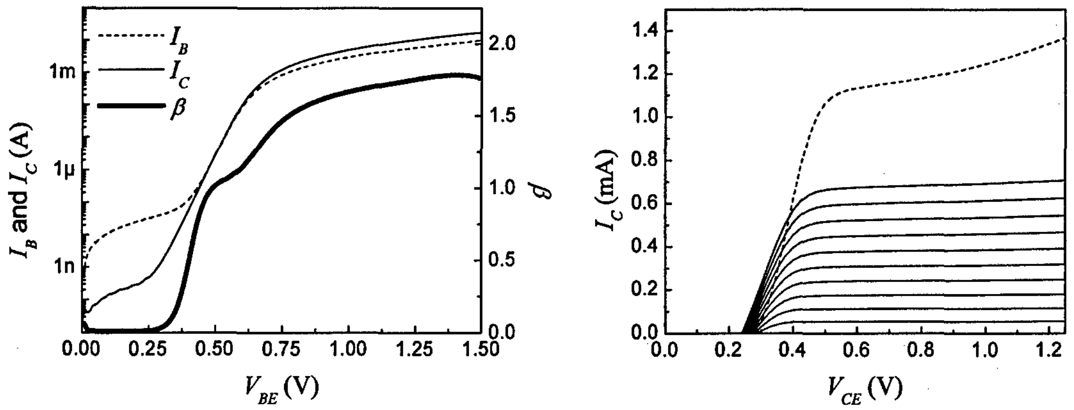
I_B
I_C
β
1m
1µ
1n
I_B and I_C (A)
0.00
0.25
0.50
0.75
1.00
1.25
1.50
V_{BE} (V)
2.0
1.5
1.0
0.5
0.0
β
1.4
1.2
1.0
0.8
0.6
0.4
0.2
0.0
I_C (mA)
0.0
0.2
0.4
0.6
0.8
1.0
1.2
V_{CE} (V)

(c)

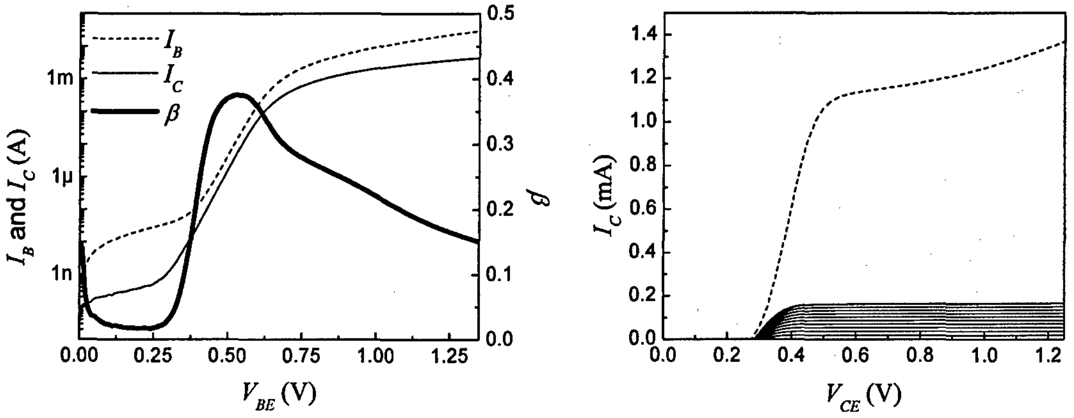
I_B
I_C
β
1m
1µ
1n
I_B and I_C (A)
0.00
0.25
0.50
0.75
1.00
1.25
V_{BE} (V)
0.5
0.4
0.3
0.2
0.1
0.0
β
1.4
1.2
1.0
0.8
0.6
0.4
0.2
0.0
I_C (mA)
0.0
0.2
0.4
0.6
0.8
1.0
1.2
V_{CE} (V)

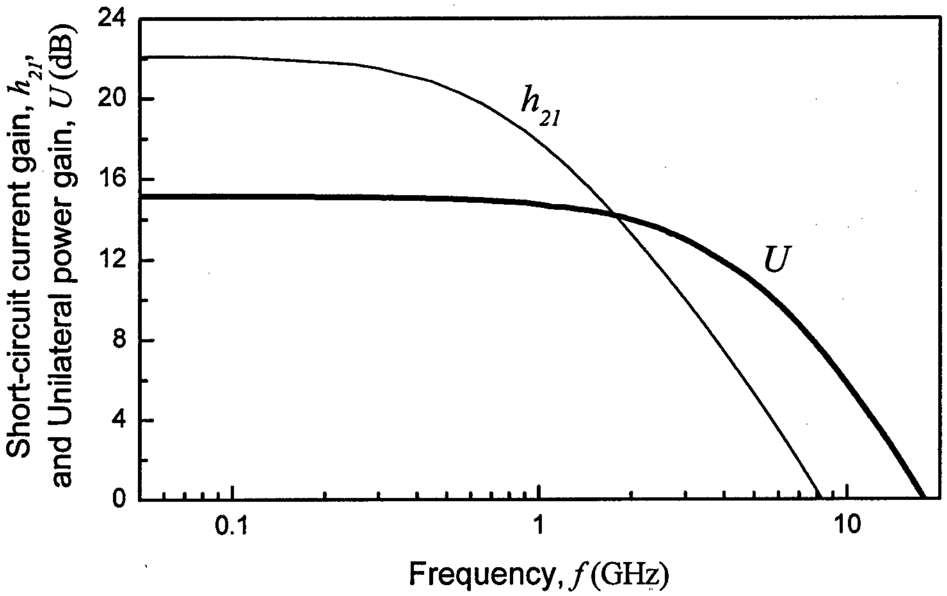

Short-circuit current gain, h_{21},
and Unilateral power gain, U (dB)
24
20
16
12
8
4
0
h_{21}
U
0.1
1
10
Frequency, f (GHz)

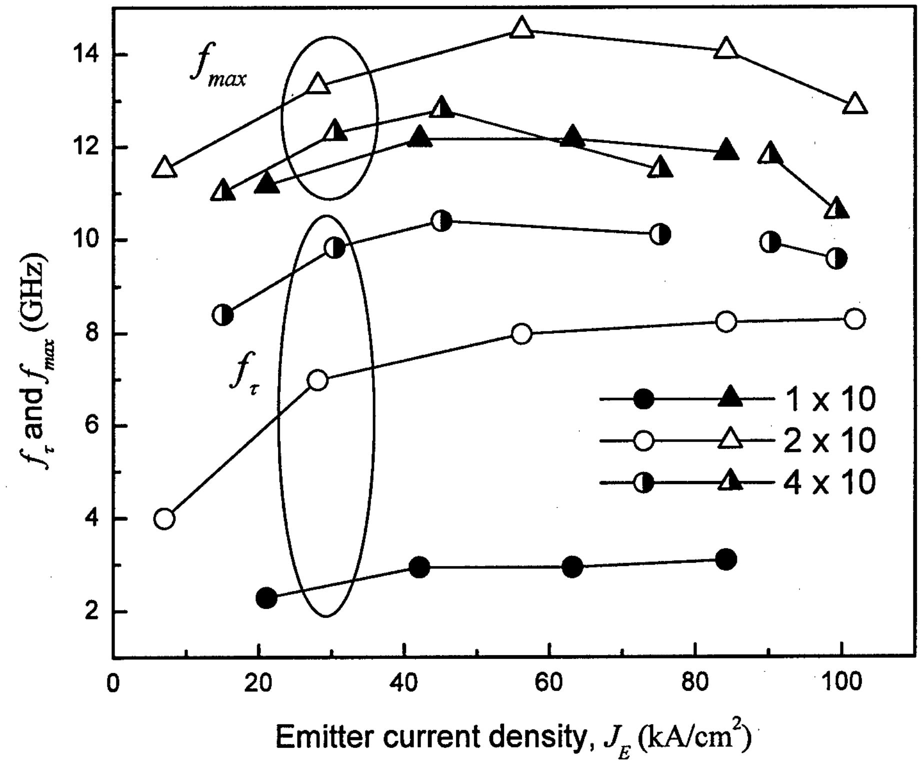
f_{max}
f_τ
1 x 10
2 x 10
4 x 10
14
12
10
8
6
4
2
0
20
40
60
80
100
f_τ and f_{max} (GHz)
Emitter current density, J_E (kA/cm^2)

(a)

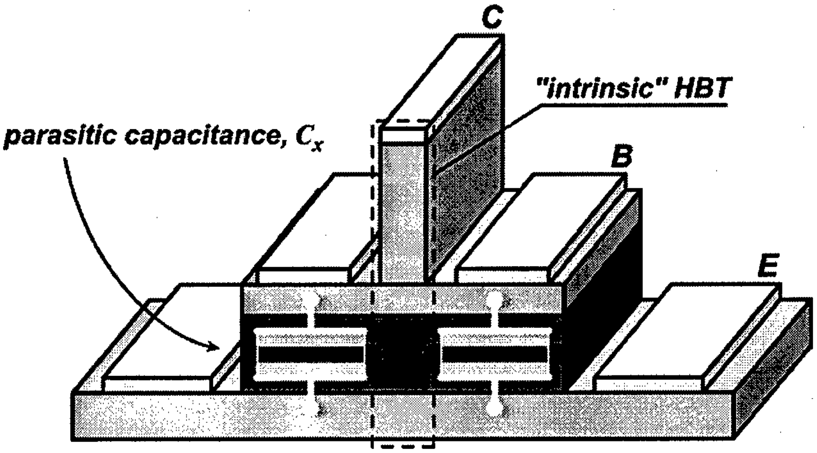
C
"intrinsic" HBT
parasitic capacitance, C_x
B
E

(b)

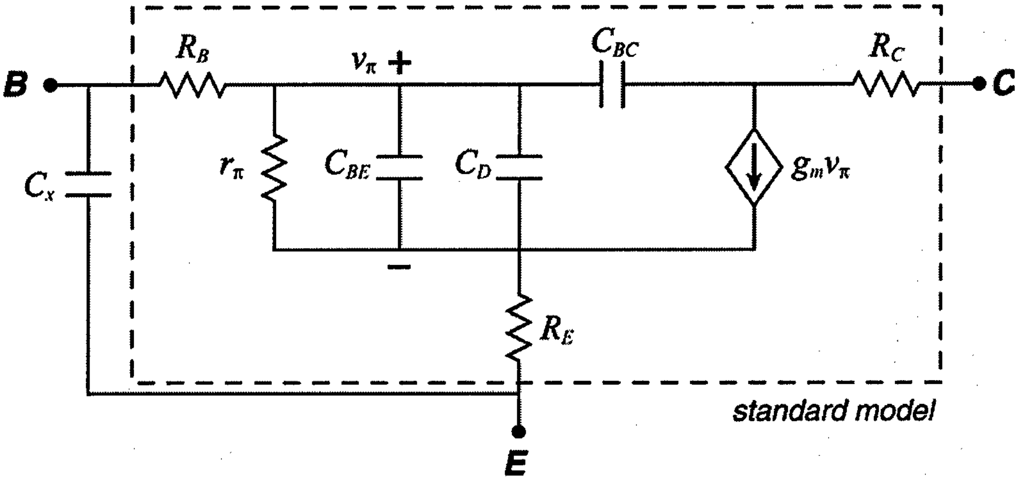
B
R_B
v_π +
C_{BC}
R_C
C
C_x
r_π
C_{BE}
C_D
$g_m v_\pi$
−
R_E
standard model
E

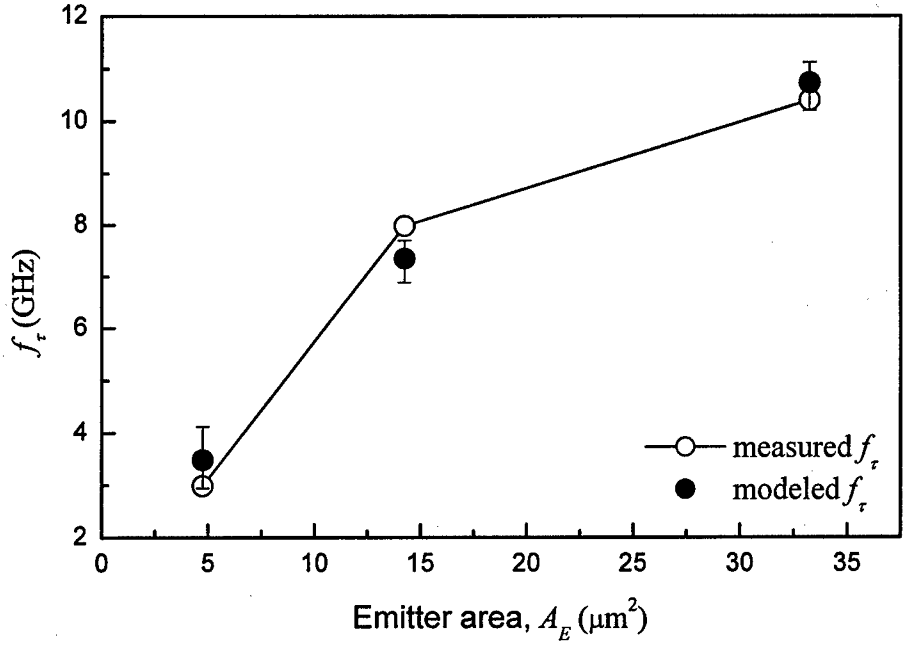
12
10
8
6
4
2
0
5
10
15
20
25
30
35
f_τ (GHz)
Emitter area, A_E (μm^2)
measured f_τ
modeled f_τ

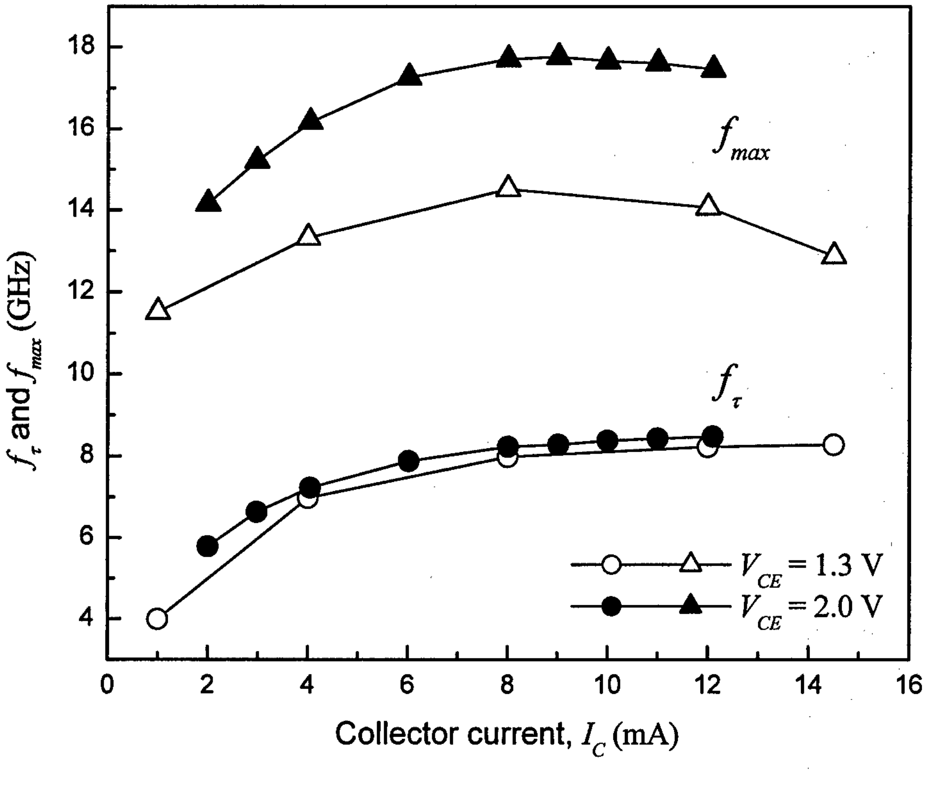
f_τ and f_{max} (GHz)
18
16
14
12
10
8
6
4
0
2
4
6
8
10
12
14
16
Collector current, I_C (mA)
f_{max}
f_τ
V_{CE} = 1.3 V
V_{CE} = 2.0 V

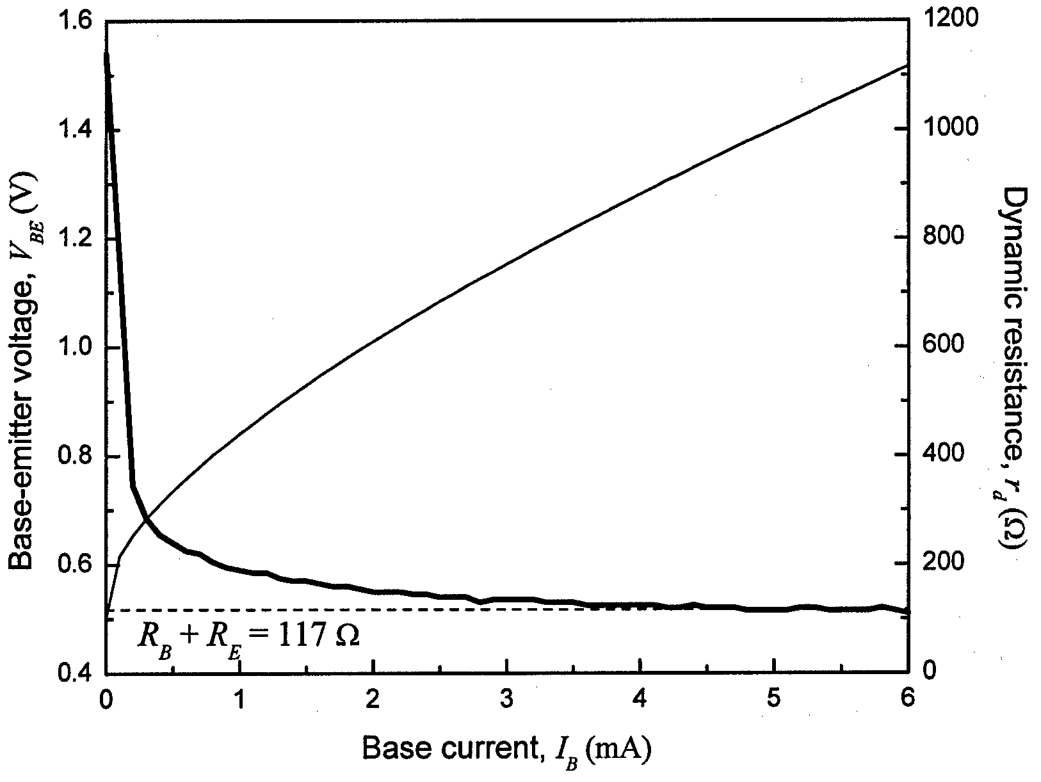
1.6
1.4
1.2
1.0
0.8
0.6
0.4
Base-emitter voltage, V_{BE} (V)
1200
1000
800
600
400
200
0
Dynamic resistance, r_d (Ω)
0
1
2
3
4
5
6
Base current, I_B (mA)
$R_B + R_E = 117\ \Omega$

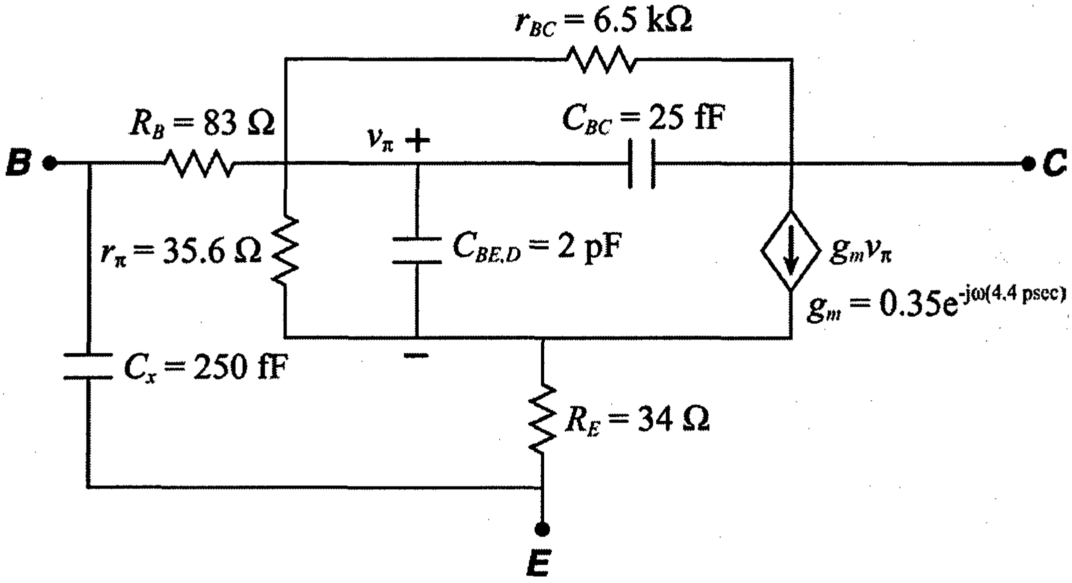
$r_{BC} = 6.5\ k\Omega$
$R_B = 83\ \Omega$
$C_{BC} = 25\ fF$
B
v_π +
C
$r_\pi = 35.6\ \Omega$
$C_{BE,D} = 2\ pF$
$g_m v_\pi$
$g_m = 0.35e^{-j\omega(4.4\ psec)}$
−
$C_x = 250\ fF$
$R_E = 34\ \Omega$
E

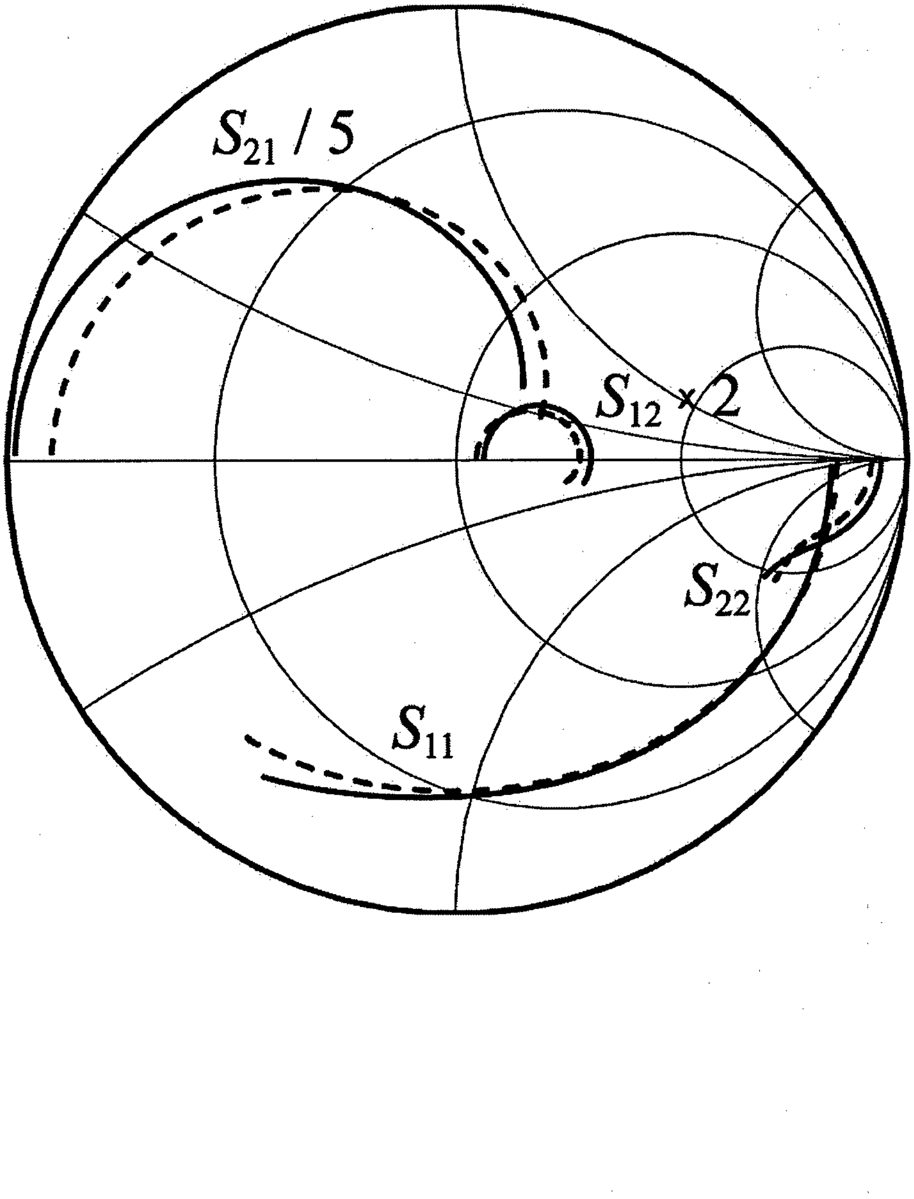
$S_{21}/5$
$S_{12}\times 2$
S_{22}
S_{11}

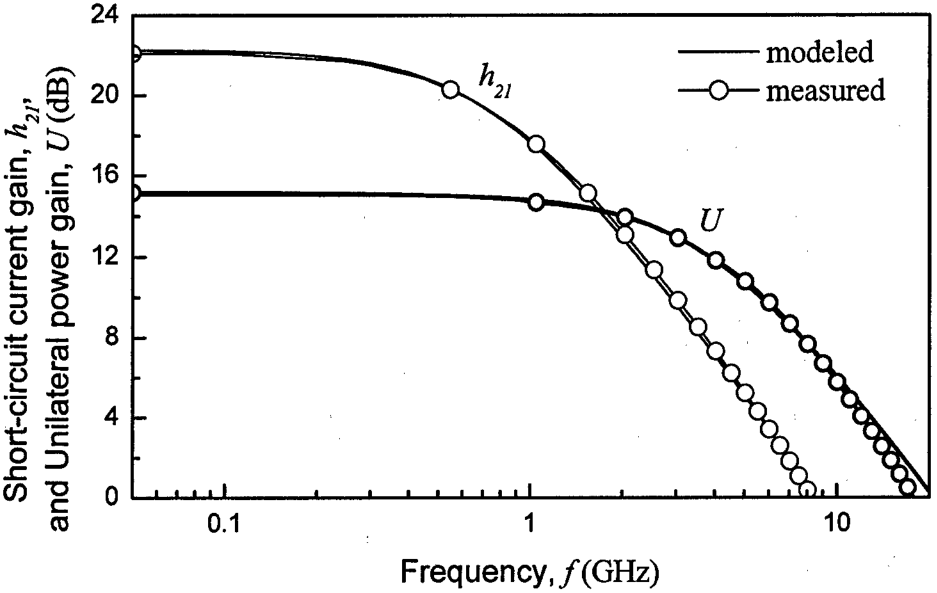
24
20
16
12
8
4
0
0.1
1
10
Frequency, f (GHz)
Short-circuit current gain, h21,
and Unilateral power gain, U (dB)
h21
U
modeled
measured

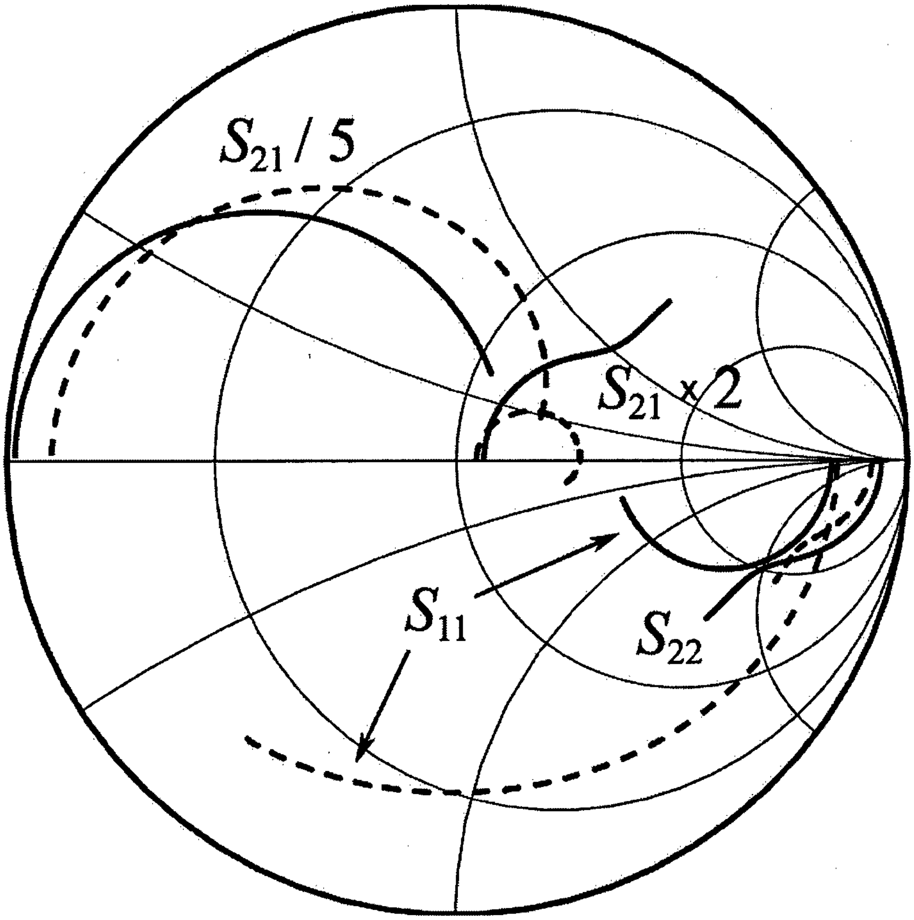
$S_{21}/5$
$S_{21} \times 2$
S_{11}
S_{22}

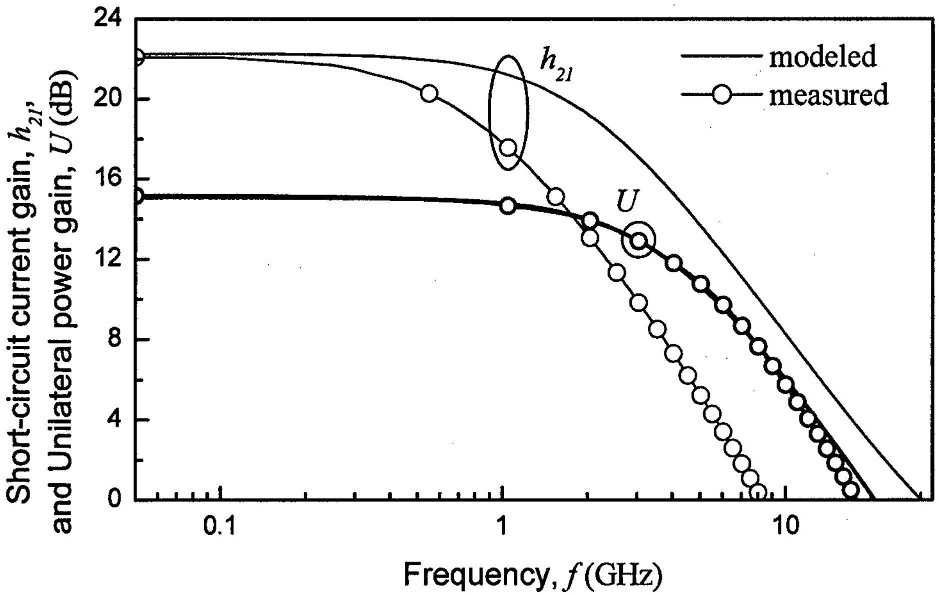

24
20
16
12
8
4
0
0.1
1
10
Frequency, f (GHz)
Short-circuit current gain, h_{21},
and Unilateral power gain, U (dB)
h_{21}
U
modeled
measured

Appendix VI

Antimony segregation in the oxidation of AlAsSb interlayers

A. M Andrews, K. L. van Horn, T. Mates, and J. S. Speck[a]
Materials Department, University of California, Santa Barbara, California 93106

(Received 13 February 2003; accepted 4 August 2003; published 2 October 2003)

The lateral wet oxidation of strained AlAsSb was studied. $AlAs_{0.80}Sb_{0.20}$ interlayers were grown on a GaAs substrate and capped with a lattice-matched $In_{0.25}Ga_{0.75}As$ layer. The AlAsSb was oxidized between 350 and 450 °C. Oxidation temperatures >400 °C resulted in poor surface morphology and delamination. Oxidation of thicker AlAsSb interlayers ($h \approx 2000$ Å) resulted in metallic Sb layers forming between the AlO_x and the semiconductor interfaces. The remaining Sb metal at the oxide–semiconductor interface was ~15% oxidized. Lateral wet oxidation of thinner AlAsSb interlayers ($h \leq 500$ Å) resulted in Sb inclusions at the oxide–semiconductor interface. The Sb inclusions were 1.5–2.0 μm in diameter and the inclusion thickness was approximately equal to the AlAsSb layer thickness. Methanol (CH_3OH) was added to the water mixture with the intent to stabilize the otherwise unstable stibine (SbH_3) such that Sb could be removed from the oxidizing structure. However, methanol addition resulted in a decreased oxidation rate and a change in the Sb precipitate morphology. The Sb inclusions observed in pure water oxidation changed to a Sb finger-like morphology with increasing methanol concentration. The Sb fingers were 1.0–2.0 μm wide and as long as the oxidation depth. Oxidation of AlAsSb interlayers $h \leq 200$ Å were limited by the incorporation of Ga from the substrate and capping layer into the oxidation layer. Doping the oxidation AlAsSb interlayer 1×10^{18} cm^{-3} *n* type (Si or Te) did not result in any improvement in Sb segregation. © *2003 American Vacuum Society.* [DOI: 10.1116/1.1613954]

I. INTRODUCTION

Dallesasse *et al.* first discovered the lateral wet oxidation of III–V interlayers when they noted the anisotropy in the oxidation of $Al_xGa_{1-x}As$–AlAs–GaAs superlattices.[1] Mesa structures were produced by etching, exposing buried Al-rich III–V layers and the structure was oxidized at temperatures in the range of 300–500 °C in a H_2O–N_2 gas environment. Today the lateral oxidation of III–V interlayers is of crucial importance to the fabrication of high-efficiency devices on III–V substrates. Lateral oxidation has proved essential in high-efficiency vertical-cavity surface emitting lasers (VCSELs).[2,3] A combined optical and electrical aperture is created by partially oxidizing the epilayer, which reduces scattering losses from the pillar edges and improves lasing efficiency. Although lateral oxidation is of greatest importance to the VCSEL community, the oxidation of the underlying material below transistors enables oxide gate insulators and device isolation in III–V electronic devices.[4–7]

For lateral oxidation structures on GaAs substrates, the oxidation reaction in the AlAs interlayers is limited by the removal of the oxidation byproduct AsH_3.[8] The porous oxide provides a route for the diffusion of the reactants and byproducts. The formation of atomic hydrogen and the formation of AsH_3 limit the oxidation rate and the final oxide composition. The oxidation rate of AlAs shows a strong dependence on the layer thickness when $h \leq 500$ Å, where the thinner structures oxidize more slowly.[9] Linear oxidation rates are observed in thicker films between 400 and 500 °C, where the oxidation is reactant limited.

The transition to larger lattice parameter substrates requires a different oxidation interlayer in order to be lattice matched to the substrate. The available III–V oxide precursors between the lattice parameters of the GaAs (5.654 Å), InP (5.869 Å), InAs (6.058 Å), and GaSb (6.095 Å) substrates are variations of AlAs and alloys with Ga and In on the group III site and Sb on the group V site. During oxidation, the addition of only a few percent of Ga or In to the oxidation layer reduced the oxidation rate while the addition of Sb increases the oxidation rate.[10–15] The decreased oxidation rate in the Ga or In containing compounds requires an increase in oxidation temperature or time that is usually unacceptable for device processing.[13–15] Using the acceptable processing temperatures for InP, that leaves only one practical choice for an oxidation interlayer, $AlAs_{1-x}Sb_x$. The $AlAs_{1-x}Sb_x$ alloys oxidize between 300 and 450 °C, depending on alloy composition but result in an undesired byproduct of metallic Sb.[11] An AlAs interlayer shrinks ~20% after oxidation, but in the case of $AlAs_{1-x}Sb_x$, there is an overall swelling of the interlayer due to Sb segregation.[12] The oxidation of $AlAs_{1-x}Sb_x$ alloys result in Sb segregation to one of the oxide–semiconductor interfaces. Most reported experiments involved $AlAs_{1-x}Sb_x$ alloys lattice matched to InP substrates. In some cases, the Sb layer was reported to be at the upper interface,[12,16] while others reported Sb segregation to the lower interface.[17] Salesse reported that wet oxidation using water:methanol mixtures can suppress or eliminate the Sb segregation layer in *n*-type $AlAs_{0.56}Sb_{0.44}$ lattice matched to InP.[18] The same was not true for *p*-type $AlAs_{0.56}Sb_{0.44}$, while unintentionally doped epilayers were not investigated.

Seo *et al.* reported the first observation of strain relaxation by wet oxidation.[19] A schematic for a generic strain enhanced structure is shown in Fig. 1. The strain relaxation in the

---

[a] Electronic mail: speck@mrl.ucsb.edu

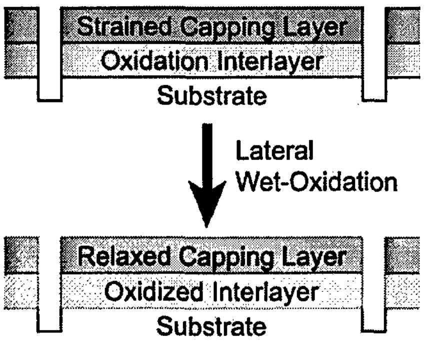

FIG. 1. Schematic of the relaxation enhanced structures before and after lateral wet oxidation. Mesas are produced by etching to expose the oxidation interlayer. The strained capping layer is partially relaxed after the interlayer is wet oxidized.

InGaAs/GaAs superlattice grown on an AlAs oxidation layer was found to increase with increasing indium composition or AlAs thickness. They concluded that a larger residual strain would result in a greater driving force for relaxation. Chavarkar *et al.* showed that the strain relaxation of $\mathrm{In}_x\mathrm{Ga}_{1-x}\mathrm{As}$ layers ($x=0.2$, 0.3, and 0.4) in $\mathrm{In}_x\mathrm{Ga}_{1-x}\mathrm{As}$/AlAs/GaAs structures after oxidation depended greatly on the as-grown relaxation.[20] As the indium composition increased, so did the as-grown relaxation for the $h \approx 20h_c$ films, where h_c is the Matthews–Blakeslee critical thickness.[21] The critical thickness h_c is defined as the film thickness where it first becomes energetically favorable to introduce misfit dislocations at the film-substrate interface to relieve strain energy in the film, and as a result, the film thickness must be greater than h_c for relaxation to occur. The greater initial relaxation resulted in less strain relaxation after oxidation. Mathis *et al.* showed that the relaxation after lateral oxidation was due to the reduction of the misfit dislocation (MD) array line length at the InGaAs/AlAs interface by 2 orders of magnitude.[22] The threading dislocation (TD) density is relatively unchanged after oxidation. The removal of the MD cores reduced the energetic barrier to TD motion and thus relaxation. Films grown beyond the equilibrium critical thickness h_c show an additional strain relief of ~0.5% after lateral oxidation. Mathis also showed that the strain relaxation occurred at the oxidation front and not gradually over the oxidized layer.[22,23] Romanov *et al.* noted that the removal of the MD core correlates to an open core dislocation and the elastic fields are reduced on the order of the open core diameter, thus a more porous oxide would correlate to a lower energetic barrier to TD motion.[24] Therefore, the ideal structure for enhancing film relaxation would be a highly strained as-grown capping layer and the oxidation material and conditions that would form a highly porous oxide.

The goal of this study is to characterize and evaluate $\mathrm{AlAs}_{1-x}\mathrm{Sb}_x$ interlayers as a viable material for lateral wet oxidation interlayers in strained film relaxation and relaxation enhanced templates.

II. EXPERIMENT

Epitaxial $\mathrm{In}_x\mathrm{Ga}_{1-x}\mathrm{As}/\mathrm{AlAs}_{1-x}\mathrm{Sb}_x$ films were grown on GaAs (100) semi-insulating substrates by molecular beam epitaxy with cracked arsenic (As_2) and antimony (Sb_2) sources. For this study, lattice matched "analog alloys" of $\mathrm{In}_{0.25}\mathrm{Ga}_{0.75}\mathrm{As}/\mathrm{AlAs}_{0.80}\mathrm{Sb}_{0.20}$ layers, which correspond to 1.8% lattice mismatch with the underlying GaAs substrate, were deposited at 500 °C. The Matthews–Blakeslee critical thickness for these films was $h_c \approx 50$ Å. The structures studied are in Table I, which are referred to as structures A–I. Each sample had the same lattice matched $\mathrm{In}_{0.25}\mathrm{Ga}_{0.75}\mathrm{As}$ capping layer on an $\mathrm{AlAs}_{0.80}\mathrm{Sb}_{0.20}$ oxidation layer grown on a GaAs substrate. For these growth conditions and alloy compositions, a 250 Å layer ($5h_c$) was completely strained.

On-axis and off-axis high-resolution x-ray diffraction scans were performed on the (004), (115), and ($\bar{1}\bar{1}5$) reflections to determine the layer composition and the extent of strain relaxation. The in-plane and relaxed lattice parameters were calculated from the substrate-layer peak separation using the technique in Ref. 25. The highly relaxed as-grown films were unsuitable for a study of enhanced relaxation from AlAsSb oxidation layers.

TABLE I. Samples used in this study were of the same $\mathrm{In}_{0.25}\mathrm{Ga}_{0.75}\mathrm{As}/\mathrm{AlAs}_{0.80}\mathrm{Sb}_{0.20}$ composition grown at 500 °C on a GaAs substrate but with varying layer thickness and *n*-type doping.

Sample	*h* InGaAs (Å)	*h* AlAsSb (Å)	Doping (cm^{-3})	As grown ~% relaxed	Oxidized ~% relaxed
A	3000	2000	UID[a]	98	98
B	500	500	UID[a]	76	90
C	350	200	UID[a]	30	X[b]
D	300	200	UID[a]	0	X[b]
E	250	200	UID[a]	0	X[b]
F	200	200	UID[a]	0	X[b]
G	200	150	UID[a]	0	X[b]
H	500	500	Si (1×10^{18} cm^{-3})	80	90
I	500	500	Te (1×10^{18} cm^{-3})	80	90

[a] Unintentionally doped structures.

[b] Poor crystal quality in the capping layer for determining the film relaxation.

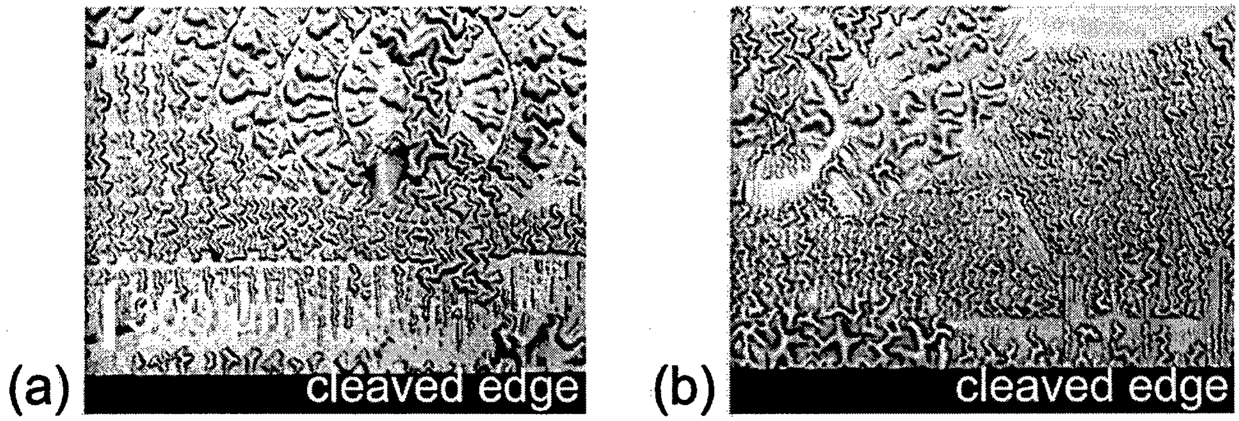

FIG. 2. Optical Nomarski micrographs of an oxidized cleaved edge of sample A at 450 °C. The water:methanol ratio during the wet oxidation was 1:0 in micrograph (a) and 1:3 in micrograph (b). The large variations in surface morphology are attributed to Sb segregation.

Etching 100-μm-square mesas and trenches exposed the oxidation layers. Reactive ion etching (RIE) of the mesas and trenches with Cl_2/Ar produced superior results to a $H_3PO_4:H_2O_2:H_2O$ wet etch. The Sb-containing layer was preferentially removed by the wet etch (>10:1) creating an undercut. The undercut became a stress concentration and resulted in delamination in most oxidation conditions. The RIE produced a less severe undercut and nearly eliminated the delamination.

The samples were wet oxidized in a furnace by bubbling nitrogen through a water:methanol solution at 70 °C. The oxidation was done at furnace temperatures between 350 and 450 °C with water:methanol mixtures of 1:0, 3:1, 1:1, 1:3, and 0:1. The films were characterized both before and after oxidation to evaluate the effects of the water:methanol mixture on the oxidation reactions. Following oxidation, the samples were optically photographed using a Nomarski interference microscope. The technique revealed large surface and subsurface features in the case of the thinner ($h \leq 500$ Å capping layer) samples. The average oxidation rates were determined by the known magnification of the Nomarski photographs.

The films were examined in cross-sectional high-resolution scanning electron microscopy (SEM). With the SEM, the Sb segregation, oxide shrinkage, and overall structure swelling were evident. The cross-sectional SEM samples were mounted with the surface oriented 70° to the incident electron beam and some surface features seen in Nomarski were evident. Atomic force microscopy (AFM) was used to determine the surface height profile and film roughness. Selective area secondary ion mass spectrometry (SIMS) and x-ray photoelectron spectroscopy (XPS) were used to determine the chemical composition as a function of depth in the oxidized layers. The SIMS and XPS were done to corroborate the images seen in the SEM. The SIMS data were collected with a Physical Electronics 6650 with an O_2^+ plasma source and a quadrupole detector. The XPS spectra was collected with a Kratos Axis Ultra with a 4 keV Ar gun, an $Al_{k\alpha}$ (1486 eV) x-ray source, and a 165 mm hemispherical detector.

III. RESULTS

A. Oxidation dependence on temperature

Samples A and B were oxidized at temperatures between 350 and 450 °C. The average oxidation rate of $AlAs_{0.80}Sb_{0.20}$ at temperatures below 350 °C was considered not sufficient for the lateral wet oxidation of the 100 μm mesas in 12 h. Lateral wet oxidation at temperatures above 400 °C resulted in extensive Sb segregation and frequent delamination of the mesa structures. Sample A was cleaved and then laterally wet oxidized at 450 °C. The raised features of the $In_{0.25}Ga_{0.75}As$ capping layer, seen in the Nomarski micrograph of sample A in Fig. 2, are attributed to the Sb segregation during the lateral wet oxidation of the $AlAs_{0.80}Sb_{0.20}$ interlayer. The extensive surface height variation makes temperatures >400 °C undesirable for future processing. The measured average oxidation rates at 400 °C of AlAs, $AlAs_{0.80}Sb_{0.20}$, and $AlAs_{0.56}Sb_{0.44}$ in pure water were 1.1, 2.0, and 4.5 μm/min.[12] The oxidation rates for samples A and B are plotted in Fig. 3. The oxidation rate scaling proportional to the interlayer thickness is negligible when the oxidation layer thickness h was greater than 500 Å.

B. Water:methanol oxidation

The AlAsSb interlayers oxidize rapidly at low oxidation temperatures compared to AlAs. Methanol was added to the wet oxidation water mixture in an attempt to provide more hydrogen free radicals to stabilize the SbH_3 so the byproduct could diffuse out of the mesa.[18] The introduction of methanol to the wet oxidation process reduced the oxidation rate. At 375 and 400 °C a water:methanol mixture of 1:3 reduced the wet oxidation rate to 50% of pure water and a pure methanol mixture did not oxidize at all. The oxidation front as well as the Sb inclusions and fingers can be seen in Fig. 4. At furnace temperatures of 350 °C and lower, the higher methanol fraction mixtures reduced the oxidation rate that is not practical for a 100 μm mesa. Lateral wet oxidation with

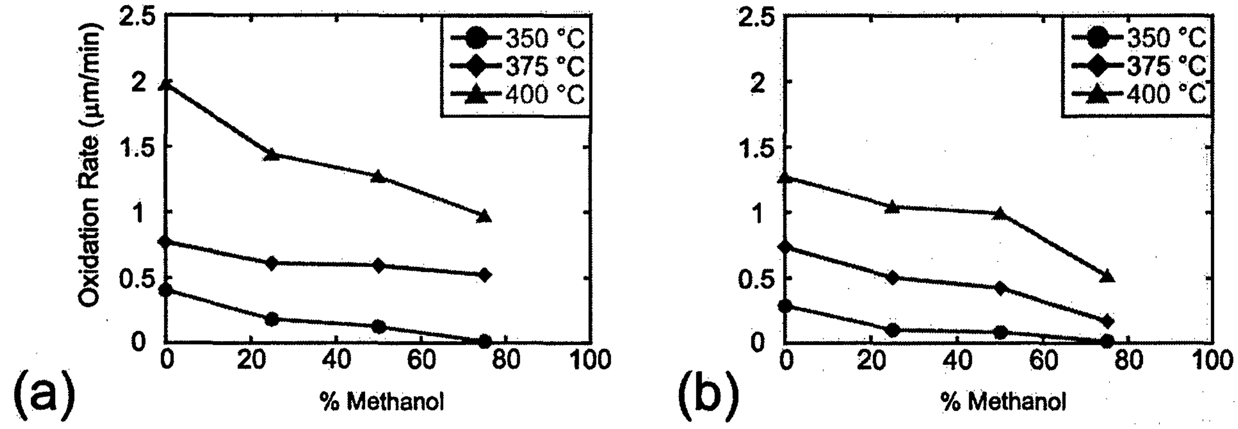

FIG. 3. Oxidation rates for $AlAs_{0.80}Sb_{0.20}$ interlayers. The average lateral wet oxidation rates for a 2000 Å $AlAs_{0.80}Sb_{0.20}$ interlayer are shown in (a) while the wet oxidation rates for a 500 Å interlayer are shown in (b). The increasing methanol concentration in the water:methanol mixture decreases the average lateral wet oxidation rate. Oxidation did not occur in pure methanol.

water:methanol mixtures also significantly reduced the delamination of the strained layer seen with pure water, which can be a side effect of the reduced oxidation rate.

AFM characterization of the surface of sample A showed an increase in surface roughness with increasing oxidation temperature. X-ray diffraction, after oxidation, showed little change in the relaxation of the $h=3000$ Å $In_{0.25}Ga_{0.75}As$ layer, but this was expected due to the large extent of initial relaxation. There is more information about the laterally oxidized interlayer in the optical Nomarski micrographs of

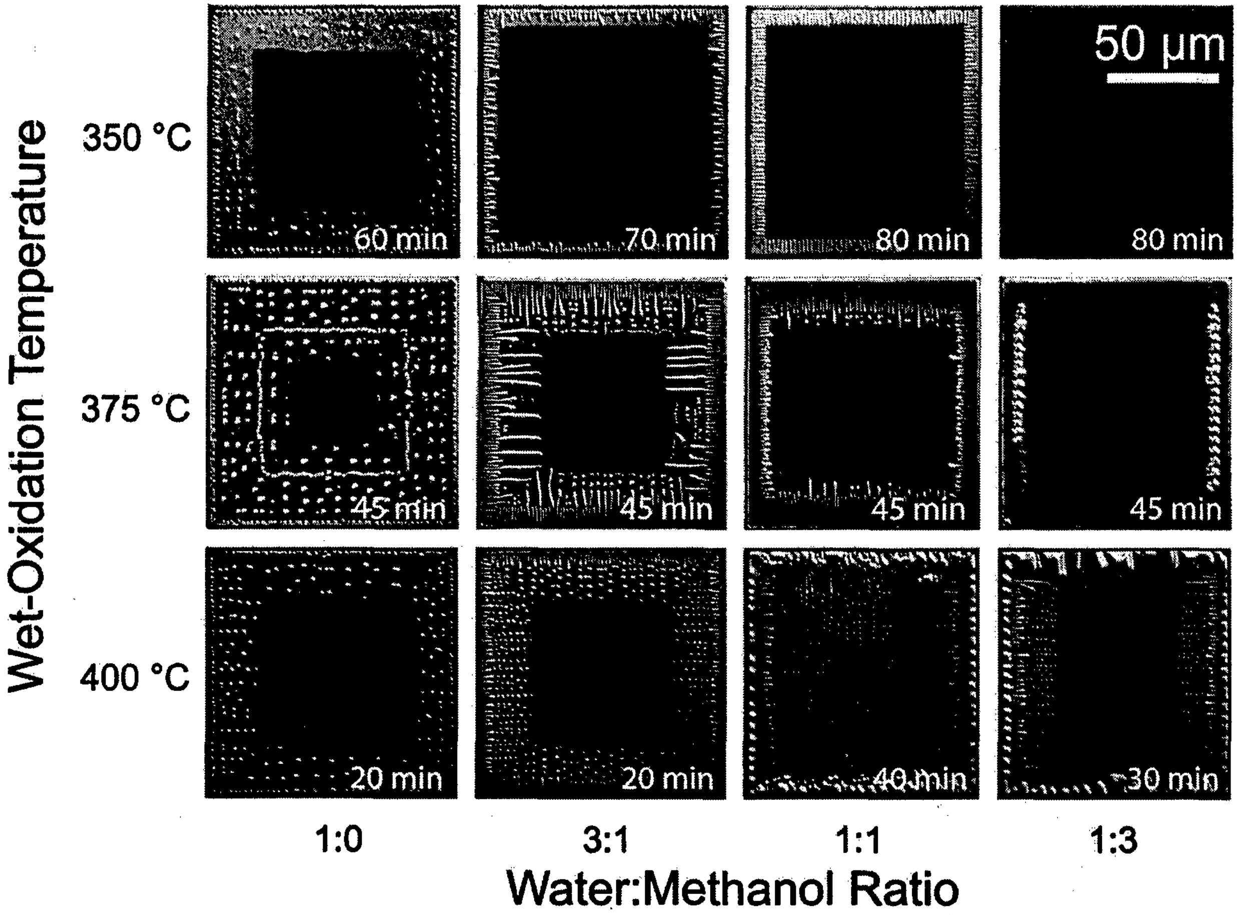

FIG. 4. Optical Nomarski micrographs of sample B after lateral wet oxidation. The oxidation temperatures are shown vs the ratio of water:methanol in the wet oxidation mixture. Increasing the wet oxidation temperature produced a rougher surface morphology. The increase of methanol in the water:methanol mixture reduced the average wet oxidation rate and at lower temperatures improved the surface morphology. The 1.5–2.0 μm diam inclusions turned to 1.5–2.0 μm wide fingers with the increasing methanol concentration.

1 µm
InGaAs
AlOx
GaAs
Sb

FIG. 5. Cross-sectional SEM of sample A wet oxidized at 375 °C with a solution of 3:1 water:methanol. Sb (bright layers in the micrograph) appears on both the top and bottom interface independent of oxidation temperature and water:methanol concentration.

sample B, shown in Fig. 4, due to the semitransparent $h = 500$ Å $In_{0.25}Ga_{0.75}As$ capping layer. The 1.5–2.0 μm diam inclusions seen in the micrograph resulted from Sb segregation and the inclusions were measured by AFM to be approximately the height of the oxidation interlayer thickness. With the increasing methanol concentration, the inclusions were observed as 1.0–2.0 μm wide fingers. The Sb inclusions and film delamination increased with oxidation temperature. The anisotropy between the two orthogonal $\langle 011 \rangle$ oxidation directions was more prevalent with the Sb segregation in the 375 °C 1:3 water:methanol oxidized sample. The Sb segregates into visible fingers only in the $[0\bar{1}1]$ direction and appears to neither blister nor form Sb fingers in the $[011]$ direction.

C. Oxidation dependence on interlayer thickness

Cross-sectional SEM of sample A was performed to observe the oxidized AlAsSb interlayer, as shown in Fig. 5. The Sb segregation was seen at the upper interface, lower interface, or both, independent of oxidation temperature or water:methanol mixture. The segregation was observed concurrently at both interfaces or either at the upper or lower interface within the same oxidation layer. To confirm the presence of Sb at both interfaces, selective area SIMS depth profiles were measured on as-grown, oxidized with pure water, and oxidized with different water:methanol mixtures by a $100\ \mu\text{m} \times 100\ \mu\text{m}$ trench with a 10% gate (i.e., chemical analysis was performed on $\sim 30\ \mu\text{m} \times 30\ \mu\text{m}$ area in the $100\ \mu\text{m} \times 100\ \mu\text{m}$ trench). Antimony from the oxidation layer segregated to both interfaces independent of the oxidation conditions, as shown in Fig. 6. XPS, in Fig. 7, showed that the remaining Sb was ~15% oxidized.

The relatively constant ratio of Sb segregation to layer thickness implies that a sufficiently thin AlAsSb oxidation layer would lead to only a few monolayers of Sb at the oxide–semiconductor interface. Oxidation layers with a thickness $h \leq 200$ Å in principle should have 2 monolayers of Sb at the interface. However, the thinner AlAsSb oxidation layers form Sb inclusions instead of thin Sb layers. The analysis of structures B–I by SEM and XPS only showed the Sb at the upper interface. Oxidation of the thinner layers resulted in the average oxidation rate decreasing with time. For example, the average oxidation rate for a 3 h oxidation was 0.13 μm/h, while the average oxidation rate for a 12 h oxidation was 0.07 μm/h.

Examination by depth dependent XPS of an unoxidized region of sample F that had been at 375 °C for 12 h showed diffusion of Ga into the oxidation layer, as shown in Fig. 8(a) with the cross section of the Ga and Al profiles shown in Fig. 8(b). The presence of Ga in the AlAsSb layers can explain the slow oxidation rate. As in AlGaAs oxidation, the concentration of Ga greatly affects the oxidation rate.[1]

D. *n*-type doping affect on oxidation

To investigate the influence of *n*-type doping, as published by Salesse *et al.*,[18] on the oxidation of AlAsSb, the oxidation layers of samples H and I were doped with Si and Te to $\sim 1 \times 10^{18}\ \text{cm}^{-3}$. The samples were grown with a semitransparent 500 Å $In_{0.25}Ga_{0.75}As$ cap to simplify the characterization of the effect of doping on Sb segregation. As seen in Fig. 9, there is no significant effect of *n*-type doping on the segregation of Sb. The Sb inclusions were observed in the oxidized interlayers. There was also little difference between the Te and Si *n*-type doping. For the oxidation of large lateral distances, as in the 100 μm mesas used, the *n*-type doping did not affect Sb segregation.

IV. DISCUSSION

This study was motivated by the need for high crystalline quality growth templates with lattice parameters not available from binary III–V substrates. Competing characteristics of a highly strained film before lateral wet oxidation and a large lattice parameter film limit the application of lateral wet oxidation for strain relaxation on GaAs substrates. The next largest lattice parameter III–V substrate after GaAs is InP. Due to processing time and temperature limitations, AlAsSb is the best alloy for an oxidation interlayer on InP but AlAsSb lateral wet oxidation results in Sb segregation at the oxide–semiconductor interface.

GaAs substrates were used for a starting lattice parameter and lattice matched $AlAs_{0.80}Sb_{0.20}$ and $In_{0.25}Ga_{0.75}As$ for the oxidation and capping layer. This is a strained oxidation and capping layer when most studies on AlAsSb oxidation were lattice matched to InP. The oxidation temperatures were limited between 350 and 450 °C. The average oxidation rates for lateral wet oxidation at temperatures below 350 °C were considered insufficient for the 100 μm mesas while lateral wet oxidation at temperatures above 400 °C resulted in large surface features attributed to the Sb segregation, at the oxide–semiconductor interface, and possible delamination of the mesas.

In oxidized sample A ($h = 2000$ Å), the Sb segregates from the AlO_x into a layer that is ~85% Sb metal and ~15% SbO_x, as shown in the XPS depth profiles in Fig. 7. This layer, as shown in Fig. 6, can be at the upper or lower oxide–semiconductor interface in the oxidized InGaAs/AlAsSb/GaAs structure. This Sb segregation layer resulted in a weak bond between the capping layer and oxide, which often resulted in the delamination of the InGaAs capping layer in subsequent film processing. The oxidation of samples B–I, $h \leq 500$ Å, resulted in the formation of Sb inclusions at the oxide–semiconductor interface instead of Sb layers. The Sb

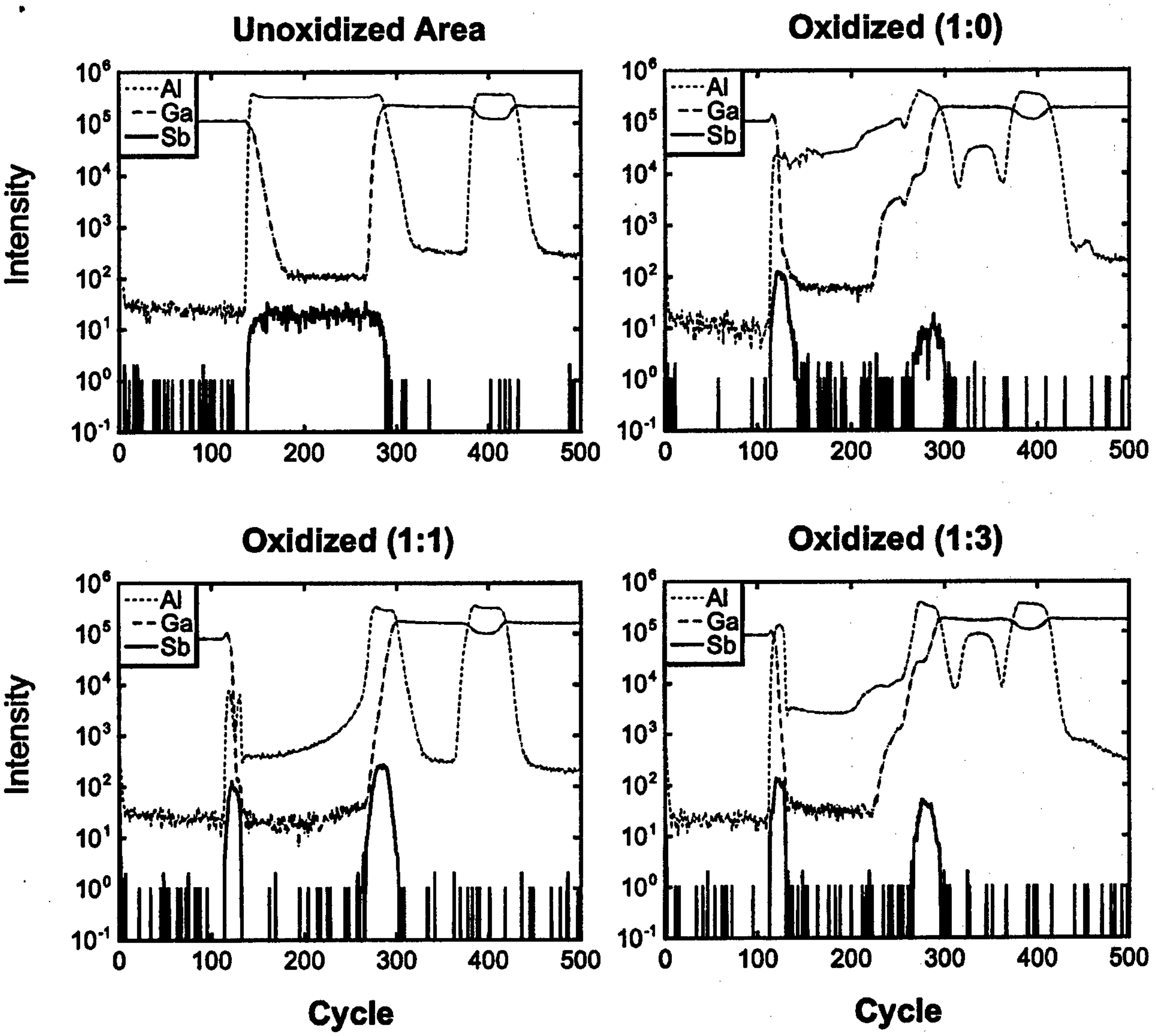

FIG. 6. SIMS depth profiles of sample A. After the oxidation of the AlAsSb interlayer, the Sb segregates to both the upper and lower oxide–semiconductor interfaces. The ratio of water:methanol during wet oxidation has little effect on the Sb segregation.

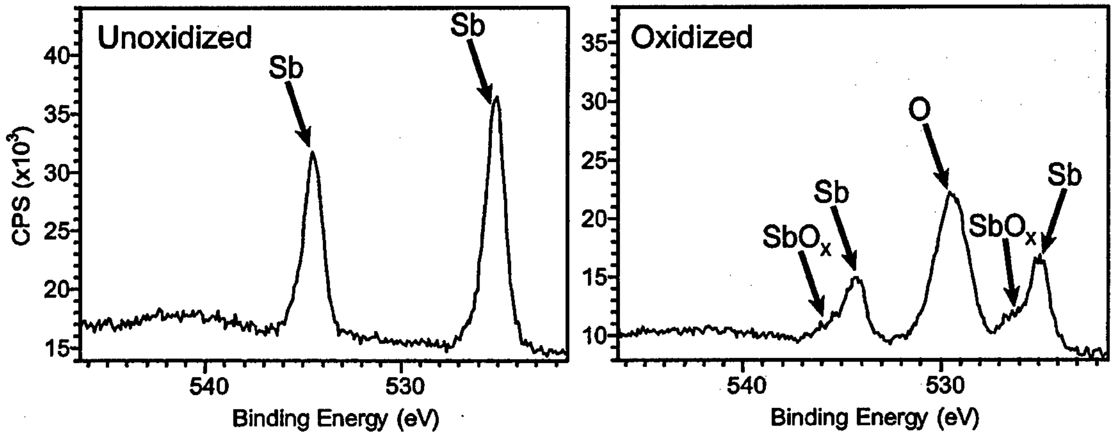

FIG. 7. XPS spectra of the $AlAs_{0.8}Sb_{0.2}$ interlayer before and after oxidation. The unoxidized spectrum shows the Sb in the AlAsSb interlayer. After lateral wet oxidation, the spectrum peaks corresponded to the remaining Sb that was 15% oxidized and the oxygen in the AlO_x interlayer.

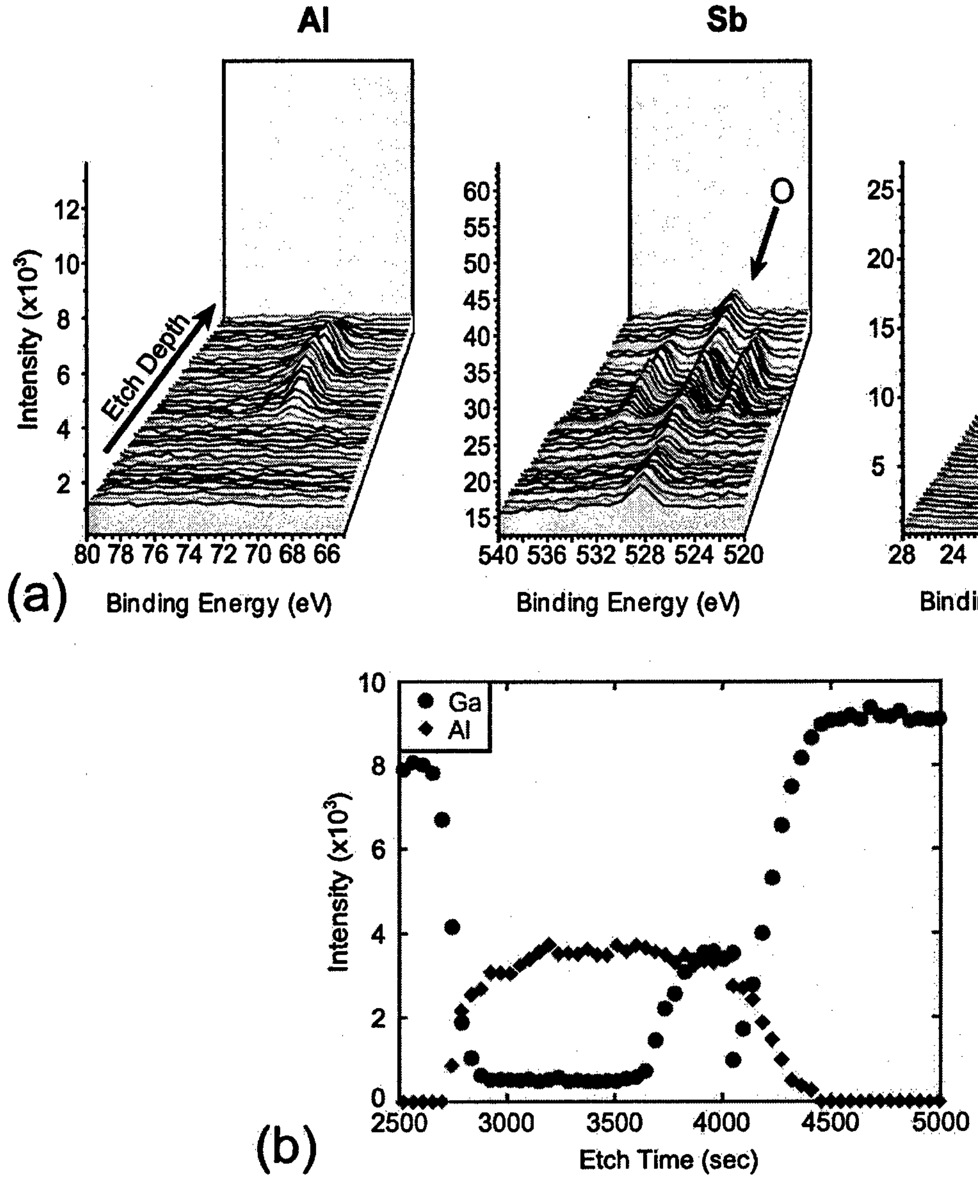

FIG. 8. X-ray photoelectron spectroscopy depth profiles of an unoxidized area of sample F annealed at 375 °C for 12 h. The InGaAs/AlAsSb/GaAs sample was Ar$^+$ etched between each scan. (a) The depth profiles of Al, Sb, and Ga are shown. (b) The plot of the Ga and Al peaks as a function of depth shows that the Ga has diffused into the AlAsSb layer from the GaAs substrate.

segregation did not disappear in the thinner samples but only reduced the number Sb of inclusions after lateral wet oxidation. Thicker capping layers may prevent the formation of Sb inclusions through the increased stiffness of thicker films, but that would defeat the purpose of growing a highly strained capping layer since thicker InGaAs capping layers would be relaxed. The oxidation rate becomes highly depressed when the AlAsSb thickness is $h<500$ Å. When the oxidation rate is slow enough, the diffusion of Ga into the AlAsSb interlayer from the surrounding layers further inhibits the AlAsSb oxidation.

The addition of an n-type dopant, Si or Te, to the AlAsSb interlayer at $\sim 1\times 10^{18}$ cm^{-3} did not affect the oxidation or the Sb segregation. The differences between the two different n-type dopants were negligible. It is possible that the surface charges, due to the dangling atomic bonds at the free surface, in the thinner structures B–I dominate the Sb migration and the doping of the oxidation layers is only useful in thicker structures where the oxidation layer is isolated from the surface charges.

Efficient electronic devices such as high electron mobility transistors should not have parallel conduction or current leakage paths. The formation of a metallic Sb layer between the oxide and the strain relaxed semiconducting layers thwarts any subsequent device fabrication. A thick insulating buffer layer would have to be grown on the relaxed capping layer in order to isolate the device and that would be counterproductive to the purpose of starting with a growth template. The growth template is supposed to be an epitaxy-ready substrate without a backside Schottky contact.

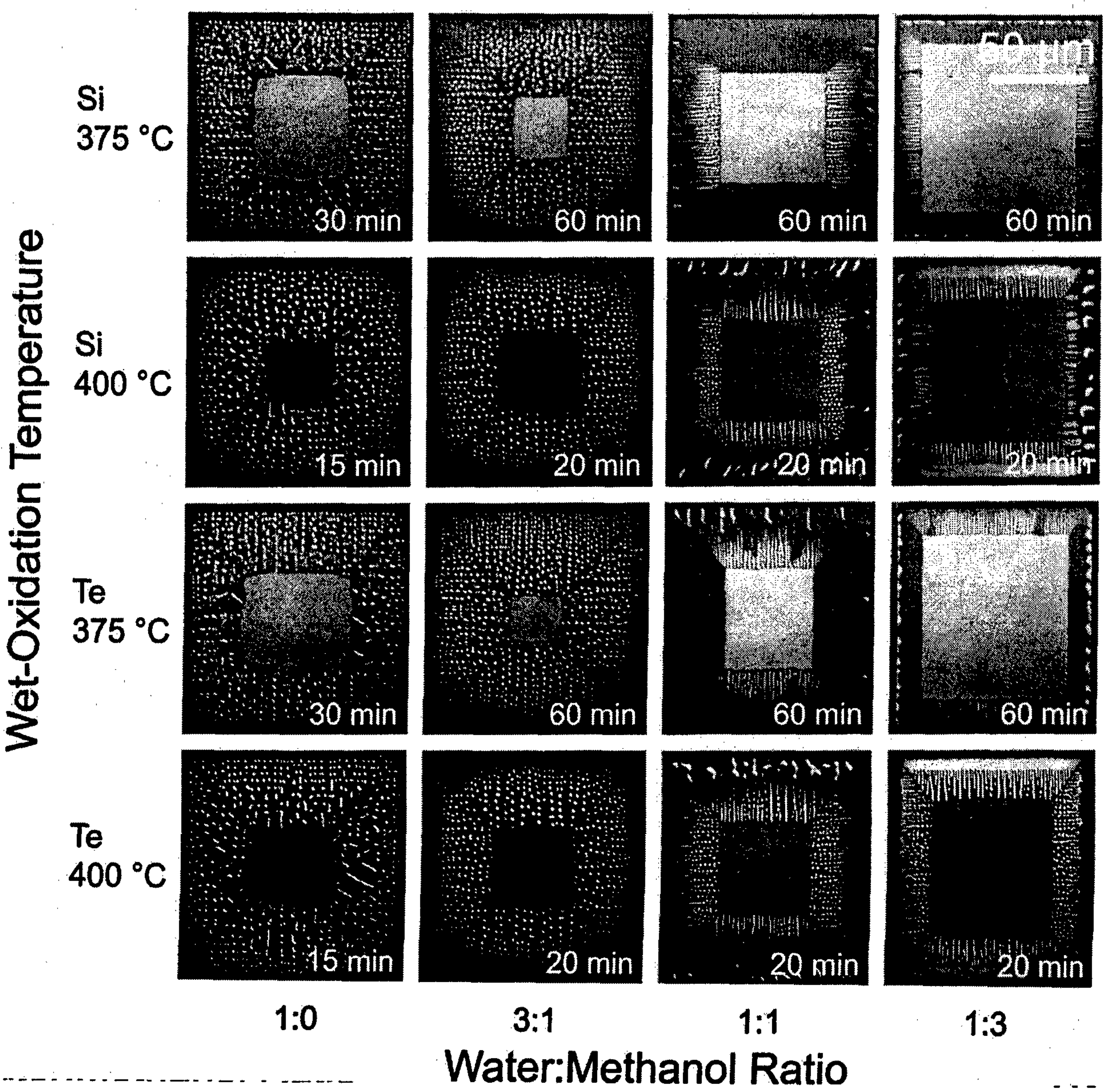

FIG. 9. Optical Nomarski micrographs n-type $AlAs_{0.80}Sb_{0.20}$ after oxidation. The oxidation temperatures and dopant species, Si and Te, are shown vs the ratio of water:methanol in the wet oxidation mixture. There is little effect of n-type doping to prevent the Sb segregation and inclusion formation during the oxidation of AlAsSb with or without methanol.

However, the oxidation of AlAsSb has been used in VCSEL technology to successfully form current and optical apertures.[26] The Sb precipitates present less of a problem with the optoelectronic devices when the current path is perpendicular to the oxidation layer and the precipitates are not contacted by either the n- or p-type ohmic metals.

V. SUMMARY

AlAsSb interlayers were laterally wet oxidized to enhance strain relaxation of misfitting layers. Different water:methanol environments were used to hinder the segregation of Sb at the oxide–semiconductor interfaces. Low lattice mismatch $AlAs_{0.80}Sb_{0.20}$ interlayers were grown on GaAs substrates to evaluate the oxidation. Lateral wet oxidation of AlAsSb interlayers at temperatures above 400 °C resulted in extensive Sb precipitation and delamination of the 100 μm mesas. Average lateral wet oxidation rates at temperatures below 350 °C were insufficient for the oxidation of the 100 μm mesas in 12 h. After lateral wet oxidation, the thicker $h = 2000$ Å $AlAs_{0.80}Sb_{0.20}$ interlayers formed an Sb layer at the oxide–semiconductor interface that was ~15% oxidized. The Sb layers can form at either oxide–semiconductor interface and seem to be independent of the lateral wet oxidation conditions. The lateral wet oxidation of the thinner $h \leq 500$ Å $AlAs_{0.80}Sb_{0.20}$ interlayers resulted in Sb inclusions forming blisters in the capping layer. The addition of methanol to the wet oxidation mixture, to increase the available hydrogen free radicals and help stabilize the oxidation byproduct SbH_3, only seemed to decrease the average wet-oxidation rate. The decreased average wet oxidation rate of the $AlAs_{0.80}Sb_{0.20}$ interlayers coincided with a change in the segregated Sb morphology from inclusions to fingers. The *n*-type doping ($1\times10^{18}\ cm^{-3}$) with Si or Te of the $AlAs_{0.80}Sb_{0.20}$ interlayers did not suppress or result in any real change in the Sb precipitate morphology after lateral wet oxidation.

ACKNOWLEDGMENTS

This work made use of MRL Central Facilities supported by the National Science Foundation under Award No. DMR00-80034. This work was also supported by DARPA and AFOSR (W. Coblenz and G. Witt program managers).

[1] J. M. Dallesasse, N. Holonyak, Jr., A. R. Sugg, T. A. Richard, and N. El-Zein, Appl. Phys. Lett. **57**, 2844 (1990).
[2] N. Ohnoki, N. Hatori, A. Mizutani, F. Koyama, and K. Iga, J. Cryst. Growth **195**, 603 (1998).
[3] E. C. Vail, G. S. Li, W. Yuen, and C. J. Chang-Hasnain, Electron. Lett. **32**, 1888 (1996).
[4] A. C. Alonzo, X.-C. Cheng, and T. C. McGill, J. Appl. Phys. **84**, 6901 (1998).
[5] B.-K. Jun, D.-H. Kim, J.-Y. Leem, J.-H. Lee, and Y.-H. Lee, Thin Solid Films **360**, 229 (2000).
[6] H. Gebretsadik, K. Zhang, K. Kamath, X. Zhang, and P. Bhattacharya, Appl. Phys. Lett. **71**, 3865 (1997).
[7] E. I. Chen, N. Holonyak, Jr., and S. A. Maranowski, Appl. Phys. Lett. **66**, 2688 (1995).
[8] C. H. Ashby, J. P. Sullivan, K. D. Choquette, K. M. Geib, and H. Q. Hou, J. Appl. Phys. **82**, 3134 (1997).
[9] R. L. Naone and L. A. Coldren, J. Appl. Phys. **82**, 2277 (1997).
[10] P. Chavarkar, U. K. Mishra, S. K. Mathis, and J. S. Speck, Appl. Phys. Lett. **76**, 1291 (2000).
[11] O. Blum, M. J. Hafich, J. F. Klem, K. Baucom, and A. Allerman, Electron. Lett. **33**, 1097 (1997).
[12] S. K. Mathis, K. H. Lau, A. M. Andrews, E. M. Hall, G. Almuneau, E. L. Hu, and J. S. Speck, J. Appl. Phys. **89**, 2458 (2001).
[13] G. W. Pickrell, J. H. Epple, K. L. Chang, K. C. Hsieh, and K. Y. Cheng, Appl. Phys. Lett. **76**, 2544 (2000).
[14] J. P. Loehr and S. A. Feld, Proc. IEEE **2**, 110 (1998).
[15] B. Koley, F. G. Johnson, O. King, S. S. Saini, and M. Dagenais, Appl. Phys. Lett. **75**, 1264 (1999).
[16] O. Blum, K. M. Geib, M. J. Hafich, J. F. Klem, and C. I. H. Ashby, Appl. Phys. Lett. **68**, 3129 (1996).
[17] P. Legay, P. Petit, G. Le Roux, A. Kohl, I. F. L. Dias, M. Juhel, and M. Quillec, J. Appl. Phys. **81**, 7600 (1997).
[18] A. Salesse *et al.*, Appl. Surf. Sci. **161**, 426 (2000).
[19] J. H. Seo and K. S. Seo, Appl. Phys. Lett. **72**, 1466 (1998).
[20] P. Chavarkar, L. Zhao, S. Keller, A. Fisher, C. Zheng, J. S. Speck, and U. K. Mishra, Appl. Phys. Lett. **75**, 2253 (1999).
[21] J. W. Matthews and A. E. Blakeslee, J. Cryst. Growth **27**, 118 (1974).
[22] S. K. Mathis, P. Chavarkar, A. M. Andrews, U. K. Mishra, and J. S. Speck, J. Vac. Sci. Technol. B **18**, 2066 (2000).
[23] S. K. Mathis, A. M. Andrews, P. Chavarkar, U. K. Mishra, E. L. Hu, and J. S. Speck, Presented at Electronic Materials Conference, Denver, CO, 2000.
[24] A. E. Romanov and J. S. Speck, J. Electron. Mater. **29**, 901 (2000).
[25] A. Krost, G. Bauer, and J. Woitok, in *Optical Characterization of Epitaxial Semiconductor Layers*, edited by G. Bauer and W. Richter (Springer, New York, 1996), p. 287.
[26] M. H. M. Reddy, D. A. Buell, A. S. Huntington, T. Asano, R. Koda, D. Feezell, D. Lofgreen, and L. A. Coldren, Appl. Phys. Lett. **82**, 1329 (2003).

Appendix VII

APPLIED PHYSICS LETTERS VOLUME 83, NUMBER 13 29 SEPTEMBER 2003

Stress relaxation in mismatched layers due to threading dislocation inclination

A. E. Romanov[a] and J. S. Speck[b]
Materials Department, University of California, Santa Barbara, California 93106

(Received 23 May 2003; accepted 29 July 2003)

A recently observed mechanism of elastic stress relaxation in mismatched layers is discussed. The relaxation is achieved by the inclination of pure edge threading dislocation lines with respect to the layer surface normal. The relaxation is not assisted by dislocation glide but rather is caused by the "effective climb" of edge dislocations. The effective dislocation climb may result from the film growth and it is not necessarily related to bulk diffusion processes. The contribution of the dislocation inclination to strain relaxation has been formulated and the energy release due to the dislocation inclination in mismatched stressed layers has been determined. This mechanism explains recently observed relaxation of compressive stresses in the (0001) growth of $Al_xGa_{1-x}N$ layers. © *2003 American Institute of Physics.* [DOI: 10.1063/1.1613360]

It is well known that the processes of stress relaxation in lattice mismatched epitaxy play a crucial role for materials properties and electronic and optoelectronic device performance. The most common mode of misfit stress relaxation is normally related to the formation of misfit dislocations (MDs) at the layer/substrate interface. For layers that grow in a two-dimensional mode (i.e., step flow or layer-by-layer growth), the formation of MDs is usually accomplished by dislocation motion, i.e., by glide.[1] The dislocation gliding can proceed by bending the pre-existing threading dislocations (TDs).[1,2] To operate, this mechanism needs to involve the shear stresses in the dislocation glide plane. This is the standard case for epitaxial growth of (001) oriented semiconductor layers with face centered cubic lattices (e.g., diamond cubic or zinc blende structures), where the biaxial stress state is responsible for shear stresses on the inclined ⟨111⟩ glide planes. The corresponding TDs and their Burgers vectors are inclined with respect to [001] growth direction of the layer.

The different case is realized for (0001) growth of layers with a hexagonal crystal structure, e.g., the group III-nitride semiconductors.[3] For (0001) oriented layers, the TDs usually have pure edge character with [0001] line direction and Burgers vector in the basal plane. The $\{1\bar{1}00\}$ prismatic glide planes of these dislocations are normal to the biaxial stress plane and there is no shear stress in the glide planes. Nevertheless, such edge dislocations may contribute to the misfit stress relaxation by inclining their line direction that corresponds to their effective climb. Recently, such TD behavior was observed in the (0001) growth of compressively stressed $Al_xGa_{1-x}N$ layers.[4]

In the present letter we propose a glide-free mechanism of misfit stress relaxation related to the inclination of the TDs with respect to their original direction. The contribution of TD inclination to the relaxed strain will be determined and the energy change resulting from the dislocation inclination will be found. The critical conditions for dislocation inclination will be established.

Our modeling efforts were motivated by the experimental observations of systematic inclination of TDs in Si-doped 200-nm-thick $Al_{0.49}Ga_{0.51}N$ layers which were grown on relaxed $Al_{0.62}Ga_{0.38}N$ buffer layers on (0001) sapphire, see Ref. 4 for details. The total compressive mismatch for the upper layer at the growth temperature was found $\varepsilon_m \approx 0.003$. It was established that Si doping promoted the relaxation of the elastic stresses caused by the lattice mismatch. The degree of strain relaxation was determined by x-ray diffraction and reached 50%–100% depending on the doping level. It was also found that Si doping enhanced the layer surface roughness during growth. Transmission electron microscopy (TEM) structure investigations proved the presence of high density of TDs with $\rho_{TD} \geqslant 10^{10}$ cm^{-2}. The majority of the observed TDs were edge dislocations with Burgers vectors of the type $\frac{1}{3}\langle 11\bar{2}0\rangle$. The lines of these dislocations were inclined with respect to the [0001] growth direction (see schematics in Fig. 1) with inclination angles α as large as 20°. Cross-section and plane-view TEM studies showed that the TDs inclined toward the $\langle 1\bar{1}00\rangle$ directions. The specific inclination direction is perpendicular to the direction of the Burgers vector, e.g., for TD with $\mathbf{b} = \pm\frac{1}{3}[2\bar{1}\bar{1}0]$ the inclination is in the $\pm[01\bar{1}0]$ direction.

When viewed down the growth direction [see Fig. 1(b)], the inclined TDs have an average projected length L. The Burgers vectors of the dislocations are projected on the layer/substrate interface without any distortion. Therefore, in the far field, the projected dislocation segments are equivalent to the sections of misfit dislocations. The MD segments can be hypothetically combined to form straight line MD arrays with the distance l between MDs. Assuming that the total treading dislocation density ρ_{TD} is evenly distributed between the three families [as it is for the case of (0001) growth of nitrides], we find that the distance between effective MDs in each of the $\langle 11\bar{2}0\rangle$ directions will be $l = 3/\rho_{TD}L$. The plastic relaxation associated with the array of effective MDs is given as $\varepsilon^1_{pl} = b/l$, where b is the magnitude of the dislocation Burgers vector. The total biaxial far

---

[a] Present address: A.F. Ioffe Physico-Technical Institute, 194021 St. Petersburg, Russia.

[b] Electronic mail: speck@mrl.ucsb.edu

0003-6951/2003/83(13)/2569/3/$20.00

© 2003 American Institute of Physics
Downloaded 23 Sep 2003 to 128.111.74.212. Redistribution subject to AIP license or copyright, see http://ojps.aip.org/aplo/aplcr.jsp

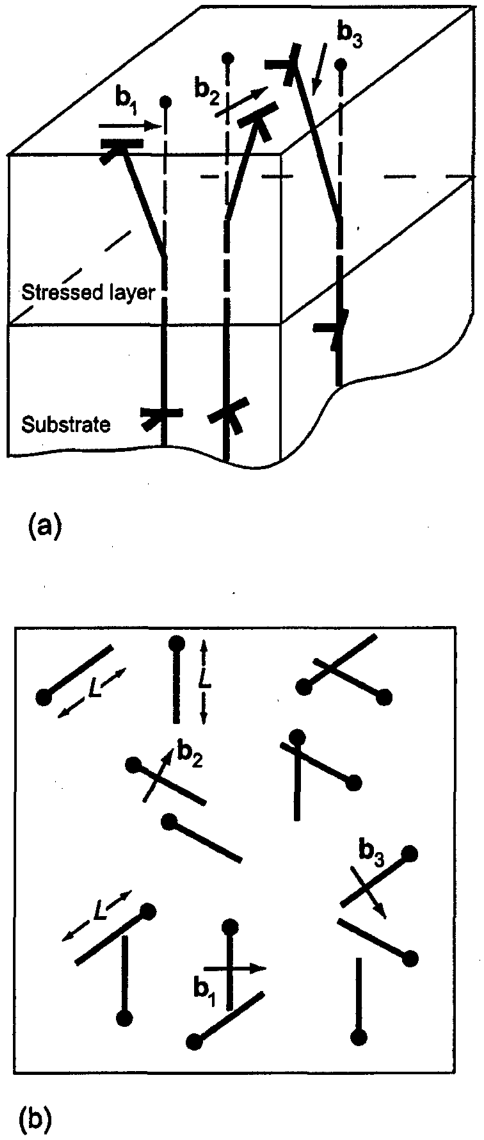

FIG. 1. Inclined pure edge dislocations in a stressed layer. (a) Three families of edge dislocations corresponding to three possible orientations of the Burgers vector in the (0001) plane of the layer with a hexagonal crystal structure. (b) Plan-view showing the average dislocation projected length L.

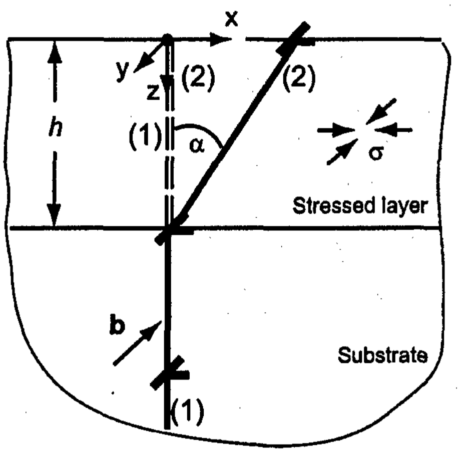

FIG. 2. Representation of the inclined dislocation as a superposition of straight dislocation (1) and angular dislocation (2). The dislocation Burgers vector b is in the yz plane. There is a compressive biaxial stress $\sigma_{xx}=\sigma_{yy}=\sigma=2G\,\varepsilon_m(1+\nu)/(1-\nu)$ in the layer.

field plastic relaxation at the top layer surface resulting from the triangular MD grid $\varepsilon_{\mathrm{pl}}^{\mathrm{top}}$ is given by

$$\varepsilon_{\mathrm{pl}}^{\mathrm{top}}=\tfrac{3}{2}\varepsilon_{\mathrm{pl}}^{1}=\tfrac{1}{2}b\rho_{\mathrm{TD}}L. \qquad (1)$$

The projected length L is directly related to the layer thickness h and the inclination angle α by $L=h\tan\alpha$. This also means that the projected length varies linearly with layer depth. Therefore, the average plastic relaxation for the layer of the thickness h is

$$\bar{\varepsilon}_{\mathrm{pl}}=\tfrac{1}{4}b\rho_{\mathrm{TD}}h\tan\alpha. \qquad (2)$$

For $\rho_{\mathrm{TD}}=3\times10^{10}\ \mathrm{cm}^{-2}$, $h=200\ \mathrm{nm}$, $\alpha=17°$, and $b=0.318\ \mathrm{nm}$ (corresponding to the observations in Ref. 4), Eq. (1) gives the plastic relaxation at the layer surface $\varepsilon_{\mathrm{pl}}^{\mathrm{top}}=0.0029$ that is comparable with the initial misfit $\varepsilon_m\approx0.003$.

To understand the conditions for TD inclination in a stressed layer, we consider the energy balance similar to those used in the "energy approach"[5,6] for deriving the critical thickness for the introduction of MDs in strained films. The energy release ΔE due to dislocation inclination can be formulated as

$$\Delta E=E_{\mathrm{inclined}}-E_{\mathrm{straight}}-W_{\mathrm{int}}, \qquad (3)$$

where E_{inclined} is the self-energy of the dislocation in the inclined configuration, E_{straight} is the self-energy of the dislocation in the initial configuration with the line direction normal to the surface, W_{int} is the work done by the biaxial misfit stress σ (see Fig. 2) in the process of dislocation inclination. To find E_{inclined}, we use the representation of the inclined dislocation as the superposition of the straight dislocation (1) and an angular dislocation (2) as shown in Fig. 2. In this case, E_{inclined} can be found as

$$E_{\mathrm{inclined}}=E_{\mathrm{straight}}+E_{\mathrm{angular}}+W_{\mathrm{straight}}^{\mathrm{angular}}, \qquad (4)$$

where E_{angular} is the self-energy of the angular dislocation and $W_{\mathrm{straight}}^{\mathrm{angular}}$ is the interaction energy with the initial dislocation. Exact calculations[7] of the energy E_{angular} include the contribution of the dislocation core region which is proportional to the change in dislocation length. Numerical estimates show that the interaction contribution $W_{\mathrm{straight}}^{\mathrm{angular}}$ cancels in the first approximation the dislocation core contribution. As a result the energy balance takes the simpler form

$$\Delta E=E_{\mathrm{angular}}-W_{\mathrm{int}}. \qquad (5)$$

The interaction part is calculated as

$$W_{\mathrm{int}}=b\sigma S_{\mathrm{angular}}=G\frac{1+\nu}{1-\nu}bh^2\varepsilon_m\tan\alpha, \qquad (6)$$

where S_{angular} is the area bounded by the angular dislocation, G is shear modulus, and ν is Poisson ratio.

The first step in the calculation of the self-energy of the angular dislocation involves the determination of the elastic fields of the dislocation in the presence of the free surface. Subsequently, integration of the elastic fields yields the elastic self-energy term in the Eq. (5). The results of these calculations will be presented elsewhere.[7] Here we use the approximate expression for E_{angular} based on the physical arguments of varying screening for the dislocation elastic field in the process of TD inclination. Actually, for very

Downloaded 23 Sep 2003 to 128.111.74.212. Redistribution subject to AIP license or copyright, see http://ojps.aip.org/aplo/aplcr.jsp

small inclination angles, the angular dislocation is equivalent to the dipole with the separation of the order $h \sin\alpha \approx h\alpha$. For large inclinations ($\alpha \rightarrow \pi/2$), the dislocation acquires a parallel orientation with respect to the layer surface and the characteristic screening length becomes the layer thickness h. Accordingly, the dislocation length changes as $h/\cos\alpha$ with inclination α. These observations permit to propose the following dependence for E_{angular}:

$$E_{\text{angular}} = \frac{Gb^2}{4\pi(1-\nu)} \frac{h}{\cos\alpha} \log\left[\left(\frac{h}{b}-1\right)\sin\alpha+1\right], \quad (7)$$

where we assume the value of b for the dislocation core radius. The developed approximation fits closely to numerical solutions of E_{angular} for a wide range of film thicknesses and inclination angles.[7]

Finally, we analyze the following dependence for the energy release:

$$\Delta E(\tilde{h},\alpha) = \frac{Gb^3}{(1-\nu)}\left\{\frac{\tilde{h}}{4\pi\cos\alpha}\log[(\tilde{h}-1)\sin\alpha+1] - (1+\nu)\tilde{h}^2\varepsilon_m \tan\alpha\right\}, \quad (8)$$

where $\tilde{h} = h/b$ is the normalized film thickness.

A typical dependence for ΔE is given in Fig. 3(a). It is clear that for sufficiently large thickness or angle α, ΔE becomes negative and gives the favorable parameters for plastic relaxation via dislocation inclination. By applying the requirement $\Delta E = 0$, we can map the regions for favorable dislocation inclination in coordinates layer thickness-inclination angle as shown in Fig. 3(b). The plots define the energetic conditions for dislocation inclination for the given misfit strain. For $\alpha \rightarrow \pi/2$, the plots demonstrate the usual critical thickness behavior for MD formation in mismatched layers.

The other important feature of $\Delta E(\tilde{h},\alpha)$ dependence is the existence of the energy barrier to dislocation inclination at finite values of the layer thickness h. The typical heights for this barrier are of the order of 5–10 Gb^3, which lead to reasonable values of the order up to 10 eV per dislocation. Such barriers can be overcome when additional factors come into play. We believe that surface roughness helps to diminish the energy barrier. The last statement is supported by the models proposed for dislocation nucleation during the development of morphological instabilities at stressed surface of crystals.[8,9] Once inclined, the TDs may maintain their orientation. Typically, the TD line direction becomes frozen-in and thus demonstrates that dislocation climb does not occur in the bulk of the material. The possible mechanism of the crystal growth with inclined dislocations may then include directional surface diffusion and the incorporation of adatoms at the intersection of pre-existing TDs with the growing crystal surface. Therefore, we may refer this mechanism as "effective climb." We suppose that actual inclination angle is determined by the growth conditions, such as temperature, reactor pressure, precursor flow ratios, etc. To check this proposal, additional experiments must be performed. The other important experiments may include the growth of the samples with inclined dislocations to larger thickness, where the layers become fully relaxed or the layer strain *reverses* due to the inclined TDs.

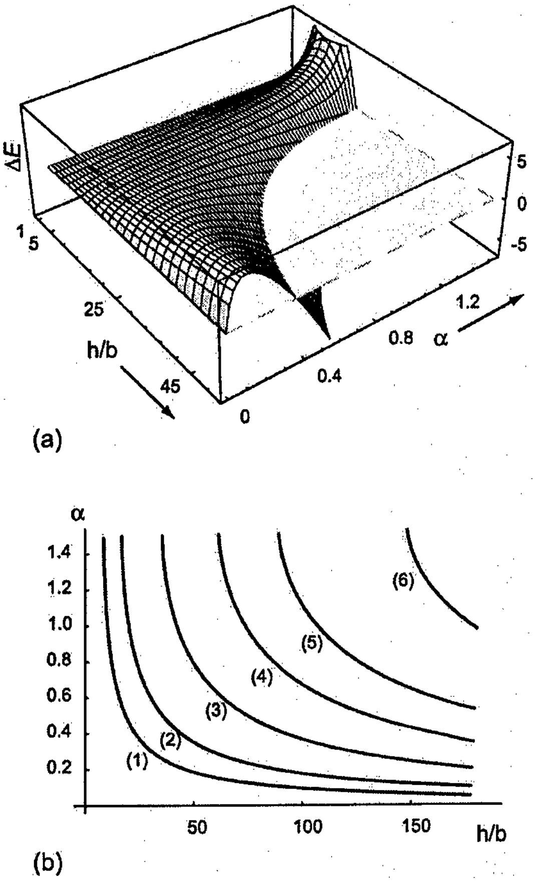

FIG. 3. Critical conditions for edge dislocation inclination in stressed layer. (a) Energy release due to the inclination of the initial straight dislocation. Parameters used for the plot: misfit strain in the layer $\varepsilon_m = 0.01$, dislocation core radius $R_c = b$, Poisson ratio $\nu = 1/3$. The energy change ΔE is in the units of Gb^3. (b) Inclination stability diagram in coordinates layer thickness h—inclination angle α for the misfit strain $\varepsilon_m = 0.015$ (1), 0.010 (2), 0.006 (3), 0.004 (4), 0.003 (5), and 0.002 (6), correspondingly.

In conclusion, a mechanism of elastic stresses relaxation in growing mismatched layers has been considered. The mechanism involves the TD lines inclination and their effective climb. The energetically favorable conditions for the operation of this mechanism have been determined.

This work was supported by the DARPA SUVOS program (J. Carrano, program manager) by a separate DARPA program (W. Coblenz, program manager) administered by AFOSR (G. Witt, contract monitor).

[1] L. B. Freund, MRS Bull. 17, 52 (1992).
[2] J. W. Matthews and A. E. Blakeslee, J. Cryst. Growth 27, 118 (1974).
[3] J. S. Speck and S. J. Rosner, Physica B 274, 24 (1999).
[4] P. Cantu, F. Wu, P. Waltereit, S. Keller, A. E. Romanov, U. K. Mishra, S. P. DenBars, and J. S. Speck, Appl. Phys. Lett. 83, 674 (2003).
[5] V. I. Vladimirov, M. Y. Gutkin, and A. E. Romanov, Poverkhnost 6, 46 (1988) (in Russian).
[6] J. R. Willis, S. C. Jain, and R. Ballough, Philos. Mag. A 62, 115 (1990).
[7] A. E. Romanov and J. S. Speck (unpublished).
[8] J. Grilhe, Europhys. Lett. 23, 141 (1993).
[9] H. Gao, J. Mech. Phys. Solids 42, 741 (1994).

Downloaded 23 Sep 2003 to 128.111.74.212. Redistribution subject to AIP license or copyright, see http://ojps.aip.org/aplo/aplcr.jsp

Appendix VIII

JOURNAL OF APPLIED PHYSICS VOLUME 93, NUMBER 1 1 JANUARY 2003

Modeling the extended defect evolution in lateral epitaxial overgrowth of GaN: Subgrain stability

A. E. Romanov,[a] P. Fini, and J. S. Speck[b]
Materials Department, University of California, Santa Barbara, California 93106

(Received 23 April 2002; accepted 2 October 2002)

The topic of extended defect structure stability in lateral epitaxial overgrowth (LEO) of GaN is addressed. We first summarize experimental results of growth morphology and dislocation structure in LEO GaN on sapphire substrates in the context of the crystallographic orientation of the stripe window openings. For $\langle 11\bar{2}0\rangle$-oriented stripes, the LEO material often exhibits a triangular cross-section morphology with inclined $\{10\bar{1}1\}$ facets. The threading dislocations (TDs) propagate vertically in the window region and then become unstable and bend toward the inclined sidewalls, to eventually lie in the basal plane. In the case of $\langle 1\bar{1}00\rangle$-oriented stripes, vertical $\{11\bar{2}0\}$ sidewalls may develop and, when realized, yield the lowest density of extended defects in the wing (overgrown) regions. Most of the TDs propagate vertically in the window regions and remain in loosely organized cell walls (subgrain boundaries). For this stripe orientation, a discernable crystallographic tilt of the LEO wing regions relative to the window region is also observed. This tilt is related to the appearance of edge dislocation arrays in the transition region between windows and wings. To understand the growth of dislocation-free wing regions, we present a model for dislocation subboundary cell structure stability during lateral overgrowth. The model provides a relation between structural parameters (such as cell size and misorientation) under which lateral defect-free growth is energetically favorable. © *2003 American Institute of Physics.*
[DOI: 10.1063/1.1524013]

I. INTRODUCTION

In the past five to six years, there has been rapid progress in GaN-based optoelectronic and electronic devices. The successes in nitride-based devices have been quite remarkable in light of the high extended defect densities for this semiconductor system. Currently, state-of-the-art GaN grown either on silicon carbide or sapphire substrates has a threading dislocation (TD) density on the order of 10^8-10^9 cm^{-2}. Early Nichia light emitting diodes (LEDs) had TD densities on the order of 10^9-10^{10} cm^{-2}, which led to speculation that TDs were innocuous in GaN or perhaps even *beneficial* for the optical emission. However, a growing body of work has evolved that shows TDs are deleterious for the optoelectronic and electronic properties of nitrides. Rosner *et al.* used cathodoluminescence and atomic force microscopy to correlate TD positions with reduced optical emission and attributed this behavior to nonradiative recombination at TDs.[1] The conclusions of the Rosner *et al.* study were confirmed by Sugahara *et al.* in a combined cathodoluminescence and transmission electron microscopy study.[2] Weimann *et al.* have adopted models for carrier scattering at TDs and have shown consistency with experimental data.[3] More recently, Look and Sizelove developed a comprehensive model for transport in the nitrides, including scattering at charged TD lines, and were able to successfully predict TD densities based on experimental data.[4] Alternative models of dislocation scattering at dislocation walls has been developed by Farvacque *et al.*[5] Research showing that TDs are deleterious to the physical properties of the nitrides has recently been reviewed.[6]

The technique of lateral epitaxial overgrowth (LEO) of GaN was developed by R.F. Davis and group at North Carolina State University and by the NEC group for the growth of low-TD density GaN from mask openings.[7–10] In this method, a planar GaN layer is grown on a foreign substrate, such as sapphire, silicon, or SiC, by metal-organic chemical-vapor deposition (MOCVD) or hydride vapor phase epitaxy (HVPE). This layer will typically have TD densities in the range of 10^8-10^{10} cm^{-2}. The GaN layer is subsequently removed from the growth reactor and covered with a mask material such as SiO_2 or SiN_x. Openings (termed "windows"), usually in an oriented stripe geometry as shown in Fig. 1, are produced in the mask using standard photolithography. The patterned layer is then reintroduced into the growth reactor. The regrowth takes place with GaN growing first from the window openings and then laterally over the mask, as shown schematically in Fig. 1. Throughout this article we will refer to the material that grows through the opening as the "window" region and the material that grows over the mask as the "wing" region. The stripe orientation and growth conditions directly affect the morphology of the overgrown material,[11,12] which in turn affect the dislocation orientation and distribution in the window and wing region.[13] When the stripe orientation and growth process are optimized, the wing regions typically have TD densities in the range $<10^4-10^6$ cm^{-2}. Thus, this relatively simple tech-

---

[a] Permanent address: A.F. Ioffe Physico-Technical Institute, St. Petersburg, 194021 Russia.

[b] Electronic mail: speck@mvl.uscb.edu

Downloaded 05 Feb 2003 to 128.111.74.212. Redistribution subject to AIP license or copyright, see http://ojps.aip.org/japo/japcr.jsp

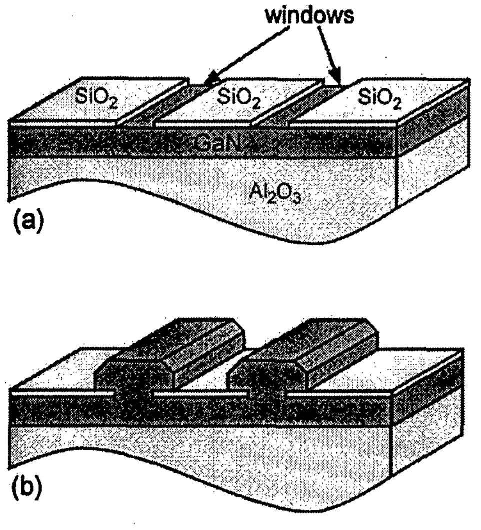

FIG. 1. Schematics of lateral epitaxial overgrowth (LEO) processing. (a) GaN layer on sapphire substrate covered by mask material with opened window regions. (b) Lateral growth of GaN over the mask subsequent to growth through the window regions.

nique provides a means of realizing local crystal quality comparable to that available in bulk III-V semiconductor substrates.

Using LEO, Nakamura *et al.* were able to demonstrate a 10 000 h projected continuous operation blue nitride-based lasers.[14] LEO-based experiments have been used to demonstrate that TDs behave as current leakage paths.[15,16] Additionally, LEO GaN has been used to show that TDs act as fast diffusion pathways for Mg.[17]

In this article, we first describe details of our experimental approach and main results for LEO growth of GaN on sapphire. Most of the results reported here are directly applicable to LEO growth of GaN on SiC or Si substrates. We then identify the three main areas open to explanation for the evolution of extended defects in LEO growth: (i) The basis for the growth of dislocation-free wings; (ii) the role of facet orientation in TD redirection; and (iii) the origin of the crystallographic tilt of the LEO wing regions relative to the window region and underlying GaN layer (referred to as "wing tilt"). In this article we focus on topic (i), namely, we develop a model to describe the growth of dislocation-free wing regions. We then briefly discuss TD redirection due to inclined facet formation for the sidewalls of the LEO wing regions and also comment on possible causes for wing tilt.

II. EXPERIMENTAL METHODS AND FEATURES

In our MOCVD LEO studies, we first grew 1–3-μm-thick GaN layers on (0001) sapphire substrates using a standard two-step process.[18] Approximately 200 nm of SiO_2 was then deposited at 250 °C by plasma-enhanced chemical-vapor deposition. Subsequently, 5 to 10 μm wide stripes with periodicity in the range of 10 to 100 μm in either the GaN $\langle 1\bar{1}00\rangle$ or $\langle 11\bar{2}0\rangle$ direction (see Fig. 2) were patterned with conventional photolithography and etched using buffered HF acid. Subsequent MOCVD regrowth was carried out at temperatures in the range of 1015–1100 °C at a reactor pressure of 76 Torr and precursor flow for trimethylgallium of ~50–100 μmol/min and a NH_3 flow in the range of 1–2 slpm. Complete experimental details for the results presented here may be found in Refs. 18 and 19. For the HVPE LEO GaN described below, the reader is referred to the work of Sakai *et al.*[9,20]

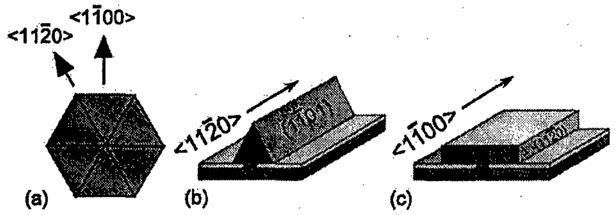

FIG. 2. Typical morphologies of LEO GaN material in relation to crystallographic orientation of stripe windows. (a) Two possible directions of the stripe window with respect to the GaN basal (0001) plane. (b) Triangular morphology with inclined facets for $\langle 11\bar{2}0\rangle$-oriented windows. (c) Rectangular morphology with perpendicular facets for $\langle 1\bar{1}00\rangle$-oriented windows.

A. $\langle 11\bar{2}0\rangle$-oriented stripes

Overgrowth of MOCVD LEO GaN from $\langle 11\bar{2}0\rangle$-oriented stripe window openings will tend to develop a triangular cross section with inclined $\{10\bar{1}1\}$ facets, as shown schematically in Fig. 2(b) and in a micrograph in Fig. 3. Depending on the growth conditions and stripe period, the (0001) basal plane may also appear, lending the stripe a "trapezoidal" cross section. The $\{10\bar{1}1\}$ facets appear to be stable in GaN MOCVD growth under a wide range of conditions – these are the same facets that initiate at threading dislocations in low-temperature GaN or alloy growth and lead to inverted hexagonal pyramids ("V-defects").[21] We also note that it is possible to develop vertical $\{1\bar{1}00\}$ sidewalls perpendicular to the basal plane on $\langle 11\bar{2}0\rangle$-oriented stripes, by using "pulsed" NH_3 LEO at low V/III ratios.[22]

Growth of LEO GaN by HVPE yields a similar morphology to that obtained with MOCVD, shown above. We therefore may assume that the resulting dislocation structure will also be similar [Sakai *et al.* have reported on the similarity in defect structures for MOCVD and HVPE LEO (Ref. 23)]. Cross-section TEM images, shown in Fig. 4, demon-

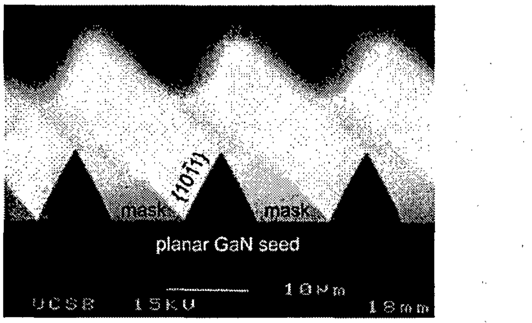

FIG. 3. Cross-section scanning electron microscopy (SEM) micrograph of $\langle 11\bar{2}0\rangle$-oriented stripes grown by MOCVD from 5 μm openings, which are dominated by stable inclined $\{10\bar{1}1\}$ facets.

Downloaded 05 Feb 2003 to 128.111.74.212. Redistribution subject to AIP license or copyright, see http://ojps.aip.org/japo/japcr.jsp

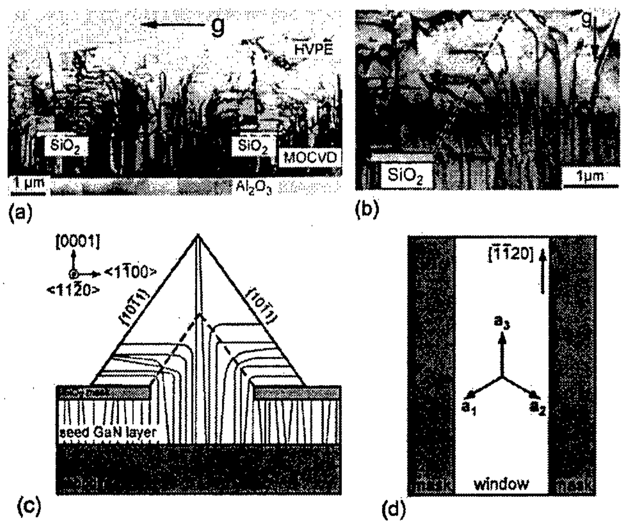

FIG. 4. Threading dislocation behavior in $\langle 11\bar{2}0\rangle$-oriented GaN LEO regions grown by HVPE, after A. Sakai *et al.* (Ref. 9). (a) Cross-sectional TEM micrograph obtained under $g=1\bar{1}00$ diffraction conditions. (b) Cross-sectional TEM micrograph obtained under $g=000\bar{1}$ diffraction conditions. (c) Schematic of dislocation bending in LEO regions. The dashed line is drawn to indicate the projection of $\{10\bar{1}1\}$ facets from the window edges. (d) Plan-view schematic for a specific $[\bar{1}\bar{1}20]$ LEO stripe with three basis vectors $\mathbf{a}_1=1/3[2\bar{1}\bar{1}0]$, $\mathbf{a}_2=1/3[\bar{1}2\bar{1}0]$, and $\mathbf{a}_3=1/3[\bar{1}\bar{1}20]$ shown in the (0001) plane.

strate that the majority of the TDs which have line directions parallel or nearly parallel to [0001] in the underlying planar layer and window region bend laterally into the LEO region and assume line directions in the basal plane. The locus of junctures where the TDs change line directions trace out the position of the $\{10\bar{1}1\}$ facets prior to the formation of the wing regions.

B. $\langle 1\bar{1}00\rangle$-oriented stripes

Growth with $\langle 1\bar{1}00\rangle$-oriented stripes can lead to inclined sidewalls, vertical sidewalls [as presented schematically in Fig. 2(c)], or combinations of both.[18] As shown in Fig. 5, vertical $\{11\bar{2}0\}$ sidewalls are typical for conditions of high temperature and high fill-factor (the ratio of the window opening to the stripe period) whereas inclined $\{11\bar{2}n\}$ facets ($n\sim 1$-2.5) are observed for conditions of lower temperature or low fill-factor. Marchand *et al.* proposed that the sidewall facet morphology is controlled by the "local" V/III ratio during growth.[18]

We have found that the highest-quality wing regions are realized for growth with vertical sidewalls. For these cases [e.g., Fig. 5(c)], the TDs propagate vertically through the window opening and do not extend into the wing regions, as shown in the cross-section TEM image in Fig. 6(a). Plan-view TEM images [e.g., Fig. 6(b)] show that the laterally overgrown GaN is essentially free of TDs and the window openings have a high-TD density. Wu *et al.* and Fini *et al.*[24,25] have shown that the TDs in the underlying GaN (and thus in the window region) result from the coalescence of high-temperature GaN islands. Quite often it is easy to discern a subgrain structure for the TDs in the window region. We will use this result in the modeling section. The inset to the cross-section image in Fig. 6(a) also shows an array of edge dislocations near the window edge. These dislocations are also easily seen in the plan-view image in Fig. 6(b) as relatively long dislocation lines that run parallel to the stripe direction. They are associated with the crystallographic tilt of the wing regions relative to the window openings, as shown schematically in Fig. 7. Later, we will consider the possible causes for the wing tilt. However, here we focus on understanding the basis for defect-free growth of the wing regions.

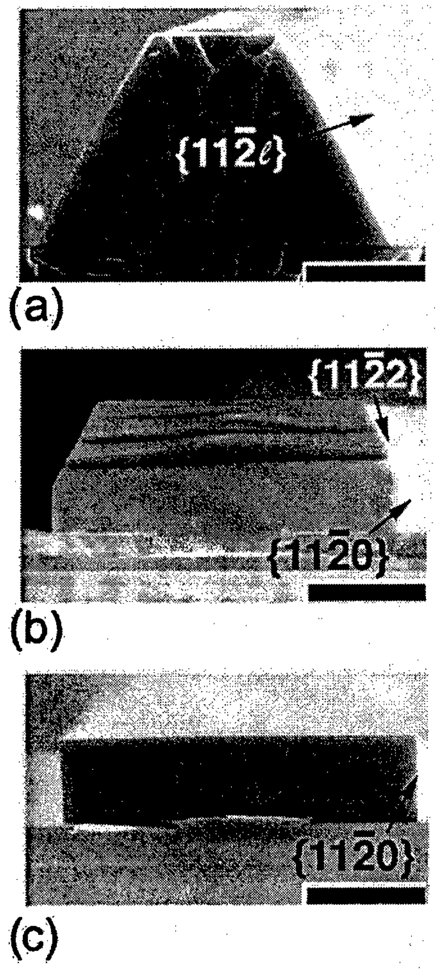

FIG. 5. SEM micrographs of GaN overgrown from 5 μm openings aligned along the $\langle 1\bar{1}00\rangle$. The fill factor is 0.05 and overgrowth time was 15 min. The growth temperatures were: (a) 1015 °C; (b) 1060 °C; and (c) 1100 °C. Each marker represents 5 μm.

III. MODELING SUB-BOUNDARY STABILITY IN LATERAL OVERGROWTH

Figure 8 schematically shows the TD structure for LEO growth (here we neglect boundary TDs associated with wing tilt). Even without analyzing the details of the defect structure, it is clear that the growth with defect-free wings is energetically favorable. TDs are always thermodynamically nonequilibrium defects. Their appearance in growing films is

Downloaded 05 Feb 2003 to 128.111.74.212. Redistribution subject to AIP license or copyright, see http://ojps.aip.org/japo/japcr.jsp

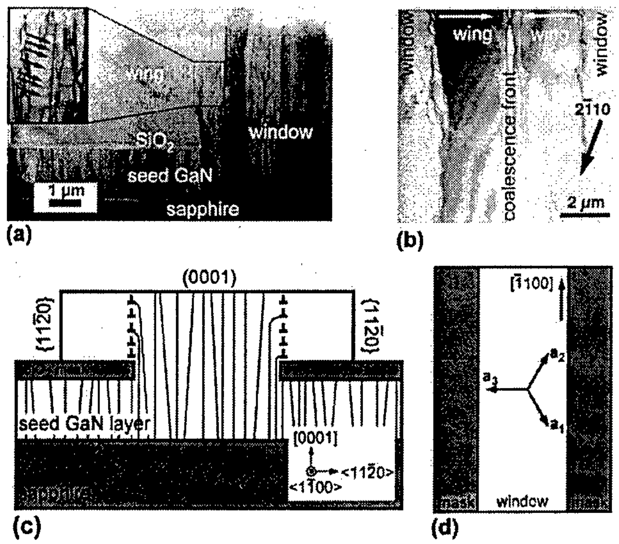

FIG. 6. Threading dislocation behavior in $\langle 1\bar{1}00\rangle$-oriented GaN LEO regions. (a) Cross-section (bright field, $g=1\bar{2}10$) TEM micrograph of GaN overgrown from 5 μm stripe openings with a 0.33 fill factor pattern. The inset is a high-magnification view of the boxed area; the arrows indicate edge dislocations with line directions parallel to the basal plane. (b) Plan-view (bright field, $g=2\bar{1}\bar{1}0$) TEM micrograph of GaN overgrown from 5 μm wide stripe openings with a 0.5 fill factor pattern. The LEO GaN grew laterally from window regions at the left and right of the figure as indicated by the arrows; the coalescence front is at the center of the image. (c) Schematic of TDs in LEO wing and window regions. (d) Plan-view schematic for a specific $[\bar{1}100]$ LEO stripe with three basis vectors $\mathbf{a}_1=1/3[2\bar{1}\bar{1}0]$, $\mathbf{a}_2=1/3[\bar{1}2\bar{1}0]$, and $\mathbf{a}_3=1/3[\bar{1}\bar{1}20]$ shown in the (0001) plane.

only due to kinetically governed processes. When specific kinetic pathways are excluded or suppressed, TDs will not be generated in the film. The suppression of the lateral development of TDs by introducing a mask interlayer is the principal purpose of LEO.

It may happen, however, that defect-free growth of the wings is only possible after overcoming an energy barrier. In this case, the ability of the system to overcome the barrier will determine the final growth mode. The value of the barrier depends on internal factors, such as the type of dislocations, their density, and distribution. External factors, such as growth conditions, will also affect whether the wing regions will grow defect free. To illustrate the possible nature of the energy barrier, consider the schematic defect structure in a LEO window region [Fig. 8(b)] for $\langle 1\bar{1}00\rangle$-oriented stripes with vertical sidewalls. Based on the experimental observations, we may assume that there is a distance x between the edge [designated as α in Fig. 8(b)] of the wing and the interface that separates the LEO window and wing regions [designated as β in Fig. 8(b)]. The interface β is similar to an interphase boundary between a defect phase with internal energy density e_d and a defect-free phase with internal energy density e_f. We take the energy density of the defect-free phase to be the reference and thus define $e_f=0$. By analogy to phase transitions, we assume that there is a specific interfacial energy γ_β associated with the interface between the defect-phase and the defect-free phase (below, we will discuss the origin of γ_β).

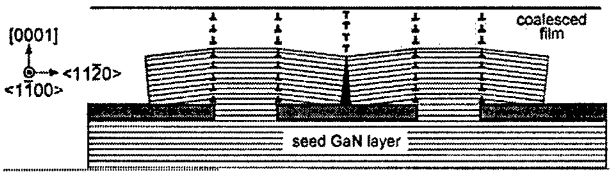

FIG. 7. Schematic of wing tilt and coalescence of two adjacent stripes, with (0001) planes shown in cross section. Hypothetical arrays of edge dislocations (with line directions parallel to stripes) are shown at the edges of the window regions.

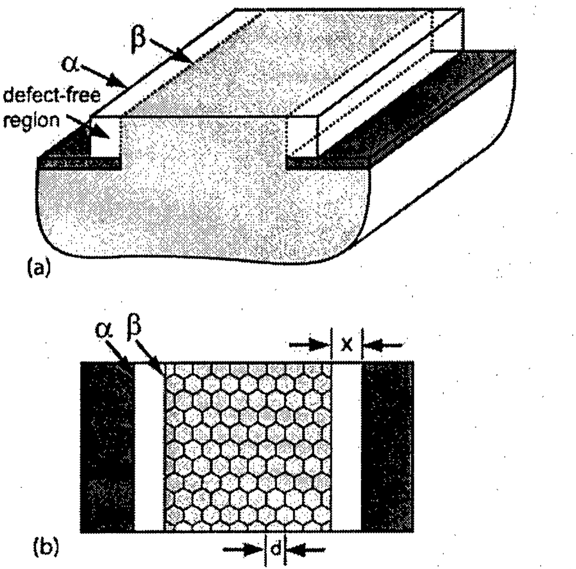

FIG. 8. Schematic illustration of the defect structure development during epitaxial lateral overgrowth with vertical sidewalls. The sidewalls are indicated by α and β, which indicates the interface between high- and low-defect density regions. (a) Perspective view. The regions with high-TD density are indicated by shading. (b) Plan view. The TDs are shown to be arranged in a cell structure with average cell size d.

We now consider the system energy difference per unit interface area between the wing and window region, $\Delta E=E_2-E_1$ for two possible structures: When the wings grow defect free and the interface β forms (E_2); and the case when the wing regions have the same dislocation structure and distribution as the window region (E_1)

$$\Delta E=\gamma_\beta-e_d x. \tag{1}$$

Neglecting the functional dependence of γ_β and e_d, it follows that for distances $x<x_c=\gamma_\beta/e_d$ the formation of defect-free regions is energetically unfavorable. However, at $x>x_c$, defect-free growth is favorable. Thus, there may be an energy barrier for the transition from defected to defect-free growth. In real cases, there can be contributions to γ_β that may depend on the distance x thus changing the value of the barrier.

To proceed further with the energy considerations, we need to develop a physically relevant and analytically tractable model for the dislocation structure in the window regions. It follows from experimental observations that TDs in GaN form a "loose" columnar structure when viewed down the [0001] direction.[24,25] The majority of TDs have edge

Downloaded 05 Feb 2003 to 128.111.74.212. Redistribution subject to AIP license or copyright, see http://ojps.aip.org/japo/japcr.jsp

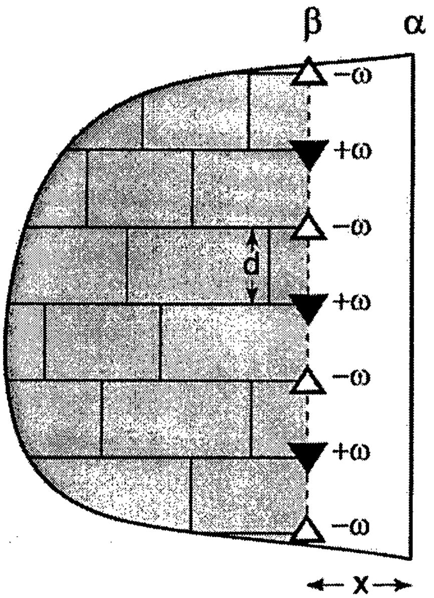

FIG. 9. Plan-view schematic showing the geometry for modeling the defect structure evolution during LEO. The interface β is defined by the termination of subgrain (cell) boundaries. The cell boundary terminations are represented by a chain of wedge disclinations of alternating sign, where the individual disclinations are shown by triangles: ▼ for positive $(+\omega)$ disclinations and △ for negative $(-\omega)$ disclinations.

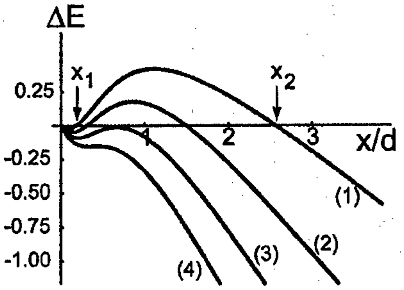

FIG. 10. The energy difference $\Delta E=-e_d x$ for defect-free and defected growth modes for increasing overgrowth distance x. The curves are shown for different values of the parameter $C=4k\,b/d\omega$. Curves (1), (2), (3), and (4) correspond to $C=0.5$, 0.75, 1.0, and 1.25, respectively. The energy is given in units of $G\omega^2 d/4\pi(1-\nu)$. Note that d corresponds to the subgrain size and ω is the average in-plane misorientation between adjacent grains.

character with Burgers vectors $1/3\langle 2\bar{1}\bar{1}0\rangle$. The average cell size is usually from 0.2 to 1.0 μm, misorientations between neighboring cells are in the range of 0.2–0.5°,[25] and the total TD density is of the order of 10^9-10^{10} cm^{-2}.[24,26] A schematic plan-view image of such a structure is shown in Fig. 8(b). Each cell has an average size (column cross-section) d and an average misorientation ω about [0001] between neighboring columns.

To model the energetics of such a structure, we assume that the cells form a pattern with equally spaced boundaries with alternating misorientations $\pm\omega$ to maintain the average orientation in the window region, as shown in Fig. 9. During lateral overgrowth, the sub-boundary pattern may continuously grow into the wing region or the sub-boundaries may abruptly terminate at the interface β between the window and wing regions (note in Fig. 9 that the substructure is now represented by a rectangular cell structure. This pattern has been chosen because in the overgrowth, there is no driving force to form sub-boundaries parallel to the window/wing interface). For the latter case, the cell wall termination becomes a source of additional energy which corresponds to the interfacial energy γ_β. When we accept that the film thickness is much larger than the cell size d and the distance x, then the terminated cell walls can be represented as wedge disclinations of strength $\pm\omega$.[27]

The energy density (per unit area of growing sidewall) of the continuously growing defect phase may be calculated as the energy of cell boundaries γ_{cb}

$$e_d x=\frac{\gamma_{cb}}{d}x=\frac{k}{\pi(1-\nu)}\frac{Gb\omega x}{d}, \tag{2}$$

where we have used the linear dependence of γ_{cb} on the angle of misorientation ω with $k\approx 1$, G is the shear modulus, ν is Poisson's ratio, and b is the magnitude of the Burgers vector. Equation (2) is based on the specific energy of a small angle tilt boundary, which is derived in the framework of simple dislocation models.[28]

The value of γ_β can be determined within the framework of the disclination theory.[22] In such a description, γ_β is associated with the elastic energy of a chain of alternating sign disclinations. The elastic energy E_Δ of period d of the chain near the free surface (sidewall of the growing region) can be calculated by taking into account all interactions between disclinations and also between disclinations and the free surface.[29] The energy E_Δ obviously depends on the distance x of the disclination chain to the surface. It is possible to demonstrate (see Ref. 24) that an expression for E_Δ can be derived in the quadrupole approximation

$$\gamma_\beta=\frac{E_\Delta}{d}=\frac{G\omega^2 d}{4\pi(1-\nu)}\ln\frac{4h^2+d^2}{h^2+d}. \tag{3}$$

In the quadrupole approximation, the energy of a disclination chain is calculated taking into account the interactions between disclinations from two neighboring periods only.[29] Equation (3) gives a finite value for γ_β for $d\rightarrow\infty$ and thus provides the same description as given above in the simple model with a constant γ_β. For small h, $(h\ll d)$, γ_β tends to zero. This behavior helps explain the diminishing barrier for the transition to defect-free lateral overgrowth. To understand the influence of the model parameters on this transition, we plot the dependence of ΔE on the size x of the defect-free region in Fig. 10. When the function $\Delta E(x/d)$ is negative, it is energetically favorable to have growth with defect-free wings. When $\Delta E(x/d)$ is positive, growth with a continuation of the subgrain structure is favored.

There are two types of system behavior, which depend on the parameter $C=4k\,b/d\omega$, as shown in Fig. 10. For $C>1$, the formation of defect-free wings is favorable for any extent of lateral growth x. For $C<1$, there is a range of distances $x_1<x<x_2$ where the existence of the defect phase is favorable. $C=1$ defines the critical combination of model parameters that ensures defect-free lateral growth.

Downloaded 05 Feb 2003 to 128.111.74.212. Redistribution subject to AIP license or copyright, see http://ojps.aip.org/japo/japcr.jsp

IV. DISCUSSION

The stability of dislocation structures (both for individual dislocations or dislocation sub-boundaries) in LEO GaN is an important issue for growing high-quality material on lattice-mismatched substrates. For *c*-plane growth of GaN on common substrates (such as Al_2O_3 or SiC) the majority of the TDs have their line direction parallel to the *c* axis, which is also normal to the surface of the growing film. Experimental studies[24,25] show that the TDs in GaN originate from the coalescence of misoriented islands. They are mainly pure edge TDs with Burgers vectors $\vec{b}=1/3\langle 2\bar{1}\bar{1}0\rangle$ resulting from the coalescence of islands with a twist misorientation about the [0001] axis. These dislocations are not inclined with respect to the film surface and therefore demonstrate lower probability for their mutual reactions.[30] Therefore, the continuous growth of planar layers is not effective in the reduction of TD density in GaN, which is contrary to the phenomena observed for TD reduction in (001) epitaxial growth of cubic materials.[31]

On the level of individual defects, the instability manifests itself as TDs interact with the sidewalls of LEO regions. In the case of inclined $\{10\bar{1}1\}$ sidewall facets, TDs emerge in the plane of these facets during lateral growth. Once emerging, the TDs may change to lateral line directions. As a result, the dislocations in LEO wing regions become "bent," as shown in Fig. 4.

The effect of bending can be understood by considering the energetics of dislocation lines emerging at a free surface of a crystal. From the viewpoint of dislocation line tension (the energy of a dislocation per unit length), any dislocation should tend to become perpendicular to a free surface to diminish its energy. As a result, dislocations gradually change their line direction towards the normal of the facet plane, i.e., $\{10\bar{1}1\}$, as can be seen in Fig. 4. Locally, the change in the direction of the dislocation line is driven by the configurational force, which is caused by elastic interaction of a dislocation with a free surface. This type of interaction was studied in detail both for isotropic and anisotropic crystals.[32] Most commonly when the LEO growth proceeds with inclined facets, such as shown in Fig. 4, the bent dislocations eventually have line directions in the (0001) plane. We attribute this line redirection primarily to two factors. First, if the angle between the sidewall facet plane and the (0001) plane is greater than $\pi/4$, then the dislocation will have shorter line length in the basal plane than parallel to [0001]. The second factor concerns the dislocation energy per unit length, which we now consider.

The line energy of a dislocation depends on both elastic anisotropy and the edge/screw character of the dislocation. For all anisotropic materials, the dislocation energy depends both on the dislocation line direction and Burgers vector,[33] whereas in isotropic materials, the dislocation energy only depends on the dislocation character. For isotropic materials, the energy of screw dislocations is lower by a factor of $1-\nu$ compared to the energy of edge dislocations (here, ν is the Poisson ratio for an isotropic elastic material).[28] Therefore, it may happen that as a result of bending, dislocations acquire more screw component to diminish their energy.

In the case of dislocations in hexagonal crystals (with GaN being a particular example) the above arguments can be supported by quantitative estimates by exploring the analytical results for dislocation energy factors summarized by Savin *et al.*[34] Here, we consider three possible line orientations for dislocations with Burgers vector $1/3\langle 2\bar{1}\bar{1}0\rangle$: (i) Edge dislocation with [0001] line direction (this is the orientation of TDs in the window region and underlying GaN); (ii) edge dislocation with the line direction in the basal plane, and (iii) screw dislocation with the line direction in the basal plane. Using the formalism of Steeds,[33] the energy of a dislocation per unit length is given as $E=Kb^2/4\pi \ln(R/r)$ where K is the so-called energy factor, b is the magnitude of the dislocation Burgers vector, and R and r are the outer and inner cutoff radii of the dislocation elastic field. It follows from the results presented by Savin *et al.* that the dislocation energy factors for these three cases are:

$$K_{\text{edge}}^{\perp}=\frac{C_{11}^2-C_{12}^2}{2C_{11}}, \tag{4a}$$

$$K_{\text{edge}}^{\parallel}=\frac{C_{11}+C_{13}}{C_{33}}\left(\frac{(C_{11}-C_{13})C_{11}C_{44}}{C_{11}+C_{13}+2C_{44}}\right)^{1/2}, \tag{4b}$$

$$K_{\text{screw}}^{\parallel}=\left(\frac{(C_{11}-C_{12})C_{44}}{2}\right)^{1/2}, \tag{4c}$$

where C_{ij} are the elastic constants for a hexagonal crystal under the standard convention of the *c* axis parallel to the axis of transversal isotropy.

Substitution of the elastic constants for GaN (which can be found in the work by Pollian *et al.*[35]) $C_{11}=390$ GPa, $C_{12}=145$ GPa, $C_{13}=106$ GPa, $C_{33}=398$ GPa, and $C_{44}=105$ GPa in Eqs. (4a)–(4c) gives the following energy factors for dislocations in GaN: $K_{\text{edge}}^{\perp}=168$ GPa, $K_{\text{edge}}^{\parallel}=160$ GPa, and $K_{\text{screw}}^{\parallel}=113$ GPa. Comparing these values, we conclude that in the case of a dislocation with its Burgers vector in the basal plane of GaN, the minimum energy will be realized when the line direction is in the basal plane with the lowest-energy value for a dislocation of completely screw character.

Tilting of crystallographic planes in the wing regions may also be understood in the framework of stability of particular dislocation structures in LEO regions. As has been experimentally confirmed [see Figs. 6(a) and 6(b)], one or more edge dislocation arrays form at the edge of the window region of $\langle 1\bar{1}00\rangle$-oriented stripes. The origin of these edge dislocation arrays needs more clarification. They can form, for example, as a result of the bending of existing TDs as shown schematically in Fig. 6(c). In such a case, the reasons for the bending are quite similar to those discussed above for the stripes with triangular cross section. The $\{10\bar{1}1\}$ inclined facets (which are necessary to initiate bending) develop in the direction parallel to the stripes at the nucleation stage of LEO, and correspondingly, dislocations appear to be bent in the direction of stripes but not towards the wing regions.

However, to account for the observed tilt, edge dislocations of only one particular sign must accumulate at the edge of window regions. For such a "directional" bending and accumulation of dislocations of only one sense of the edge

Downloaded 05 Feb 2003 to 128.111.74.212. Redistribution subject to AIP license or copyright, see http://ojps.aip.org/japo/japcr.jsp

component is necessary. For wurtzite crystals, the possible dislocations Burgers vectors in the basal plane are $\mathbf{b}=\pm\mathbf{a}_1$, $\pm\mathbf{a}_2$, and $\pm\mathbf{a}_3$, where $\mathbf{a}_1=1/3[2\bar{1}\bar{1}0]$; $\mathbf{a}_2=1/3[\bar{1}2\bar{1}0]$; and $\mathbf{a}_3=1/3[\bar{1}\bar{1}20]$. We now consider specific crystallographic orientations. For $[\bar{1}\bar{1}20]$-oriented stripes [see Fig. 4(d)] and $[\bar{1}\bar{1}20]$ dislocation line directions, dislocations with Burgers vectors $\mathbf{a}_1$ and $-\mathbf{a}_2$ can both contribute to the tilt in the sense shown in Fig. 7. The $\mathbf{b}=\mathbf{a}_3$ dislocations have their Burgers vectors parallel to the stripe direction and thus cannot contribute to the wing tilt. For $[\bar{1}100]$-oriented stripes [see Fig. 6(d)] and $[\bar{1}100]$ dislocation line directions, all three basal plane Burgers vectors dislocations can contribute to the tilt, however, the $\mathbf{a}_3$ Burgers vector dislocations have twice the edge component as dislocations with $-\mathbf{a}_1$ and $-\mathbf{a}_2$ Burgers vector. Finally, we note that mixed character dislocations with $\mathbf{b}=\pm\mathbf{a}_i\pm\mathbf{c}$ $(i=1,2,3)$ can also be present in the tilt boundary. For these dislocations, the same considerations apply to the basal plane component of the Burgers vector as dislocations with Burgers vector $\pm\mathbf{a}_i$.

A number of recently published articles[36–38] addressed the role of elastic stresses in LEO. However, none of these works clarifies definitive mechanisms for elastic stress generation during the LEO process. One can speculate on various reasons for stress development in LEO samples:

(i) Elastic stresses may arise from a mismatch between the mask material and the film.[36] One possible explanation for this can be a "volume" mismatch between dislocated material inside the window region and dislocation-free material in the wing region. It is known (e.g., Ref. 39) that dislocations change the mass density of crystals. Estimates obtained for dislocations in a geometry similar to the columnar structure of GaN give average volumetric strains of 10^{-5} to 10^{-3} for total dislocation density in the cell walls from 10^{10} to 10^{12} cm^{-2}, respectively.[40] Therefore, for extremely heavily dislocated window regions this volume change can give rise to internal stresses up to 100 MPa.

(ii) Tensile stresses typically preexist in a growing GaN seed layer on sapphire.[41] These tensile stresses likely originate from high-temperature island coalescence and may have a magnitude of 1 GPa for growing GaN films.[41,42] These stresses can be modified near the mask edges due to the difference in thermal expansion coefficients of the mask and the GaN seed. The presence of the Al_2O_3 substrate with its own thermal expansion mismatch is also important.[43]

(iii) The appearance of nonuniform elastic stresses in the GaN film near the mask layer edges can be attributed to surface tension effects in small volumes.[19] Capillary forces near the edges of the mask can be essential but they have a rather limited spatial range.

Regardless of the origin of stress that gives rise to the wing tilt, the tilt boundary dislocations that form at the wing/window interface likely involve climb processes especially at the typical growth temperatures where tilt has been directly measured during growth.[44] The natural slip planes for wurtzite III-N crystals are (0001) and $\{1\bar{1}00\}$. Slip on the $\{10\bar{1}1\}$ planes can only be initiated at extremely high stresses.[45] There is no shear stress on the $\{1\bar{1}00\}$ prism planes for either $\langle 11\bar{2}0\rangle$- or $\langle 1\bar{1}00\rangle$-oriented stripes with uniform sidewalls. Thus, threading dislocations with [0001] line directions have no force on the prism planes to glide. Because the sidewall of the wing region must be free of normal stresses, shear stresses may be present on the (0001) plane near the junction of the wing sidewall and mask. However, there is no experimental evidence for dislocation injection from the sidewall in LEO GaN. Thus, it seems most likely that the tilt boundary dislocations form by climb. This climb can be realized either by "bending" (parallel to the stripe) of existing threading dislocations or by nucleation from the upper surface.

We have shown in the previous section that a qualitative model for the explanation of dislocation-free LEO can be developed based on a simple statement that the state of the film without dislocations (defects) always possesses lower energy. The introduction of an additional "interfacial" energy between the "defect phase" in the window region and the "defect-free phase" in the wing region provides the existence of an energy barrier for the transition from defected growth to defect-free growth. We propose two approaches to define interface energy between phases: (i) Constant interfacial energy (no dependence on the distance to the surface of the wing) and (ii) interfacial energy associated with a disclination chain, which represents the terminated dislocation cell walls in a mosaic structure of GaN. In the latter case, the "interfacial" energy has a dependence on the distance to the growing (moving) free surface of the wing ($\{11\bar{2}0\}$ sidewalls).

Our quantitative model for the stability of defect-free overgrowth is based on the comparison of the energies of a film with a continuously growing dislocation substructure versus one whose substructure terminates abruptly in the material. The energy of the continuously growing structure is proportional to the film growth distance, which is defined as x in Figs. 8 and 9. The energy of the terminated structure calculated in the framework of a disclination approach [given by Eq. (3)] demonstrates saturation at a large growth distance. In this model, there are two possible regimes for lateral growth: No energy barrier to defect-free growth, and growth with a barrier, as shown in Fig. 10. Here, we emphasize the critical parameter of the model (with cell size d and cell misorientation ω) as C, where $C=4kb/d\omega>1$ indicates no barrier defect-free lateral growth. Fini *et al.* demonstrated that the high-temperature GaN growth conditions could be changed such that the GaN cell size and average misorientation could be varied.[25] In the work of Fini *et al.*, the high-TD density material ($\rho_{\mathrm{TD}}\sim10^{10}-10^{11}$ cm^{-2}) had a cell size of ~0.1 μm and an average misorientation of $\sim0.4°$ for 2-μm-thick films—using $k=1$, $d=0.1$ μm, $\omega=0.4°$, and $b=0.32$ nm gives a C value of ~1. The low-TD density material ($\rho_{\mathrm{TD}}<10^{9}$ cm^{-2}) in Fini *et al.* had a cell size of ~0.5 μm and an average misorientation of $\sim0.1°$ for 2-μm-thick films – the corresponding C value for these films is also ~1. Thus, using either type of material as the seed (window region) for LEO, the model predicts growth of defect-free wings – this is consistent with the experimental results shown in Fig. 6(b).

Alternatively, we can assume that all dislocations are in cell walls and have edge character and therefore contribute to

Downloaded 05 Feb 2003 to 128.111.74.212. Redistribution subject to AIP license or copyright, see http://ojps.aip.org/japo/japcr.jsp

the average in-plane cell misorientation ω. The stability condition $C=4k\,b/d\omega>1$ can be rewritten in terms of dislocation density ρ: $\rho<8k\,1/d^2$. Using typically observed values of d from 0.1 to 1.0 μm, ρ ranges from 10^9 to 10^{11} cm^{-2}. We again conclude that the experimentally observed dislocation cell structure in the window region of GaN allows defect-free overgrowth in the wing regions.

Finally, we outline the similarity between the problems of dislocation cell (subgrain) stability and misfit dislocation (MD) generation in elastically stressed epitaxial layers growing on thick substrates. In the latter case, the Matthews–Blakeslee critical thickness $h_c\approx b/f$ (where b is the magnitude of the MD Burgers vector, and f is crystal lattice mismatch between layer and substrate) describes the equilibrium thickness where MD formation becomes favorable at the layer/substrate interface.[46] Below h_c, it is energetically favorable to have an elastically strained layer with the stored energy proportional to its thickness. We note that in the case of a dislocation cell structure, the stored energy of the "defect phase" is also linear with the growing layer thickness. Far above the critical thickness h_c, the stored energy of the layer/substrate system in the fully relaxed state is associated with interfacial energy, which in practice does not depend on layer thickness for $h\gg h_c$. In the case of a subgrain/defect-free region boundary, the energy of the disclination chain also becomes independent of the defect-free wing size.

The above analogy allows us to introduce a critical distance (designated as x_2) above which defect-free growth becomes favorable. This distance x_2 is analogous to h_c. However, in consideration of the stability of subgrain structure we have introduced additional parameters: Namely, subgrain size d and the average in-plane misorientation ω. As a result, the value equivalent to misfit f strain is analogous to the dimensionless parameter $b\omega/d$. The critical distance x_2 and the energy release ΔE (shown in Fig. 10) both depend on $b\omega/d$. The condition $\Delta E=0$ defines the collapse of x_2 and x_1 at some critical value x_c for the prescribed condition $C=4k\,b/d\omega=1$. We can therefore classify the problem of subgrain stability as a double critical thickness problem. The first critical thickness (x_2) is quite similar to the critical thickness h_c known in lattice-mismatch epitaxy. The second critical thickness has a different meaning – it permits one to define an additional relationship between the parameters of the subgrain structure that allows defect-free overgrowth.

V. SUMMARY AND CONCLUSIONS

In this study, we have addressed the problem of extended defect structure stability during lateral epitaxial overgrowth of GaN. We have reported on experimental results for LEO growth of GaN on sapphire. These results describe the development of different growth morphology and dislocation structure in relation to the crystallographic orientation of the window openings from which LEO proceeds.

For $\langle 11\bar{2}0\rangle$-oriented stripe window openings, the LEO material exhibits a triangular cross section with inclined $\{10\bar{1}1\}$ facets. The threading dislocations (TDs) growing up in the window region become unstable and bend toward inclined facets. Eventually, the lines of bent TDs may become parallel to the (0001) basal plane of GaN. We attribute the effect of bending to the emergence of TDs at inclined facets and the dependence of dislocation self energy on the orientation of dislocation line direction in the anisotropic wurtzite structure.

In the case of LEO from $\langle 1\bar{1}00\rangle$-oriented stripes, the conditions of growth can be readily found for which vertical sidewalls develop. These conditions provide material in the wing regions with the lowest density of extended defects. Most of the TDs grow straight up in the window regions and remain in cell walls (subgrain boundaries). This columnar cell structure is thought to originally form as a result of island coalescence during growth of the GaN layer on a mismatched substrate. Two effects of dislocation structure stability are important for LEO from stripes: (i) Growth of dislocation-free wings and (ii) the origin of the crystallographic tilt of the LEO wing regions relative to the window region. We relate the observed tilt to the appearance of edge dislocation arrays in the transition region between windows and wings, and discussed possible causes for the formation of such dislocation arrays.

The main modeling effort in this article has been focused on understanding the growth of dislocation-free wing regions. We presented a quantitative model for the analysis of dislocation sub-boundary cell structure stability during lateral growth. The model is based on the results obtained in the framework of a disclination approach and describes sub-boundary cell structure stability as a double critical thickness problem. The model provides a relation between structural parameters (such as cell size and misorientation) under which lateral defect-free growth is possible. It has been shown that LEO from a GaN seed layer with a typical subgrain size from 0.1 to 1.0 μm, a subgrain misorientation $<1°$, and a total dislocation density from 10^9 to 10^{11} cm^{-2} satisfies the conditions for defect-free growth.

ACKNOWLEDGMENTS

This work was supported in part by AFOSR (D. Johnstone and G. Witt), DARPA (W. Coblenz), and ONR (J. Zolper and Colin Wood). Support for AER was also provided by the program "Physics of Solid State Nanostructures" by the Ministry of Industry and Science of Russia.

[1] S. J. Rosner, E. C. Carr, M. J. Ludowise, G. Girolami, and H. I. Erikson, Appl. Phys. Lett. **70**, 420 (1997).

[2] T. Sugahara, H. Sato, M. S. Hao, Y. Naoi, S. Kurai, S. Tottori, K. Yamashita, K. Nishino, L. T. Romano, and S. Sakai, Jpn. J. Appl. Phys., Part 2 **37**, L398 (1998).

[3] N. G. Weimann, L. F. Eastman, D. Doppalapudi, H. M. Ng, and T. D. Moustakas, J. Appl. Phys. **83**, 3656 (1998).

[4] D. C. Look and J. R. Sizelove, Phys. Rev. Lett. **82**, 1237 (1999).

[5] J. L. Farvacque, Z. Bougrioua, and I. Moerman, Phys. Rev. B **63**, 115202 (2002).

[6] J. S. Speck and S. J. Rosner, Physica B **273–274**, 24 (1999).

[7] T. S. Zheleva, O. H. Nam, M. D. Bremser, and R. F. Davis, Appl. Phys. Lett. **71**, 2472 (1997).

[8] O. H. Nam, M. D. Bremser, T. S. Zheleva, and R. F. Davis, Appl. Phys. Lett. **71**, 2638 (1997).

[9] A. Sakai, H. Sunakawa, and A. Usui, Appl. Phys. Lett. **71**, 2259 (1997).

[10] C. Sasaoka, H. Sunakawa, A. Kimura, M. Nido, A. Usui, and A. Sakai, J. Cryst. Growth **189/190**, 61 (1998).

[11] J. Wang, R. S. Qhalid Fareed, M. Hao, S. Mahanty, S. Tottori, Y. Ishikawa,

Downloaded 05 Feb 2003 to 128.111.74.212. Redistribution subject to AIP license or copyright, see http://ojps.aip.org/japo/japcr.jsp

T. Sugahara, Y. Morishima, K. Nishino, M. Osinski, and S. Sakai, J. Appl. Phys. **85**, 1895 (1999).

[12] K. Hiramatsu, K. Nishiyama, A. Motogaito, H. Miyake, Y. Iyechika, and T. Maeda, Phys. Status Solidi A **176**, 535 (1999).

[13] Z. Liliental-Weber and D. Cherns, J. Appl. Phys. **89**, 7833 (2001).

[14] S. Nakamura, M. Senoh, S.-I. Nagahama, N. Iwasa, T. Yamada, T. Matsushita, H. Kiyoku, Y. Sugimoto, T. Kozaki, H. Umemoto, M. Sano, and K. Chocho, Jpn. J. Appl. Phys., Part 2 **36**, L1568 (1997).

[15] P. Kozodoy, J. P. Ibbetson, H. Marchand, P. T. Fini, S. Keller, J. S. Speck, S. P. DenBaars, and U. K. Mishra, Appl. Phys. Lett. **73**, 975 (1998).

[16] L. McCarthy, I. Smorchkova, H. Xing, P. Fini, S. Keller, J. S. Speck, S. P. DenBaars, M. J. W. Rodwell, and U. Mishra, Appl. Phys. Lett. **78**, 2235 (2001).

[17] N. Kuroda, C. Sasaoka, A. Kimura, A. Usui, and Y. Mochizuki, J. Cryst. Growth **189/190**, 551 (1998).

[18] H. Marchand, J. P. Ibbetson, P. T. Fini, S. Keller, S. P. DenBaars, J. S. Speck, and U. K. Mishra, J. Cryst. Growth **195**, 328 (1998).

[19] P. Fini, H. Marchand, J. P. Ibbetson, S. P. DenBaars, U. K. Mishra, and J. S. Speck, J. Cryst. Growth **209**, 581 (2000).

[20] A. Sakai, H. Sunakawa, and A. Usui, Appl. Phys. Lett. **73**, 481 (1998).

[21] X. H. Wu, C. R. Elsass, A. Abare, M. Mack, S. Keller, P. M. Petroff, S. P. DenBaars, J. S. Speck, and S. J. Rosner, Appl. Phys. Lett. **72**, 692 (1998).

[22] R. S. Qhalid Fareed, J. W. Yang, J. Zhang, V. Adivarahan, V. Chaturvedi, and M. Asif Khan, Appl. Phys. Lett. **77**, 2343 (2000).

[23] A. Sakai, H. Sunakawa, A. Kimura, and A. Usui, Appl. Phys. Lett. **76**, 442 (2000).

[24] X. H. Wu, P. Fini, E. J. Tarsa, B. Heying, S. Keller, U. K. Mishra, S. P. DenBaars, and J. S. Speck, J. Cryst. Growth **189/190**, 231 (1998).

[25] P. Fini, X. Wu, E. J. Tarsa, Y. Golan, V. Srikant, S. Keller, S. P. DenBaars, and J. S. Speck, Jpn. J. Appl. Phys., Part 1 **37**, 4460 (1998).

[26] K. A. Dunn, S. E. Babcock, R. Vaudo, V. Phanse, and J. Redwing, Mater. Res. Soc. Symp. Proc. **482**, 417 (1998).

[27] A. E. Romanov and V. I. Vladimirov, in *Dislocation in Solids*, edited by F. R. N. Nabarro (Elsevier, New York, 1992), Vol. 9, p. 241.

[28] J. P. Hirth and J. Lothe, *Theory of Dislocations*, 2nd ed. (Wiley, New York, 1982).

[29] A. E. Romanov, M. J. Lefevre, J. S. Speck, W. Pompe, S. K. Streiffer, and C. M. Foster, J. Appl. Phys. **83**, 2754 (1998).

[30] S. K. Mathis, A. E. Romanov, L. F. Chen, G. E. Beltz, W. Pompe, and J. S. Speck, J. Cryst. Growth **231**, 371 (2001).

[31] J. S. Speck, M. A. Brewer, G. Beltz, A. E. Romanov, and W. Pompe, J. Appl. Phys. **80**, 3808 (1996).

[32] J. Lothe, in *Elastic Strain Field and Dislocation Mobility*, edited by V. L. Indenbom and J. Lothe, (North-Holland, Amsterdam, 1992), p. 329.

[33] J. W. Steeds, *Introduction to Anisotropic Elasticity Theory of Dislocations*. (Oxford University, New York, 1973).

[34] M. M. Savin, V. M. Chernov, and A. M. Strokova, Phys. Status Solidi A **35**, 747 (1976).

[35] A. Pollian, M. Grimsditch, and I. Grzegory, J. Appl. Phys. **79**, 3343 (1996).

[36] S. Einfeldt, A. M. Roskowski, E. A. Preble, and R. F. Davis, Appl. Phys. Lett. **80**, 953 (2002).

[37] Z. Feng, E. Lovell, R. Engelstad, T. Kuech, and S. Babcock, Appl. Phys. Lett. **80**, 1547 (2002).

[38] M. Benyoucef, M. Kuball, B. Beaumont, and P. Gibart, Appl. Phys. Lett. **80**, 2275 (2002).

[39] A. Seeger and P. Haasen, Philos. Mag. **3**, 470 (1958).

[40] A. A. Nazarov, A. E. Romanov, and R. Z. Valiev, Scr. Mater. **34**, 729 (1996).

[41] T. Böttcher, S. Einfeldt, S. Figge, R. Chierchia, H. Heinke, D. Hommel, and J. S. Speck, Appl. Phys. Lett. **78**, 1976 (2001).

[42] J. Han, K. E. Waldrip, S. R. Lee, J. J. Figiel, S. J. Hearne, G. A. Petersen, and S. M. Myers, Appl. Phys. Lett. **78**, 67 (2001).

[43] T. S. Zheleva, W. M. Ashmawi, O.-H. Nam, and R. F. Davis, Appl. Phys. Lett. **74**, 2492 (1999).

[44] P. Fini, A. Munkholm, C. Thompson, G. B. Stephenson, J. A. Eastman, M. V. R. Murty, O. Auciello, L. Zhao, S. P. DenBaars, and J. S. Speck, Appl. Phys. Lett. **76**, 3893 (2000).

[45] A. Seifert, A. Berger, and W. F. Muller, J. Am. Ceram. Soc. **75**, 873 (1992).

[46] J. W. Mathews and A. E. Blakeslee, J. Cryst. Growth **27**, 118 (1974).

Downloaded 05 Feb 2003 to 128.111.74.212. Redistribution subject to AIP license or copyright, see http://ojps.aip.org/japo/japcr.jsp